The Design and Performance of a Twenty Barrel Hydrogen Pellet Injector for Alcator C-Mod

John A. Urbahn

Plasma Fusion Center
Massachusetts Institute of Technology
Cambridge, MA 02139

May 1994

THE DESIGN AND PERFORMANCE OF A TWENTY BARREL HYDROGEN PELLET INJECTOR FOR ALCATOR C-MOD

by

John A. Urbahn

B.S. in Physics, University of Connecticut
B.S. in Mechanical Engineering, University of Connecticut
(1984)

Submitted to the Department Of Nuclear Engineering
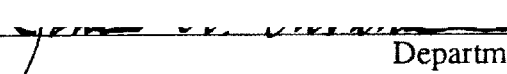in partial fulfillment of the Requirements for the Degree of

Doctor of Philosophy
in Fusion Technology

at the

Massachusetts Institute of Technology

March 1994

Signature of Author_____
Department of Nuclear Engineering

Certified by_____
Dr. Martin J. Greenwald
Thesis Supervisor

Accepted by_____
Dr. Ian H. Hutchinson
Thesis Reader

Accepted by_____
Allan F. Henry
Chairman, Department Committee on Graduate Students

1

THE DESIGN AND PERFORMANCE OF A TWENTY BARREL HYDROGEN PELLET INJECTOR FOR ALCATOR C-MOD

by

John A. Urbahn

Submitted to the Department Of Nuclear Engineering in partial
fulfillment of the Requirements for the Degree of Doctor of Philosophy in
Fusion Technology

ABSTRACT

A twenty barrel hydrogen pellet injector has been designed, built and tested both in the laboratory and on the Alcator C-Mod Tokamak at MIT. The injector functions by firing pellets of frozen hydrogen or deuterium deep into the plasma discharge for the purpose of fueling the plasma, modifying the density profile and increasing the global energy confinement time.

The design goals of the injector are: 1) Operational flexibility, 2) High reliability, 3) Remote operation with minimal maintenance. These requirements have lead to a single stage , pipe gun design with twenty barrels. Pellets are formed by *in-situ* condensation of the fuel gas, thus avoiding moving parts at cryogenic temperatures. The injector is the first to dispense with the need for cryogenic fluids and instead uses a closed cycle refrigerator to cool the thermal system components. The twenty barrels of the injector produce pellets of four different size groups and allow for a high degree of flexibility in fueling experiments. Operation of the injector is under PLC control allowing for remote operation, interlocked safety features and automated pellet manufacturing. The injector has been extensively tested and shown to produce pellets reliably with velocities up to 1400 m/sec.

During the period from September to November of 1993, the injector was successfully used to fire pellets into over fifty plasma discharges. Experimental results include data on the pellet penetration into the plasma using an advanced pellet tracking diagnostic with improved time and spatial response. Data from the tracker indicates pellet penetrations were between 30 and 86 percent of the plasma minor radius. Line averaged density increases of up to 300 percent were recorded with peak densities of just under $1 \times 10^{21} / m^3$, the highest achieved on C-Mod to date. A comparison is made between the ablation source function derived from tracker data with that predicted by four different variations of the neutral shield model. Results suggest rapid heat flow from the interior of the plasma maintains temperatures on the ablation flux surface. Localized density perturbations with a specific m=1,n=1 structure and location on the q=1 flux surface were observed following injection .

Thesis Supervisor: Dr. Martin Greenwald

Titles: Principal Research Scientist

For Deyanne

TABLE OF CONTENTS

4

Chapter 5: Injector Diagnostics

Chapter 6 : Initial Injection Experiments

Chapter 7 : Conclusions

Chapter 1 : Background and Motivation
For Pellet Fueling

1.1   Fusion Essentials

Fusion is the process by which two light nuclei join to create a single heavier nuclei plus reaction products and energy. The reactions of greatest interest to fusion researchers are:

$$^2D + {}^2D \rightarrow {}^3He(.82MeV) + {}^1n(2.45MeV) \tag{1.1}$$

$$^2D + {}^2D \rightarrow {}^3T(1.01MeV) + {}^1H(3.02MeV) \tag{1.2}$$

$$^2D + {}^3T \rightarrow {}^4He(3.5MeV) + {}^1n(14.1MeV) \tag{1.3}$$
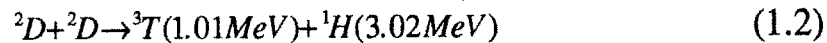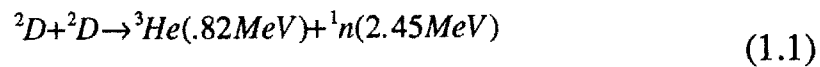
Of these, reaction (1.3) has the largest reaction cross section for temperatures below twenty keV and is therefore the easiest to achieve in the laboratory. Fusion energy, along with fission and solar are the three most plausible sources for mankind's long term energy needs. Fossil fuels are anticipated to be seriously depleted within one to two centuries (2).Well before that time however , their use is expected to cause serious environmental degradation , only the degree to which is uncertain.   Though not technologically mature, fusion is a theoretically attractive energy alternative for three reasons:

1)   <u>Abundant fuel Supply</u>:   Deuterium is available in enormous quantities since it occurs as .015 percent of all naturally occurring hydrogen (2). Earth's oceans contain enough deuterium to meet the word's energy demand for millions of years. Tritium has a 12.3 year half life, and therefore does not exist naturally in any abundance. It may however be bred in fusion reactors by bombarding lithium with fusion neutrons.
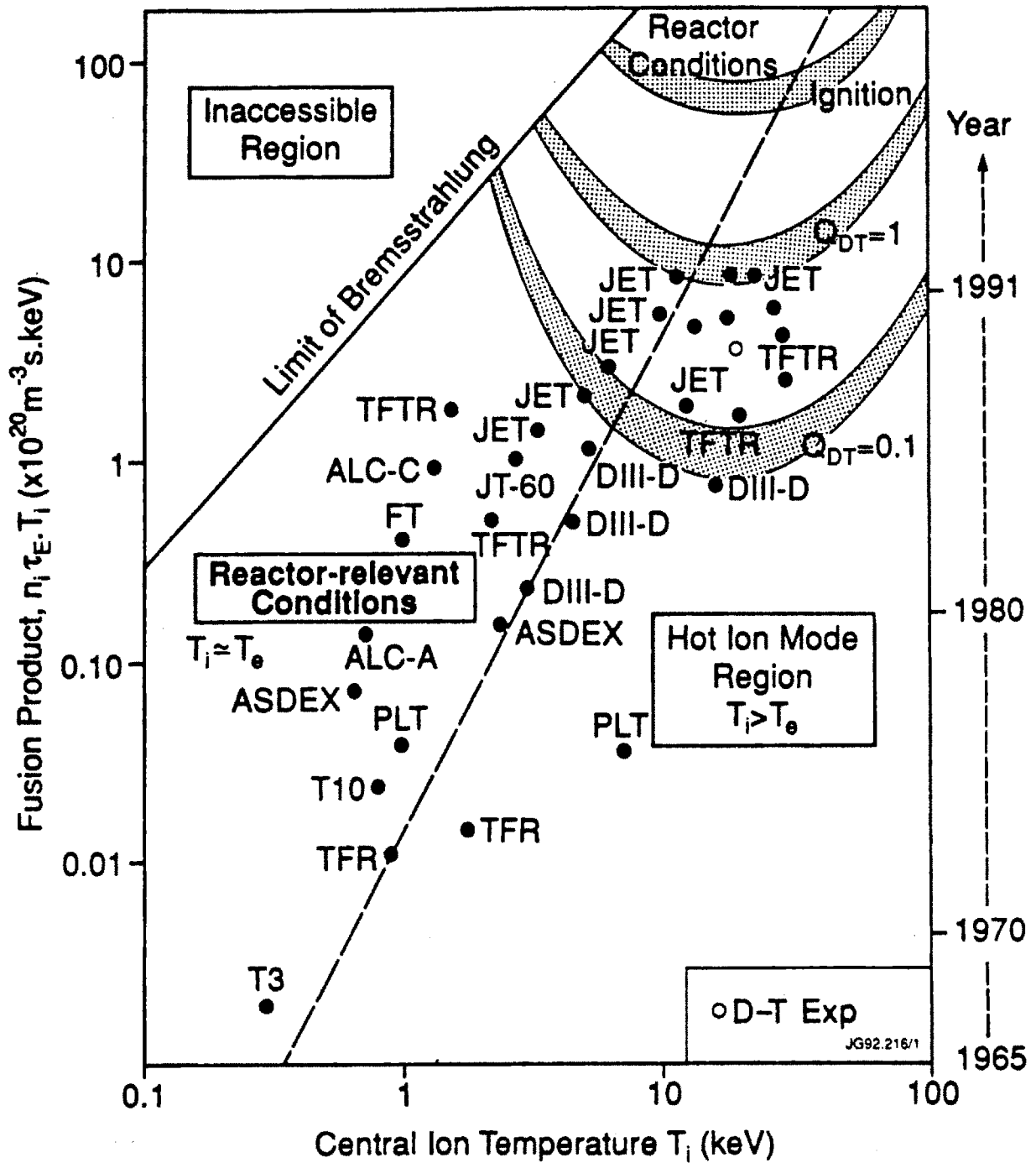
Currently known lithium reserves used in fusion fuel cycles could provide 3000 times the 1970 world energy consumption, and this figure does not include the potential reserve present in sea water [2].

2) Safety: probably a more important issue in the near term than fuel availability, is that of safety. Fusion reactors have a greater inherent safety than fission reactors because fusion reactors operate with radioactive fuel inventories many orders of magnitude smaller than fission reactors , and while tritium is more mobile than fission products , it has a short biological and physical half life. A systems failure in a fusion reactor would , in general, imply a "snuffing out" of the reaction since the reaction conditions are critical and require active systems to maintain them. This is not the case for conventional fission reactors where reactor cooling and shutdown are generally dependent on active systems.

3) Environmental: Fusion reactors cannot be sold to the public as "radiation free" since neutrons produced in the reaction activate vessel wall materials. Analysis by Holdren [5][2] and others has shown that by carefully selecting the first wall and blanket materials with respect to activation cross section and radioactive half life, the radioactive inventory may be reduced between one and three orders of magnitude compared to fission reactors for equal decay times.

The preceding arguments for the benefits of fusion energy form the motivation for fusion research, the majority of which has been directed towards creating the conditions under which the reaction can be sustained in a controlled way. For deuterium and tritium, the required temperature is between ten and twenty keV and the Lawson parameter, $n\tau$, or central density times confinement time must exceed 6×10^{19} sec/ m^3 . These parameters have not been achieved simultaneously to date, but progress towards the goal has been steady as shown in Fig. 1.1.1. Once these conditions are reached in a research facility, there still remains the equally challenging task to design reactors which are both reliable and attractive economically.

Spontaneous fusion does not occur in low temperature matter because of the coulomb energy barrier between nuclei. This barrier may be overcome by supplying reacting nuclei with an energy comparable to the coulomb energy. In thermonuclear fusion, this kinetic energy is not directed as in a beam, but thermal as in the velocity

8

Fig1.1.1: Fusion figures of of merit. Fusion triple product $n_i \tau_e T_i$ versus T_i with the year results were achieved on the right . (extracted from ref. (19) JET-P(92)91)

distribution of a gas. Here however, the temperature must be high enough to create a plasma; a charged collection of nuclei and electrons . Fusion reactions in the plasma occur primarily between nuclei in the high energy 'tail' of the Maxwellian thermal distribution.

In stars, gravitational forces create the high pressures and temperatures needed to fuse nuclei. Creating these conditions in a reactor using gravitational forces would be impractical because of the scale requirements. A comparison of the electromagnetic and gravitational forces between like nuclei show the electromagnetic force to be a least thirty five orders of magnitude stronger than the gravitational . Because charged particles are confined to move along field lines, magnetic fields may be used to hold the plasma and keep it away from material walls. This approach is termed " magnetic confinement".

1.2   Tokamaks

The magnetic field geometry which has been the most successful at confining plasmas has been that of the Tokamak, the essential components of which are shown in Fig. 1.2.1. In a Tokamak, the plasma is created by filling a toroidal vacuum vessel with a gas such as hydrogen, and inducing a current to flow toroidally by induction. Once the current begins to flow, the gas breaks down and forms a plasma which acts as the secondary of a transformer, the primary being the "ohmic heating coil" usually located within the center of the torus. The plasma thus created is stabilized by a powerful toroidal magnetic field generated by magnets external to the vacuum chamber. The toroidal and ohmic heating coils are complimented by the "equilibrium" field coils. These coils carry current in the toroidal direction and act both to affect the shape of the plasma and to provide radial equilibrium for the plasma. In a modern tokamak, the ohmic heating and equilibrium field coils form an integrated system called the poloidal field system. The combination of plasma current, and currents in the toroidal and poloidal field coils generates the complex magnetic field geometry of a tokamak.

induction coils
poloidal coils (OHMIC HEATING)   toroidal coils

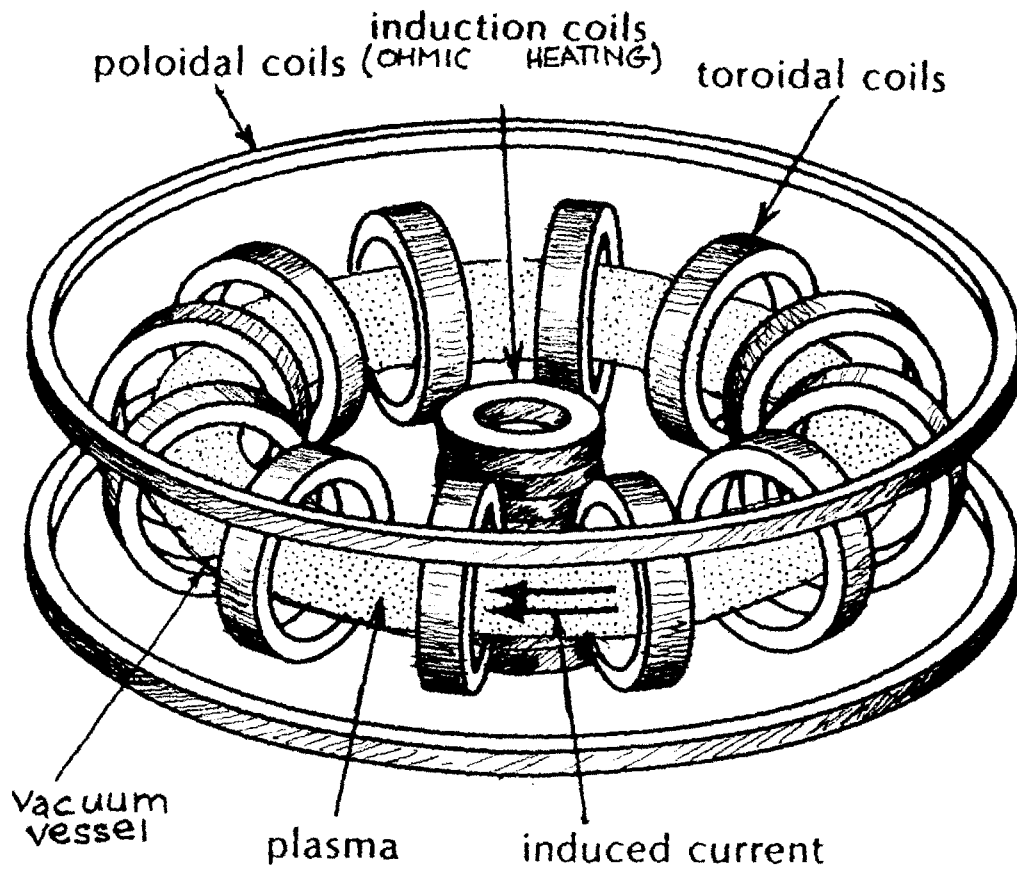Vacuum vessel   plasma   induced current

Fig. 1.2.1: Schematic drawing of a tokamak showing the toroidal, poloidal and OH field coils.

This field can best be visualized as a series of nested and closed toroidal helices, where the degree of twist increases towards the center of the plasma cross section. Since the plasma current in a tokamak is driven inductively, reactor designs must operate with either a finite pulse length or employ some form of non-inductive current drive. Plasma heating by current flow becomes less effective as temperatures rise, therefore most advanced tokamaks have some form of auxiliary heating installed either in the form of neutral beam injection or radio frequency heating.

1.3   Alcator C-Mod

The Alcator C-Mod tokamak is the third in a series of tokamak experiments at MIT designed to investigate the compact, high field approach towards tokamak design. Alcator C, the predecessor to C-Mod, achieved a record Lawson parameter, $n\tau$ of 8 x 10^{19} sec / m^3, a value in excess of the Lawson Parameter. Both Alcators A and C were of conventional circular cross section and employed toroidal field coils of Bitter plate construction.

The Alcator C-Mod design is similar to Alcator A and C in its high field compact design but differ in that it incorporates the successful design features of more modern tokamaks. These features include a non-circular , or shaped plasma cross section, a poloidal divertor, and strong ICRF heating. The C-Mod vacuum vessel and coil configuration (shown in figure 1.3.1) also provides for greater access to the plasma, allowing greater freedom in the design and implementation of plasma diagnostics and heating methods.

The C-Mod toroidal field system consists of twenty jointed toroidal field coils of six turns each. The coils represent a novel design approach in that the coils are composed of a central core with separate outer horizontal and vertical coil segments. These segments are connected with sliding joints capable of carrying high current density. The sliding joints allow for a toroidal coil system which is demountable permitting the installation of a single piece vacuum vessel and internal poloidal field coils. The magnetic forces on the TF coils are taken in part, by a massive stainless steel
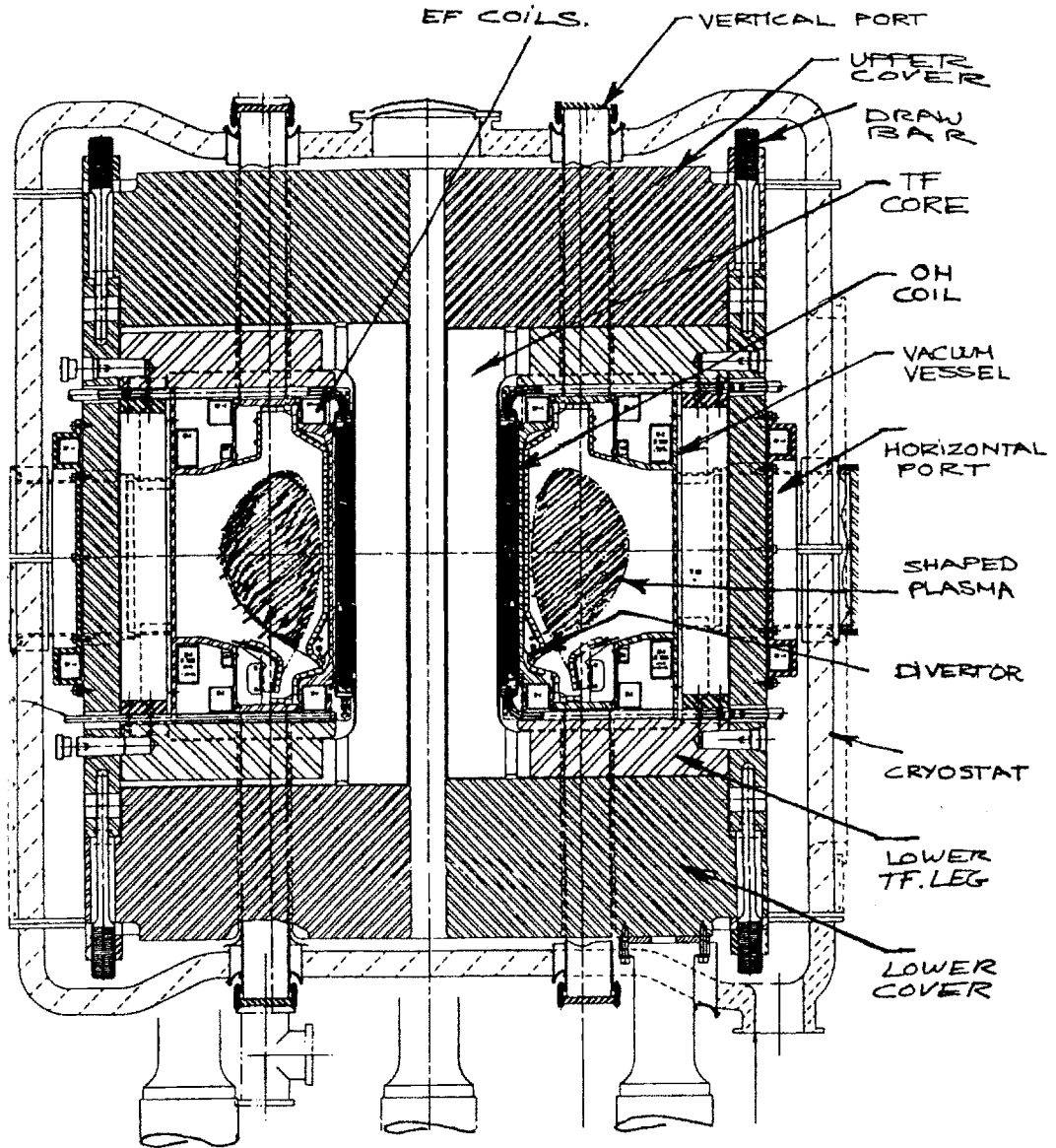
Major Radius	R	=	0.665 m.	Triangularity	,	δ =	0.4	
Minor Radius	a	=	0.21 m.	Flat-top Duration	$_\ominus$ τ =	1		s
Toroidal Field	B_T	=	9 T.		$\ominus$ ST =	7		s
Plasma Current	I_p	=	3 MA.	Inductive Volt-seconds = 7.5				Wb
Elongation	κ	=	1.8 (typical)	Required energy	=	500		MJ.

Fig. 1.3.1: Cross section of the Alcator C-Mod tokamak and machine parameters.

external superstructure. Permitting the coils to bear directly against this superstructure reduces the TF coil internal forces. The single piece vacuum vessel design allows far greater structural integrity than a segmented vessel. This gives the vessel greater rigidity when subjected to eddy current induced forces and allows the vessel to serve as the structural mount for the poloidal field coils.

The poloidal field coils consist of an upper and lower set of five coils each. These coils acting together with the ohmic heating coils provide for plasma shaping, stability, and current control. The size and current requirements of these coils are greatly reduced by the close proximity to the plasma afforded by the demountable toroidal field magnets.

The objectives of the Alcator program may be broadly separated into four groups:

1)   Explore the confinement properties of a compact ohmically heated, high field tokamak with advanced shaping and a single piece vacuum vessel.

2)   Study ICRF heating on high density, shaped tokamak plasmas and establish its' applicability to ignited reactor like plasmas.

3)   Investigate different regimes of divertor operation on C-Mod and study the effect on confinement with and without auxiliary heating. Divertor operation on C-Mod could provide results relevant to the design of the ITER divertor configuration.

4)   Investigate the control of density profiles (via pellet injection) and temperature and current profile (via RF heating) and its effect of stability and confinement. The effect of plasma shaping plus edge and impurity control will also be explored.

1.4 Tokamak Fueling

In any steady state or long pulse reactor, fuel Ions lost through D-T fusion must be replaced . As an example, to generate 1 GW of power, a reactor would need to fuse about .002 grams per second of deuterium and tritium. The actual fueling rate required could be two orders of magnitude greater since most fuel ions are pumped away before undergoing fusion. Short pulse length experiments also require some form of fueling to maintain density profiles because energetic fuel ions are buried in the first few micro meters of the vacuum chamber or limiter.

Fueling of tokamak discharges may be done with edge fueling by gas puffing or by direct injection with either neutral beams or solid pellets. Plasmas are gas fueled when neutrals enter the tokamak and ionize forming a cold plasma at the edge of the discharge. These ions diffuse inwards against the density gradient. Inward diffusion may be assisted by ExB drifts in the radial direction. Experiments performed on Alcators A and C showed anomalous radial particle transport whereby fuel ions were convected radially inwards at a rate much greater than that predicted by neoclassical theory [2] . One worrisome aspect in all this is that the same anomalous transport processes which are so helpful in converting fuel ions inwards from the plasma edge may also convect energy away from the plasma core. Therefore, measures which improved energy confinement might decrease the effectiveness of gas fueling.

Modern tokamaks such as Alcator C-Mod employ highly pumped diverted discharges. Gas puffing to maintain density profiles in these discharges would likely be inefficient since the majority of fuel ions introduced would be unable to penetrate beyond the scrape off layer plasma [5,6]. Attaining H-Mode in tokamak plasmas has been shown to be aided by steep edge temperature gradients. While H-Mode has been obtained in gas fueled discharges, pellet fueling is effective in obtaining the steep edge temperature gradients. Gas fueling, on the other hand, tends to increase the plasma density between the scrape off layer and the vacuum vessel, thereby enhancing recycling and impurity production.

Effective fueling of diverted discharges requires that the fuel be injected directly into the plasma, at least beyond the scrape off layer. This was first proposed by Lyman

Spitzer as early as 1954 and later by Rore [1]. Such methods might include injection of solids, liquid hydrogen, or neutral beam injection. Neutral beam injection when viewed solely as a method of fueling is extremely energy intensive. As an example, a typical reactor might require beam energies of around 100 keV coupled with 10's of kilo amps of current. [1]. This leads to beam powers in the gigawatt range. Neutral beam injection becomes even less attractive when the high cost and complexity of the injection system is considered.

1.5 Pellet Injection Experiments

The first pellet injection experiments were performed with frozen hydrogen pellets of 10 m/sec. velocity into an ExB rotating plasma ,"Puffatron" . In a similar way, pellets were dropped into the Pulsator vessel and the discharge was fired when the pellet reached the tokamak center.

The first experiments with pellets injected at moderate velocity were made by Foster and others on the ORMAK tokamak at Oak Ridge National Laboratory [6]. In these experiments, liquid hydrogen droplets were injected with a velocity of 100 m/sec. The small pellet size (100 μg) and modest speed allowed for only a small density increases of 1% and a penetration of only 8 cm. These experiments were followed by work on the ISX A and B tokamaks at ORNL [8]. For these experiments, injection velocities were over 1000 m/sec, and plasma mass was doubled by the injection process. In the ISX B tokamak, the density could be raised by over 300% and energy confinement was found to improve from 9 to 25 m/sec. Following these experiments, systems for freezing and injecting hydrogenic pellets were installed on a large number of plasma confinement devices.

In 1982, pellet injection experiments commenced on the Alcator C tokamak at MIT, and were primarily motivated by the desire to study the effects of density profile modification on anomalous thermal losses. The density profiles obtained with gas fueling on Alcator C were relatively flat, and models of anomalous ion thermal diffusivity by Coppi and others predicted that peaked density profiles would reduce losses through the Ion thermal loss channel [4]. Pellet fueled discharges did, in fact,

display remarkably improved particle and energy confinement. Analysis indicated that these pellet fueled discharges displayed ion thermal diffusivities nearly consistent with that predicted by neo-classical theory. These results were encouraging in that they were consistent with the original premise that anomalous ion thermal transport was caused by the " η_i mode" or ion temperature gradient driven turbulence [3]. Experiments involving the injection of trace impurities to the plasma followed by a tracking of their transport through the plasma via x-ray spectroscopy indicated particle confinement times increased by factors of 5 to 20 for the injected ions [3].

Pellet injection therefore serves several important purposes: first, to replace the fuel which has been lost to either fusion reactions, or pumping, and second to generate the high density, peaked profiles shown to improve particle and energy confinement. As a final benefit, the high average densities obtainable through pellet injection are beneficial in that the fusion reaction rate , varies as the density squared (all other factors being equal).

To date, pellet injection experiments have been performed on many of the world's tokamaks, including TFTR and DIII-D in the United States and JET, Asdex and JT-60 in Europe and Japan. It is notable that in all these machines, the highest recorded line averaged densities and confinement times were reached with pellet injection [7].

1.6   Pellet Injection Experiments on Alcator C-Mod

Pellet injection experiments form an important part of the Alcator experimental program. In a sense, it is somewhat artificial to separate injection experiments from others on Alcator. The high density regimes in which Alcator is designed to operate will probably be accessed through pellet injection . The injection process is therefore relevant to experiments performed with high density plasmas following pellet injection. Several broad areas of investigation will include:

1) Density limit studies: Pellet injection will be used to fuel to the density limit and to establish and or verify the parameters affecting the limit.

2) <u>Enhanced confinement physics:</u> The peaked density profiles following injection increase energy and particle confinement times. Pre and post injection confinement times will be determined and compared to plasma parameters such as the peak and average density.   The goal will be to quantify the factors affecting access to the enhancement confinement regime following injection. Also of central importance is an understanding of why peaked density profiles enhance confinement. This research may also be thought of as falling under the broader heading of "transport issues".

3) <u>Pellet ablation and Fueling issues :</u>   Ablation physics is relevant in determining fueling depth and the ability of injectors to peak density profiles in large tokamak designs like TPX and ITER. Injection experiments will also determine what coupling there is if any between pellet fueling at the plasma core and the edge neutral pressure.   Observations will also be made of the experimental ablation rates and these will be compared with the results from current ablation models in a check of their predictive power and validity.

1.7 Objective and Scope of Thesis Research

The goal of the work presented here was first to design and construct a hydrogenic pellet injector for use on Alcator C-Mod and to then to test its operational characteristics both in the lab and as installed on Alcator. In the later section, the focus will shift to include observations not just on the injector but also about the effect of this fueling method has on the plasma.

The design of the injector is unique in that it is the first to use a closed cycle refrigerator to freeze the fuel gas. This eliminates the problems associated with the periodic cryogenic ressupply needed for injectors with conventional, liquid helium heat exchangers.   Also novel is the large number of barrels used in the design (twenty). The goal here was to achieve a high degree of operational flexibility in fueling experiments. Operators may choose from among four different basic barrel sizes and sequence their firing either simultaneously or with any desired time sequencing.

The results of the thesis research are presented by first providing the motivation and background for the research in chapter one followed by a general engineering

description of the injector design in chapter two. Laboratory performance characterization of the injector has been separated into chapters three and four . Chapter three focuses on the thermal performance of the refrigerator and thermal system while Chapter four presents the results of experiments on pellet formation and acceleration. This includes data on barrel operational reliability and pellet mass and velocity measurement.

Diagnostics associated with the pellet injector are described in chapter 5, these include the apparatus for velocity measurement, pellet photography, and the pellet tracker . The tracker is a diagnostic designed to follow the pellets trajectory into the plasma as a function of time in three dimensions. The system is advanced over other methods in that it is designed to provide improved time and spatial resolution by using two , two-dimensional photo diodes. The improved resolution will facilitate studies on pellet ablation and transport issues associated with injection.

The final chapter of the thesis, chapter six, presents data and observations from injection experiments on Alcator C-Mod. This will include data from the pellet trackers and general observations on the perturbed density and temperature profiles following injection. This chapter will compare experimentally derived ablation rate measurements with the predictions of four different variations of the neutral shield ablation model. Also presented are observations on localized density Phenomena observed on the $q=1$ flux surface following injection.

Chapter 2 : Injector Engineering and Design

2.1 Introduction

The C-mod injector employs twenty , single stage light gas guns to accelerate pellets into the Tokamak plasma. Pellets are formed inside the barrels by cooling a small region of the barrel to below the freezing point of the fuel gas. The method is termed *in-situ* pellet freezing and increases reliability by avoiding moving parts at cryogenic temperatures [18]. Schematically the geometry is shown in Fig.2.2.1. The pellet freezing cells are maintained at low temperature by thermal connection to a closed cycle refrigerator. The C-Mod injector is the first to use closed cycle refrigeration , and the first to employ such a large number of barrels. The following two sections of this chapter discuss some of the factors influencing the current design and provide an engineering overview. Successive sections will then focus on each engineering subsystem.

2.2 Design Criteria

The criteria which guided the eventual design of the injector are:

1) High reliability
2) Operational flexibility
3) Remote operation with limited access

High reliability is a necessary design goal since the primary purpose of the injector is to perform fueling experiments on C-Mod, and operation of the injector is not meant to be part of the experiment. Pellet fueling will be needed consistently later on in
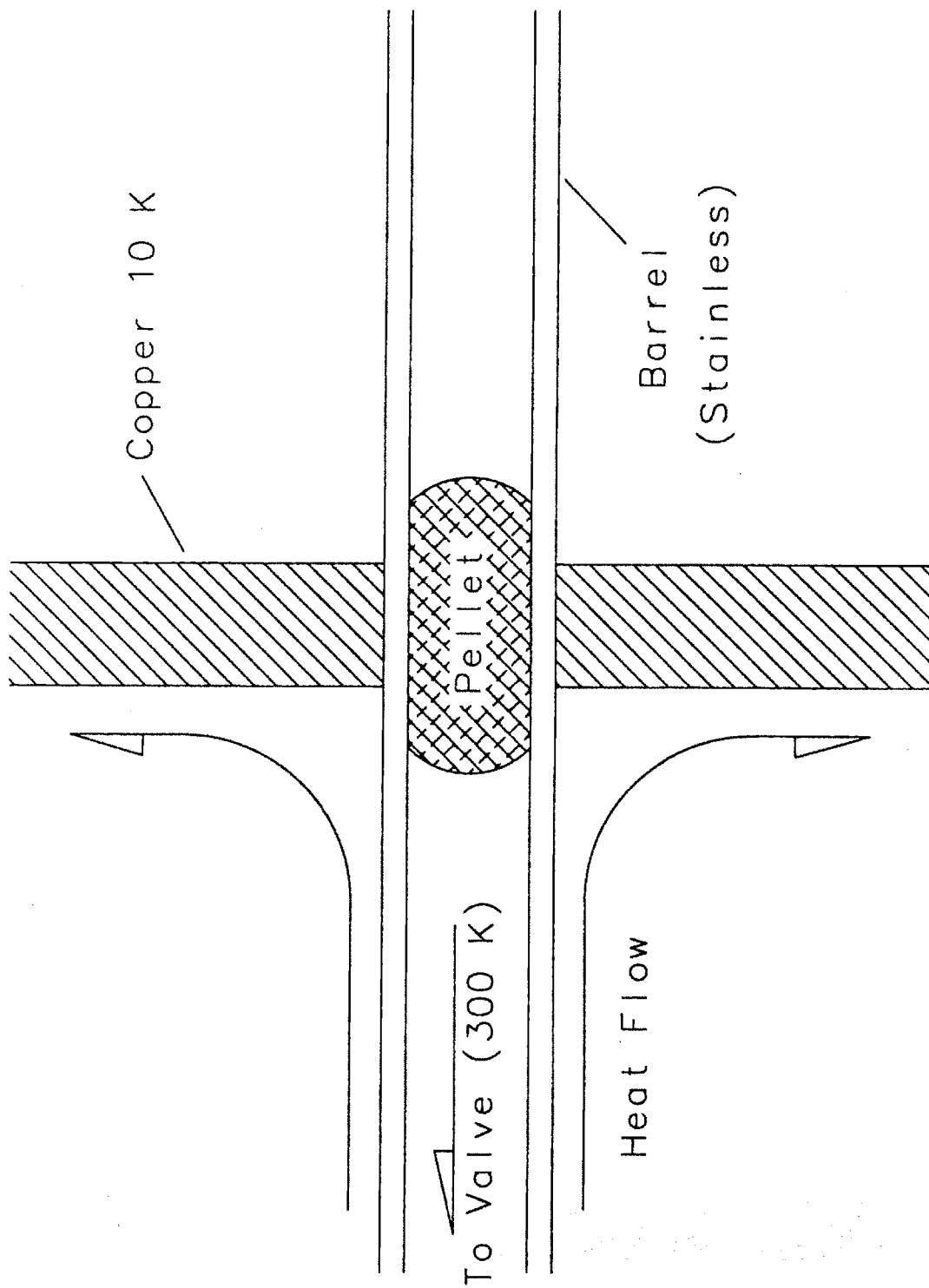
Fig. 2.2.1 : *In-Situ* pellet freezing. Gas flowing through the barrel freezes
on the inner barrel wall adjacent to the cold conduction disc.

the Alcator experimental program to help create the very high density discharges sought and the use of the injector should in no way impede tokamak operation.

A single stage light gas gun design is employed on the C-Mod injector because it is currently the most well developed and reliable acceleration method. Because maximum attainable pellet velocity is not the primary goal , less developed concepts such as two-stage gas guns were eliminated from consideration . Two stage guns have components with limited lifetimes and are only capable of low repetition rates.

The term "Operational flexibility" refers to the requirement that the injector be capable of making pellets of several different sizes and firing them in any desirable sequence desired. This capability is not possessed by centrifugal type injectors which must operate at a fixed injection frequency [45] Similarly, designs using extruded pellets such as the Oak Ridge repeating pellet injector (RPI) are limited to injection frequencies below 3 Hz per barrel [9][45]. Overcoming this limitation by using multiple barrels is expensive with extrusion type injectors because each barrel has independent freezing and extrusion systems. These requirement for fueling flexibility were most effectively met in the C-Mod design by building the injector with twenty separate barrels allowing for five pellets each in four different size groups. Because the barrels may be operated independently of each other , they may be fired simultaneously or sequentially with any desired time spacing. The design employs the largest number of barrels used on any injector to date and necessitates that the parts count and space requirements per barrel be minimized. The use of *In-Situ* pellet freezing is advantageous here because the per barrel parts count and space requirements are low and all barrels share a common thermal cooling system. Because each barrel may be used only once during the shot cycle the injector is limited to a total of twenty pellets per shot. This is not a problem for C-Mod because pulse lengths are typically one to two seconds and only a fraction of the available pellet inventory is needed to fuel to the density limit. The injector design is therefore somewhat tailored to its use on Alcator .

Remote operation with limited access is a necessary requirement for the injector because Alcator cell entry is limited due to hazardous power supplies, possibly low oxygen levels and most importantly, due to neutron and X-ray radiation from the plasma. The injector is therefore designed to operate for periods in excess of one week without direct access. This requirement was met, in part, by using a closed cycle helium
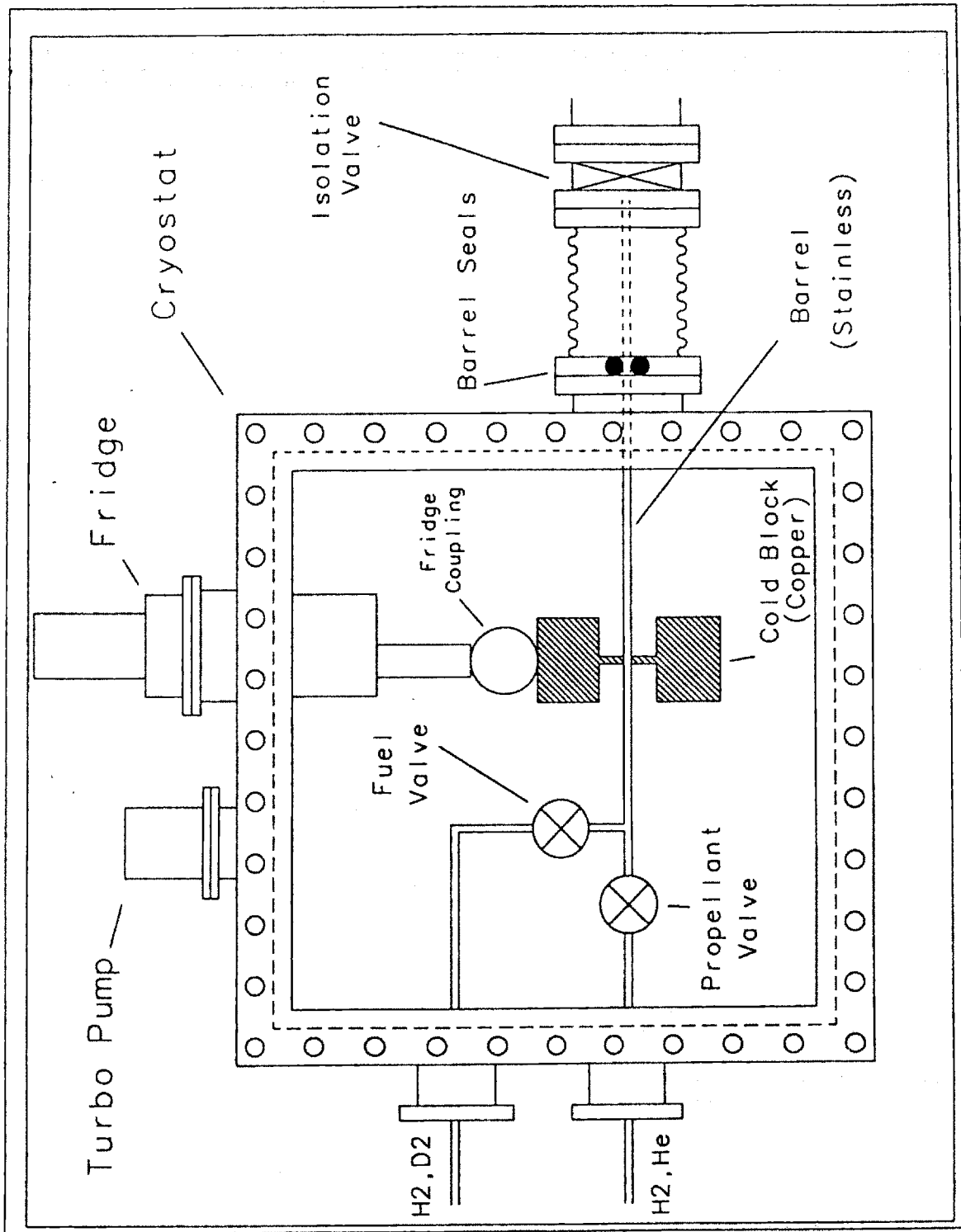
23

Fig.2.2.2: Schematic of the cryostat internal components.

refrigerator to freeze the fuel gas. The closed cycle refrigerator avoids the problems associated with liquid helium heat exchangers but introduces other design challenges. The minimum available temperature of the refrigerator is 9 K, well above that available with liquid helium. Therefore, the thermal connection linking the refrigerator to the pellet freezing zone must have an extremely low thermal resistance in order to maintain temperatures below the freezing point of hydrogen.

Remote operation requires that all injector valves and pumps needed for normal operation be remotely operable by the PLC under commands issued from an operator using a PC.

2.3   Design Overview

The C-MOD injector employs single stage, light gas guns to accelerate pellets into the tokamak plasma. There are a total of twenty barrels having three different internal diameters, 10 of 1.8 mm and 5 each of 1.37 and 1.04 mm. Pellets are formed in place inside the barrel by opening all twenty solenoid fueling valves to a small plenum containing low pressure (100-200 torr) deuterium or hydrogen. This fuel then flows through the barrels between the volumes on either end of the barrel. At around 20 to thirty torr the pressure equilibrates and freezing of the fuel gas begins . A small copper disk which is silver brazed to the barrel is cooled to between 11 and 14 K by thermal connection to a closed cycle helium refrigerator . Fuel gas pressure is below the triple point , causing the gas to freeze directly from the vapor to solid phase on the internal barrel wall in the small annular region cooled by the disk . After a few minutes, a cylindrical pellet is fully formed within the barrel, the diameter and length of which are controlled, in part, by the barrel diameter and the thickness of the copper cooling disk. The pellet is fired by opening high speed propellant valves which connect to a regulated high pressure gas supply . The pressure differential applied to the pellet shears the pellet away from the freezing zone and accelerates it down the barrel length.

The 20 barrels, cooling disks, thermal connections, propellant and fuel valves are all contained within a rectangular vacuum vessel, or cryostat which provides thermal insulation for the cold temperature components. The cryostat configuration is shown in figs. 2.3.1-3. The doors of the cryostat are removable for internal access. A closed
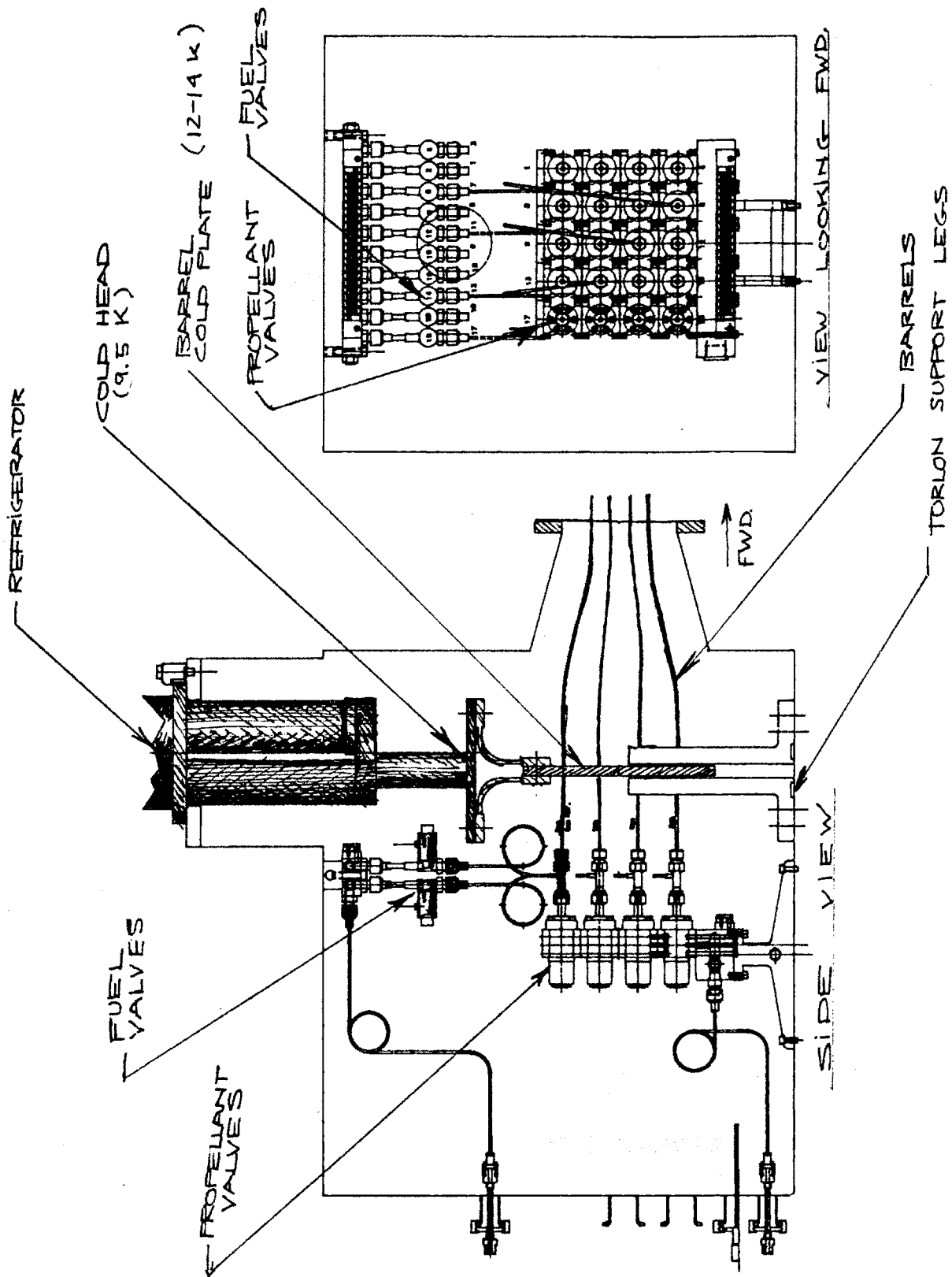
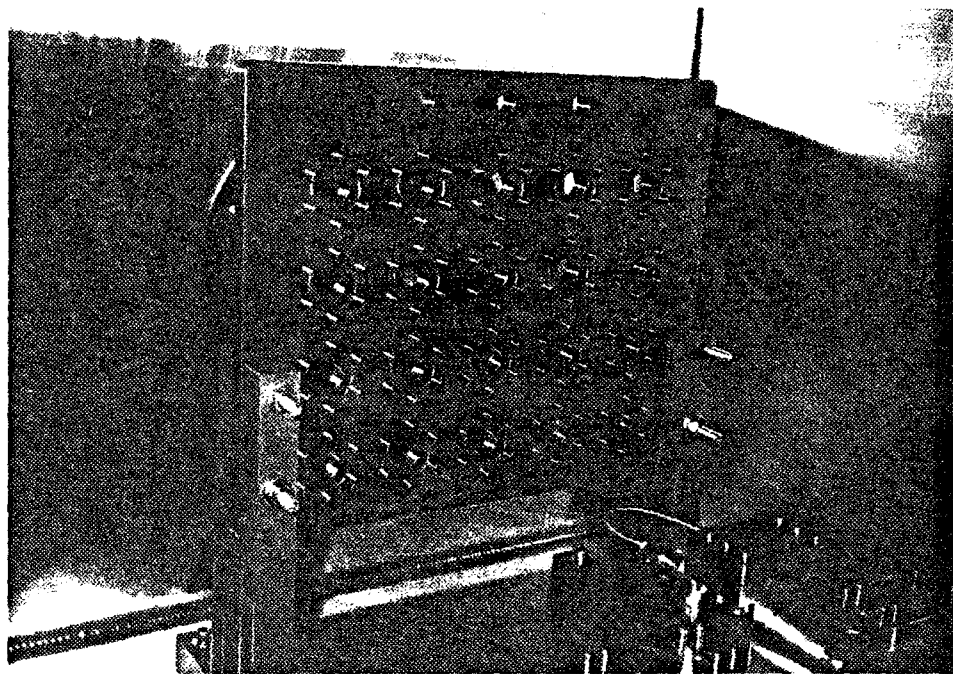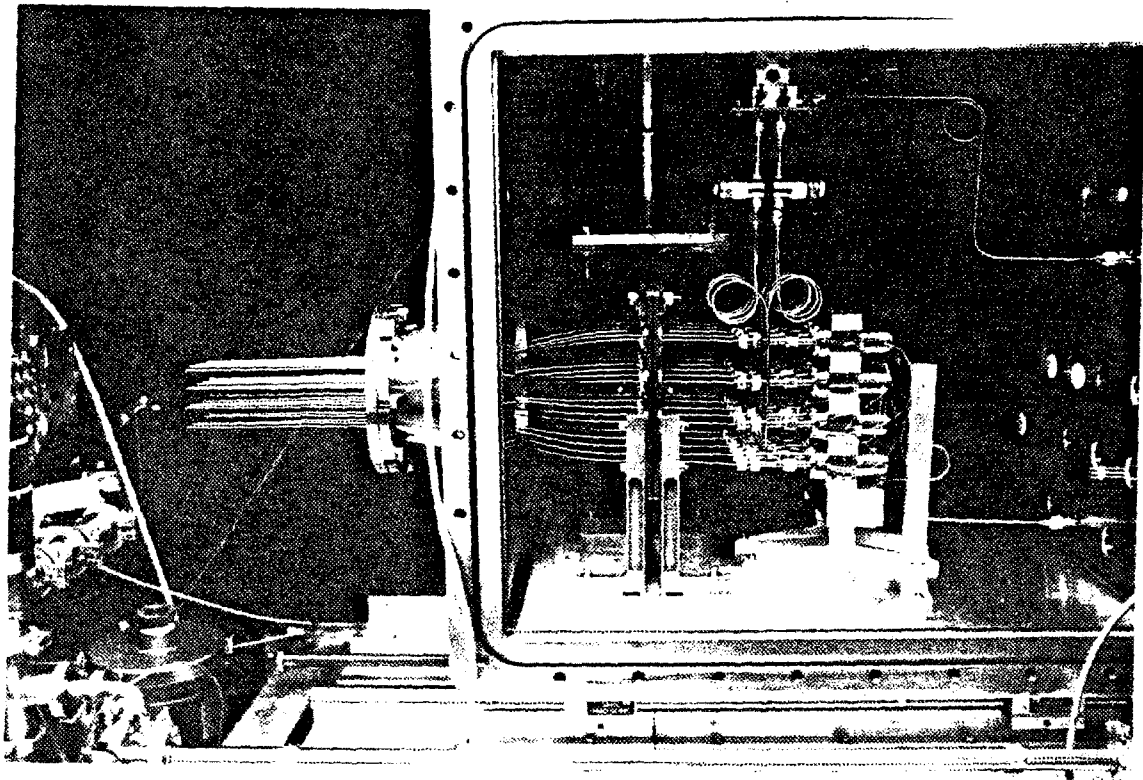Fig. 2.3.1: Cryostat internal layout.

Fig. 2.3.2: (top) View of cryostat with doors and bellows section removed
to expose internal components and forward barrel ends.
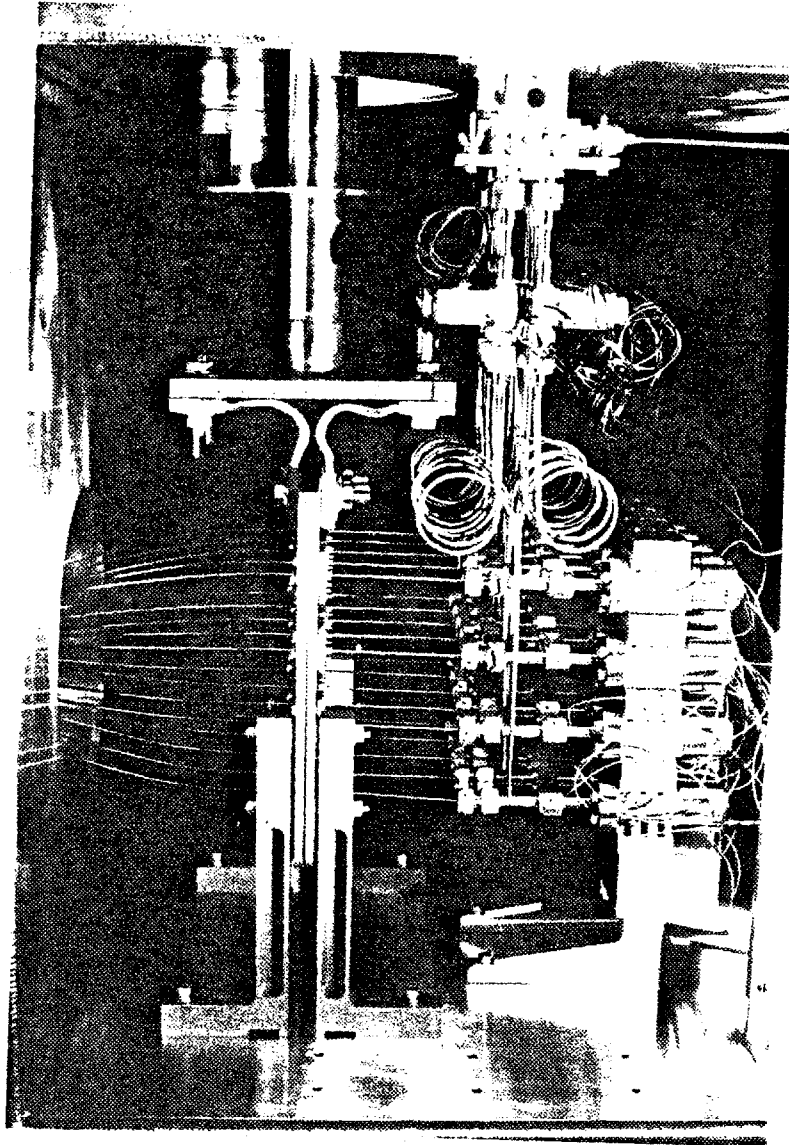(bottom) View of barrel cold plate prior to barrel instalation.

Fig. 2.3.3: Close up view of thermal system and propellant and fuel valves.

cycle refrigerator is mounted on top of the vessel , the cold head of which is internal to the cryostat and thermally connected to the barrel cold plate.

Pellets leaving the barrels pass through the injection line prior to entering the tokamak . The injection line functions as an independent vacuum system which is separated by a gate valve from that of the torus . Two time of flight laser - photodiode gates located in the injection line are used to measure pellet velocity . A series of baffles and pellet "guide tubes" serve to direct propellant gas away from the tokamak and into the expansion tank where it can be pumped away. Forward of the guide tubes and photo- diode gates is a test cell with two windows to facilitate pellet photography . The cell is equipped with a retractable target plate to which is attached a microphone for detecting pellet impacts.

The injection line, cryostat vacuum system, fuel and propellant systems contain over 100 valves. Those which are required to freeze and fire pellets are operated by programmable logic controllers (PLC) with a menu driven P.C. user interface. These systems allow for both the automatic control of the pellet freezing process and the monitoring of injector pressures and temperatures.

Firing of the propellant valves and high speed data acquisitions from the pellet diagnostics are made by CAMAC system timing and digitization modules. Data storage and manipulation is via MDSplus software run on a network of interconnected digital workstations. Shot data from the injector and other diagnostics are stored in a hierarchical data structure or 'tree' which can be accessed by the MDSplus software for analysis of the shot data.
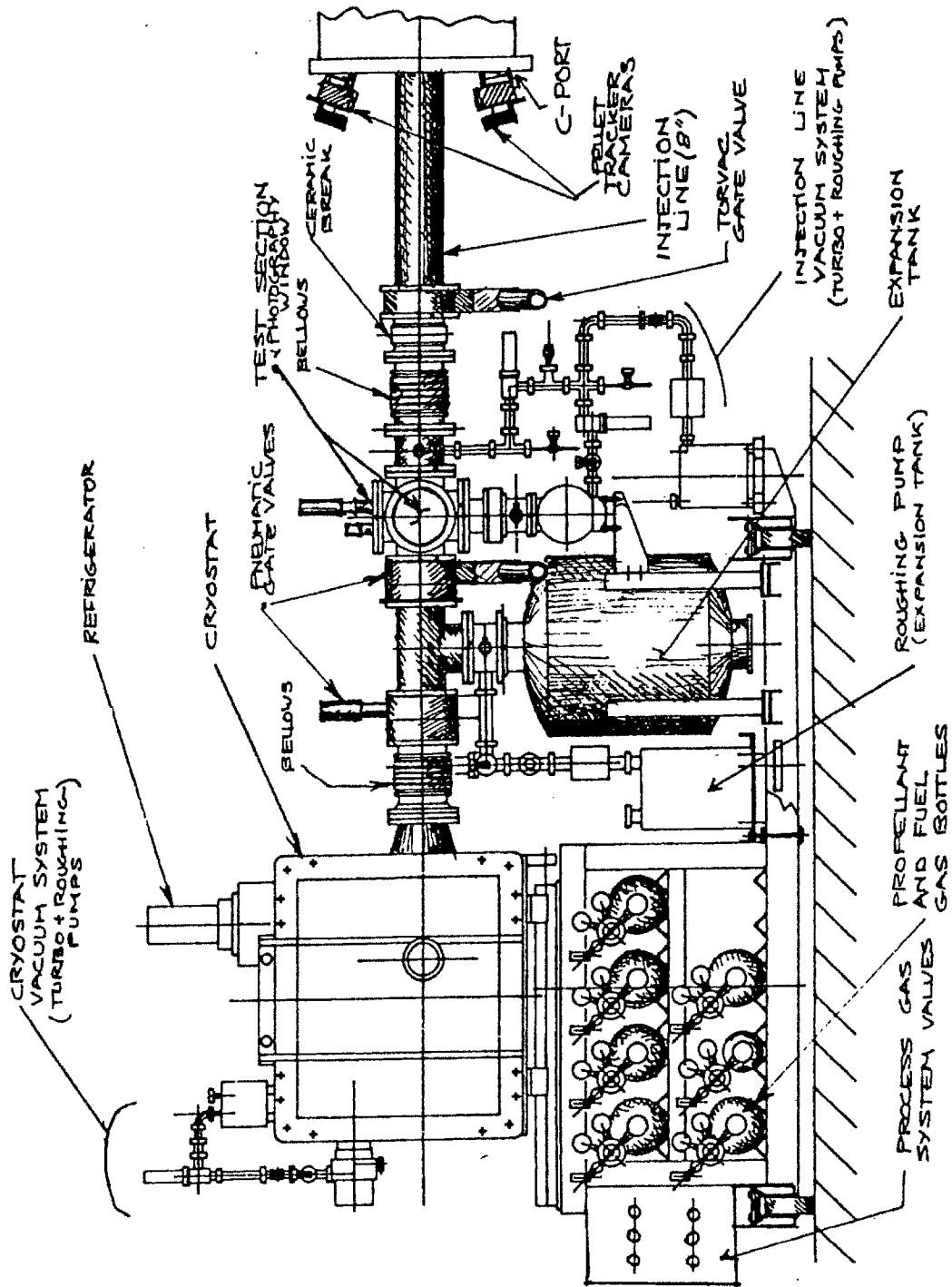
Fig. 2.3.4: The Injector, showing cryostat and injection line to C-port.

2.4   Barrel and Thermal Systems Design

The pellet injector barrels are arranged in a 5 x 4 rectangular grid with an inter barrel spacing of 2 inches. The minimum possible spacing is dictated by the dimension necessary for the propellant valves at the aft ends of the barrels. The modular , "building block" design of these valves minimizes the space needed per valve. Gun barrels are made of type 304 stainless steel. The tubing used is manufactured for use in hypodermic needles and has a wall thickness and outside diametric tolerance of .001 and .0005 inches respectively. Close tolerances are desirable to minimize gas blow-by of the pellet. The barrels are approximately 73 cm in length and have a reflex curve (see fig. 2.4.1). The curve reduces the forward inter-barrel spacing to one inch so that the 4 x 5 array of barrels may fit within an 8 inch injector line. The top two rows of 5 barrels are 13 gauge with nominal outside diameters of 2.4 millimeters . The lower rows of barrels are 15 and 17 gauge with diameters of 1.8 and 1.5 mm. Minimum burst pressure for all barrels is over 7500 psi.

Heat conduction to the pellet freezing zone is made through a copper disk silver brazed to the barrel. A cross sectional view of this geometry is given in fig. 2.4.2. The disks are made of high purity OFHC copper for good conductivity (RRR $\geq$ 50) and are one inch in outside diameter. Disk thickness is used to control the pellet length and is .060 in. for the top row of 13 gauge barrels and .040 in. for the 13 , 15 and 17 gauge barrels, (rows 2, 3 and 4).. Initial attempts at brazing the conduction disks to the barrels employed a vacuum furnace with a tungsten filament heater to melt a small loop of silver braze wire into the disk-barrel joint. Control of the flowing solder proved to be more difficult than anticipated with much of the solder flowing away from the joint and wicking onto the surface of the copper disks. The method also produced gaps in the barrel to disk joint, the uniformity of which is critical for efficient heat transfer. A second method involved hand brazing using a gas torch with an argon gas shield. This produced a uniform and continuous braze connection, but it became difficult to later remove the braze fillet without affecting the disk thickness. Removal of the braze fillet is necessary to accurately control the length of the pellet freezing zone. Ultimately, new barrel disks
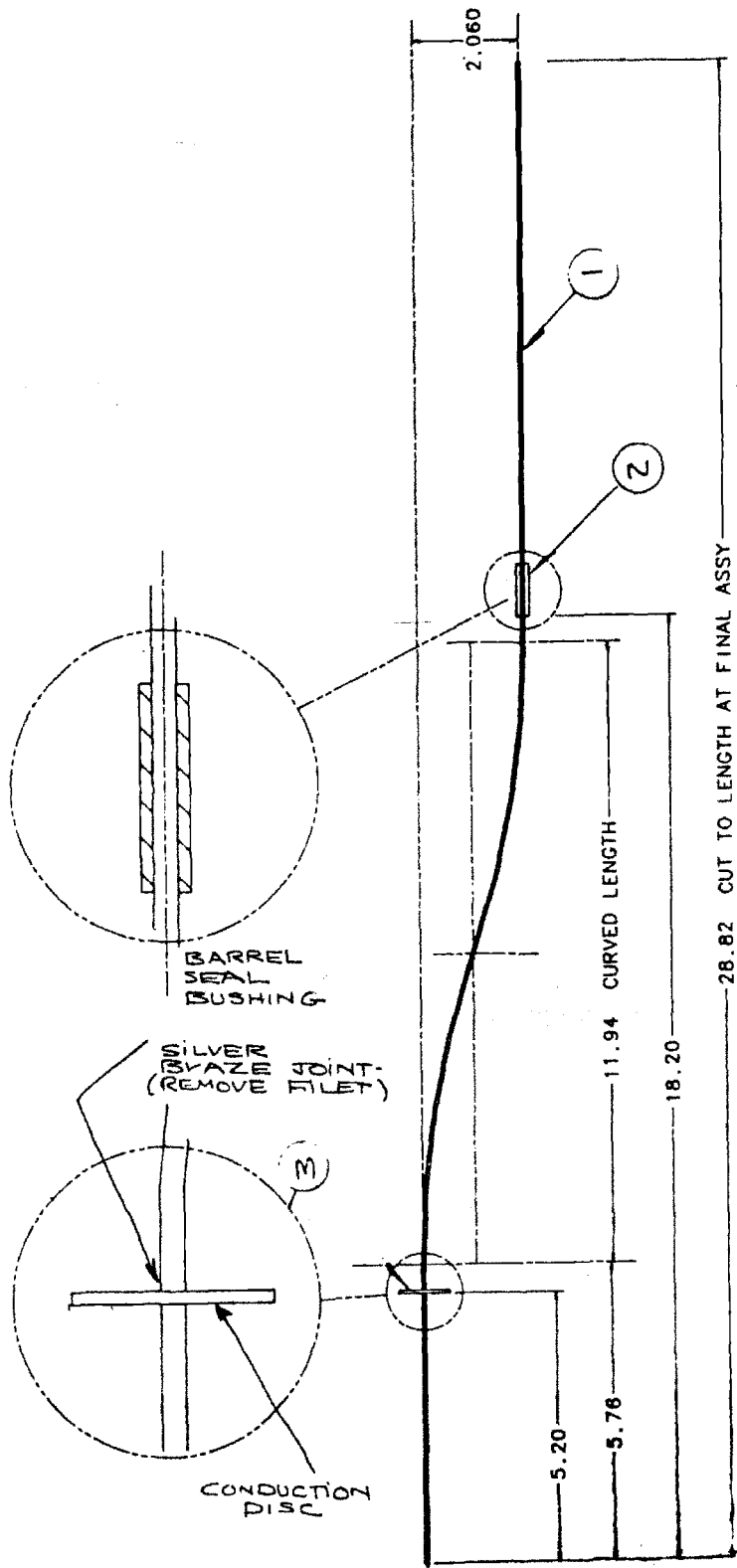
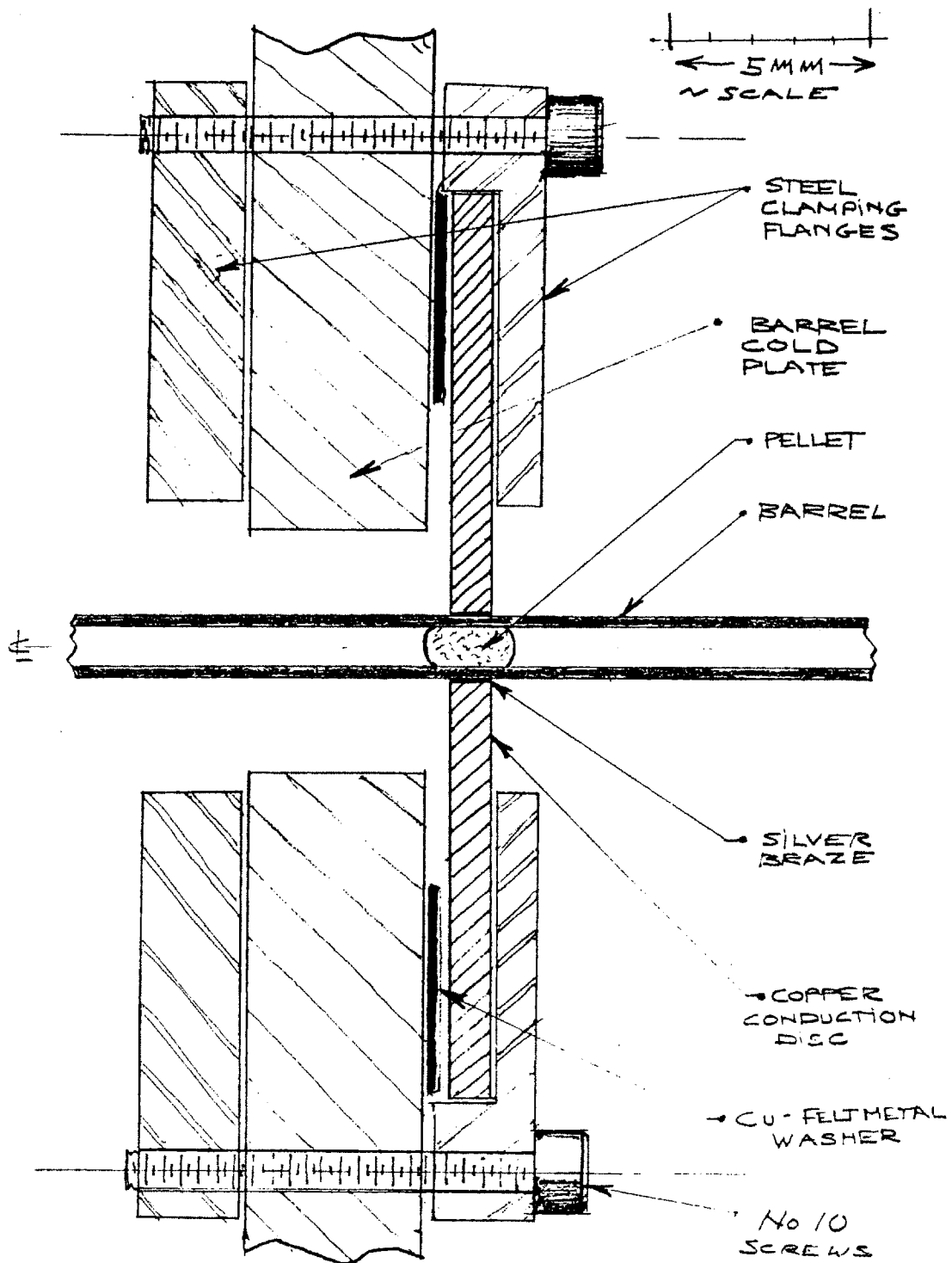Fig. 2.4.1: Barrel with copper conduction disc.

Fig. 2.4.2: Close up sectional view of barrel conduction disc to barrel cold plate connection.

were cut and machined oversize. After hand brazing, these barrel disk assemblies were then turned in a lathe both to remove the braze fillet and cut the disk to the correct thickness.

The twenty barrels are held in a rectangular array by clamping them to a single 10 x 12 x .5 inch copper "barrel cold plate", using two small, circular bolted flanges for each barrel disk. Thermal contact resistance was reduced by placing felt metal washers between the two parts. The muzzle ends of the barrels pass through a single sealing flange which separates the cryostat vacuum from that of the injection line. The barrels have steel bushings brazed in place where they pass through this sealing flange. o-rings are used to seal between the barrel bushing O.D. and the sealing plate. Forward of the sealing plate, the barrels are straight and are angled towards the injection line central axes so that all barrel lines of sight are aimed to converge at a common point on the plasma centerline. The muzzle of each barrel is held in place with Torlon bushings located in the first laser -photodiode gate. The inside of each barrel therefore communicates to the injection line vacuum, and it is sealed from the cryostat vacuum. Aft of the cold plate, the barrels connect to " T " shaped gas fittings which link each barrel to a propellant and fuel valve. Barrel seals are made with small O-rings sealing on the barrel O.D.. All seals are designed to function despite the slight axial movement which accompanies thermal expansion and contraction of the barrel.

The thermal connection between the barrel cold plate and the refrigerator was initially made with two flexible copper joints which consist of a sandwich of 16 copper plates .012" in. thick   The sandwich of plates is L-shaped with solid copper plates brazed to each end. The two flexible joints are parallel and thermally link the barrel cold plate with the refrigerator cold plate which is bolted directly to the refrigerator cold head. Thermal contact resistance between the barrel cold plate, flex joints and refrigerator cold plate was minimized by soldering copper backed felt metal pads to both ends of the flex bus on all contacting surfaces. A felt metal pad is also soldered to the refrigerator cold plate where the bolted connection is made to the cold head in order to reduce the temperature drop across the connection. The barrel cold plate, flexible joints and refrigerator cold plates are all plated with 30-50 micro inches of gold to prevent the formation of copper oxide on mating surfaces. The oxide has low thermal conductivity and increases the contact resistance between components in the thermal chain.

The original thermal configuration , while successful at freezing deuterium, proved incapable of freezing hydrogen. Modifications to the thermal connection between the cold head and the barrel cold plate were made in order to reduce temperatures in the pellet freezing zone to below the freezing point of hydrogen. Heat flow experiments showed the thermal resistance between the barrel freezing zones and the cold head to be dominated by the contact resistance between components . A re-design of the connection replaced the refrigerator cold plate and flexible joints with a single piece of copper, thereby eliminating one joint. Contact resistance is minimized by replacing the feltmetal pads with highly polished surfaces coated with vacuum grease. A surface finish of 6 micro inches and flatness to within .0001 inches of ideal is required to ensure contact across the entire joint surface. Positive contact pressure is maintained across all joints by using bellville washers in the bolted connections. The thermal system changes proved successful in enabling hydrogen freezing. Discussion of thermal tests and a more detailed rationale behind the design changes to the thermal system components are presented in chapter three.

The barrel cold plate is mounted on the cryostat floor with four L-shaped TORLON legs. The legs have low heat conductivity (.20 W/m^2K @ 50 K) and a H-shaped cross section for increased stiffness with a minimum cross sectional area. Thermal expansion and contraction of components during cooldown is estimated to be approximately one millimeter. This movement , which was formerly taken by the flexible joints, is permitted on the redesign through the use of undersize, loosely fitting bolts on the connection between the TORLON mounting legs and the cold plate . The decreased contact pressure between the legs and the barrel cold plate further reduces the refrigerator heat load. The arrangement of the cryostat internal components for both configurations is shown in figures 3.1.1 and 3.1.3.

2.5   Closed Cycle Refrigeration

Apart from the liquid helium ressuply and cell access issue, The use of a closed cycle refrigeration system may be justified from a purely economic standpoint.. Typically, an injector may use 100 liters of liquid helium per day of operation. At a cost
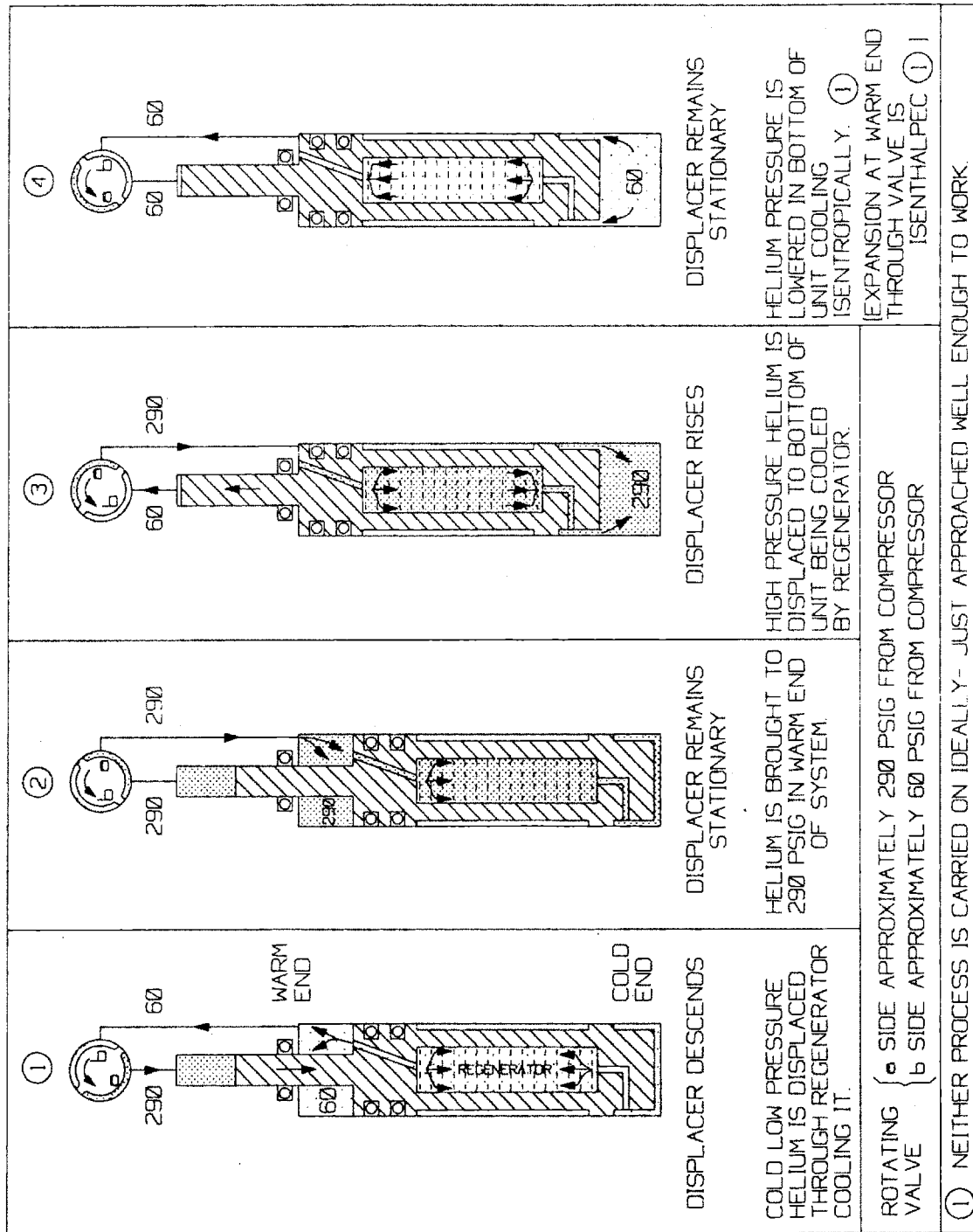
Fig. 2.5.1: The Gifford-McMahon cycle showing associated valve and displacer positions (courtesy of Cryomech inc.).

of four and one half dollars per liter and 50 days of operation per year, annual helium expenses may exceed $20,000. For these reasons, the C-Mod injector uses a closed cycle

helium refrigerator to freeze the fuel gas. The use of the closed cycle refrigerator is justified not only by the reduced access requirements but also by economics. The cost of the Cryomech GB-37 unit used was $35,000 (1989 $) and may be amortized over a period of less than two years when considering the liquid helium expense estimate given above.

With no heat load, the minimum cold head temperature for the GB-37 is 8.5 K. The cold head temperature increases with increased heat load and it is a critical parameter in the pellet freezing process. The minimum cold head temperature as a function of heat load for the refrigerator is given in fig. 2.5.2.

The refrigerator consists of 3 basic elements (See fig. 2.5.3 refrigerator cross section) . A synchronous motor driven "plate" valve (2) the first and second stage "displacers" or pistons (21) and (7) and the first and second stage regenerators (22) and (25). In operation, the refrigerator is fed a flow of compressed helium at 290 psi from a separate compressor package. The valve is rotated by the synchronous electric motor at 72 RPM and permits helium to flow at nearly constant pressure down through the first and second stage regenerators. The regenerator cools the helium which simultaneously lifts both the first and second stage displacers upwards in an isobaric process. Next, the valve plate rotates linking the top of the regenerator to the low pressure compressor return line. The high pressure helium then expands through the regenerator, dropping in pressure and temperature and removing heat from both the regenerator beds and the refrigerator cold head. Helium from the first stage displacer flows only through the first stage regenerator, but helium from the second stage displacers flows through both the second and first stage regenerators

The regenerators consist of cylindrical tubes filled with heat conductive shot. The beds are cooled by expanding the helium and in turn, remove heat from the incoming high pressure helium, so that gas entering the displacer is only a few degrees warmer than the low pressure expanded helium. As a final step in the cycle, the rotating valve plate connects the top of the displacers to a high pressure supply forcing the displacers down and into position to move upwards and accept the next charge of high pressure helium.
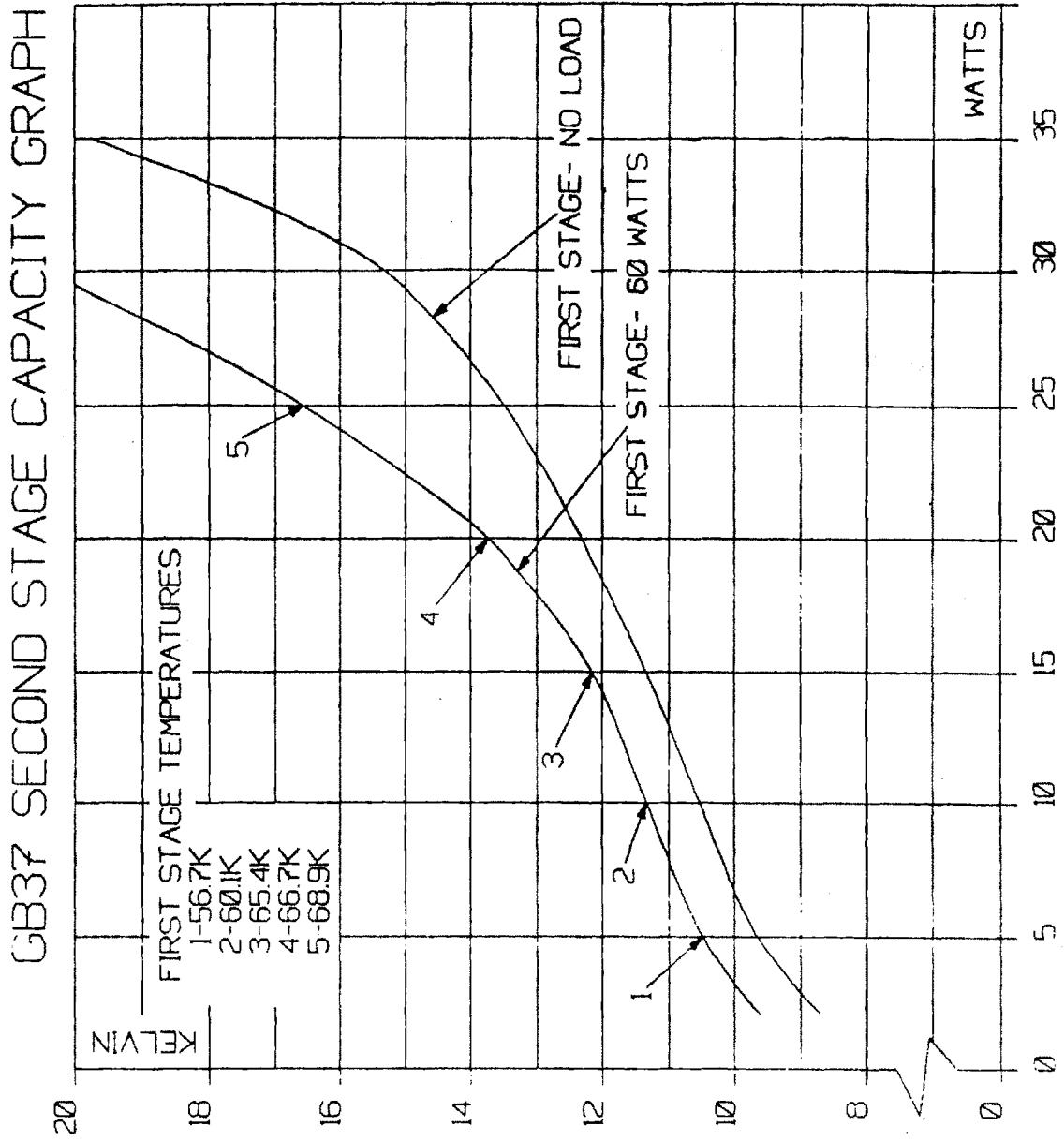
Fig. 2.5.2: The GB37 minimum cold head temperature as a function of heat load.
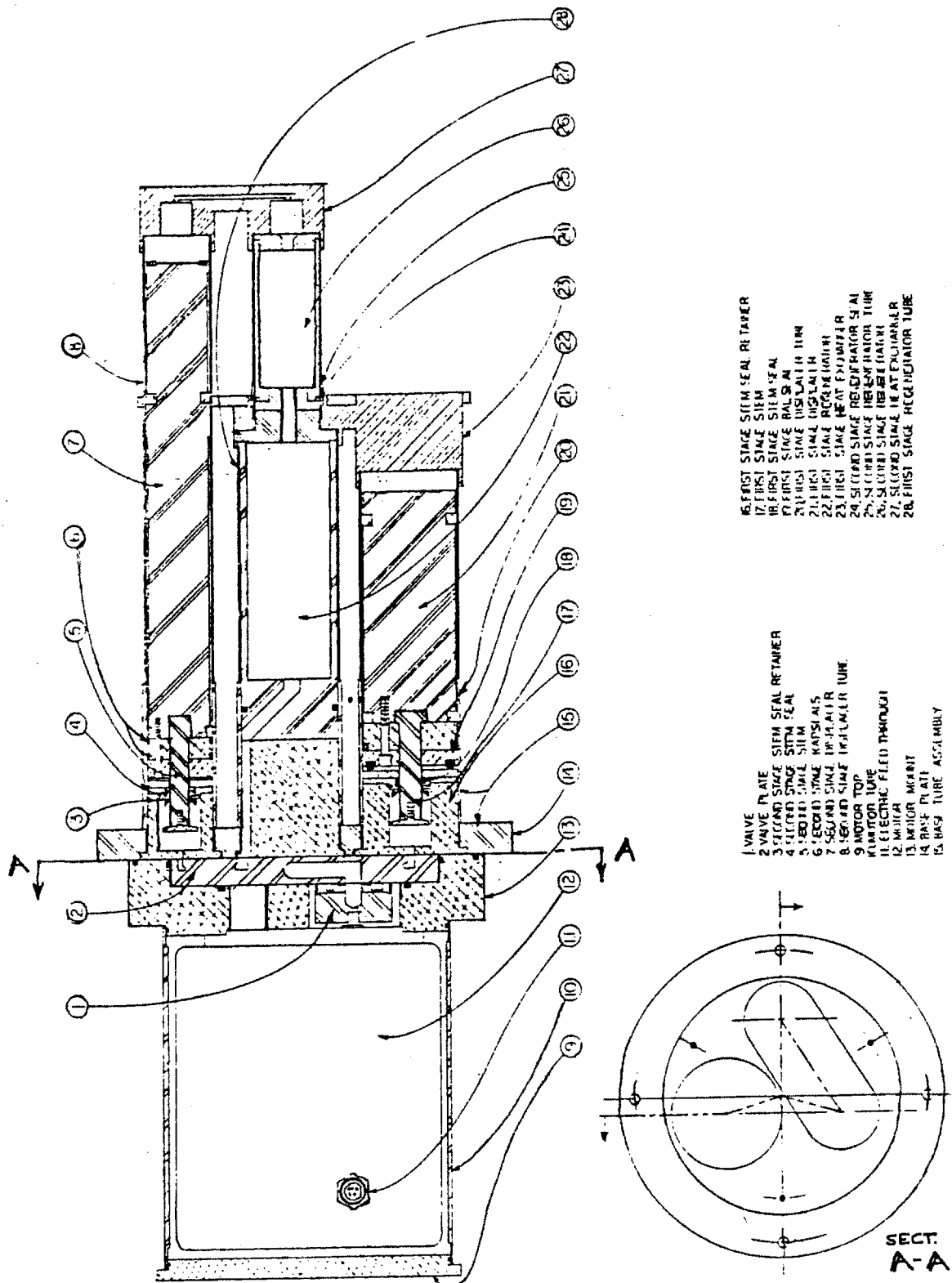
Fig 2.5.3: The Cryomech GB37 refrigerator (courtesy of Cryomech inc.).

1.VALVE
2.VALVE PLATE
3.SECOND STAGE STEM SEAL RETAINER
4.SECOND STAGE STEM
5.SECOND STAGE STEM SEAL
6.SECOND STAGE DISPLACER
7.SECOND STAGE DISPLACER TUBE
8.SECOND STAGE DISPLACER TUBE
9.MOTOR TOP
10.VIBRATION TUBE
11.ELECTRIC FEED THROUGH
12.MICA
13.MOTOR MOUNT
14.BASE PLATE
15.BASE TUBE ASSEMBLY

16.FIRST STAGE STEM SEAL RETAINER
17.FIRST STAGE STEM
18.FIRST STAGE STEM SEAL
19.FIRST STAGE SEAL SEAL
20.FIRST STAGE DISPLACER TUBE
21.FIRST STAGE DISPLACER
22.FIRST STAGE REGENERATOR
23.FIRST STAGE HEAT EXCHANGER
24.SECOND STAGE REGENERATOR SEAL
25.SECOND STAGE REGENERATOR TUBE
26.SECOND STAGE REGENERATOR TUBE
27.SECOND STAGE HEAT EXCHANGER
28.FIRST STAGE REGENERATOR TUBE

The Gifford McMahon (G-M) cycle and the corresponding displacer positions are shown schematically in fig. 2.5.1 .

The refrigerator is mounted on top of the cryostat on an O-ring sealed circular flange. The refrigerator cold head is internal to the cryostat vacuum system preventing freezing of both air and water on exposed cold surfaces. Two flexible, stainless steel hoses are used to connect the refrigerator to the compressor package. The high pressure line carries helium at about 280 psi and the low pressure return line at 60 psi. The lines are fitted with self sealing aeroquip couplings at each end to prevent contaminates from entering the system during hookup or removal of the lines.

The compressor unit consists of an electrically driven helium compressor and water cooled heat exchanger. Helium leaving the compressor is passed through air /oil strainers, agglomerators and coalescers to remove oil entrained in the helium. A charcoal adsorber bed removes any remaining contaminants from the helium flow. High purity of the helium is required to prevent impurities from condensing and accumulating in the refrigerator. The compressor displays the inlet and outlet pressures and has provisions for helium recharge. A thermal shutoff switch protects the compressor should overheating occur. Water flow to the heat exchanger is monitored through two flowmeters . Power to the compressor is interrupted if the cooling water flow rate drops below a preset value.
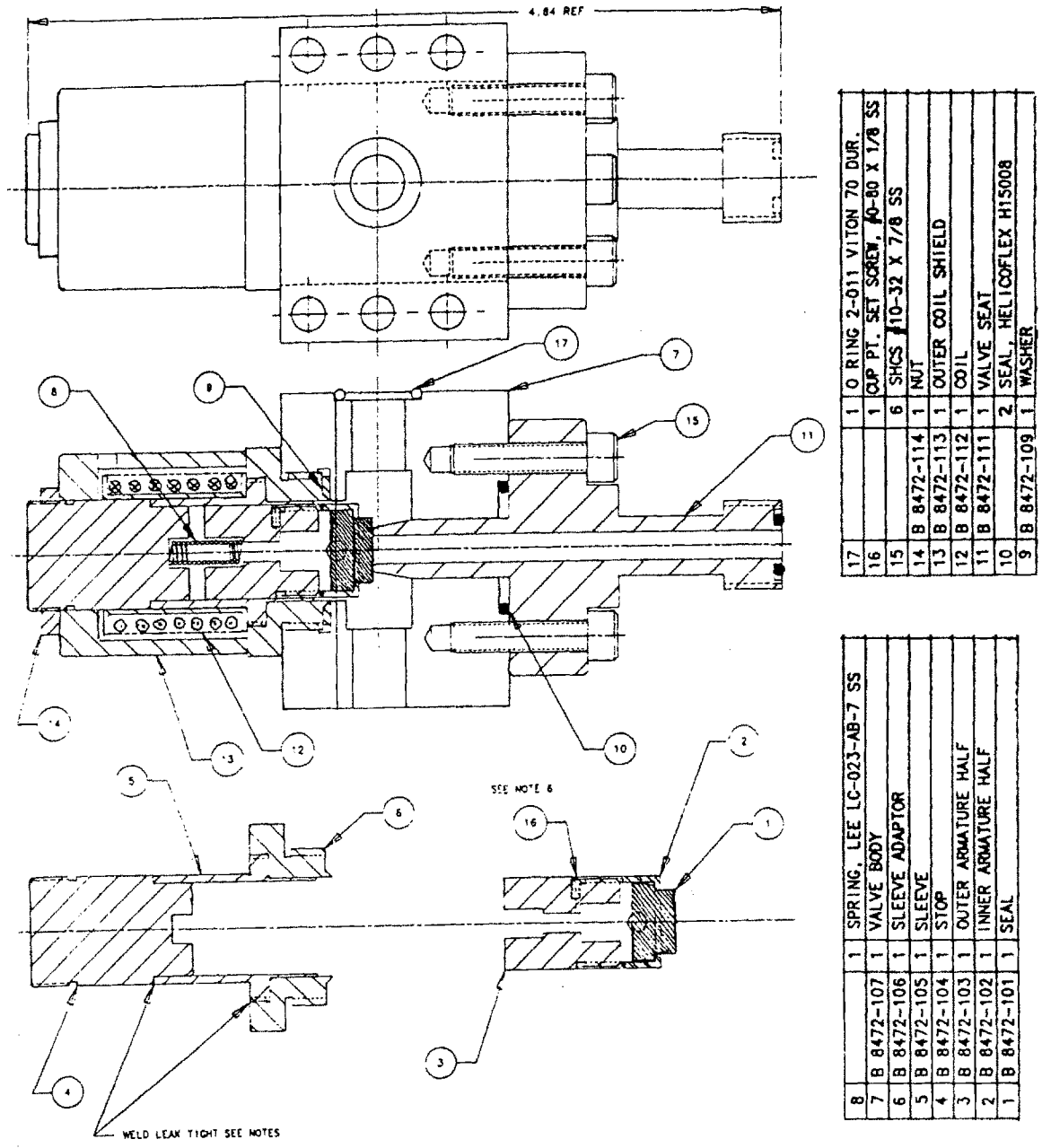
2.6 Propellant and Fuel Valves

Each of the twenty injector barrels is connected to both a propellant and a fuel valve. The propellant valve is a high pressure, solenoid driven valve capable of opening and closing in less than one millisecond. Fast opening and closing of the propellant valve is needed to ensure that barrel pressure rises to a maximum before the pellet has left the barrel (100's of μ seconds) and closes fast enough to minimize the propellant gas load behind the pellet.

The twenty fueling valves are simultaneously cycled during the pellet freezing process. Each barrel requires its own valve, not to control freezing in individual barrels, but to isolate other barrels from the pressure pulses generated when propellant valves fire. Valve orientation is such that propellant gas pressures acts to close the valve.

The C-Mod injector propellant valves design is essentially identical to that developed at the Oak Ridge National Laboratory by the pellet fueling group [45]. Externally , however, changes were made to permit closer valve spacing. The changes were needed because the C-Mod injector was designed with twenty barrels. It was therefore important to reduce the inter-barrel spacing, both to minimize the cryostat size and to reduce the amount of curvature needed to converge the barrel ends into the injector line. Inter-barrel separation is governed by the space needed for propellant valves. Staggering or remote placement of the propellant valves from the barrel cold plate is not desirable because the applied pressure pulse from the valves are flattened in time, prior to reaching the pellet and barrel. To minimize the inter-barrel spacing, the propellant valve housing block was configured to bolt together in "stacks" of four. The valve housings seal together in vertical groups of four forming a single supply manifold for all four valves. Five stacks of four valves are mounted onto a single aluminum manifold to form a 4 x 5 rectangular array.

The valve internal design is shown in fig. 2.6.1 and consists of a cylindrical plunger with a Teflon seal insert. (Parts 1,2,3) which is held by gas pressure against the valve seat. (Part 11) The plunger forms part of a magnetic circuit and is drawn off the

17		O RING 2-011 VITON 70 DUR.	1
16		CUP PT. SET SCREW, #0-80 X 1/8 SS	1
15		SHCS #10-32 X 7/8 SS	6
14	B 8472-114	NUT	1
13	B 8472-113	OUTER COIL SHIELD	1
12	B 8472-112	COIL	1
11	B 8472-111	VALVE SEAT	1
10		SEAL, HELICOFLEX H15008	2
9	B 8472-109	WASHER	1

8		SPRING, LEE LC-023-AB-7 SS	1
7	B 8472-107	VALVE BODY	1
6	B 8472-106	SLEEVE ADAPTOR	1
5	B 8472-105	SLEEVE	1
4	B 8472-104	STOP	1
3	B 8472-103	OUTER ARMATURE HALF	1
2	B 8472-102	INNER ARMATURE HALF	1
1	B 8472-101	SEAL	1

Fig. 2.6.1: The propellant valve with sectional view showing internal parts.

valve seat when the drive solenoid is energized. The valves are opened impulsively with the majority of plunger travel governed by spring and inertial forces after an initial magnetic "kick" from the drive solenoid.

Propellant valves were manufactured using numerically controlled machines at STC Incorporated. This ensures a high degree of uniformity in the machined valve components and reduces performance variations between valves . Valve components 4,5, and 6 of figure 2.6.1 were electron beam welded to form a gas tight assembly within which the valve plunger or armature moves. The Teflon seal , (9) between this assembly and the valve body was found to leak and was replaced with an O ring seal as were all Helicoflex seals indicated in the design. All valves were leak tested using a helium leak detector in the "sniffer" mode to check for high pressure leaks past the valve seat and from the valve body. Any leaks were corrected by polishing the valve seat sealing surfaces.

The propellant valves are driven by MOSFET transistor switched capacitor (2900 μF). The power transistors are triggered by signals from the CAMAC timing modules through an opto-coupler for electrical isolation. Each board has an independent DC power supply linked through isolation transformers to a single variable AC power supply thus preventing crosstalk between driver boards. Each board has current and voltage monitoring resistors for diagnosing the driver circuits and valves. The boards are mounted in groups of ten in two rack mounted chassis.

Propellant valves were tested by determining the minimum capacitor voltage necessary to just open the valve for fixed pulse lengths and propellant supply pressures. The results indicate that for shorter pulse lengths greater driver voltages are required for valve operation, regardless of supply pressure. The intention is to operate the valves with the shortest pulse length needed for reliable valve operation. Valve operation in this mode minimizes the propellant gas load from the injector to the Tokamak vacuum vessel. Valves are typically operated with pulse lengths of 950 microseconds at 80 volts.

Fuel valves are located in two rows of ten above and behind the barrel cold plate . The valves are mounted to a rectangular, aluminum manifold block which supports and supplies fuel to all 20 valves. The valves are commercially available Skinner solenoid valves and are mounted with the high pressure side of the valve towards the barrels. With

this orientation , firing pressures force the valves closed preventing propellant gas leaks into the fuel system. The valves are held open for several minutes during the pellet freezing process. Since the fuel valves operate in a vacuum and dissipate heat primarily by conduction and radiation , the minimum DC valve operating voltage is used to prevent valve overheating. Temperatures on the valves are monitored by thermocouples. Initial operation of the injector showed that the fueling valves were not cooling sufficiently between batches of pellets but were instead "ratcheting" up to high temperatures. The valves require approximately six volts to open initially but only three to keep open. By operating the valves with a circuit which drops the supply voltage by fifty percent after initial switching, valve input power was reduced by 75% , thereby eliminating overheating.

2.7 Process Gas System

The propellant and fuel systems together form the "process gas system", the majority of which is located on the aft end of the injector carriage. Hydrogen, helium and neon are selectable as propellant gases and are stored in high pressure gas cylinders on the injector carriage. A schematic of this system is presented in fig. 2.7.1.

Each gas bottle has a manual tank shutoff valve, a high pressure regulator (100-2000 psi) and a line valve. Flex lines connect the propellant gas tanks to the process gas system. Each gas line has pressure sensors, solenoid valves and a check valve to isolate each bottle. Gas lines from each bottle connect through solenoid valves to a single propellant feed line fitted with a flow restricting needle valve (N2). A 1/4 inch flex line carries the propellant gas from the process gas system to the cryostat . Internal to the cryostat, a 1/8 inch stainless steel line carries gas to the propellant valve manifold block. Propellant gasses are selected by venting and purging the propellant lines, manually setting the regulator pressure, and opening the solenoid valve (S4, S5 or S6) to the selected gas by PLC control.
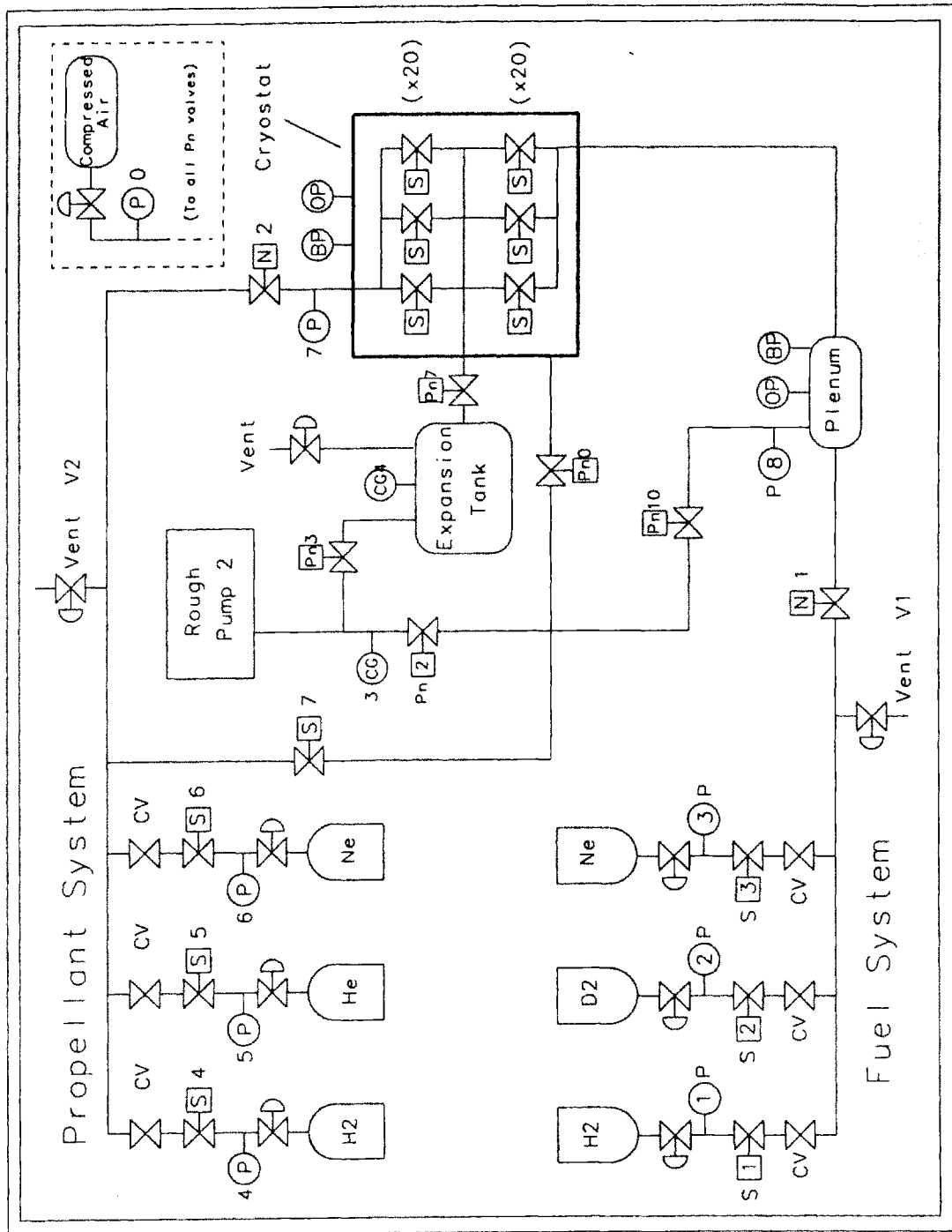
Fig 2.7.1: Schematic of the process gas system

The fuel system gases are hydrogen, deuterium and neon . Like the propellant system, each gas bottle has a low pressure regulator (20 psi) and two shutoff valves. Flex lines link each bottle to PLC controlled solenoid valves (S1, S2, S3) and isolation check valves . A single line connects all three gases through the needle valve (N1) to a one liter volume plenum. The plenum is provided with a burst disk, relief valve and pressure sensor (P8). After gas changeovers, this plenum can be purged and evacuated by roughing pump 2 through valve (PN 10). The fuel system is operated by setting the regulator pressure on the selected gas bottle to slightly above atmospheric and opening the solenoid valve to the gas plenum. Plenum fill pressure is pre-set, so that when the correct level is measured at (P8), the PLC closes the feed valve (S1,S2,or S3). Pellet freezing is initiated by then opening the twenty fueling valves inside the cryostat and bleeding the fuel gas from the plenum, through the barrels and into the bellows volume between the barrel muzzle sealing flange and the 1st injection line gate valve (PN7).

Line pressures is measured by diaphragm strain gauge sensors which are supplied with regulated DC. voltage. Output voltages are amplified , measured by the PLC and converted to the correct units for screen display.

All process gas components and lines are interconnected with VCO type O-ring fittings. These seals were found to work reliably and , unlike Swagelock seals, are easy to disconnect and later reseal. Propellant lines are made of 1/8 inch stainless steel tube. Fuel lines were initially 1/8 inch OD. but were later changed to 1/4 inch to facilitate vacuum pumping of the lines.

2.8 Injector Vacuum Systems

The injector vacuum system is functionally divided into the cryostat and injector line vacuum systems forming two independent parts. The overall layout of this system is given in figure 2.8.1. The cryostat vacuum system consists of a Balzers TPN 170 turbomolecular pump backed by a Leybold rotary vane roughing pump . A bypass line at the base of TP1 connects to the larger roughing pump RP2 to speed up initial pump down. The cryostat itself is a rectangular box, approximately 22 inches wide, 33 inches

long and 30 inches in height. The cryostat has two removable side doors which are bolted in place and sealed with viton O rings.

The vessel is mounted on two circular rails, with a manually driven screw drive to permit fore and aft translation . This facilitates the installation of the injector barrels and mating of the barrel ends to the injection line.

Leak checking of the cryostat vacuum required testing the welds and the fittings of both the cryostat and of the pressurized internal hardware. Internal components were leak checked by pressurization of the propellant and fuel systems with helium and using the leak detector in the "sniffer" mode. The cryostat vacuum was particularly susceptible to leaks in the process gas system, because the refrigerator cold plate would freeze the hydrogen, effectively pumping the cryostat volume. Once fully loaded, these surfaces would no longer trap hydrogen. Leaking hydrogen would then slowly accumulate raising the cryostat pressure to the point where the convective heat transfer became sufficient to sublimate hydrogen frozen on the refrigerator coldplate. This process would accelerate rapidly producing millitorr pressure spikes every 20 minutes. Detecting leaks during refrigerator operation was difficult since the otherwise acceptable cryostat vacuum was affected only for short periods. After a number of small leaks in the fueling system and propellant valves were found and sealed, equilibrium cryostat pressure was recorded in the low 1×10^{-8} millitorr range. This level is well below that which is necessary to provide sufficient insulation to the thermal system components.

The injection line vacuum system begins at the barrel sealing flange on the forward cryostat face, and extends to the torus gate valve on the tokamak. The first section of the system, located between the barrel sealing flange and the first gate valve (Pn 7), is closed off during pellet freezing and connected through the barrels to the plenum when the fueling valves are open. Prior to pellet firing, fuel valves are closed and (Pn 7) is opened to pump away the excess fuel gas. With gate valves (Pn 7) and (Pn 8) open, the injector line length is divided in two by the pellet guide tube array. The array consists of twenty, 1/4 inch OD. stainless steel tubes , approximately 30 cm in length. The tubes are aligned with the injector barrels with two plates at either end of the tubes. The plate nearest the barrel ends is perforated to divert gas down into the expansion tank. The array forms a low conductivity barrier between the volumes forward and aft of the gate valve (Pn 8).
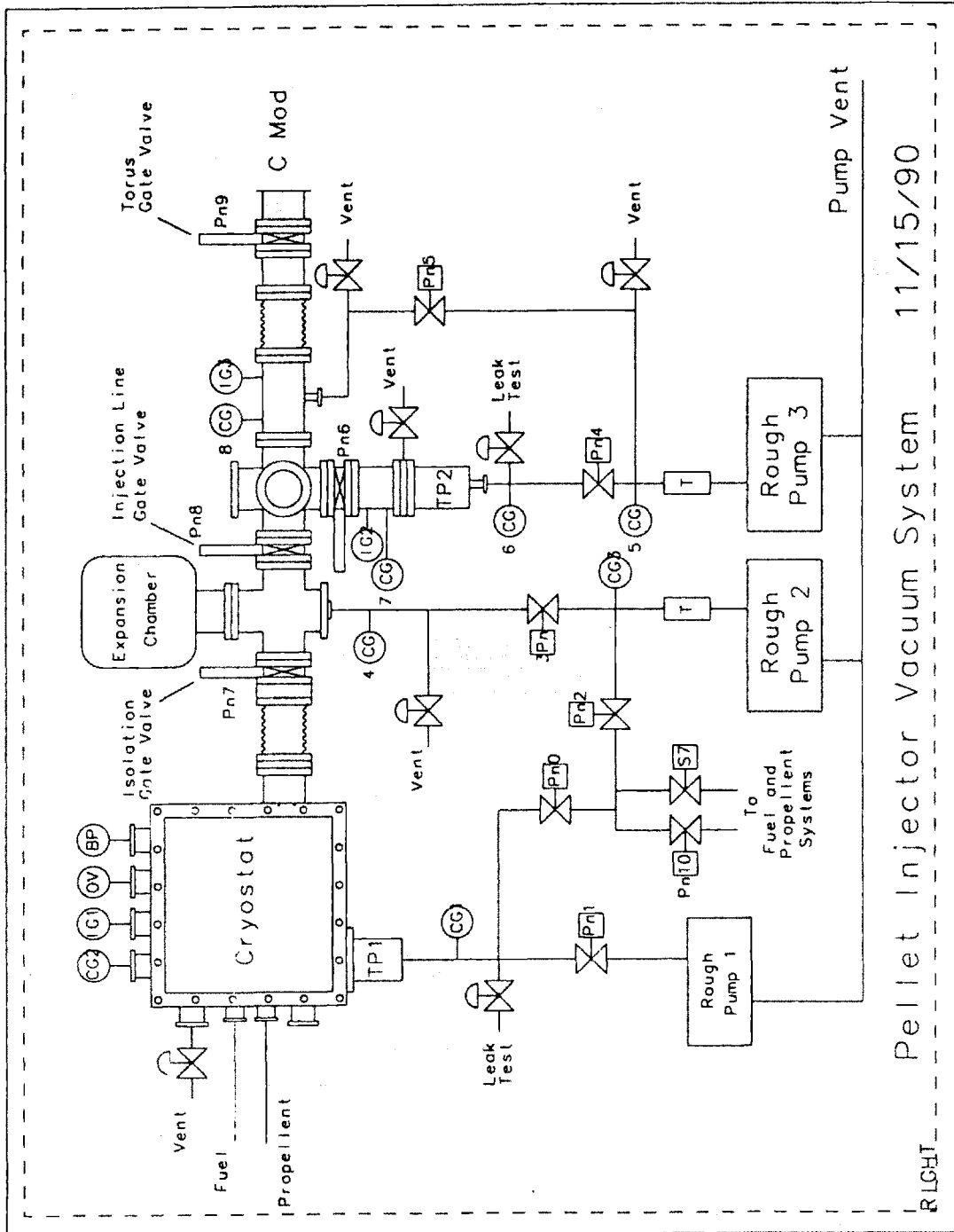
47

Fig. 2.8.1: Injector vacuum systems schematic.

Immediately after pellet firing, the guide tubes divert the majority of the propellant gas into the 100 cubic liter expansion tank, where it is pumped away by a mechanical pump (RP 2). The propellant gas load to the tokamak consists of the prompt gas load during pellet firing and a more continuous leak through component subsequent to firing. The prompt load consists of the gas in the propellant plume which is impinging directly onto the guide tube entrance and is therefore directed into the injection line. The slow component is caused by the leakage of propellant gas from the expansion tank through the guide tubes and injection line and into the tokamak. The total gas load is minimized by: (1) The large volume of the expansion tank which limits the gas pressure ahead of the guide tubes (2) The low conductivity of the guide tube array which reduces the throughput to the injection line and (3) The injection line turbopump which pumps away a large fraction of the gas in the injection line (4) A baffle plate, located in the injection line just forward of the test section. This plate has an array of 3/8 inch diameter holes through which the pellets pass, and decreases the gas conductivity of the injection line by the ratio of the hole to injection line areas (.078). The baffle plate was added after initial injection experiments on Alcator C-Mod showed an unacceptably high propellant gas load during firing.

Forward of (Pn8), the injection line gate valve, is a 6 way cross which may be used as a test section for pellet photography or other experiments. Below the cross is connected a gate valve and turbopump (TP 2). The turbo is backed through a pneumatic valve to a third roughing pump (RP 3). The roughing pump may be used to evacuate the injection line through a bypass line before the opening gate valve (PN6) to the turbo. A torus gate valve (PN9) separates the tokamak from the injection line vacuum systems and is opened prior to the tokamak discharge.

A ceramic break provides electrical isolation from the tokamak and a bellows allows the alignment of the injector so that the pellet trajectories enter the vacuum vessel along the plasma midplane towards the torus center. Convectron gauges are located upstream of all roughing pumps. Ion gauges are also placed on the injection line, cryostat, and above the injection line turbopump (TP 2). The cryostat and fuel plenum are both fitted with relief valves and burst disks to prevent over pressurization of these volumes in the event of a high pressure leaks.

2.9 Control and Data Acquisition

All injector valves and pumps, with the exception of the gas bottle shut off valves and regulators and the propellant valves, are operated by programmable logic controllers (PLC). The controllers are well developed commercially and are sold primarily for use in industrial process control. The Allen Bradley PC 5/60 used operates by continuously cycling through a sequence of logical commands called a "ladder logic program". The programs are application specific and are designed to read and implement commands issued from an operator using a P.C. . The controller samples injector temperatures and pressures plus valve and pump states. The ladder logic program compares these values and states to preset values stored in the program and implements specific commands based on the state comparisons. The logic program is designed to protect the injector by preventing harmful valve sequencing by the operator and to turn off pumps and close valves should pressures and temperatures rise above safe operating limits.

Automatic pellet manufacture is performed by the controller by cycling the injector valves through a sequence of states based on either time or pressure values. These times and pressure values are input by the operator and constitute important parameters in the pellet freezing "recipe" . The particulars of the pellet freezing process and the determination of the optimum pellet manufacturing conditions are discussed in chapter four. Automatic control of pellet manufacture ensures greater uniformity in the finished pellet batches , frees up the injector operator, and minimizes the potential for operator error.

Commands to the PLC are issued from a dedicated PC running PARAGON interface software. The PARAGON display software communicates the injector state with representational graphics. Commands are issued under cursor control from the PC screen to operate injector components. The control graphic displays are hierarchical. The top level display can be used to make pellets and configure the injector for firing. Lower level displays are used to control process gas system valves, the vacuum system, and injector power and water. Time histories of injector pressures and temperatures may also be displayed.

Fast sequencing of the propellant valves and data acquisition are handled with CAMAC system digitization and timing hardware. CAMAC modules are linked via the ethernet to a distributed network of Vax Stations. With the CAMAC system, propellant valve sequencing begins when a master start pulse is received by a decoder module. The decoder relays the pulse to two sets of Jorway 222 and 221 timing modules. This start pulse is interlocked and only relayed to the Jorways if the fueling valves are closed and the injector line gate valves are open. The Jorway modules send trigger pulses to the selected valve driver circuits. Valve timing is referenced to a master clock from the decoder. A data sampling waveform is issued from the Jorway which is in the "high" state in a "window" around each valve pulse. An 8501 timing module generates clock bursts at the data sampling frequency in sequence with the "high" state of the timing waveform. The clock bursts are relayed to two TRAQ digitizers which sample voltages on a total of sixteen channels in sequence with the clock bursts. Thus data is recorded on all channels at a selected frequency in a window about each valve firing pulse. Typically, two channels are dedicated to recording pellet times of flight from the laser-photodiode gates. One channel is connected to the target microphone and eight more channels are used to record data from the two pellet tracker cameras. Additional channels might be used to record trigger pulses to the pellet photography nanolamp or to sample current and voltage waveforms from the propellant valves. The digitizers are linked to a memory storage unit which provides for a total of 1 million samples at a maximum sampling frequency of 1 MHz. The digitizers use 16 bits over a ten volt range providing .25 millivolts of resolution. Data manipulation and storage is handled on the microvax cluster using MDS plus software. The MDS plus software stores data in a higherarchal data structure or "tree". After each shot, both raw and processed data from both the injector Diagnostics and other machine diagnostics are stored in "nodes" on the tree. The system greatly facilitates access to and manipulation of shot data.

Chapter 3: Injector Thermal Analysis

3.1 Introduction

The operation of the C-Mod pellet injector is critically dependent on the performance of the closed cycle refrigerator and the thermal connection between the cold head and the pellet freezing zones. The highest possible temperature for making hydrogen pellets is 14 K . The lowest refrigerator temperature is 8.5 K at the cold head under no load conditions. The accurate determination of the refrigerator heat load is essential because this heat increases the equilibrium refrigerator temperature and determines the temperature drop to the freezing zone.

The thermal connection between the refrigerator and barrel cold plate was modified after attempts to freeze hydrogen proved unsuccessful. Where appropriate, calculations and experimental data are presented for both configurations of the thermal system. For clarity , the two designs are shown figures 3.1.1 through 3.1.4 .

The first section of this chapter outlines the heat loads to the refrigerator and the corresponding predicted refrigerator equilibrium temperature . An iterative approach is used to find the heat flow by first assuming that the refrigerator cold head is at a suitable temperature for freezing pellets (10 K) and that the ends of the support legs and barrels are at room temperature (298 K) . The heat flux may then be calculated and used with the published data on the refrigerator equilibrium temperature vs. heat load to find the actual cold head temperature. If the values are within a few degrees of each other, the temperature dependent material properties and heat flow are assumed to be correct. Temperature gradient maps were determined for the barrel cold plate and for the pellet freezing zones. The latter sections of the chapter present experimental data on refrigerator performance and contact resistance experiments.

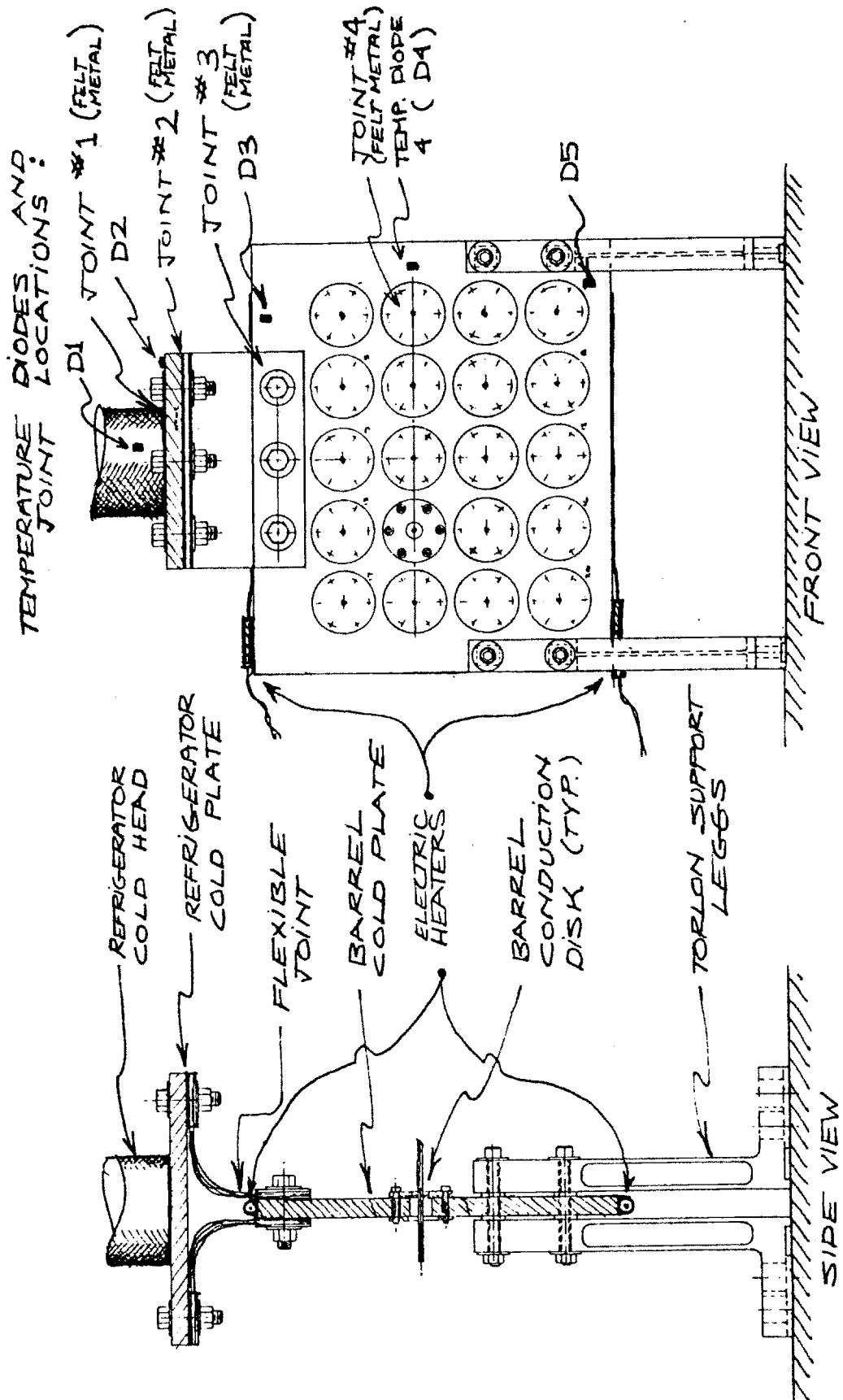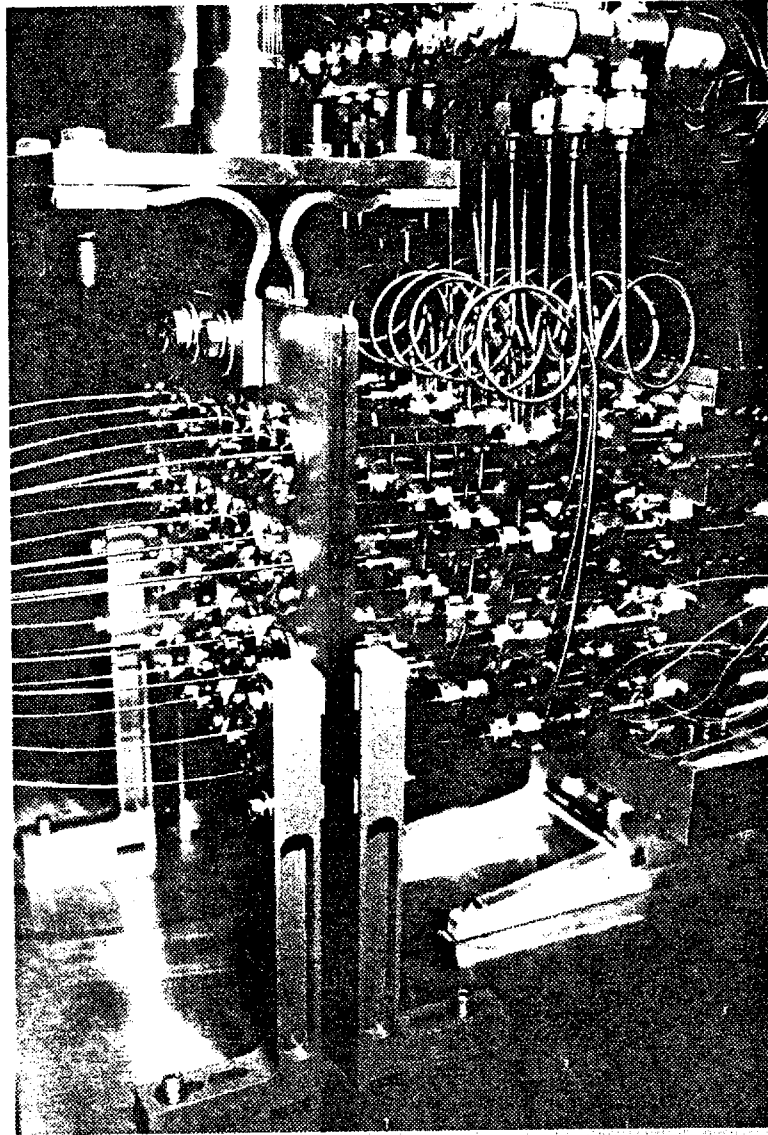Fig. 3.1.1: The thermal system components for configuration # 1.

53

Fig. 3.1.2: Close up view of configuration # 1.

CONFIGURATION #2

TEMPERATURE DIODES AND
JOINT LOCATIONS:

TEMPERATURE DIODE D1

JOINT #1 (VACUUM GREASE)

D2

JOINT #2 (VACUUM GREASE)

D3

D4

D5

REFRIGERATOR COLD HEAD

SINGLE PIECE THERMAL CONNECTION

HEATER BLOCKS

BARREL COLD PLATE
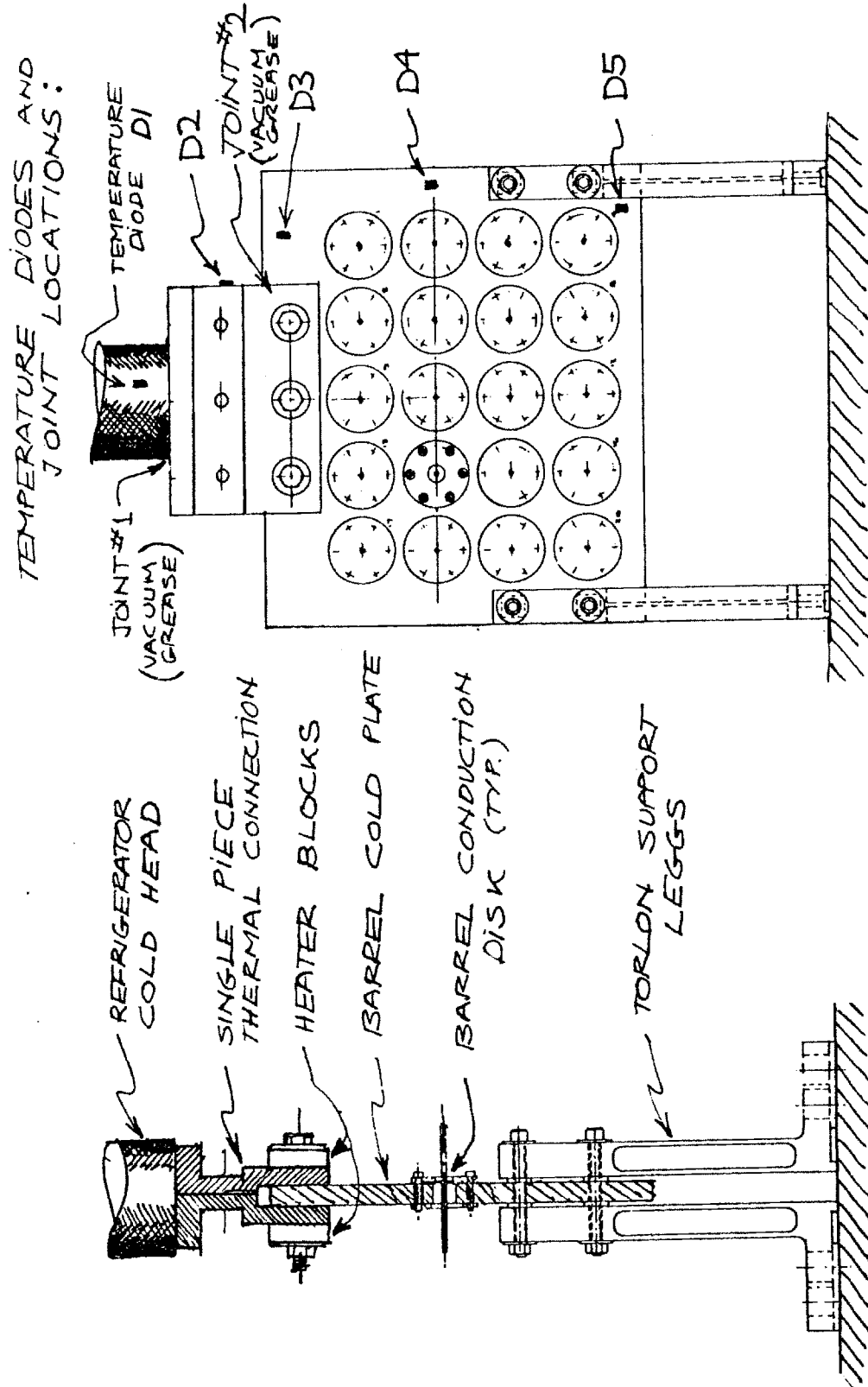
BARREL CONDUCTION DISK (TYP.)

TORLON SUPPORT LEGGS

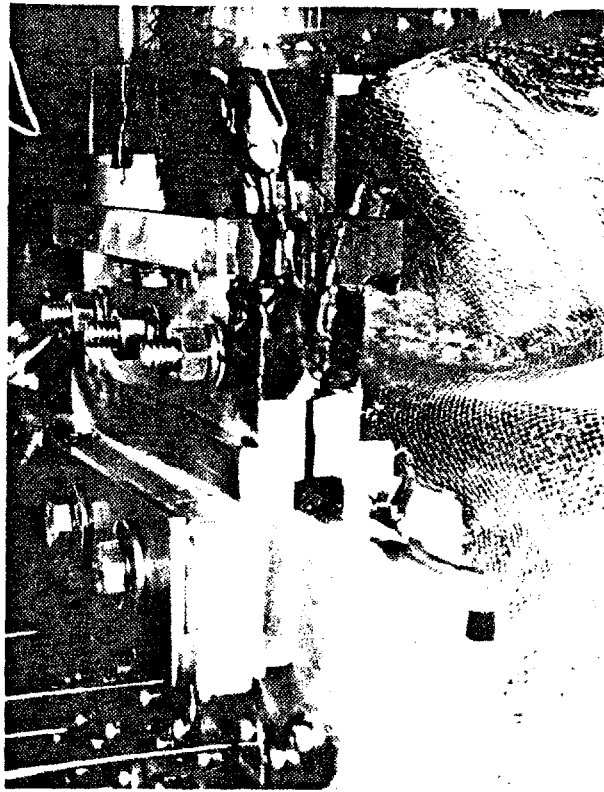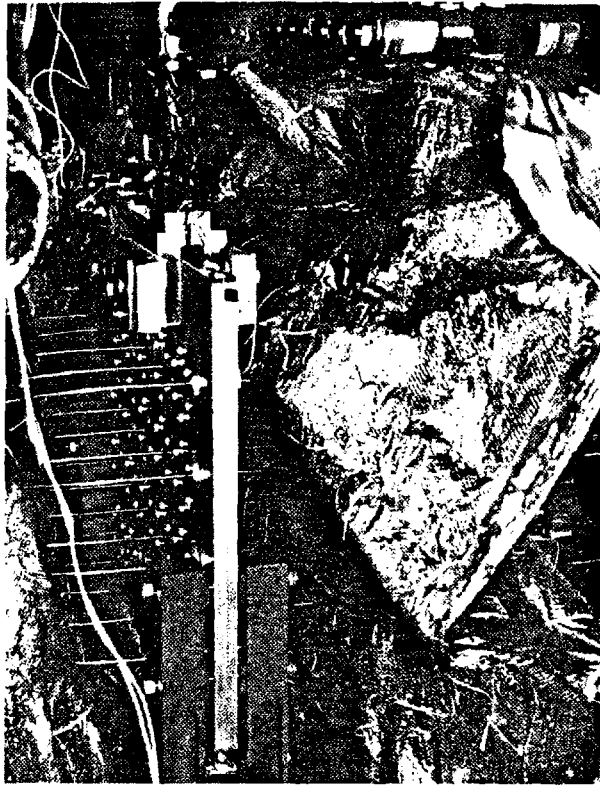Fig. 3.1.3: The thermal system components for configuration # 2.

55

Fig. 3.1.4: Close up view of configuration # 2.

3.2 Equilibrium Heat Loads

3.2.1 Conduction

Conductive heat loads to the barrel cold plate originate from three sources: along the barrels, up the support legs, and through the copper heater and diode wires. Heat flux by conduction is found using Fourier's law :

$$q = -k\frac{dT}{dx}$$

(3.2.1)

Material properties for copper, 304 stainless steel and Torlon vary considerably over the temperature range from 10 to 300 degrees Kelvin. This makes it necessary to integrate equation. 3.2.1 over the temperature range in question. Multiplying by the material sectional area , the equation becomes:

$$Q = \frac{A}{L}\int_{T_h}^{T_c} k(T)dT = \frac{A}{L}\gamma$$

(3.2.2)

The barrel cold plate support legs are made of Torlon, an organic material selected for its low thermal conductivity. The material properties of Torlon were not available over the wide range of temperatures needed. The properties of nylon were therefore used to simulate Torlon. The assumption is that since both are hard organic plastics of a similar chemical composition, it is likely their material properties vary comparably with temperature. Torlon has a slightly lower thermal conductivity than Nylon at room temperature, so the assumption is conservative with respect to the determination of heat loss. Total heat loss for the four legs was found to be .46 watts.

A similar approach was used to calculate heat flow through the barrels. The barrel ends were assumed to be connected to a constant temperature heat reservoir at 293 K. Equation 3.2 was solved by integrating an analytical expression for K(T) with fitted coefficients. Heat loss through all twenty barrels was found to be 1.46 watts. Heat to the barrel cold plate from the three temperature sensing diode leads and the four heater wires was determined to be less than .03 watts. Losses through this channel were minimized by thermally shorting the wires to the refrigerator first stage at 60 K. The sum of all conductive heat flows to the refrigerator from the three sources listed above , was 1.92 watts. The results are summarized in table 3.2.1 below:

Table 3.2.1 : Calculated Conductive Heat Load

Object	Material	Gamma (w/m)	sect. area (cm)	heat load per barrel	Number	Total Heat load (w)
Barrel (13 ga.)	SS 304	3875	.0231	.0962	10	.962
Barrel (15 Ga.)	SS 304	3875	.0131	.0546	5	.273
Barrel (17 Ga.)	SS 304	3875	.0108	.0450	5	.225
Support Legs	as Nylon	87	2.04	.116	4	.464

Total conductive heat load = 1.92 watts

3.2.2 Convection

The pressures maintained in the cryostat is typically in the 1×10^{-7} torr range. At this pressure, the mean free path is over half a meter. Since this is larger than the dimensions of the cryostat, the flow is in the molecular regime. The walls of the cryostat have a much larger area than the those of the cold thermal system components so the background gas temperature may be approximated to be that of the cryostat. Molecular heat transfer to the refrigerator is modeled by multiplying the total incident particle flux by the cold surface area and the average energy transfer per collision, i.e. :
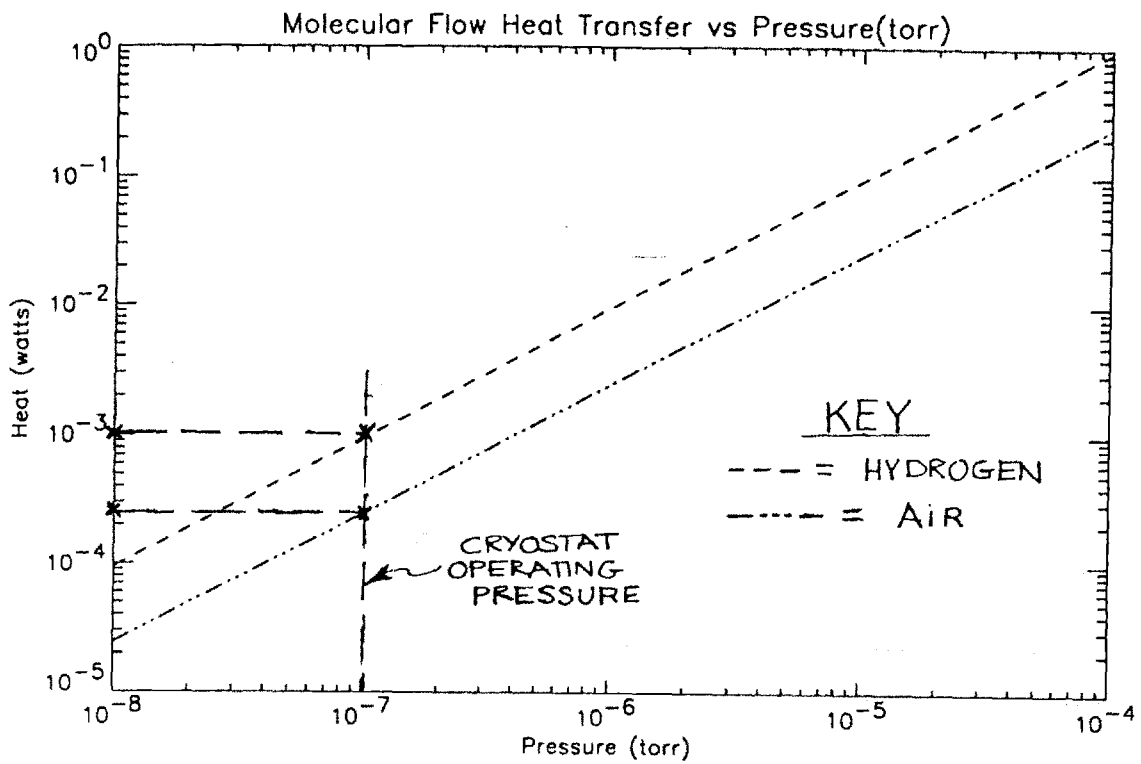
Fig. 3.2.1: Convective heat flow between the cold thermal system
components and the cryostat walls as a function of pressure.

$$H = A(\Delta E)\Phi = A(kT_h - kT_c)\left(\frac{n}{4}\overline{V}\right) \qquad (3.2.3)$$

In the equation above, A refers to the area of the cold thermal system components, ΔE the energy exchanged during collisions with the surface, and Φ the particle flux on the surface. Tc and Th refer to the temperatures of the hot and cold surfaces and k is the Boltzmann constant. The flux term is one quarter of the gas density ,n, times the mean molecular speed $\overline{V}$. The average molecular speed is dependent on the temperature and mass of the gas molecule,m, and is given by is given by:

$$\overline{V} = \left(\frac{8kT_h}{\pi m}\right)^{\frac{1}{2}} \qquad (3.2.4)$$

The total heat flow to the plate, H, has been calculated for both hydrogen and air and the results are plotted as a function of pressure in figure 3.2.1. The results show that at 1×10^{-7} torr the heat flow is below one milliwatt for both hydrogen and air. Convective heat transfer only becomes significant above 1×10^{-4} torr. This is consistent with experimental observations where diodes on the refrigerator showed small temperature increases for cryostat pressure spikes just above 1×10^{-4} torr.

3.2.3 Radiation

The maximum heat transfer by radiation between the cryostat walls and the copper cold plates may be estimated by assuming that the surfaces are perfect black bodies and that the area of the cryostat walls is much, much larger than that of the cold plate . The radiant heat flux under these conditions would then be:

$$Q_{h \to c} = A_c \sigma(T_h^4 - T_c^4) \qquad (3.2.5)$$

where T_h is the cryostat temperature, T_c is the cold plate temperature, Ac is the cold plate area , and σ is the Stephan Boltzmann constant. For the geometry where the cryostat walls surround the cold plate and the cryostat and coldplate are assumed to be diffuse gray surfaces of emissivity .4 and .2 respectively, the radiant heat transfer is given by:

$$Q_{h \to c} = \frac{\sigma(T_h^4 - T_c^4)}{\dfrac{1-\varepsilon_c}{\varepsilon_h A_c} + \dfrac{1}{A_c} + \dfrac{1-\varepsilon_h}{\varepsilon_c A_h}}$$ (3.2.6)

With the cold plate at 10 K and the cryostat at 293 K , the radiative heat transfer was calculated to be 13.5 watts . This calculation takes into account the different areas for the cold plate , refrigerator and the cryostat walls. This heat load is too large for the refrigerator to remove and still freeze hydrogen. The heat loss is minimized through the use of successive layers of "superinsulation" or aluminized Mylar. The superinsulation blanket is composed of 14 layers separated by nylon netting (see fig. 3.1.4). At equilibrium, each layer of the blanket is in radiative balance with the next. Equation 2.3.6 may be modified to include the shielding effect of the insulation. For the equation 3.2.7 given below, As and Es refer to the area and emissivity of the insulation:

$$Q_{h \to c} = \frac{\sigma(T_h^4 - T_c^4)}{\dfrac{1-\varepsilon_c}{\varepsilon_h A_c} + \dfrac{1}{A_c} + \dfrac{1-\varepsilon_h}{\varepsilon_c A_h} + \dfrac{2n(1-\varepsilon_s)}{\varepsilon_s A_s}}$$ (3.2.7)

The radiative heat transfer with fourteen layers of super insulation (n = 14) of emissivity of .02 is determined from equation 3.2.7 to be .10 watts. This calculation does not include the effect of gaps in the insulation. With the superinsulation bound in place, no bare copper is visible either through the holes for the barrels or at the support legs and refrigerator connection. This was carefully checked after the installation of the blanket using a dental mirror to view the insulation from all angles. Gaps are effectively sealed because the multiple layers shift around openings closing off any direct line of sight to the cold plate. If, however, the conservative assumption is made that one square centimeter is exposed and receives radiation directly from the cryostat walls eq. 3.2.6

may be used to calculate that the additional heat transfer is equal to .008 watts. The total radiative heat transfer would then be .108 watts, an acceptable load for the refrigerator.

3.2.4   Refrigerator Equilibrium Temperature and Heat Load:

The sum of all loads from the different modes of heat transfer is approximately two watts. Figure 2.5.2 is a plot of the refrigerator second stage temperature as a function of the applied heat load. From the graph, the temperature at two watts with no second stage heat load should be just under 9 K. The value is close enough to the 10 K initial estimate so that the assumed material properties(@ 10 k.) and calculated heat flow values are consistent.

3.3   Temperature Profiles

3.3.1   Contact Resistance and Refrigerator to Barrel Cold Plate
Temperature   Gradients

Temperatures and gradients in the cooling system may now be determined by assuming a two watt heat load at the low temperature equilibrium point and a cold head temperature of 9.3 K. No heat is lost in the thermal components joining the barrel cold plate to the refrigerator. Fourier's law is used to find the temperature drop across a length of material, l, with sectional area, A. The gradients are small so the conductivity, K, may be assumed to be constant, therefore :

$$\Delta T = \frac{QL}{KA} \qquad (3.3.1)$$

For the first configuration, the temperature drop across the refrigerator cold plate between the felt metal junction to the refrigerator and the bolted connection to the flexible joints was very small at .025 K. Conductivity was assumed to be 800 W/m K for RRR 50 copper at 10 K. The two flexible joints connecting the refrigerator and barrel cold plates were made of a sandwich of sixteen copper layers each .016 inches thick with copper plates soldered to each end. The heat load was divided evenly between the two joints and the temperature drop was computed to be .22 K .

Felt metal was used in the connection between the refrigerator cold head and the refrigerator cold plate and at connection on either end of the flexible buss contact . The feltmetal is designed to reduce the contact resistance between parts, and is composed of a fine mesh of sintered copper filaments backed by a thin copper strip. The pads were soldered to components by clamping a thin layer of solder ribbon between the felt metal and the copper plate. The sandwich was heated in an oven to a temperature of 360 K, about twenty degrees above the solder melting point.

Temperature drops across the pads are dependent on the bulk conductivity of the felt metal and solder and upon the contact resistance between the felt metal and the opposite surface. Of the two, the greater component is the contact resistance which is highly dependent on surface condition and pressure. Experimental data on the thermal contact resistance of the felt metal was not available from the manufacturer. Electrical resistance measurements were made however, as part of the Alcator C-Mod toroidal magnet development program, where feltmetal is used in the sliding joints between the magnet arms. The surface contact resistance for a .030 layer of feltmetal at 200 P.S.I.. was measured to be 10 $\mu\Omega/cm^2$ [7]. An "equivalent length" , Leq, of copper is the length of solid copper producing the same electrical resistance per unit cross sectional area. This length is calculated to be 40 cm for copper at 77 K. The assumption was made that thermal and electrical properties of felt metal scale equivalently so that the equivalent length applies also to thermal calculations. The temperature drop across Joints # 1,2,3, and 4 (see figs. 3.1.1 and 3.1.3) is then estimated based on Leq=40 cm and k=800 w / m K for copper at 10 degrees Kelvin. The results are summarized in table 3.3.2.

Table 3.3.2 :   Predicted temperature gradients across felt metal joints

Joint #	Area (cm)	Q (watts)	ΔT (K)
1	58.9	2.0	.17
2	58.1	1.0	.090
3	58.1	1.0	.090
4	3.3	.096	.13

Clearly, the temperature drops across the felt metal joints are at least the same order of magnitude as that due to conduction through the body of the copper plates.

For the single piece thermal link , the conductive temperature drop is found to be .055 degrees Kelvin. This value is approximately one fifth of that found for the first configuration and is due to the new connection's larger sectional area and shorter effective length . Estimates of the contact resistance for the new connection are based on experimental data for a copper to copper joint with Apiezon-N as the interfacial fluid [35]. The resistance is composed of two parts: the bulk resistance of the interfacial fluid and the Kapitza resistance. The Kapitza resistance arises from the acoustic mismatch between the different materials which reduce the transmission of thermal vibrations. This resistance varies as the inverse of the lattice specific heat , i.e. as T^{-3}. The resistance across the joint is then:

$$R = 2\left(\frac{c}{T^3}\right) + \frac{L}{KA} \qquad (3.3.2)$$

Measurements of the inter fluid thickness, L, were unfortunately not made during installation of the thermal link. Subsequent tests with vacuum grease sandwiched at 200 P.S.I. between copper plates of the similar area and smoothness, indicated the interfacial

grease thickness to be less than ten micrometers. The second term in equation 3.3.2 above therefore contributes only negligibly to the total resistance. The constant , c, is determined experimentally and cited in reference [33] to be 30 $cm^2 K^4$ / watt, so that R = .03 K cm / watt at 10 K. With a two watt heat flow, the temperature drops across the upper and lower joints of the single piece connection are .77 and .88 milli Kelvin respectively. As an order of magnitude check on the above calculation, reference [15] lists the bare contact resistance of a copper-copper interface at between .1 and .5 K cm /watt . With the addition of an interfacial fluid, the effective surface contact area is increased and these values are typically reduced by a factor of ten to .01-.05 K cm /watt .

3.3.2 Barrel Cold Plate Isotherms:

The physical dimensions and geometry of the barrel cold plate is shown in fig. 3.1.1. Heat enters the plate at the support leg attach points on the lower sides of the plate and also at the twenty connections between the barrel cooling disks and the plate. Heat leaves the plate from a one by six inch strip at the center, top edge on both sides. The relatively small, radiative heat load of .108 watts is neglected in the calculation for the temperature gradients. Because heat enters and exits the plate at several places, the plate may not be modeled in one dimension. The thickness to width dimension is small however, so that only two dimensions are needed in the heat transfer equations. Laplace's equation for a two dimensional slab model is:

$$q = -k\Delta T = -k\left(\frac{\partial T}{\partial X}x + \frac{\partial T}{\partial Y}y\right)$$ (3.3.3)

The equation may be solved either analytically with a Fourier series solution or numerically with a finite element analysis . The IDL code employed uses the relaxation method to solve the heat diffusion equation by first modeling the two dimensional slab as an array of discrete nodal points [57]. Initially, the boundary conditions are applied to the perimeter nodes and an initial estimate is made for the temperatures of the internal nodes. An iterative approach is used to reduce the temperature difference between the average of the nodes four neighbors and the node itself. When the difference is reduced
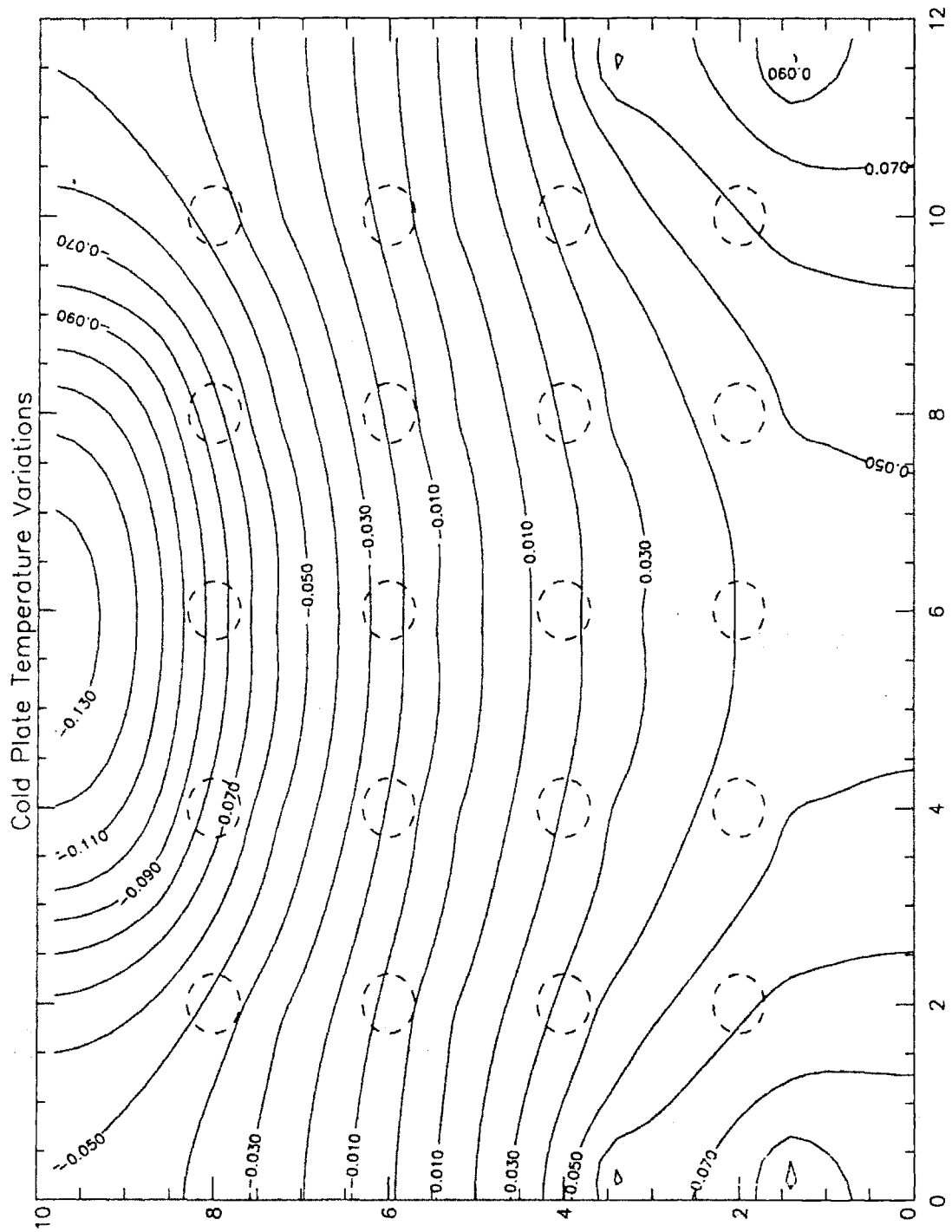
Fig. 3.3.1: Barrel cold plate temperature gradients.

to below some arbitrary value, the problem is considered solved. Because the anticipated temperature gradients are small, the material properties of the plate were taken as constant and those of RRR 50 copper at 10 K. The boundary conditions applied assumed

an average heat input of 60 mwatts for each barrel and 460 mwatts for each pair of legs. The holes for the barrels and mounting screws were not included in the model since these would have unnecessarily complicated the geometry and would have necessitated a much finer mesh size. Figure 3.3.1 shows a plot of the computed temperature gradients. The maximum difference in temperature between the top of the cold plate and the lowest corner barrel is approximately .2 K.

3.3.3   Barrel Temperature Profiles and Pellet Size

From the barrel cold plate only two remaining temperature increases occur. The first is across the felt metal joint between the barrel conduction disc and the barrel cold plate and the second is the conductive temperature drop through the disk to the freezing zone. The maximum and minimum temperature drops across the joints are determined to be approximately .13 K. for the 13 Gauge barrels and .06 K for the smaller 17 Gauge barrels. The conductive temperature difference across the barrel disc is calculated from the radial form of Fourier's law to range from .027 K. to .021 K for the 13 and 17 gauge barrels respectively. The assumption is made that temperature profiles in the conduction disc and barrel may be found with separate one dimensional conduction equations. This assumption is valid since the barrel to disk thickness ratio is small and the pellet freezing zone extends to several barrel thicknesses past the conduction disc, where the temperature profile is clearly 1-D.

A summary of the temperature drops in the thermal system is provided below for the top and bottom row barrels of both configurations. The assumed heat flow for these calculations is two watts. The second configuration is shown to have a clear advantage over the first with less than half the thermal resistance.

Table 3.3.3 :   Summary of Theoretical Thermal System Temperature Gradients For a Two Watt Refrigerator Heat Flow.

Location, (ΔT in Kelvin)	CONFIGURATION 1		CONFIGURATION 2	
	Top row 13 ga. barrels	Bottom row 17 ga. barrels	Top row 13 ga. barrels	Bottom row 17 ga. barrels
refrig. to barrel cold plate ΔT	.25	.25	.055	.055
Joint ΔT	.26	.26	.0016	.0016
Barrel cold plate ΔT	.060	.19	.060	.19
Barrel disk joint ΔT	.13	.060	.13	.060
Barrel disc cond. ΔT	.027	.021	.027	.021
Total ΔT to freeze zone	.73	.78	.27	.33
Freeze zone temperature	10.02	10.08	9.57	9.63

After the estimate for the temperature of the barrel at the conduction disk is made, the temperature profile along the length of the barrel may be determined. Figure 3.3.2 shows the barrel temperature gradients fore and aft of the conduction disk. The difference in the two is due to unequal heat flow in the two directions. Pellet size is estimated by assuming that the fuel gas freezes in the section of barrel which is below the saturation temperature of the fuel gas. Actually, the pellet itself forms a heat conduction pathway . The sectional areas of the pellet and barrel are almost equal, but the conductivity of solid deuterium is only one fifth that of stainless steel at the same temperature. Consequently, the conduction pathway through the pellet has a thermal resistance at least five times larger than that for the barrel. It is therefore reasonable to consider heat flow solely in the barrel.

The calculated pellet length and number of atoms per pellet vs freeze pressure are shown as solid lines in figures 3.3.3 (top) and 3.3.3 (bottom). Overplotted on the lower graph are the actual data based on in flight pellet photographs. Measurements of pellet length and diameter from photographs have an estimated dimensional uncertainty
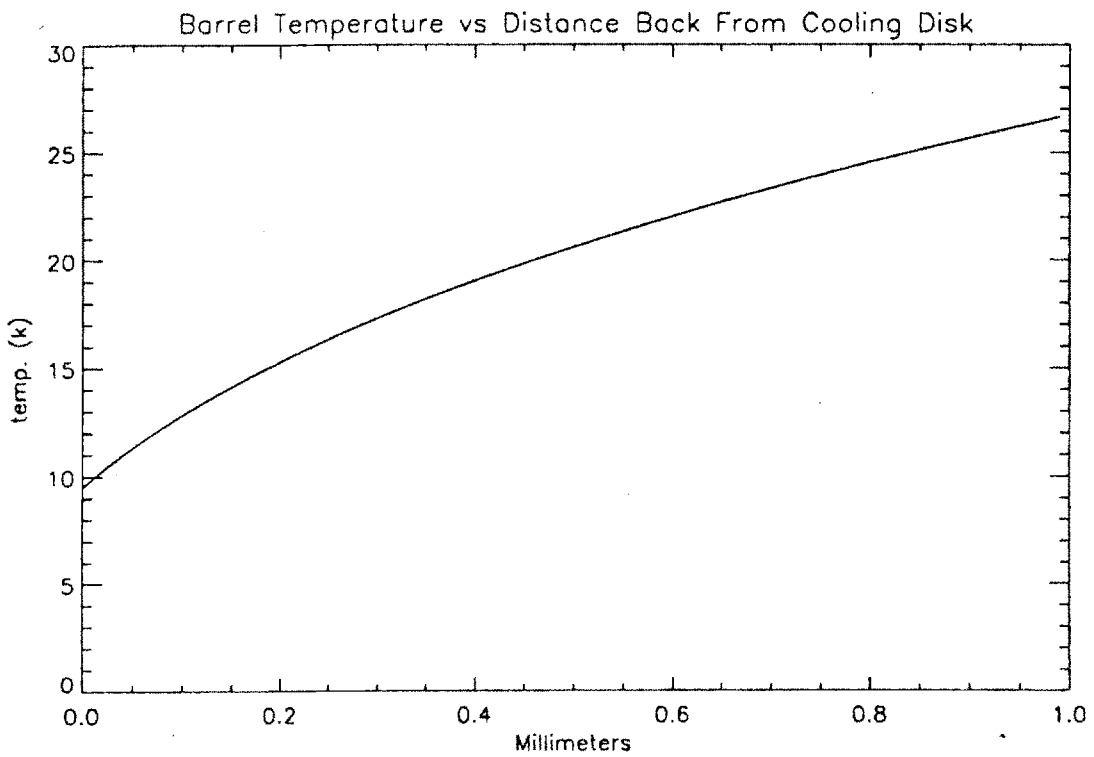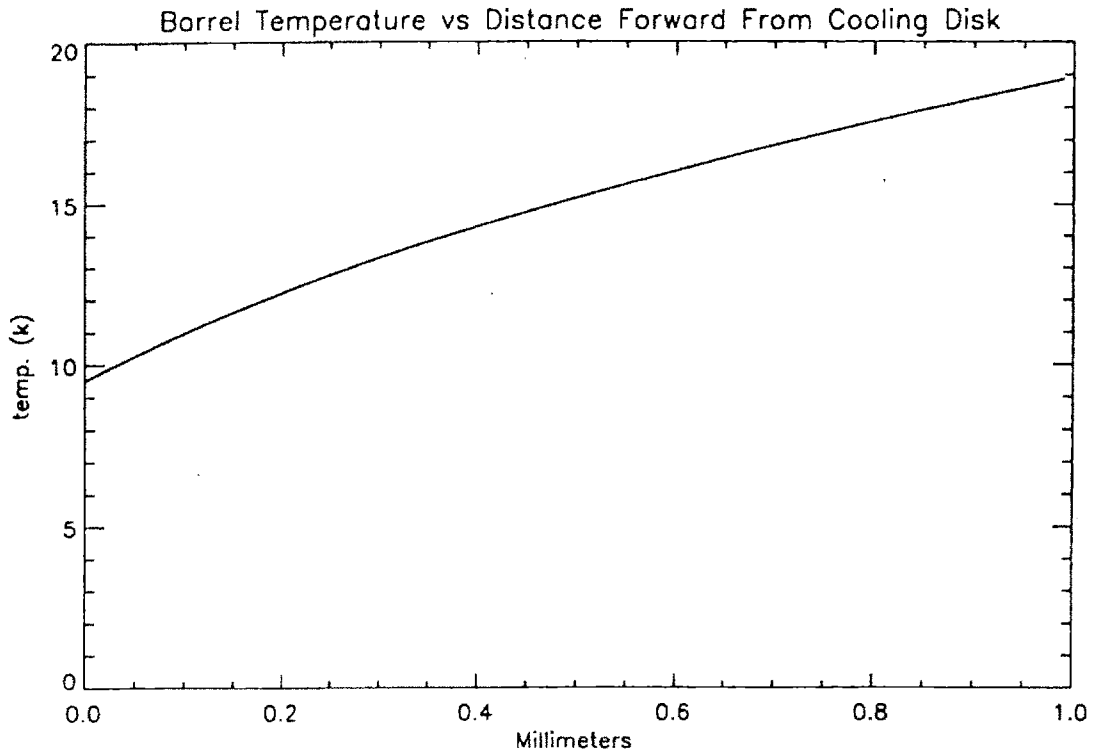
Fig. 3.3.2: Barrel equilibrium temperature profiles fore and aft of the
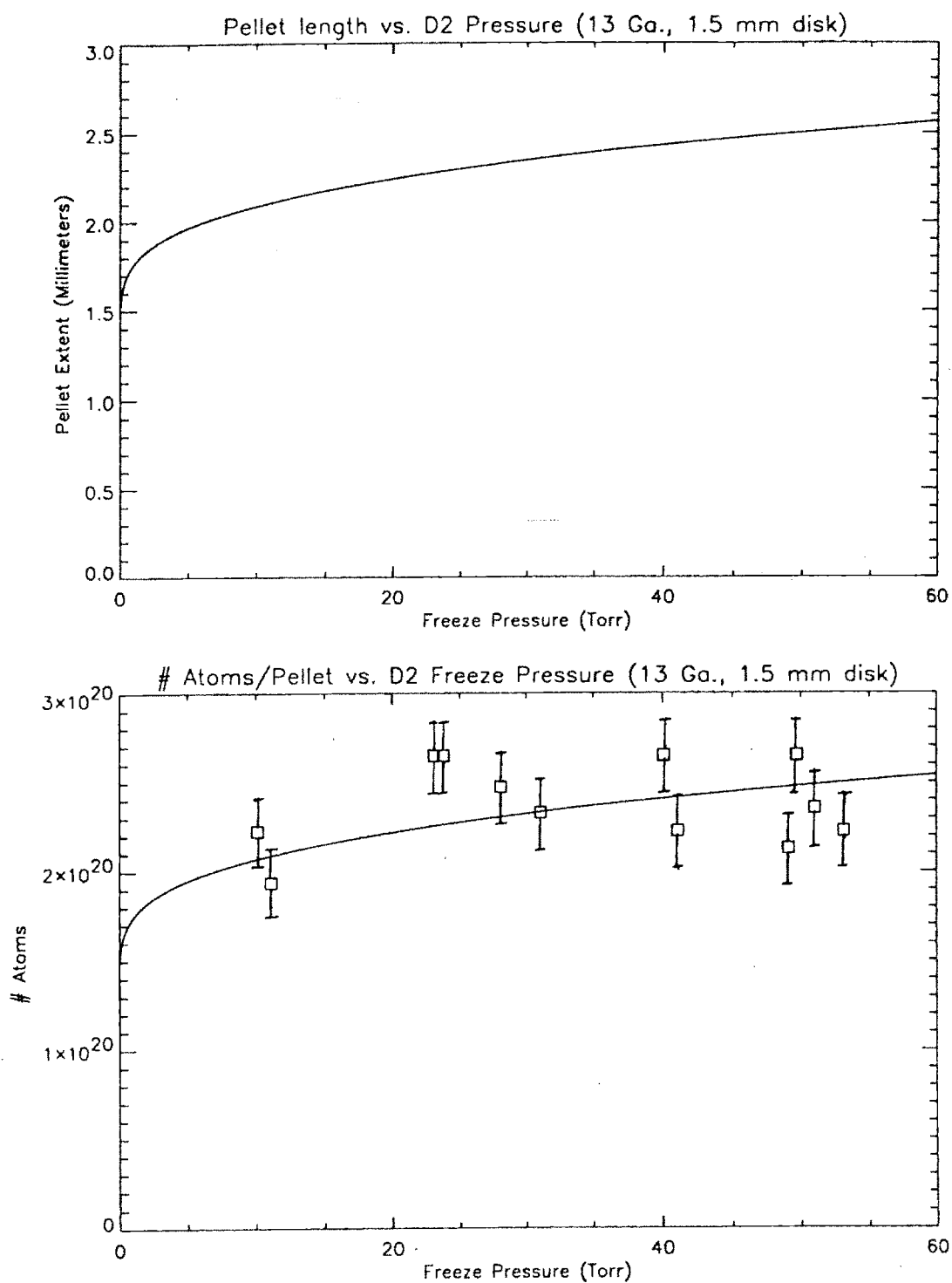barrel conduction disc.

Fig. 3.3.3: top: Theoretical pellet length vs freeze pressure for deuterium pellets. bottom: Theoretical number of atoms per pellet (13 Ga.) vs. freeze pressure. Experimental data points with error barrs are overplotted.

of ± 4 %, resulting in a derived mass uncertainty of ± 12 %. The theoretical prediction is therefore in relatively good agreement with the experimental data, at least to within the bounds of the experimental error. Pellet freezing experiments and a discussion of pellet mass measurements are presented in chapter four.

3.4   Transient Heat Loads

Two questions which need to be answered when considering transient heat transfer are: how long does it take to re-cool a barrel after firing? and does firing a pellet in one barrel heat the cold plate enough to melt pellets in adjacent barrels?. The answer to the first question is related to the minimum possible duty cycle for the injector and what we would like to do is make sure that barrel cooldown does not take longer than the tokamak duty cycle. The first step is to solve the one dimensional heat transport equation for the barrel:

$$\rho \frac{\partial}{\partial t} cT = -\frac{\partial}{\partial x}\left(-k \frac{\partial T}{\partial x} \right)$$

(3.4.1)

The boundary conditions used to solve this problem are to assume that the temperature of the barrel at the propellant valve and at the barrel sealing flange is fixed at room temperature (293 K). The temperature at the barrel conduction disk however, is fixed at 12 K. . The barrel is approximately symmetrical fore and aft of the barrel cold plate. After firing, the entire barrel length is assumed to warm up to room temperature . While this assumption clearly overestimates the barrel temperature rise after firing, it is appropriate since our goal is to find the maximum recovery time and establish it is below some minimum value.

Because the heat capacity and thermal conductivity of the stainless steel are both functions of temperature the equation is difficult to solve analytically and is instead solved numerically with the IMSL routine ("DMOLCH") [54]. Figure 3.4.1 presents the computed values for barrel temperature as a function of distance from the cooling disk . The first ten curves are taken every second for ten seconds and then every ten seconds

Barrel Temperature Profiles (every 1 s for 10 s, then every 10 s for 2 min)

1 Sec.
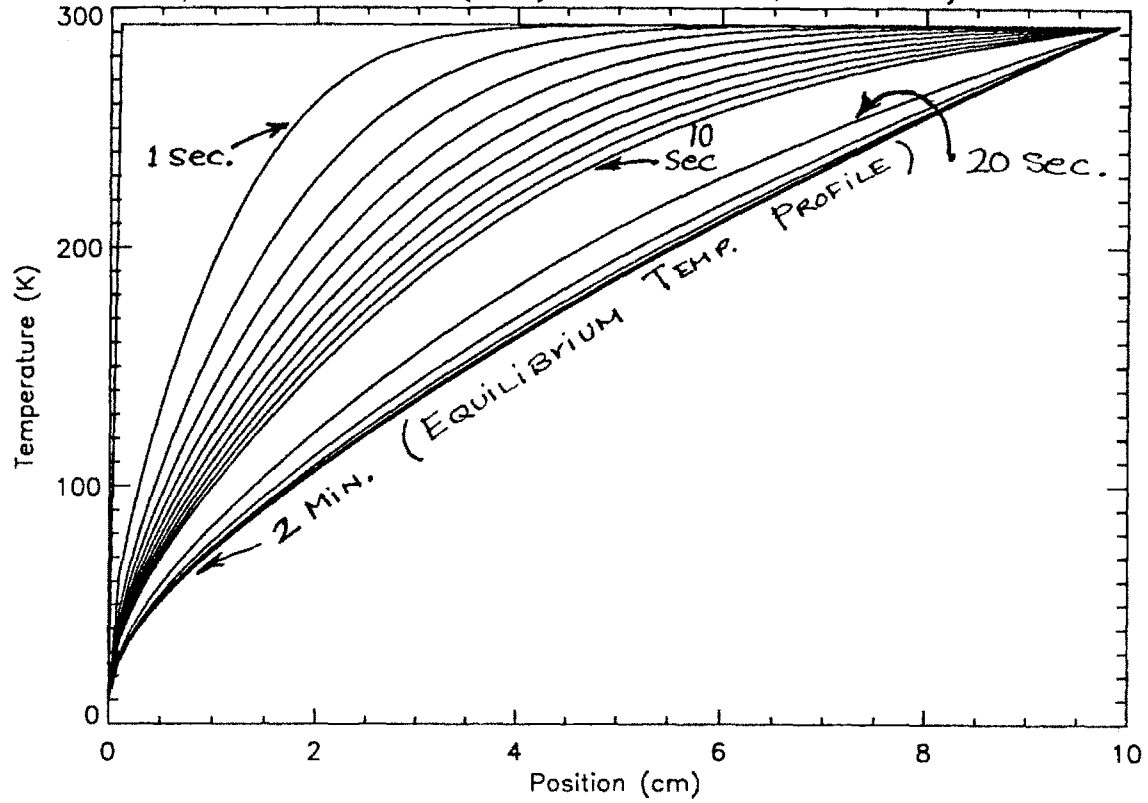
10 Sec

20 Sec.

2 MIN. (EQUILIBRIUM TEMP. PROFILE)

Fig. 3.4.1: Barrel temperature profiles following firing. The first ten curves are one second apart in time and successive curves are ten seconds apart.

for two minutes. The curves indicate that the barrel has essentially reached equilibrium within one minute after firing. The temperature at the conduction disc where pellets are made is fixed at 12 K. so one might be tempted to say that pellet freezing could begin immediately. Since the pellet does extend past the disk by about one mm, heat leaving the barrel does raise the temperature of the freezing zone. The conclusion to be reached is that pellets of maximum length may be made after a wait of no more than about sixty seconds, fortunately this is well less than the tokamak duty cycle.

The conductive heat transfer to the barrel cold plate may be found from the temperature gradient where the barrel meets the conduction disk :

$$Q = -kA\left(\frac{\partial T}{\partial x}\right)_{x=0} \tag{3.4.2}$$

If we assume a maximum time of half a second between firing barrels , the total heat to the cold plate is then found by integrating equation 3.4.2 from t=0 to t=.5 seconds. For times less than one second the barrels have the same thermal response as a semi infinite solid at room temperature subjected to a surface temperature change to 12 K. at t=0. The surface heat flux is then [57]:

$$Q = \frac{k(T_h - T_c)}{(\pi \alpha t)^{1/2}} \tag{3.4.3}$$

In the equation above, Th and Tc refer to the initial barrel temperature and the cold plate Temperature and α is the thermal diffusivity. Integrating equation 3.4.3 over half a second and multiplying by the barrel sectional area we get a total energy input of three joules. Since the barrel extends both forward and aft this value is multiplied by two for a total of six joules energy input to the cold plate in the half second following barrel firing. Because both the conductivity and thermal diffusivity of copper is an order of magnitude larger for copper than stainless steel, we can neglect the temperature gradients in the copper and assume that for this brief time interval the barrel cold plate rises uniformly in temperature. The resulting temperature increase is only .07 degrees for six joules and is therefore clearly insufficient to significantly melt pellets in adjacent barrels. Though the assumptions used for the estimation were simplistic, they are

73

accurate enough to show that at least the <u>order of magnitude</u> of the temperature rise is below that which would be problematic.

3.5   Experimental Results

3.5.1   Refrigerator Cooldown Tests

Cooling tests of the refrigerator were first conducted in July of 1992. These experiments were useful both to characterize the refrigerator cooling capacity and to estimate the thermal resistance between components. The tests were performed for both configurations of the thermal system.

Temperature measurements were made with five temperature sensing silicon diodes, the resistances of which are temperature dependent. The diodes are forward biased with two wires connected to each end of the diode . Two of these apply a fixed current flow across the diode and two sense the voltage drop. Voltage measurements are converted to temperatures through the Diode controllers non-linear internal calibration and displayed both at the controller and the PC . The diode controller internal calibration is set with reference to two fixed temperatures, the liquid nitrogen and liquid helium boiling points at atmospheric pressure. Three diodes are located near the top, middle edge, and bottom of the barrel cold plate. One diode is located on the refrigerator cold plate and one on the refrigerator cold head. All diodes are cemented into milled slots in the copper using STYCAST thermally conductive epoxy. Wire leads to the diodes are thermally shorted to the refrigerator first stage. It is essential to minimize the heat transfer through these wires both to prevent heat loads to the refrigerator and to avoid the resulting temperature difference between the diode and cold plate . The diodes have an absolute temperature accuracy of ± .5 K between 2K and 100K and ± 1.0 K from 100-305 K [64].
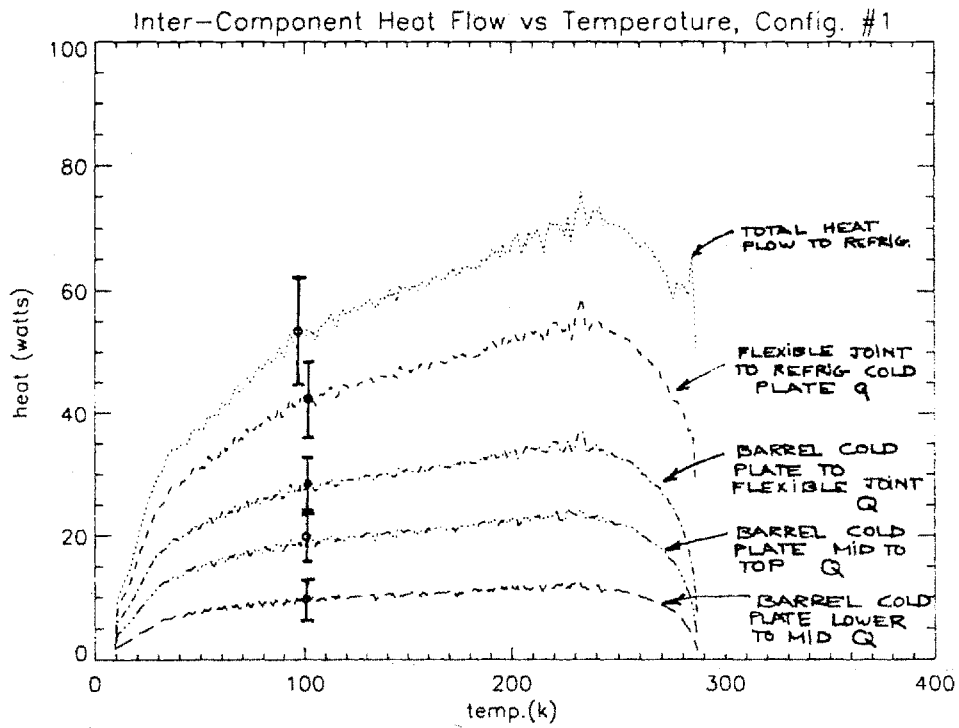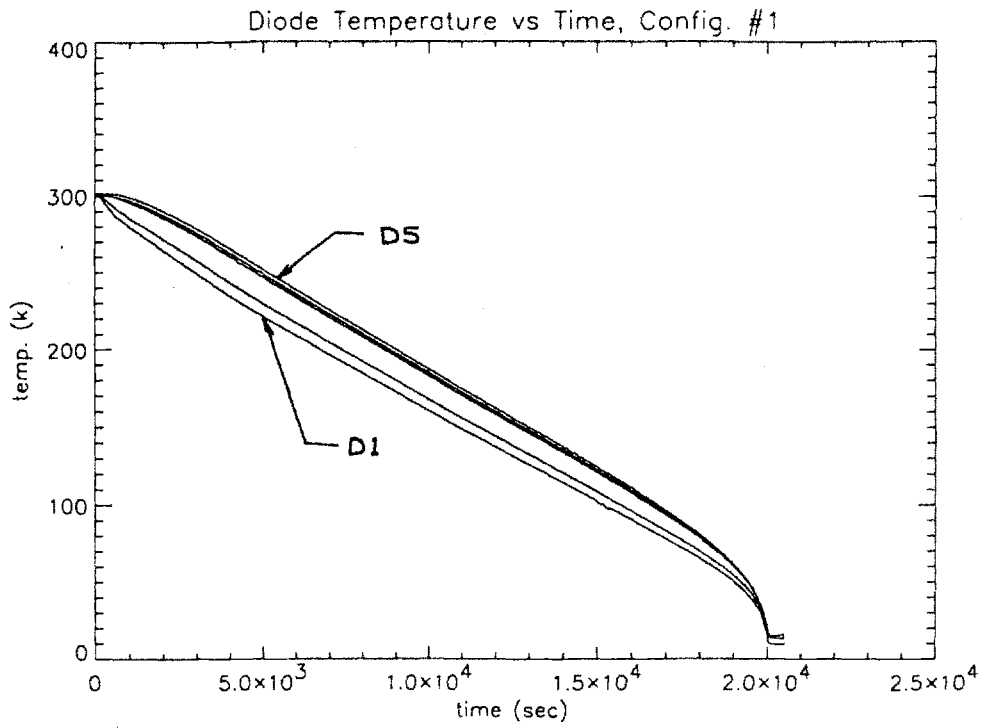
Fig. 3.5.1   (top): Refrigerator cooldown curves for config. #1.

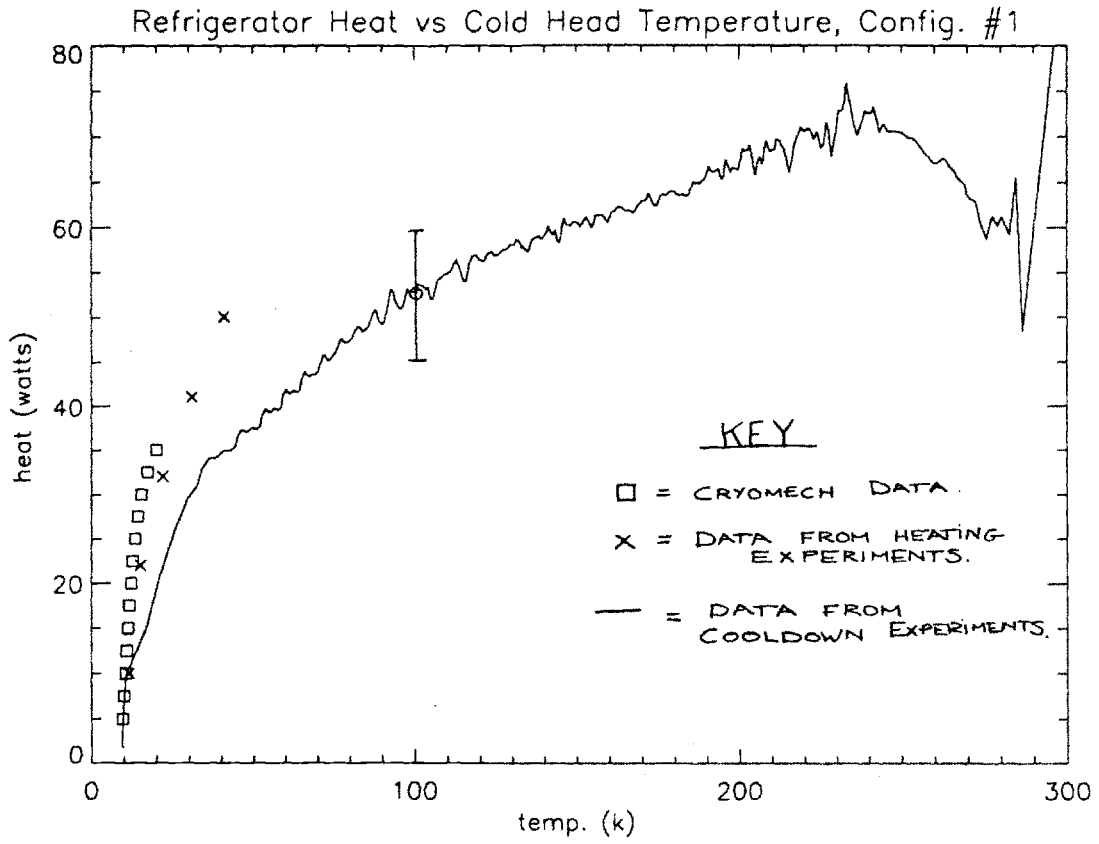(bottom): Inter-component heat flow vs. temperature for config. #1

Fig. 3.5.2 Total refrigerator heat load as a function of cold head temperature
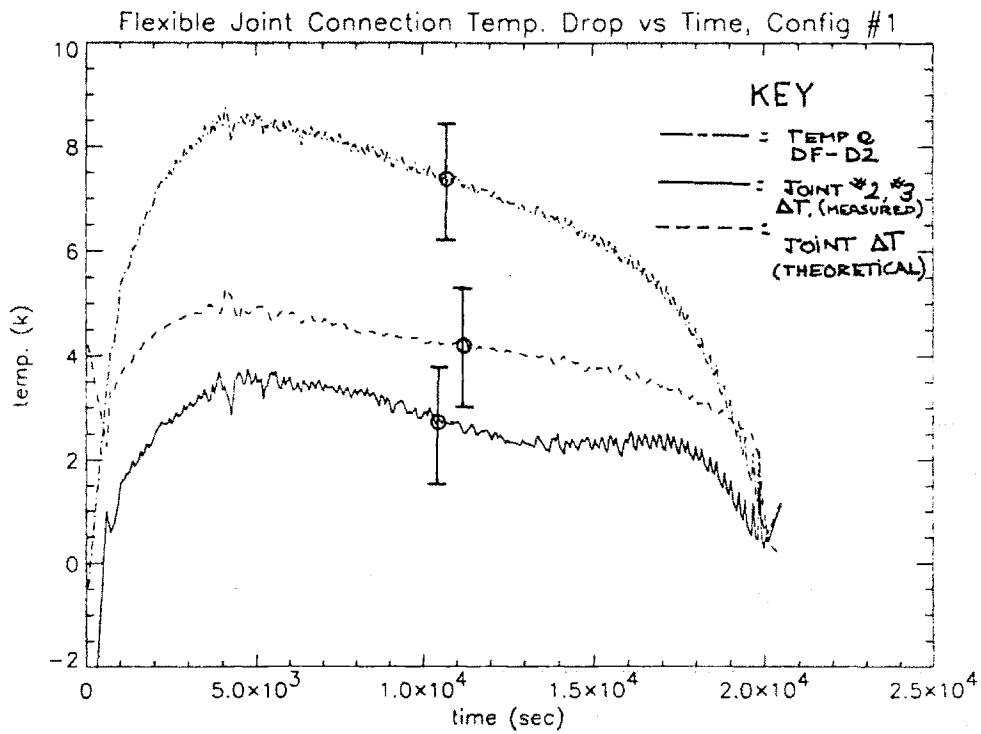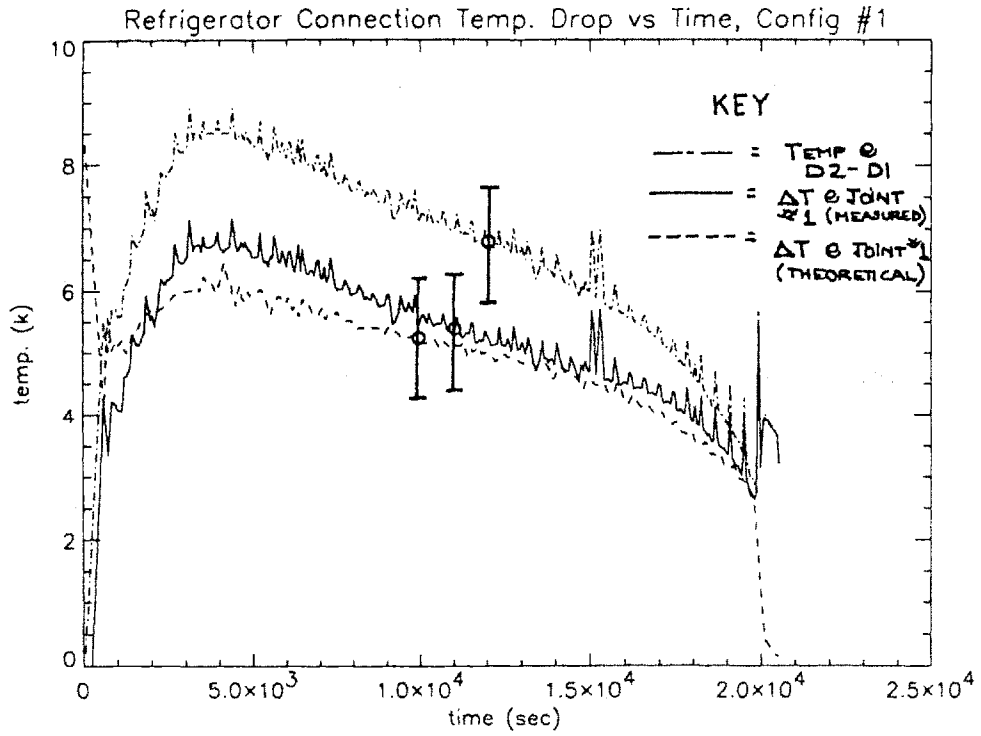as measured by cooldown test.

Fig. 3.5.3: (top): Refrigerator connection temp. drop vs. time for config.#1
(bottom): Flexible joint connection temp. drop vs. time for config. #1

During cooldown, temperature measurements were recorded automatically whenever values changed by more than one degree . The data was recorded for a six hour period beginning at the start of operation. The experiments sought to test both the basic

operation of the refrigerator, and to find the lowest attainable temperatures. The data for the first configuration is shown in figure 3.5.1 (top) and indicates a minimum cold head temperature average of 9.6 ± .5 K. . Assuming normal operation of the refrigerator , this corresponds to a heat load of between 2 and 5 watts, within the range of that predicted. At equilibrium, the average recorded barrel cold plate temperature was 14.22 K which indicates a 4.62 K temperature drop to the cold head. Total time for the cooldown was 5 hours and 33 minutes. The temperature vs. time graph shows a 10 to 15 degree temperature gradient between the barrel cold plate and the refrigerator . This was the first indication of the larger than expected thermal resistance for the first configuration.

The cooldown curve for the second configuration (Fig. 3.5.4 (top)) shows a smaller temperature spread between components, revealing that thermal resistance has been reduced for the new configuration. The total cooldown time is five hours, thirty three minutes less than for the first configuration. The difference is due to a ten percent reduction in mass for the single piece connection. The sharp drop in temperature towards the end of the cooling cycle is due to the sharply reduced specific heat of copper below 40 K. Low temperature equilibrium at the cold head and barrel cold plate are 9.8 and 12.8 degrees Kelvin respectively, for an average temperature difference of 3 degrees K .

This cooling rate data was also used to estimate the cooling capacity of the refrigerator at higher temperatures. The model used assumed thermal system components to be isothermal lumped masses. The barrel cold plate was modeled as three separate masses. The flexible joint temperature for the first configuration was taken to be the average of that between the refrigerator and barrel cold plates. The location of all diodes remained unchanged during tests on the second configuration except for the second diode which was placed on center edge of the single piece connection. Time derivatives of the temperatures were multiplied by the thermal capacitance of each mass to determine the heat flows between each component and the refrigerator. Figure 3.5.2 shows the total refrigerator cooling capacity as a function of cold head temperature. Overplotted on these results are the data from equilibrium heating experiments (described later) and performance data from CRYOMECH inc.. The manufacturer's data and the heating test
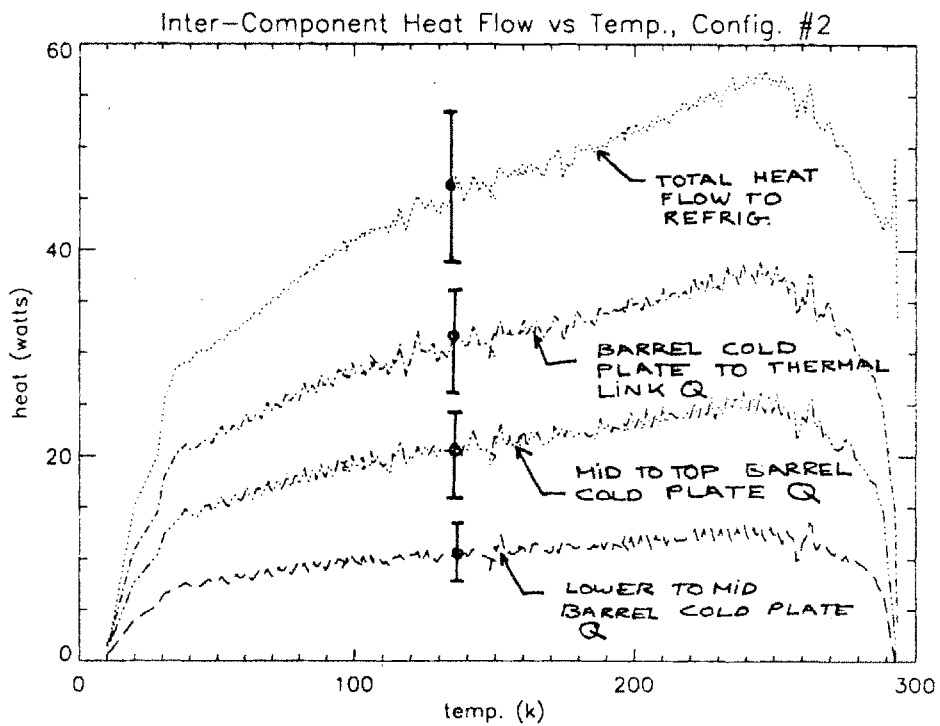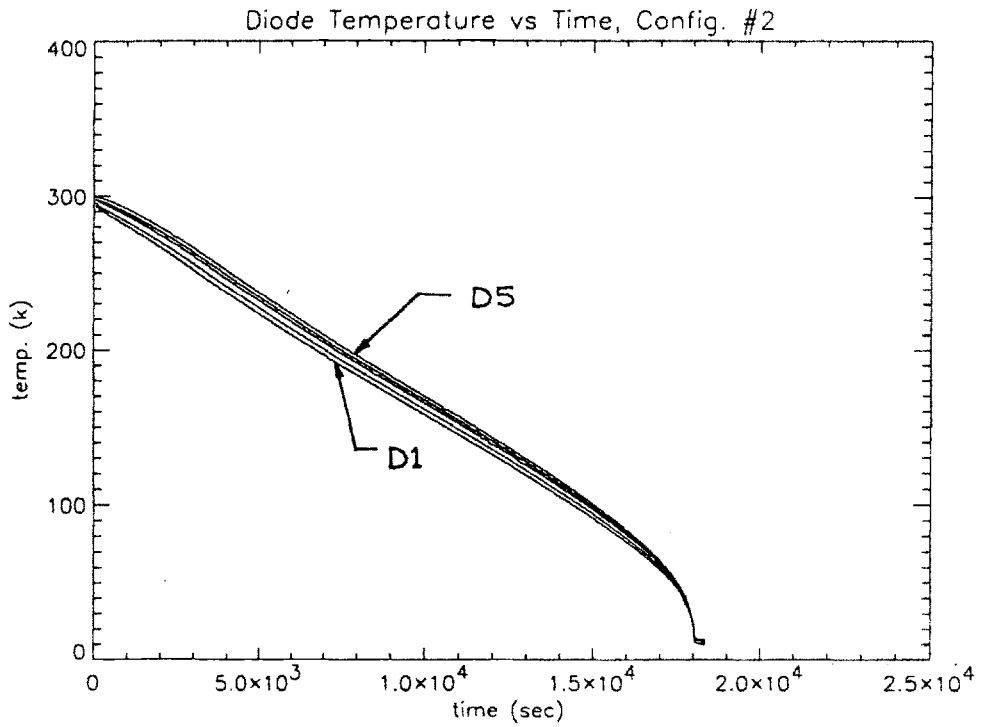
Fig. 3.5.4 (top): Cooldown test data for thermal configuration #2.

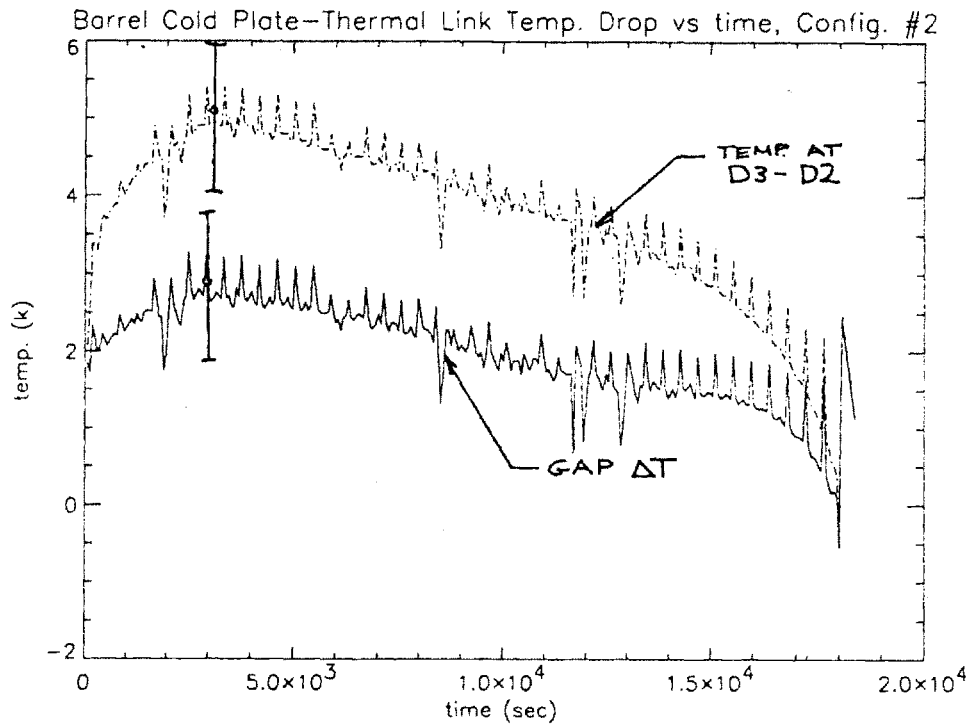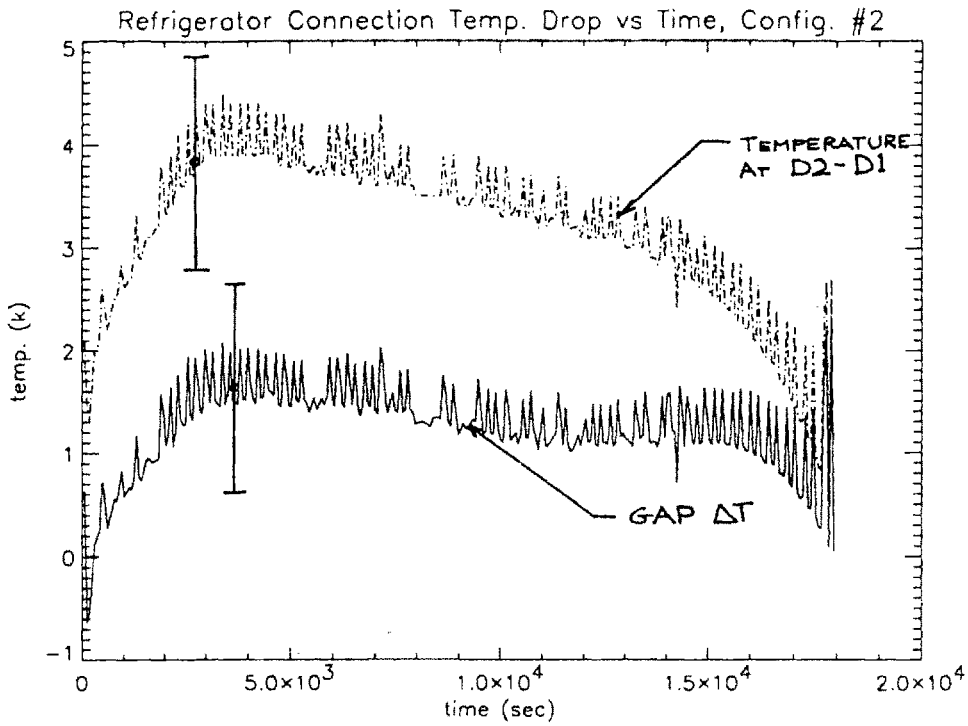(bottom) : Inter-component heat flows as derived from cooldown data.

Fig. 3.5.5 (top): Refrigerator connection temp drop vs time for config. #2.
(bottom) : Barrel cold plate to thermal link temp. drop, config, #2.

data shows a slightly higher performance at low temperature than that observed. At temperatures below 30 K. however, results from the three sources do converge. Short time scale temperature variations are artificial and result from taking derivatives of temperature data with random digital fluctuations.

While the new thermal connection shows a 1.6 degree improvement over the first, the temperature drops between the cold head and barrel cold plate are still an order of magnitude larger than that predicted. The refrigerator equilibrium temperatures measured are consistent with the predicted heat load as are the gradients within the single piece barrel cold plate. These factors suggested that the large overall temperature drop was the result of higher than expected contact resistances between components and that further tests were required to quantify the inter-component resistances.

3.5.2 Contact Resistance Measurements

The two watt heat flow at the low temperature equilibrium point produces temperature differences between the diodes of less than one degree. The half a degree measurement uncertainty below 100 K makes the accurate determination of joint temperature drops and contact resistance difficult for the fully cooled parts. Two methods were used to improve the accuracy of the measurements.

The first method used the inter-component heat flows determined from the cooling rate temperature data to calculate the conductive temperature drops in the copper between the diodes and the connection. This conductive temperature drop is subtracted from the total temperature difference between diodes on either side of the connection, to arrive at the joint ΔT. This method was used for both thermal configurations.

The second method for assessing contact resistance was used only for the first configuration and involved heating the barrel cold plate using two 26 Ω resistive heaters mounted to the top and bottom edges of the barrel cold plate. Equilibrium temperature measurements were made at the five diodes for input powers of from ten to fifty watts. The advantage in this method is that heat flows are known more accurately since they are not derived from temperature derivatives. This method was only used for the first
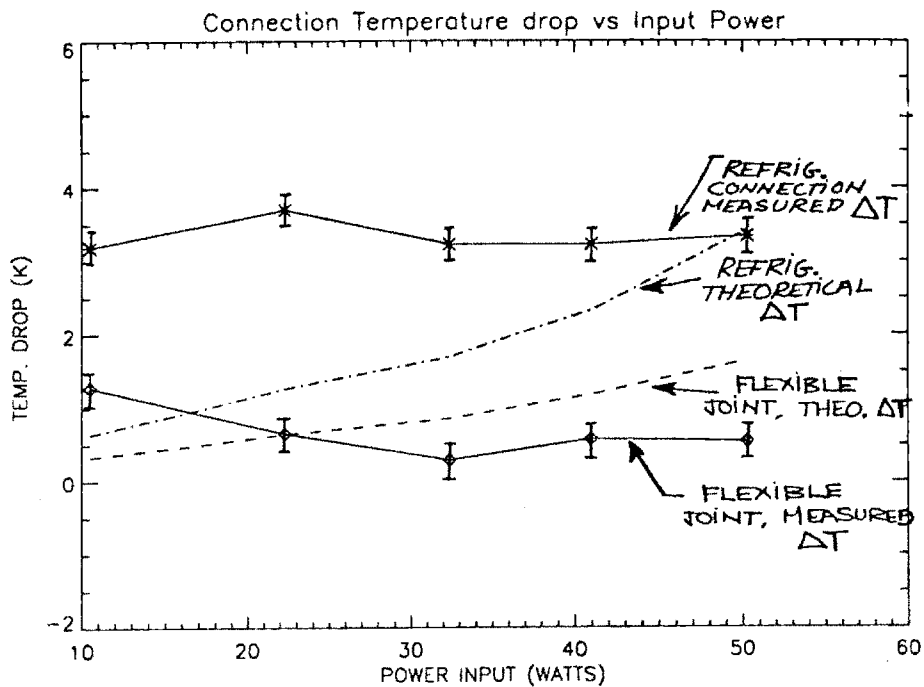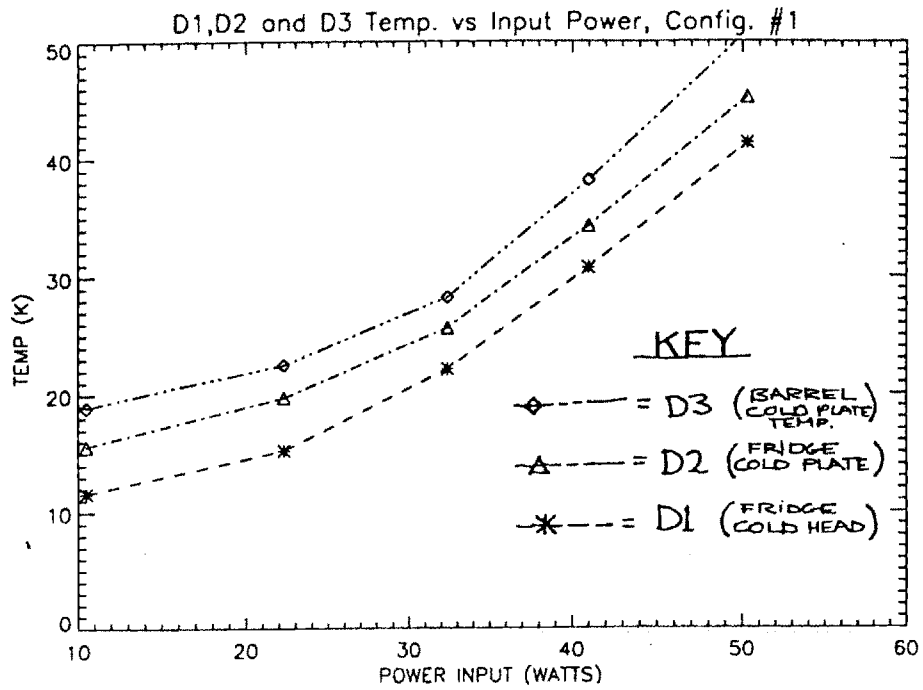
Fig. 3.5.6 (top): Equilibrium heating test data; diode temperature vs. power input.
(bottom): Connection temperature drop as a function of input power.

82

configuration both because of time constraints and because a failure in the original edge mounted heaters necessitated their replacement with more rugged block heaters. The

block heaters are bolt mounted directly to the single piece thermal link and not the barrel cold plate. As a result, the total heat flow may be measured through the top joint only.

Results for the refrigerator to refrigerator cold plate connection of configuration #1 are shown in fig. 3.5.3 (top) . The data shows that the theoretical and actual temperature drop agree to within the experimental error. The temperature drop reaches a maximum of about 6.5 degrees at a heat flow of 70 watts, or a little less than a tenth of a degree per watt. Data for the flexible joint connection are shown in figure 3.5.3 (bottom) and also match that predicted. The actual temperature drop is about 30 % lower than the predicted, which may be indicative that clamping pressures higher than the 200 PSI reference were employed. These joints show about a tenth of a degree temperature drop per watt .

The data for the second configuration are shown in figures 3.5.5 (top) and 3.5.5 (bottom). These figures indicate temperature drops of approximately .030 degrees per watt for the refrigerator connection and approximately .060 degrees for the barrel cold plate connection. Both values are much higher than that predicted theoretically and are probably the result of reduced contact area in the joint region resulting from surface irregularities. The good news however, is that both the conductive and contact temperatures drops are reduced in the new joint design. The overall thermal resistance between the refrigerator and barrel cold plate is reduced by about 1/3 from .3 degrees / watt to .2 degrees/watt.

Figure 3.5.6 shows the results from the equilibrium heating experiments made for the first configuration. The data indicates an equilibrium temperature range of from 10 to 50 degrees Kelvin for input powers of between ten and fifty watts. The connection temperature drops across the cold head and flexible joint versus input power is shown in figure 3.5.6 (bottom). The results indicate that at low temperature, the temperature drops across the joints do not increase linearly with heat flow as expected. Furthermore, the temperature drop across the refrigerator connection is three times larger than the theoretical prediction at ten watts. The data points to the conclusion that the "equivalent length model", while reasonably accurate at higher temperatures, fails at low temperature. The data are insufficient to make any specific conclusions however, and

serve primarily to indicate that in the first configuration, the contact resistance at low temperature was much higher than predicted by the model. These results led to the decision to change to a single piece thermal connection without felt metal.

Chapter 4 : Injector Performance

4.1 The Pellet Freezing Process

The Alcator C-Mod pellet injector forms pellets in all twenty barrels simultaneously by freezing them in place within the barrels. This is done by cooling a small section of the barrel to approximately 12 K and then bleeding the fuel gas through it. Because the barrel temperature is below the triple point, the hydrogen or deuterium fuel gas freezes directly from vapor to solid on the barrel walls, thus forming the pellet. These may then be fired by pulsing high pressure propellant valves connected to the selected barrels. This chapter seeks to explore some of the variables in the freezing process as well as to characterize the injector's laboratory performance.

The first step in forming pellets is to open the solenoid valve to the selected fuel gas bottle and then fill the fuel plenum . Flow into the plenum is restricted by a needle valve so that the pressure rise is slow enough for the PLC to close the solenoid valve when a pre-selected pressure is reached. With the plenum full, the aft injection line gate valve (Pn7 of fig. 2.6.1 and 2.7.1) is closed and the twenty solenoid fueling valves are opened. Fuel gas flows from the plenum through the barrels, filling the bellows volume forward of the barrels. Equalization of the pressure between the two volumes takes about thirty seconds after opening the fuel valves. Equilibration pressure is determined by the initial plenum pressure and the ratio of the volumes fore and aft of the fueling valves. After the fueling valves are opened, fuel gas begins to freeze on the barrel wall near the conduction disk. Eventually, if the barrel walls are cold enough, the pellet completely plugs the barrel. The pellet will grow to a length such that the ends of the pellet are just at the vapor-solid transition temperature for the given fuel pressure. Pellets are formed in all twenty barrels simultaneously.

After a freezing period lasting from one to five minutes, the fuel valves are closed and gate valve Pn 7 is opened to pump excess fuel gas away. Pellets are now ready for firing by pulsing the appropriate propellant valves.

4.2 Deuterium Pellet Freezing Experiments

4.2.1 Initial Results and Changes

The first pellet freezing experiments began in August of 1992. These tests sought to demonstrate pellet freezing and acceleration and to quantify the effects of varying parameters in the freezing process, such as freeze time and fueling pressure. Through these experiments reliable operation of the injector was established and the optimum parameters for freezing deuterium and hydrogen were found.

Several sources of data were used to diagnose injector performance and pellet condition. The sources are briefly outlined below in order to clarify some of the measurements presented in this chapter .

1) Diode signals from the two laser photodiode gates were used to measure pellet velocity and fragmentation. Each "gate" consist of a laser and photodiode detector. Pellets from all twenty barrels pass through the beam of each gate and a drop in signal intensity is recorded at the diode. The shape of the signal may yield information on pellet fragmentation and time the time delay between the signals from two gates may be used to make accurate velocity measurements.

2) Pressure and temperature measurements of the process gas and thermal system were used to deduce freezing conditions.

3) Pellet size and mass were determined from in-flight pellet photography. The system used employed a CCD video camera with a flashlamp light source to capture video images of the pellets as they pass through the injection line test section.

4) Foil targets provided information on pellet fragmentation and condition.

5) Photo diode velocity measurements were augmented with signals from a
target microphone. The microphone was installed on a retractable target plate
after April 1993, and provided a second timing reference with which to
measure velocity.

A more detailed description of the photodiode light gates and the photography
system is given in chapter five.

The first freezing experiments using deuterium fuel showed that pellets could be
made with plenum fill pressures between 60 and 500 torr. This corresponds to
equilibration pressures between 8 and 85 torr. Freeze times between one and six minutes
were tried successfully, but for times less than one minute pellets were highly fragmented
and incompletely formed. Increasing the freeze time beyond three minutes appeared to
have no effect on size and condition. The pellet photography apparatus was not installed
prior to September of 1992, therefore pellet size and condition in the first tests were
found with diode signals and target foils. Examples of diode signals from complete,
and fragmented pellets are shown in figure 4.2.1. . A typical target foil, displayed in
figure 4.2.2, shows the impact patterns made from complete and fragmented pellets .
The pellet trajectories in the test section are spaced far enough apart so that holes in the
foil may be identified with specific barrels.

Initially not all the barrels made pellets and a number of barrels made pellets
which were either fragmented or smaller than those from other barrels of the same gauge.
This was further complicated by the fact that occasionally pellets from a particular
barrel could be seen on the first diode and target foil but not on the second diode. The
picture that began to emerge was that all the pellets which were successfully formed and
accelerated could be seen on the first diode. Some pellets from this group were not also
seen on the second diode for any of three reasons : 1) Pellets were either highly
fragmented or not fully hardened, forming "slush". These pellets either never enter the
guides tube or are fully vaporized by the time they reach the end, so there is no
possibility of detection on the second diode. 2) Other pellets, after passing the first
diode, impact on the guide tube entrance or support plate and break up prior to reaching
the second diode. 3) The trajectories of some pellets are such that they pass a "blind
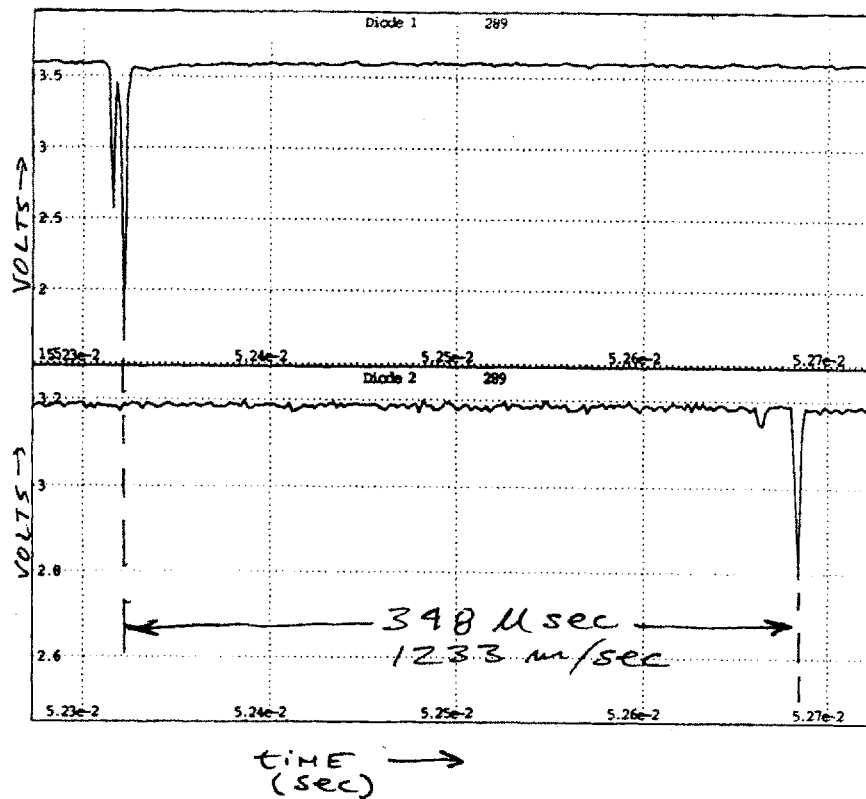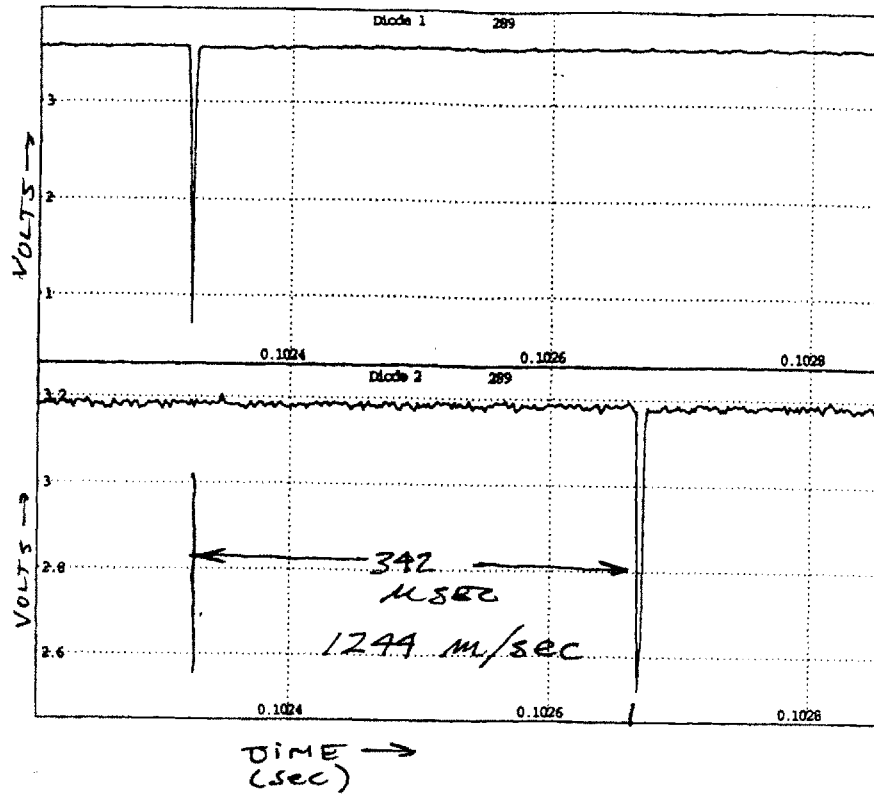spot" in the second laser-photodiode gate and are therefore undetected on the second

Fig. 4.2.1: Diode signals from complete (top) and fragmented (bottom) pellets.

88

diode, but still make it to the target foil. The third possibility, seen only rarely on barrels 17 and 20, resulted from a machining error in the manufacture of the second laser-photodiode gate. Pellets detected at both diodes are always seen on the target foil even if fragmented.

Before more systematic studies could be made on the injector performance, several steps were taken to fix the non functioning barrels and to improve barrel reliability in general. The first change was to align the guide tube array more carefully with the barrel ends so that pellets would enter the guide tubes without striking the guide tube lip or support plate. The installation and alignment of the guide tubes served to more accurately define the exact trajectory of the pellets. Blind spots in the second laser photodiode gate were eliminated by aligning the laser with the ends of all twenty guide tubes and by expanding the beam to a diameter slightly larger than that of the guide tubes.

In the first few weeks of operation, it became clear that pellets were formed most reliably only after the injector was fired several times and then degraded slightly with prolonged use. There was no change in fuel pressure or equilibrium cold plate temperature during this time and the most likely explanation was that the barrel interiors had become contaminated. Trace impurities in the vacuum or process gas system such as pump oil, water or air could condense in the barrel freezing zones, hindering pellet formation. Remnants of pellets or solidified propellant gas may also impede new pellet formation. To solve the problem two sixty watt electric heaters were mounted on the upper and lower edges of the barrel cold plate. These were used to heat the barrel to 25 K between pellet batches and once a day to 80 K. As a result of these changes, pellets detected at the first gate were now generally always seen on the second. The periodic heating was also found to improve barrel reliability and reduce fragmentation.

After the initial period of operation, the fuel system was modified to solve two problems. The first difficulty was that pumping out the small 1/8 inch diameter lines was extremely time consuming due to their low conductance. These lines were increased in size to one quarter inch O.D. and the system was simplified by removing a solenoid valve between the plenum and fueling valves. Check valves were added downstream of the main fuel and propellant valves in order to prevent back flow through the valves and upstream contamination of the fuel system. This period was also used to fix several small leaks into the cryostat from the propellant valves.
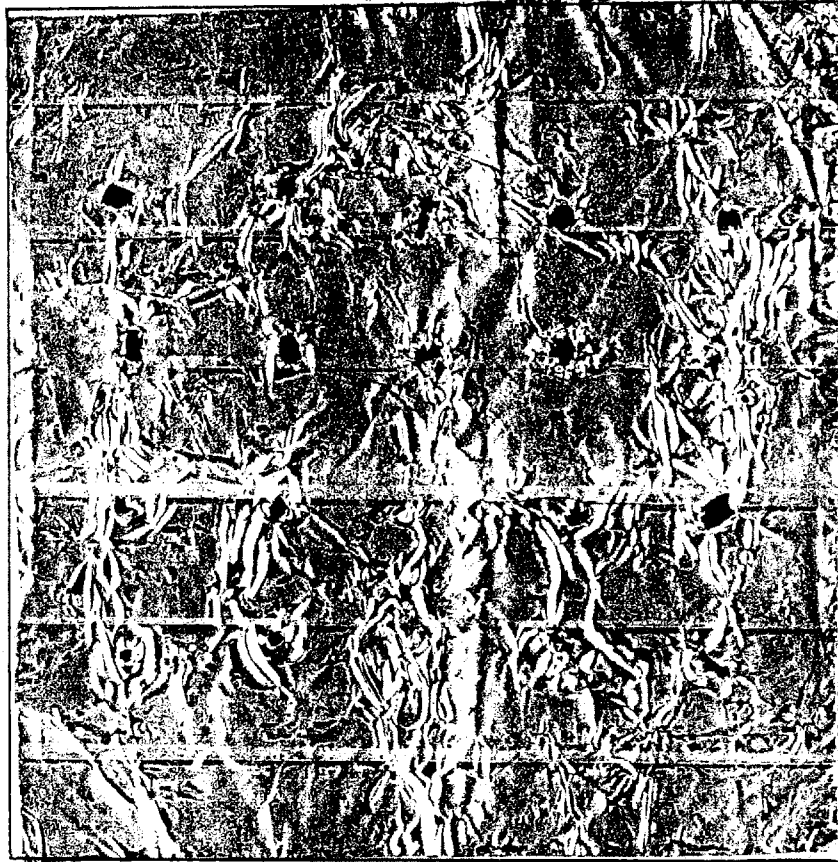
Fig. 4.2.2: Typical target foil from early freezing experiments showing two
missing and three fragmented pellets.

Several barrels did not produce signals on the first diode gate and therefore did not form pellets at all. These were identified as Barrels # 6, 10, and 14 of the 13 gauge, second row barrels, barrel # 3 of the 15 Gauge and barrels #12 and 16 of the 17 gauge. The problems were suspected to be due to poor thermal connections between the barrel cooling disk and the barrel cold plate (see fig. 2.4.2). In an effort to solve this problem, the six barrel connections were re-made, two with vacuum grease only, two with .005 mil indium foil, and two with feltmetal alone. In all cases, a slotted spacer disk was placed between the clamping flange and the barrel disk to ensure adequate contact pressure across the joint. Tests subsequent to the changes showed all barrels successfully made pellets with no variation in size between different barrels of the same gauge. The original cause of the poor thermal connection was found to be the insufficient compression of the feltmetal washer between the cooling disk and the cold plate. After the changes, no differences were detectable between pellets made from barrels with the different types of connection, therefore no further changes to the barrel connections were necessitated.

In November of 1992, the pellet photography apparatus was installed on the injection line. The reliable operation of both laser-photodiode sets was a necessary pre condition to successful photography since the diode signals are used to trigger the nanolamp light source. The principal use of the photography system is to ascertain the pellet size and mass from captured video images.

To facilitate the repetitive formation of pellets, the injector PLC control system was programmed to produce pellets automatically. The program operates by cycling the process gas system valves through a series of separate configurations or states, each for a specific time period. The Valve and heater states for each stage in the cycle are given below in table 4.1.1:

Table 4.1.1 : Automated Pellet Freezing Cycle (1=on or open , 0=off)

Function	Heater	Pn7	SFuel
start cycle	0	1	0
bake cold plate	1	1	0
cool cold plate	0	1	0
fill plenum	0	1	0
close Pn 7	0	0	0
freeze pellets	0	0	1
wait	0	1	0

In sequence, these states are: 1) The start configuration 2) Heating of the barrel cold plate. 3) Re-cool the barrel cold plate 4) Plenum fill with fuel gas to a predetermined pressure. 5) Close gate valve Pn 7 forward of the barrels. 6) Fuel valves open during the freeze period. 7) The wait period which includes opening gate valve Pn 7 and the pump out of excess fuel gas. The automatic process is menu driven through the PARAGON PC software. The pellet menu provides for the operator selection of fuel gas and plenum fill pressure, and for the freeze and bake times. The display also shows the current state of the injector and the time remaining in each state. With the laser photo diode gates and photography system functional, pellet size, mass, condition and velocity could be reliably determined. The reliable operation of the photodiode gates and photography system was necessary prior to beginning a more systematic survey of the pellet freezing parameters. The goal of these experiments would be both to determine the effects of varying such parameters as freeze time and pressure on pellet size, and to find the optimum "recipe" for pellet manufacture.

4.2.2 Pellet Mass vs. Freeze Pressure

The first systematic experiments with deuterium on the injector were to study the effect of varying the fuel gas pressure on the pellet size. The aim was to find the range of pressures under which pellets could be made and to determine if pellet size could accurately be controlled through variation of the fueling pressure. Figure 4.2.3 shows the vapor pressure vs. temperature diagram for hydrogen and deuterium in the range of interest. Fuel gas entering the freezing zone drops in temperature at a fixed pressure moving horizontally to the left on the phase diagram. For Deuterium pressures below 100 torr, the gas passes directly from vapor to solid. The pellet will freeze to a length such that the ends of the pellet are exactly at the saturation point for the given pressure. Because the barrel temperature increases away from the conduction disk, changes in the fueling pressure should affect the pellet length. The shortest pellets are made at pressures where the freezing point is just at the minimum barrel wall temperature at the conduction disk. At the cutoff pressure, or pressure below which pellets cannot be made, the fuel freezing temperature corresponds exactly to the minimum barrel temperature. Similarly, the pellet length at a specific freeze pressure, coupled with the analytically determined
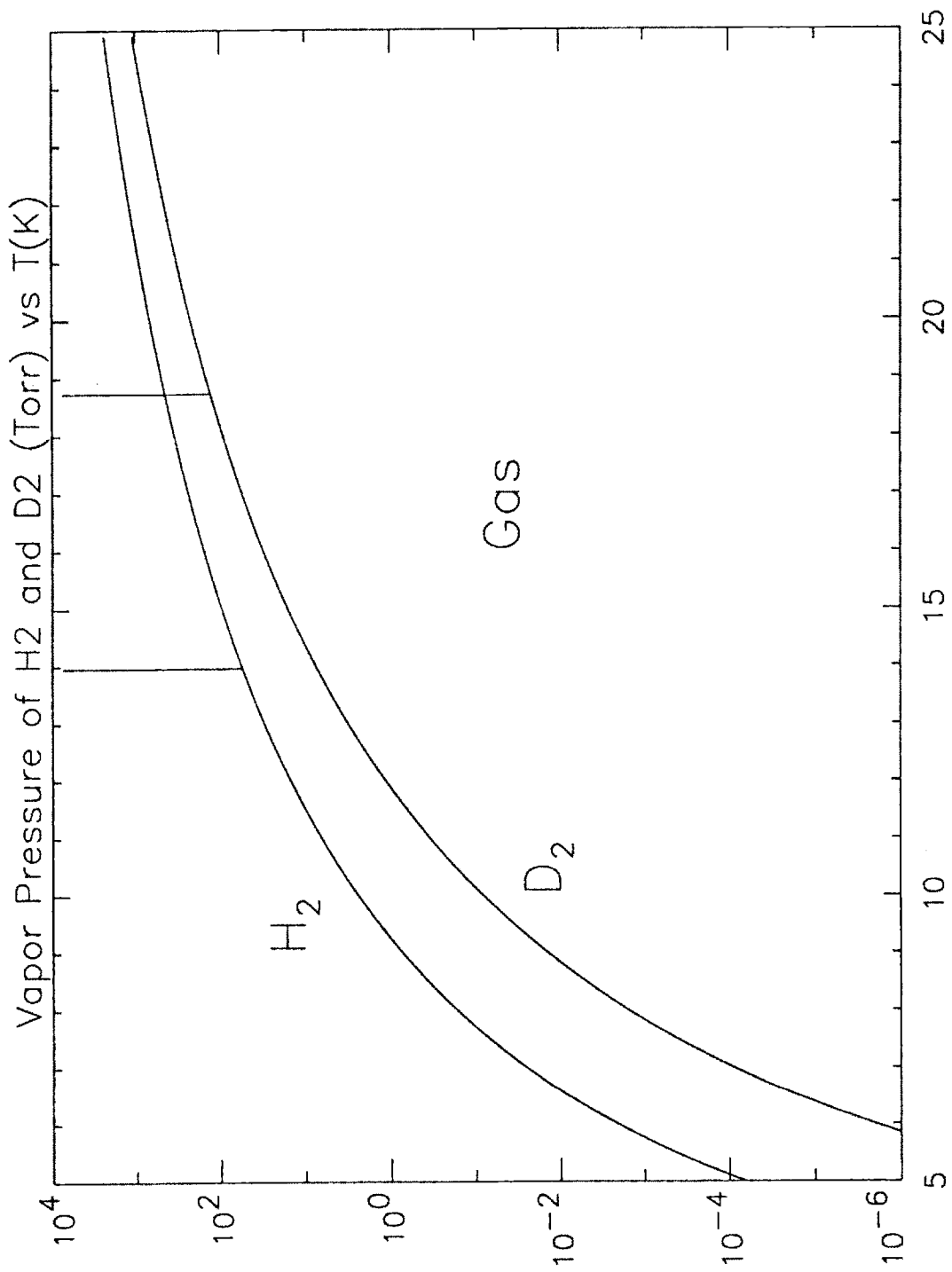
Fig. 4.2.3: Phase diagrams for hydrogen and deuterium.

temperature gradients along the barrel, may be used to determine the temperature at the center of the barrel freeze zone.

Batches of Deuterium pellets were made with fixed freeze times of 240 seconds and plenum fill pressures ranging from 36 to 349 torr. The volume ratio before and after opening the fuel valves was measured at room temperature to be 1 to 5.88 by recording the plenum pressure before and after opening the fueling valves. The procedure was repeated for a number of different fill pressures. The plenum pressure range therefore corresponds to a formation pressure range of between 7.1 and 53.1 torr. Figure 4.2.4 shows the pellet size in # atoms per pellet as a function of formation pressure in torr. The triangular data points in figure 4.2.4 are derived from the pressure drop which occurs as fuel gas freezes to form pellets. The initial pressure measurements are made at the fuel plenum prior to opening the fuel valve and are deduced by dividing by the ratio of the volumes before and after opening the fuel valve. The final pressure is recorded just prior to closing the fueling valves, after freezing is complete. The total condensed pellet mass is derived from the ideal gas law as applied to the pressure difference. The assumption is made that all pellets are of the same length and that the division of pellet mass between barrel sizes is directly proportional to their internal cross sectional areas. The estimate also assumed that three 13 gauge barrels and one each of the 15 and 17 gauge barrels were non-functional. The assumption was valid since at the time of the test the photo diodes and target foils showed no indications of pellets. It was also a necessary condition that at least one barrel be non-functional and unplugged, since fully formed pellets in all 20 barrels would effectively seal off and separate the gas volumes fore and aft of the barrel ends. The equilibrium pressure indicated at the fuel plenum would then not necessarily be indicative of the pressure in the volume connected to the barrel muzzles. Under these assumptions, barrel #13 would freeze 9.4 percent of the total mass. Clearly the greatest uncertainty in determining pellet mass through this method is in the assumptions made, and not in the ± 1 torr pressure measurement uncertainty. Quantifying the uncertainty is difficult, but the standard deviation in repetitive measurements indicate ± 10 % relative uncertainty.

The star symbols in figure 4.2.4 are pellet mass data from barrel #13 as derived from in-flight video images. The magnification factor of the lens and video system was determined by imaging 1x1 millimeter graph paper in the focal plane of the camera, and measuring the screen dimensions of the recorded image. This established the horizontal
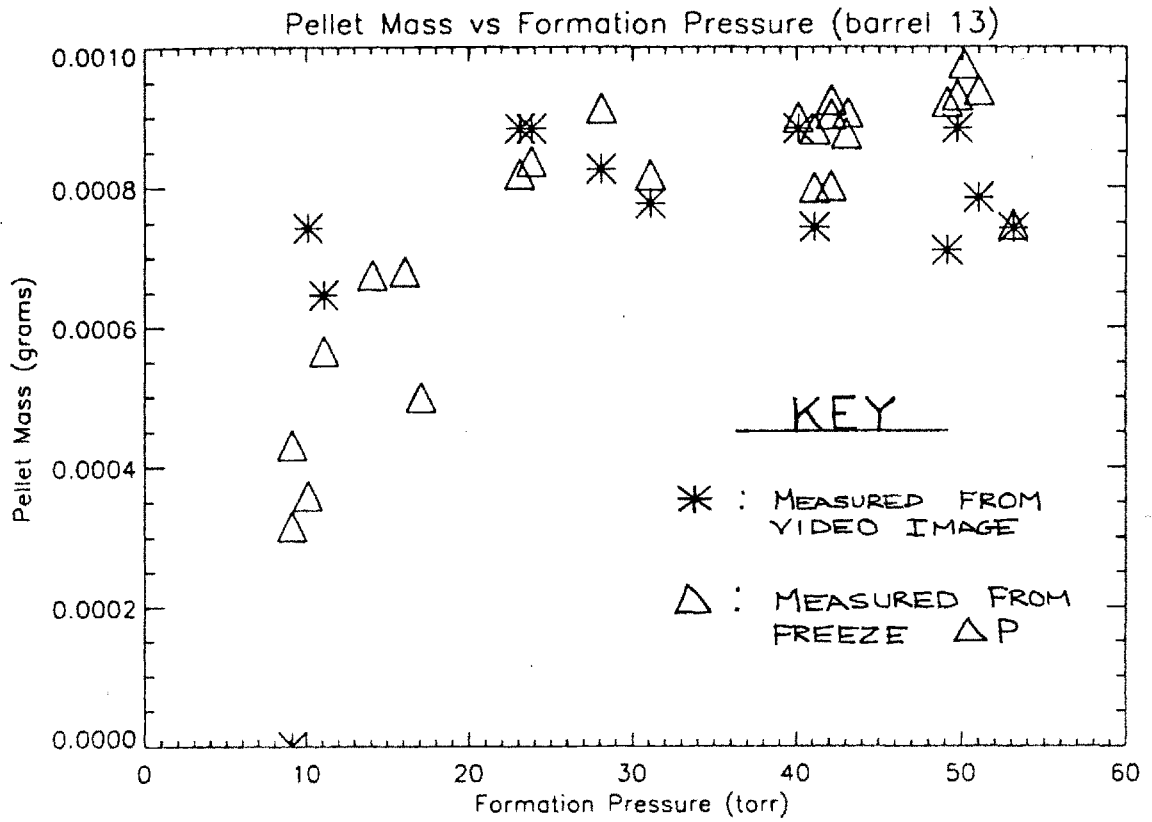
Pellet Mass vs Formation Pressure (barrel 13)

KEY

✱ : MEASURED FROM VIDEO IMAGE

△ : MEASURED FROM FREEZE △P

Fig 4.2.4: Deuterium pellet size as a function of freeze pressure.

and vertical magnification factors at 21.4 and 19.6.. The procedure for determining the pellet mass was to image pellets and estimate their volume and mass from the screen dimensions. The length used in the volume calculations was the equivalent cylinder length. Some degree of judgment is used to estimate the length of a perfect cylinder with a volume equivalent to the pellet. Pellets were also sometimes viewed end on, making the determination of pellet length impossible. In most cases however, the pellet longitudinal axis was in or only slightly angled with respect to the imaging plane, making length determination possible. The dimensional uncertainty for the optical measurements is estimated to be 4 % in both length and diameter, producing volume and mass uncertainties of 12 %.

A typical pellet image shown in fig. 4.2.5, indicates the sides are usually well formed and smooth, while the cylindrical ends are generally rounded and sometimes irregular. The aft end of the pellets are usually slightly more conical than the front. This is a result of propellant gas expansion plume shearing away the aft edges of the pellet as it exits the barrel. The diameters of the pellet are usually twenty percent less than the internal diameter of the barrel. This erosion probably occurs during firing when the pellets are exposed to the friction of the warm barrel walls.

The advantage of determining the mass optically is that the estimate is based on the size of the pellet that would actually enter the plasma and does not include fragments and debris lost during firing as is included in the pressure drop mass measurements. The disadvantage of photography is that the nanolamp is not triggered about ten percent of the time due to insufficient trigger levels from the two laser photodiode gates. The optical pellet masses are therefore a subset of the pressure derived masses. Figure 4.2.4 indicates that deuterium pellets cannot be made at fill pressures below ten torr. The freezing temperature for deuterium at this pressure is about 14 K. This is within the measurement uncertainty of the recorded diode temperatures for the first configuration of 14.2 K. Figure 4.2.4 also shows that the pressure derived pellet masses are recorded for slightly lower freezing pressures than for the optical masses. This is expected because at the very low pressure some fuel gas is frozen, but not enough to form pellets completely enough so that they are not blown apart when fired.
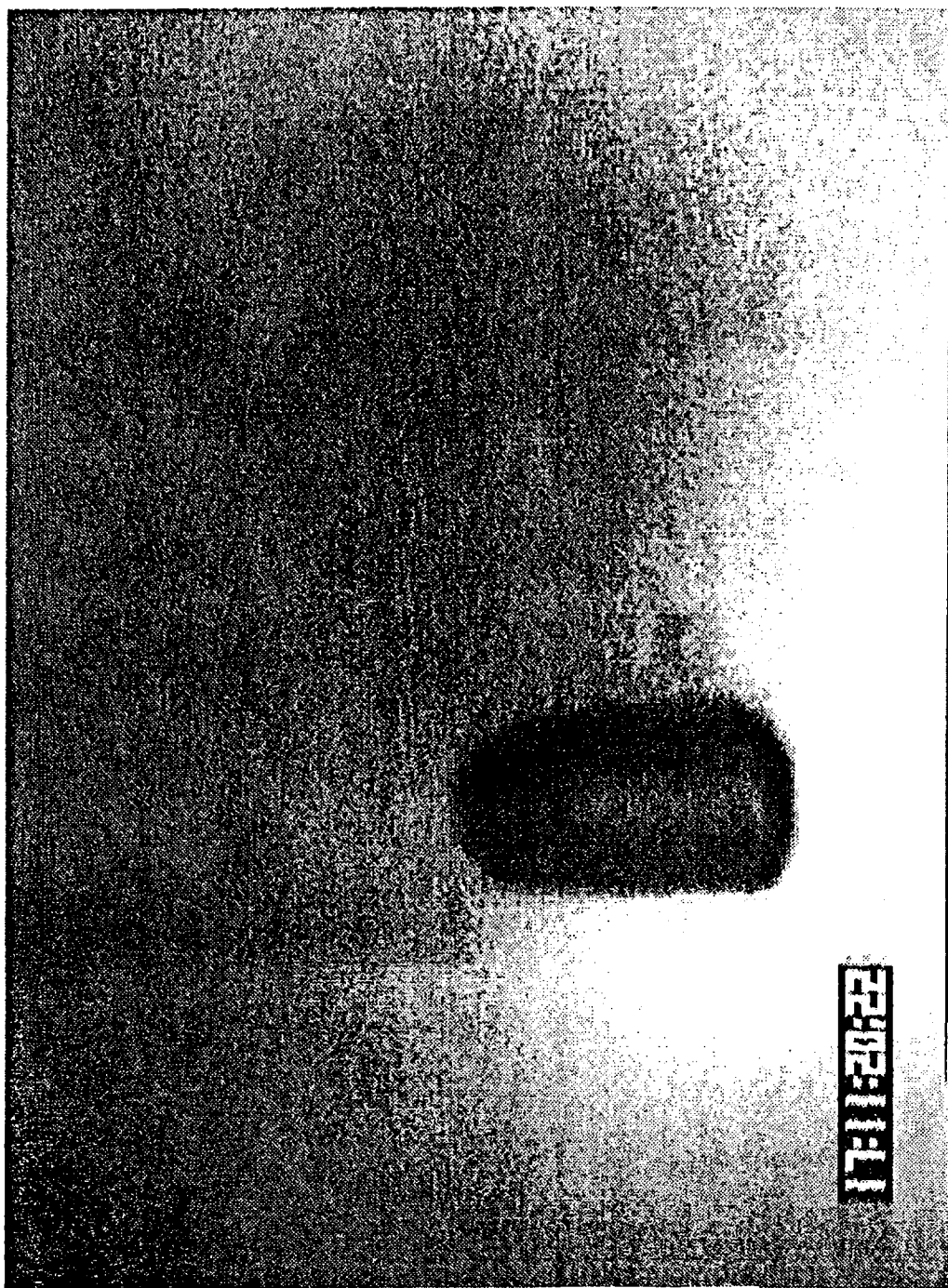
Fig. 4.2.5 : In-Flight pellet video image.

A third method used the extinction ratios of the photodiode signals as a rough measure of relative pellet mass. This ratio is the value of the maximum diode voltage drop divided by the unperturbed signal level, and is directly proportional to the pellet "shadow area". For fixed pellet diameters, the ratio therefore varies directly as the pellet mass.

The data shown indicates pellet mass to be relatively constant for fueling pressures above twenty torr. The difficulty of controlling freeze pressure over a ten torr range, combined with the large scatter in the pellet mass data below 20 torr, make it hard to accurately control pellet mass through changes in the freeze pressure. The more practical method is to geometrically control the dimensions of the freezing zone by varying barrel diameter and cooling disk thickness.

4.2.3 Pellet Size vs Vacuum and Pressurized Holding Times

Prior to firing into the tokamak, the injection line must be at low pressure with the pellets exposed to vacuum. The pellet life time is limited in this state due to slow sublimation. A second set of experiments sought to quantify the variation of pellet size with the amount of time the pellet is exposed to vacuum, and to find out how long the pellets can be held prior to firing. The experimental procedure was to make pellets with a fixed fueling pressure of around thirty torr and freeze time of four minutes. This was done for both configurations of the thermal system. Pellet mass was determined photographically for vacuum exposure or " wait" times of 0, 5 and 10 minutes. The data for the first configuration are shown in figure 4.2.6 and show a decrease in pellet mass for increased wait times. The photographs show that the pellets vary in length and not diameter, indicating sublimation occurs only on the exposed pellet end. Diode extinction ratios for the pellets are shown in figure 4.2.6 and also indicate a decrease with time. The extinction ratios are approximately constant until the pellets decrease to a length smaller than the beam width. Experiments with the second thermal configuration indicated no significant decrease in deuterium pellet size for vacuum exposure times of up to ten minutes. The vapor pressure of the solidified deuterium was therefore significantly higher in the freezing zone of the first configuration than for the second.

Additional experiments were performed to determine the effect of holding the pellets after freezing with both the fueling valves and gate valve Pn7 closed. This state
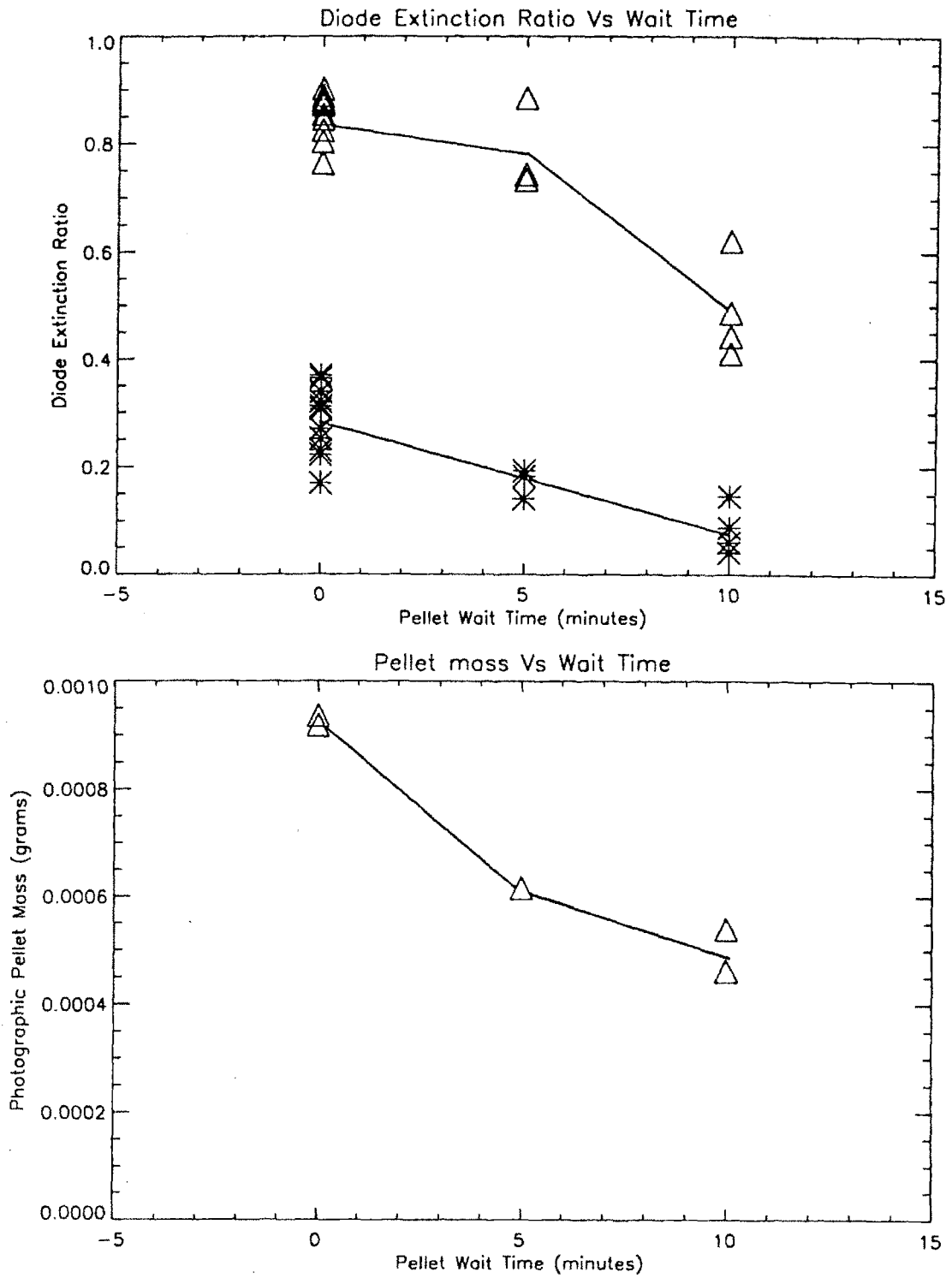
Fig 4.2.6: Deuterium pellet mass vs. vacuum exposure time as measured by extinction ratio (top) and video images (bottom).
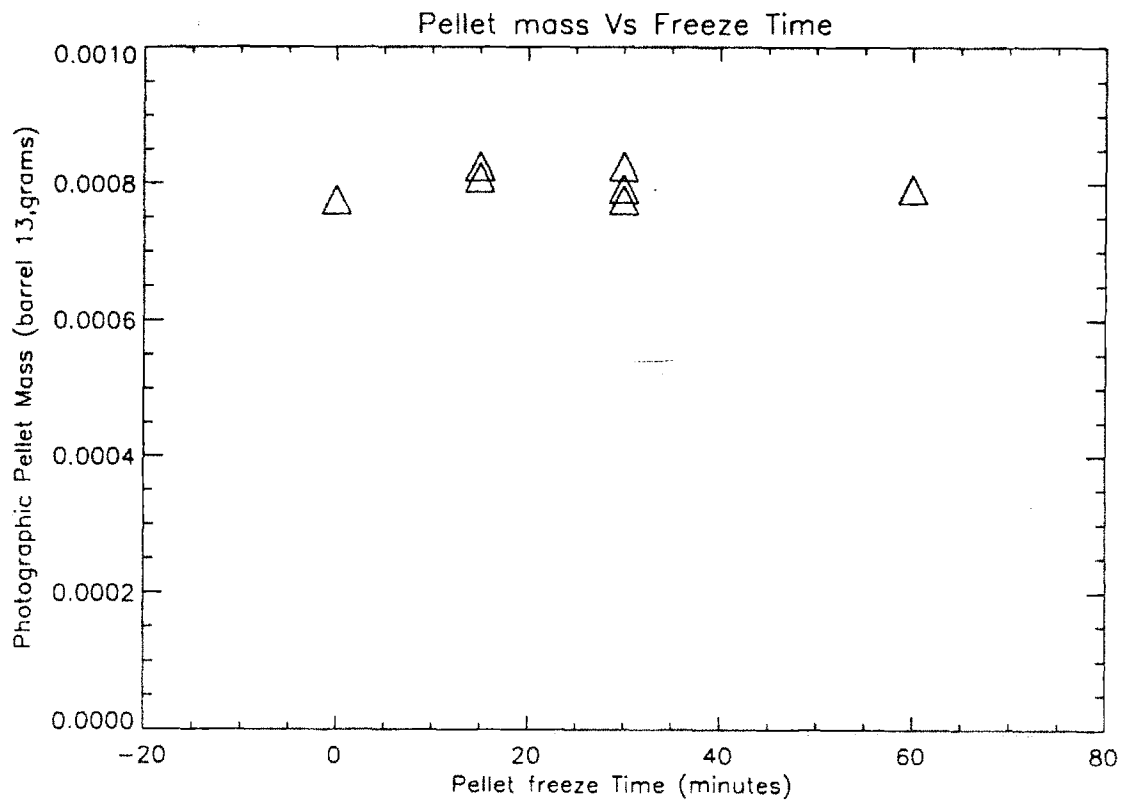
Fig 4.2.7: Deuterium pellet mass vs. freeze time (derived from video images).
Note that the "0" freeze time actually includes approximately 15
seconds during which the pellets freeze. Freezing in this case occurs
during the brief period when the fuel valves are opened and the
pressures equalize between the volumes fore and aft of the barrels.

is essentially an extended freeze time since the pellets are exposed to fuel gas from both ends of the barrel. Figure 4.2.7 shows pellet mass (from photographs) vs. freeze time for the first configuration. Pellet mass is constant for times up to the maximum recorded of one hour. This result was also found to be true for the second configuration. The result is as expected because the pellet has frozen to its maximum length after the first minute or so of freezing.

4.2.4   Statistical Data on Pellet Mass Variation and Barrel Reliability

To collect statistical data on pellet mass variation, many sets of pellets were made under similar conditions. Pellet mass histograms are presented only for the second thermal configuration since this is the final configuration of the thermal system. For cases where actual photos are not available, pellet mass will be assumed to be the average of that measured for the given barrel size. In order to increase the number of available data points, statistics were used from pellet batches made under a range of fueling pressures from 25 to 55 torr . It was found that over this pressure range the average pellet mass is constant. All batches of pellets were made automatically with fixed pellet freezing times between one hundred seconds and four minutes. For the second configuration, pellet mass was found to be constant for freeze times of greater than ninety seconds.   All mass measurements were made photographically. Data taken from different barrels of the same gauge established that there was no significant difference in pellet mass between barrels of the same size. Mass measurements for a specific barrel gauge were therefore often made using several different barrels of the same size.   The histograms of pellet size in # atoms per pellet are shown in figures 4.2.8-9. Pellet mass and atoms/pellet averages are shown below in table 4.2.1 along with percent standard deviation and error.
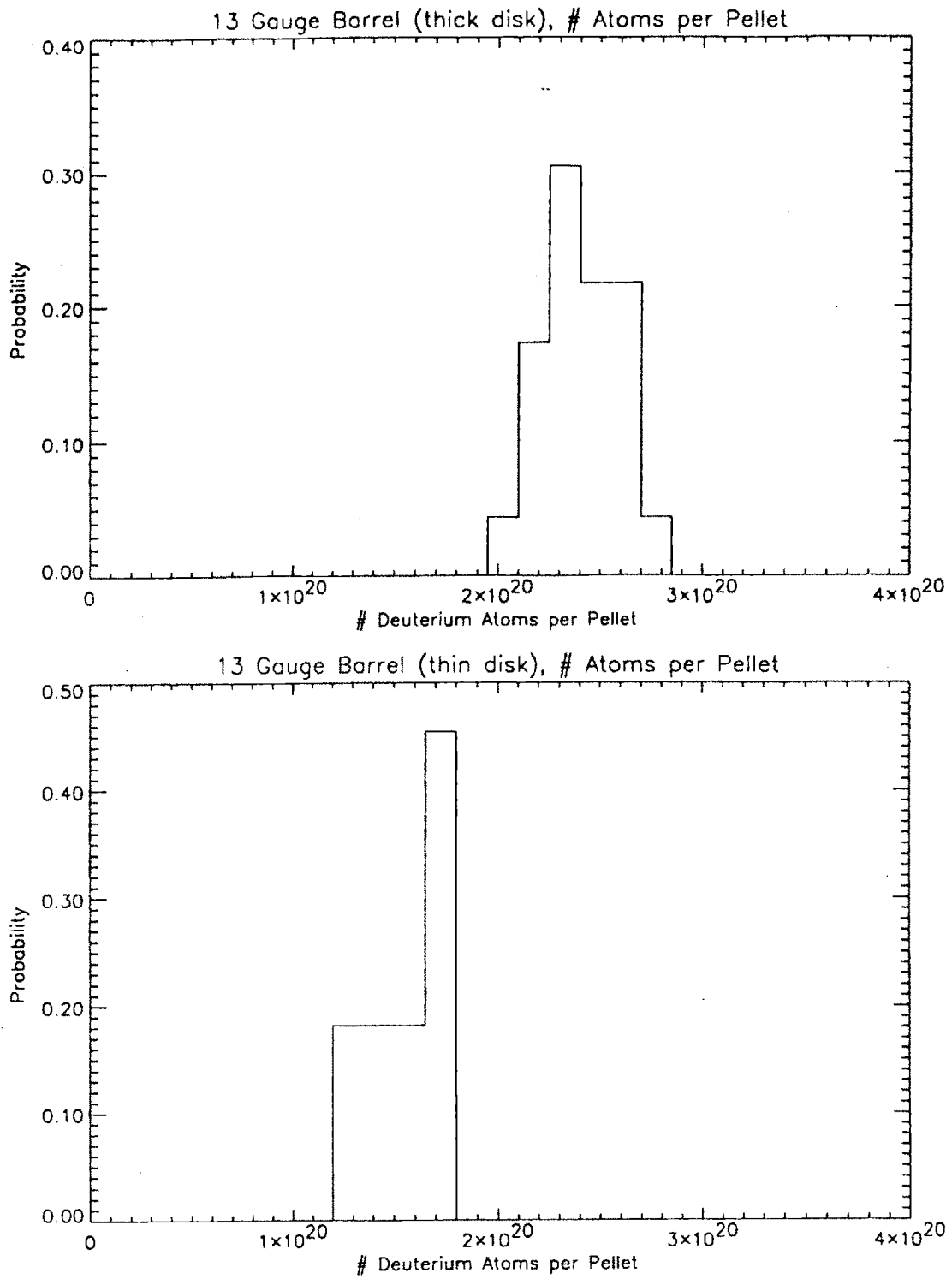
Fig. 4.2.8: top: Pellet mass histogram from 13 Ga., (1.5 mm cond. disk) barrel size.

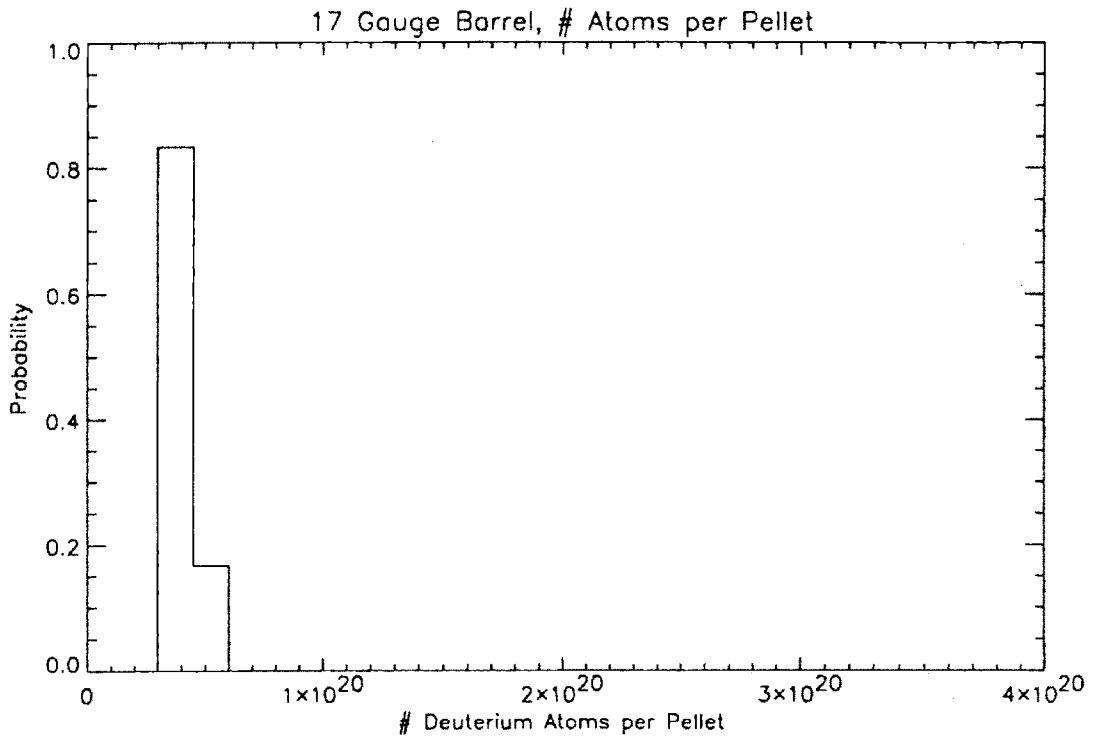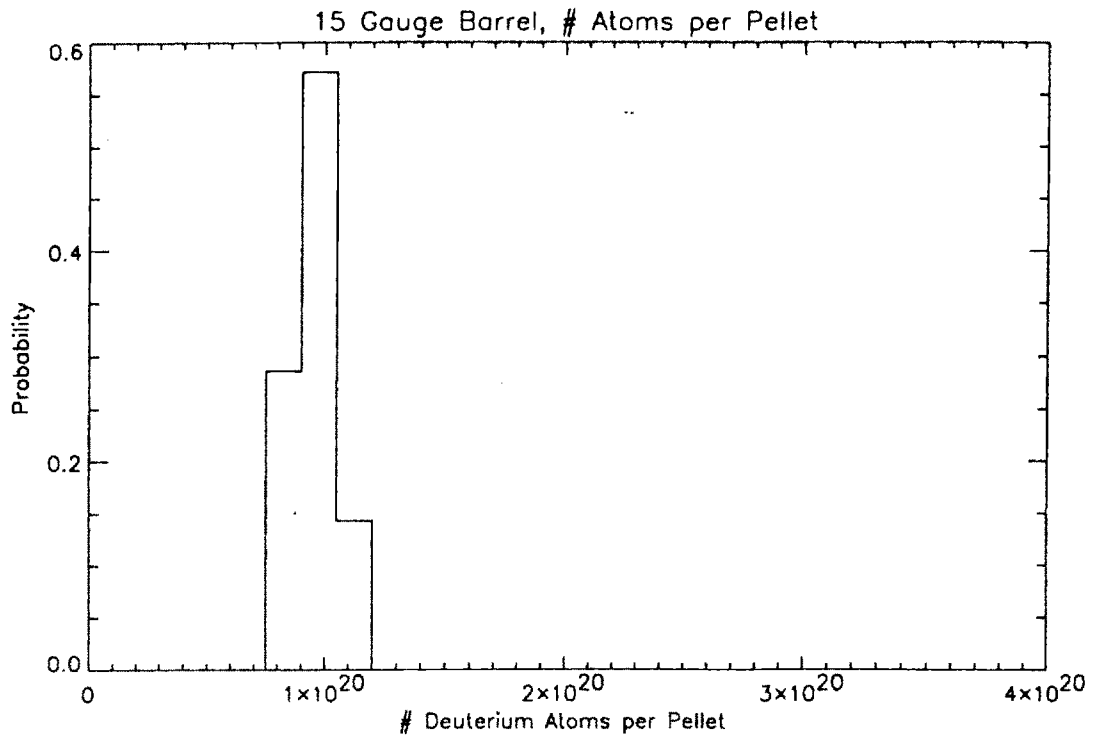bottom: Pellet mass histogram from 13 Ga., (1 mm cond. disk) barrel size.

Fig. 4.2.9: top: Pellet mass histogram from 15 Ga. barrel size.

bottom: Pellet mass histogram from 17 Ga. barrel size.

Table 4.2.1 : Pellet Mass Statistics

Barrel Size	# Points	Average Mass (grams)	Average # Atoms per Pellet	Standard Deviation (percent)	Standard Error (percent)
13 gauge 1.5 mm disk	23	8.05×10^{-4}	2.42×10^{20}	7.6 %	1.5 %
13 gauge 1 mm disk	11	5.23×10^{-4}	1.57×10^{20}	11 %	3.3 %
15 gauge	7	3.12×10^{-4}	$.94 \times 10^{20}$	11 %	1.3 %
17 gauge	6	1.43×10^{-4}	$.43 \times 10^{20}$	5.0 %	2.0 %

Barrel reliability was measured throughout the laboratory test period. The IDL program VELOSTAT was used to compute statistics on four separate groups of shots. The program calculates the average pellet velocity, velocity standard deviation and barrel reliability for each barrel size. A barrel is judged to have successfully fired when the diode extinction ratios from both laser-photodiode gates are above a predetermined minimum value. Early in the experimental period, reliability estimates based on this criteria were conservative, in that occasionally good pellets were not detected on the second diode due to laser alignment errors. This was corrected after the installation of the guide tube array. Four groups of shot data were evaluated . The first and second groups were made before and after the installation of the heaters and guide tubes. The third was made with heaters and guide tubes, and with changes to the connection between the barrel conduction disks and the barrel cold plate. The connections were changed only on the non functional barrels. The fourth group of shots are representative of the injector in its final state as installed on Alcator C-Mod for fueling experiments. In the final state, the injector is configured with heaters, guide tubes, the changed barrel connections, and most importantly with the new, single piece, refrigerator to cold plate thermal connection. For the final tests pellets were made using the standard pellet forming cycle. Table 4.2.2 shown below presents barrel reliability for each of the twenty barrels during the four stages listed above.

Table 4.2.2 : Barrel Reliability Summary

Barrel Number	Group #1, no heaters or guide tubes	Group #2, with heaters and guide tubes	Group #3 , As #2 but with new barrel connect.	Group #4, As #3 but with new thermal link
1	40 %	87 %	100 %	100 %
2	20	75	92	100
3	0	0	92 @	100
4	73	100	92	100
5	0	100	100	100
6	73	0	100 @	100
7	86	100	92	100
8	86	75	83	100
9	53	87	100	100
10	0	0	92 @	100
11	46	100	**	**
12	0	0	93 @	100
13	0	100	100	100
14	0	0	100 @	100
15	33	100	100	100
16	40	87	66 @	&
17	20	100	100	100
18	0	62	83	100
19	46	87	100	100
20	80	0	91	100

@ These barrels have replaced connections between the conduction disk and barrel cold plate.

** Data for these barrels could not be recorded due to CAMAC problems.

& This barrel temporarily non functional due to electrical feedthrough problems.

The data indicate that from the first to the second group there is a general increase in reliability, resulting from the addition of the heaters and guide tubes; however some barrels are non functional. Changes to the barrel thermal connection clearly fix the problematic barrels. The fourth group shows nearly one hundred percent reliability for twenty groups of pellets. The improvement is due both to an optimized pellet freezing cycle and due to the lower temperatures resulting from the change to the single piece thermal connection. This group also shows reduced fragmentation, probably because of increased deuterium strength and hardness at the lower temperatures of the second thermal configuration. Figure 4.2.10 shows typical diode and microphone signals recorded for pellets made under the optimum freeze conditions and after the thermal changes. Note that all pellets fired survive to impact on the target plate. The microphone
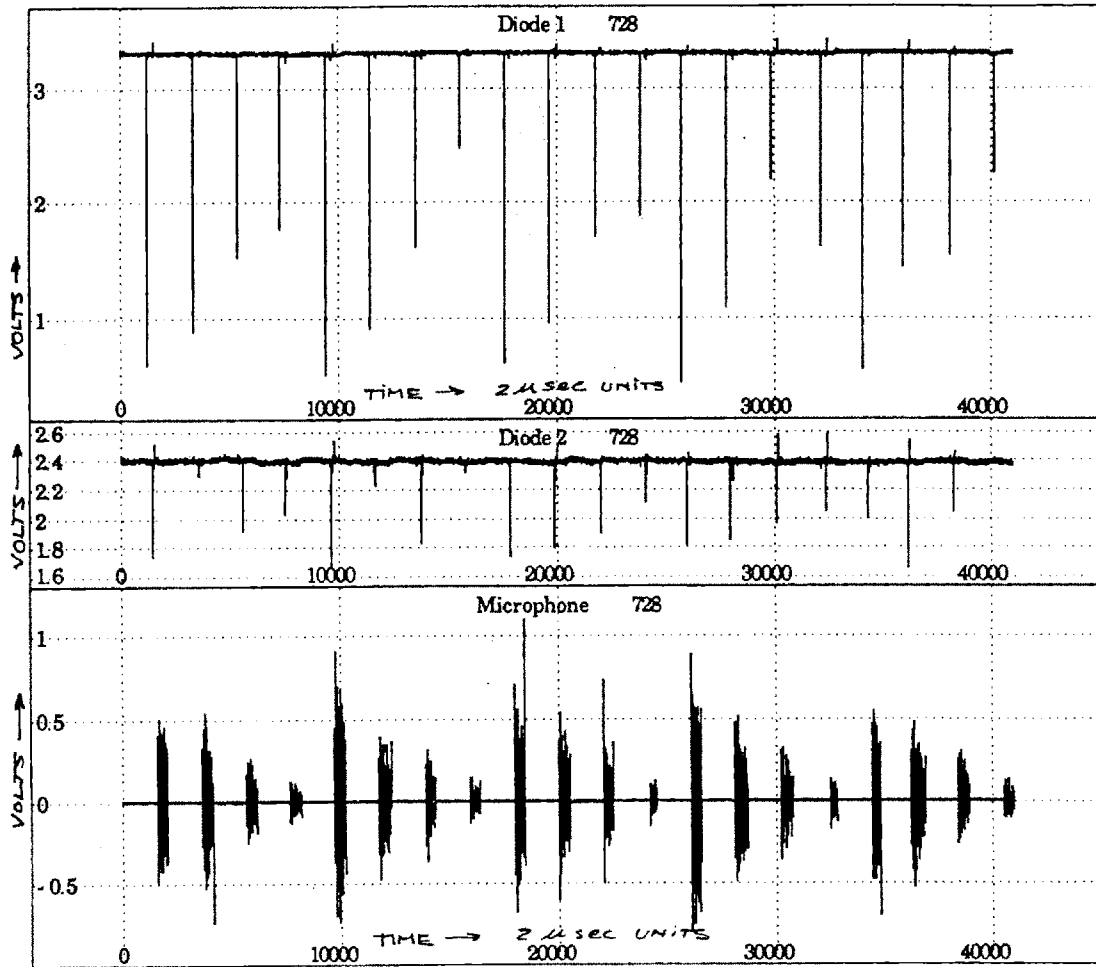
Fig. 4.2.10: Typical diode and microphone traces from D2 pellets made with the standardized freeze cycle and after all changes to the thermal system. The barrels are fired column by column so that so that every fourth pellet is from the same barrel size. Average Pellet size sequentially and in groups of four is then 2.42,1.57,.95,.43 x 10^{20} atoms/pellet.

106

data given is the time derivative of the voltage output and varies directly with the pellet mass.

4.3 Hydrogen Pellet Freezing Experiments

4.3.1 Initial Experiments

Initial attempts to freeze hydrogen were unsuccessful. Figure 4.2.3 shows the vapor pressure curve for hydrogen and indicates that formation pressures between ten and fifty torr require freezing temperatures below 12 to 13 K. Hydrogen freezing was not possible because the freezing zone temperature was approximately 14 K, just above the minimum required. This conclusion is supported by the 14.2 K average temperature recorded with the barrel cold plate diodes, and by the minimum freeze pressure for deuterium of ten torr, corresponding to a saturation temperature of 14.3 K. On several shots made with freeze pressures of around 70 torr , debris and or "slush" was detected on the first diode, but in no cases were pellets detected on the second diode. Above 14 K, only the liquid phase is accessible for freeze pressures above 80 torr.

4.3.2 Hydrogen Freezing Experiments After Thermal System Changes

The inability to freeze hydrogen pellets was a primary motivation for the re-design of the thermal connection. The thermal analysis presented in chapter three indicates larger than expected temperature drops across the three felt metal joints of the first thermal configuration. For the new configuration, diode temperature measurements on the barrel cold plate indicated an average temperature of 12.2 K. The minimum freeze pressure for deuterium pellets was found to be below that which could be accurately measured (2 torr).
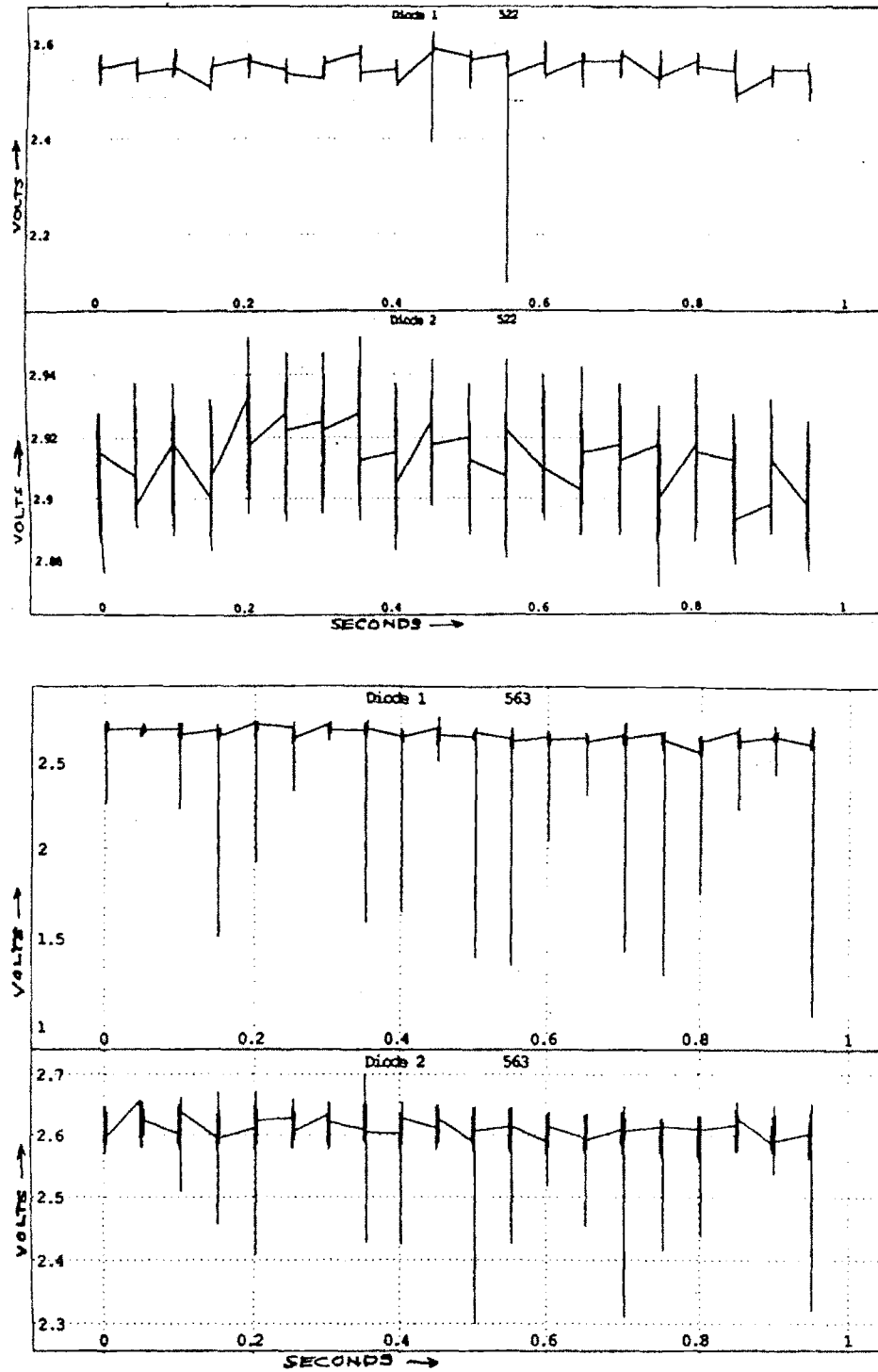
Fig. 4.3.1: Diode signals for hydrogen pellets made before (top) and after
(bottom) changes to the thermal system.

Hydrogen freezing experiments with the new thermal connection began late in May 1993. Pellets were frozen using a 25 second bake of the cold plate followed by a freezing period of between 100 seconds and four minutes. Fueling pressures between 35 and 75 torr were used. Typical diode traces for hydrogen pellets made before and after the thermal system changes is shown in figures 4.3.1. top and bottom. The signals show that after the changes pellets are frozen in most barrels and seen on both diodes. Barrel reliability for seven batches of pellets are shown below in table 4.3.1.

Table 4.3.1 : Barrel Reliability for Hydrogen Pellets

Barrel #	Reliability	Barrel #	Reliability
1	29 %	11	57 %
2	0	12	57
3	28	13	71
4	72	14	43
5	57	15	71
6	29	16	43
7	0	17	43
8	57	18	0
9	43	19	29
10	29	20	86

The data shown above indicates that for hydrogen the smaller barrel gauges are more reliable than the larger. This may be because the smaller pellets are mechanically stronger and less prone to fragmentation. Barrel reliability can probably be brought much closer to 100 percent by using standard, optimized hydrogen freezing cycles. The most successful cycle includes a 25 second bake followed by a 100 second freeze with a 60 torr freeze pressure. Further tests should be performed to establish the upper bounds of barrel reliability. Hydrogen pellets sublimate rapidly on exposure to vacuum and no pellets have been detected after more than five minutes exposure. Data on hydrogen pellet mass derived from photographs are shown in table 4.3.2.

Table 4.3.2 :   Hydrogen Pellet Mass Data

Barrel Size	Average Pellet Mass (grams)	# Atoms per Pellet
13 Ga. (1.5 mm)	1.8×10^{-4}	1.1×10^{20}
13 Ga. (1mm)	1.2×10^{-4} *	$.72 \times 10^{20}$ *
15 Ga.	$.43 \times 10^{-4}$	$.26 \times 10^{20}$
17 Ga.	$.19 \times 10^{-4}$ *	$.12 \times 10^{20}$ *

* These figures are were not estimated from photographs but are extrapolations based on freezing zone geometry.

4.4 Pellet Velocity Measurements

The C-Mod injector uses a pressure differential as the driving force to accelerate pellets down the barrel. High pellet velocities are desirable because pellet penetration into the plasma increases with higher velocities. A review of the physics of gas guns is useful to understand some of the factors influencing the maximum achievable velocity for the given design. Pellets of frozen hydrogen form a cylindrical plug within the barrel. These are accelerated pneumatically by the pressure differential across the pellet which occurs when the propellant valves are opened. Acceleration down the barrel may be modeled by considering an infinitely long frictionless tube with pellet located at X=0. Gas pressure is taken to be Po on the left side and zero on the right. Immediately after T= 0, two rarefaction waves form at the base of the pellet and move both left and right. The left moving wave propagates into the unperturbed propellant gas. The right moving wave is coincident with the base of the pellet . The geometry is depicted in figure 4.4. 1:

The assumption is made that the gas is ideal and the process adiabatic. Conditions behind the shock wave at the base of the pellet are determined from the ideal gas law and the conservation equations [61]. The pressure behind the pellet as a function of time is then given by eq. 4.4.1 :

$$P(t) = P_o\left[1 - \frac{(\gamma - 1)V(t)}{2C_o}\right]^{\frac{2\gamma}{\gamma-1}}$$

(4.4.1)

γ is the ratio of gas specific heats and C_o is the gas speed of sound. V(t) is the velocity of the pellet. The equation of motion for the pellet is then [61]:

$$\frac{d}{dt}V(t) = \frac{A}{M}P_o\left[1 - \frac{(\gamma - 1)V(t)}{2C_o}\right]^{\frac{2\gamma}{\gamma-1}}$$
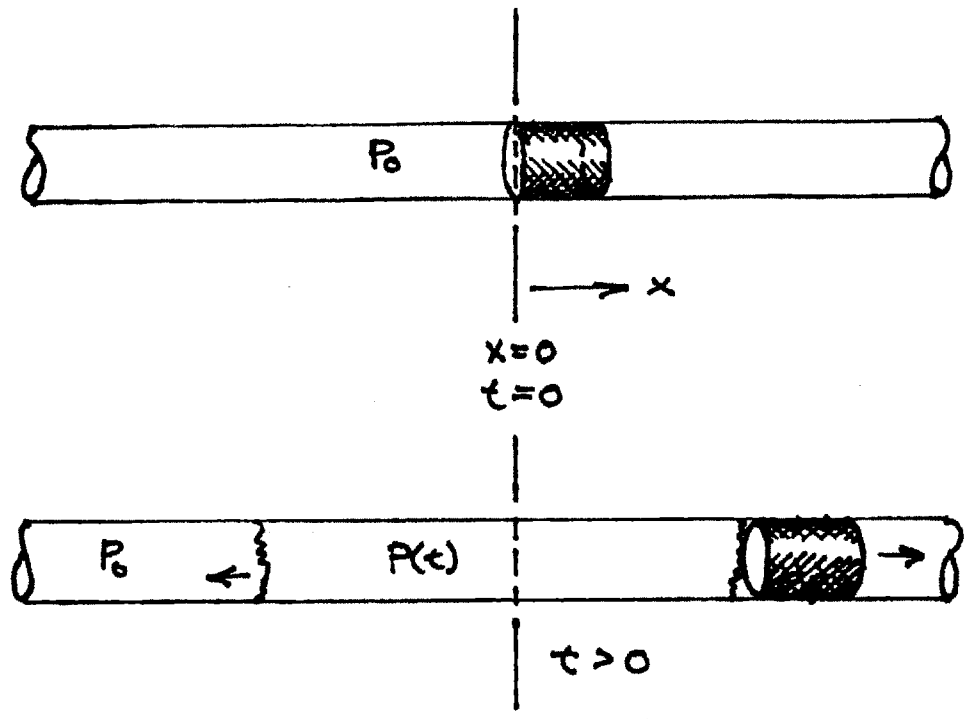
(4.4.2)

Fig. 4.4.1: Schematic of the barrel showing the pellet and moving rarefaction wave after t=0.

112

In the equation above, A is the pellet base area and M is the pellet mass. Integrating 4.4.2 V(t) is obtained [61]:

$$V(t) = \frac{2C_o}{\gamma - 1}\left[1 - \left[1 + \frac{(\gamma + 1)AP_o t}{2MC_o}\right]^{\frac{-\gamma - 1}{\gamma + 1}}\right]$$

(4.4.3)

When the limit is taken as $t \to \infty$, the maximum velocity is:

$$V_{max} = \frac{2C_o}{\gamma - 1}$$

(2.4.4)

C_o, the speed of sound of the gas, is given by:

$$C_o = \sqrt{\frac{\gamma RT}{m}}$$

(2.4.5)

In the equation above, R is the universal gas constant, T is the temperature and m is the gas molecular weight. Equations 2.4.4 and 2.4.5 indicate that the maximum velocity is achieved for propellant gases with low molecular weights such as hydrogen or helium. At 300 K, the maximum attainable speeds for hydrogen, deuterium, helium and neon are given in table 4.4.1.

Table 4.4.1 : Maximum Attainable Pellet Velocities at 300 K

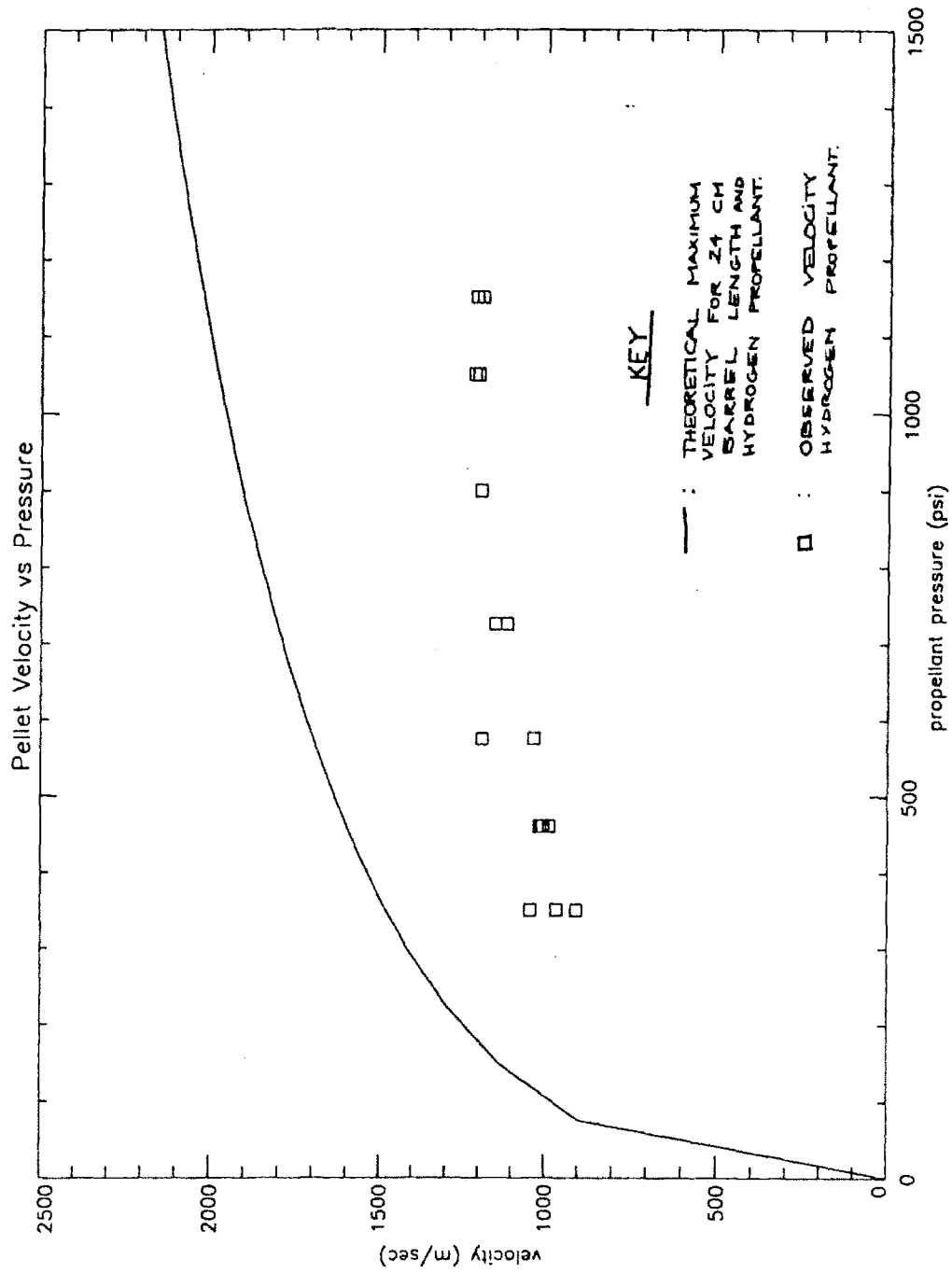| Gas	molecular weight (grams / mole)	γ	C_o (m/s)	V_{max} (m/s)
Hydrogen	2	7/5	1313	6565
Deuterium	4	7/5	928	4642
Helium	4	5/3	1013	3035

Fig. 4.4.2: Pellet velocity vs. hydrogen propellant pressure. The solid line
represents the maximum theoretical velocity for a 24 cm barrel length
with no friction.

114

The maximum velocities listed above are never achieved in practice due to non-ideal effects such as finite barrel length, friction and viscosity. Figure 4.4.2 presents the experimental data for pellet velocity as a function of propellant pressure for deuterium pellets from barrel #13 using hydrogen propellant. The solid line represents the maximum velocity calculated for a 24 cm barrel length. The actual velocities are smaller than the theoretical due to frictional forces between the pellet and barrel wall, and gas viscosity. Another factor which may contribute to reduced velocity is blowby past the pellets. Photographs indicate that the pellet diameter may be as much as 20% less than that of the barrel inside diameter due to erosion during firing. The blowby past the pellet reduces the driving force both due to a reduction in propellant pressure and because the smaller diameter of the pellet means there is less area for the pressure to act against..

Chapter 5 : Injector Diagnostics

5.1 The Pellet Tracker

The pellet tracker's purpose is to record the trajectory of the pellet into the tokamak plasma as a function of time. The position of the pellet in time is needed in order to correlate H_α signal intensity with the pellet radial location. This data is used to reconstruct ablation profiles which may then be compared to theoretical models. The ablation rate or neutral particle source function is also needed to study transport issues associated with injection on the pellet transit time scale. The transit time for the pellet is typically around 200 micro seconds so we would like a time resolution of not more than a few microseconds in order to reconstruct the trajectory with a sufficient number of data points. Plasma properties also change significantly within centimeters so a spatial resolution of less than one centimeter is needed.

The pellet tracking system designed to meet these requirements on C-Mod consists of two modified 35 mm Pentax K-1000 cameras, each of which has a two dimensional photo diode installed in the film imaging plane. The cameras serve to provide the imaging optics, aperture and the viewfinder needed for the tracking system. The UDT DLS-10 detectors have an active surface area of one square centimeter and consist of p and n doped silicon semiconductor layers. Spectral response range is from 300 nm to 1150 nm with the peak around 900 nm [63]. Sensitivity is .5 A/W at 900 nm [63]. Figure 5.1.1 depicts the electrode configuration and equivalent circuit for the DLS-10 photo diode. Current flows between layers where photons are incident on the surface. Since the top and bottom layers of the photo diode are uniformly resistive, electrodes placed on opposing edges of both the n and p layers will collect currents governed by the resistance between the current source and the collecting electrodes. Therefore:

$$\frac{y'}{l} \propto \frac{I_2 - I_1}{I_1 + I_2} \tag{5.1.1}$$
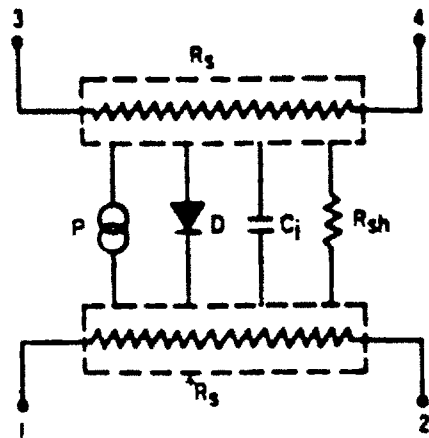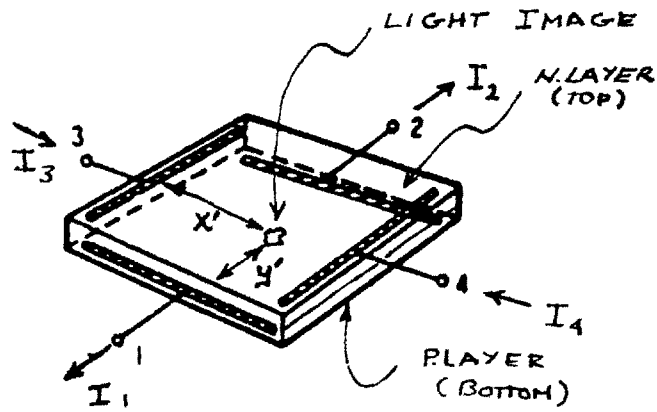
Fig 5.1.1 : Schematic of the DLS-10, two dimensional position sensing photo
detector and equivalent circuit.

In equation 5.1.1 above, l refers to the electrode length and y ' the distance between the centroid of the light image and electrode # 1. I refers to the current output with the subscripts identifying the chip pin numbers. Because electrodes on the top and bottom surfaces are oriented at 90 degrees to each other, the currents collected on each pair are proportional to the location of the centroid of the light image on the detector surface in two dimensions. The linearity of the circuit in both dimensions is increased by placing the electrodes on both the top and bottom surfaces thereby reducing the distortions caused at the corners of the chip where the two electrodes meet. The maximum position sensing error due to non linearity is one half of one percent or 50 μ meters over 90% of the detector surface area. The 10-90 % rise time is two μ seconds [63].

The two cameras are rigidly mounted on G-10 blocks which provide electrical and thermal insulation between the camera and the vacuum vessel. The mounting block also contains a circular filter holder located directly in front of the camera lens. The H-α filter used in the first tracking experiments has a peak band pass frequency 6590 angstroms with a full width at half maximum of 110 A. The camera is fixed both at its base and at the lens, ensuring a fixed and non-adjustable orientation for the camera. Cameras are mounted twenty-eight centimeters above and below the vacuum vessel mid-plane on the C port flange. The optical axes of both cameras are angled towards the mid-plane by 11.9°. During operation, the cameras' lens system images photons from the pellet ablation cloud onto the photo diode surface. Each camera generates two pairs of signals: I_1, I_2 and I_3, I_4 . The difference over the sum for each pair is proportional to the position of the light image on the photo diode Y and X axes. The camera signals are amplified and digitized at a frequency of half a megahertz. These signals are used to determine the equations of the lines of sight from each camera's optical center to the pellet's light emitting centroid. The line of sight equations are computed with respect to the flange coordinate system for each voltage sample. Because the lines need not intersect, the actual location of the pellet is determined to be the midpoint of the line segment joining the two points of closest approach. Camera orientation and the coordinate axes are shown in figure 5.1.2 . Converting the camera output voltages into the equations for the lines of sight to the pellet requires finding the calibration constants C_1 through C_{12} where:

Fig. 5.1.2: View showing tracker orientation and coordinate axes.

119

$$Tan(\alpha_1) = C_1(X_1) + C_2(Y_1) + C_3$$
$$Tan(\beta_1) = C_4(X_1) + C_5(Y_1) + C_6$$

(5.1.2)

for the second camera:

$$Tan(\alpha_2) = C_7(X_2) + C_8(Y_2) + C_9$$
$$Tan(\beta_2) = C_{10}(X_2) + C_{11}(Y_2) + C_{12}$$

In the equations above, $Tan\ \alpha_1$ and $Tan\ \beta_1$ are the slopes of the line of sight from camera # 1 to the pellet and $Tan\ \alpha_2$ and $Tan\ \beta_2$ are the slopes from camera #2 (see fig. 5.1.2). X_1 and Y_1 are derived from the amplified signals from camera #1 :

$$X_1 = \frac{V_1 - V_2}{V_1 + V_2}$$
$$Y_1 = \frac{V_3 - V_4}{V_3 + V_4}$$

(5.1.3)

All the voltages given above are corrected by their pre-injection voltage offset levels. The subscripts on X and Y in the above equations refer to the camera number and the subscripts on the voltages refer to the chip pin number. The equations for the second camera have an identical form, so that the two cameras of the tracking system generate a total of eight voltages. These voltages plus the twelve fitted calibration constants are needed to reconstruct pellet trajectories from the raw data.

During the calibration procedure, the four signals from each camera were digitized while a light source was moved before the camera through a known path in both time and space. This data was then used in a regression procedure to determine the six calibration constants for each camera. The apparatus used to collect the calibration data is shown in figure 5.1.3 and consists of a movable X-Y plotter and the fixed C-port flange to which both tracking cameras are mounted. A small five volt light bulb is fixed to the pen holder of the plotter.
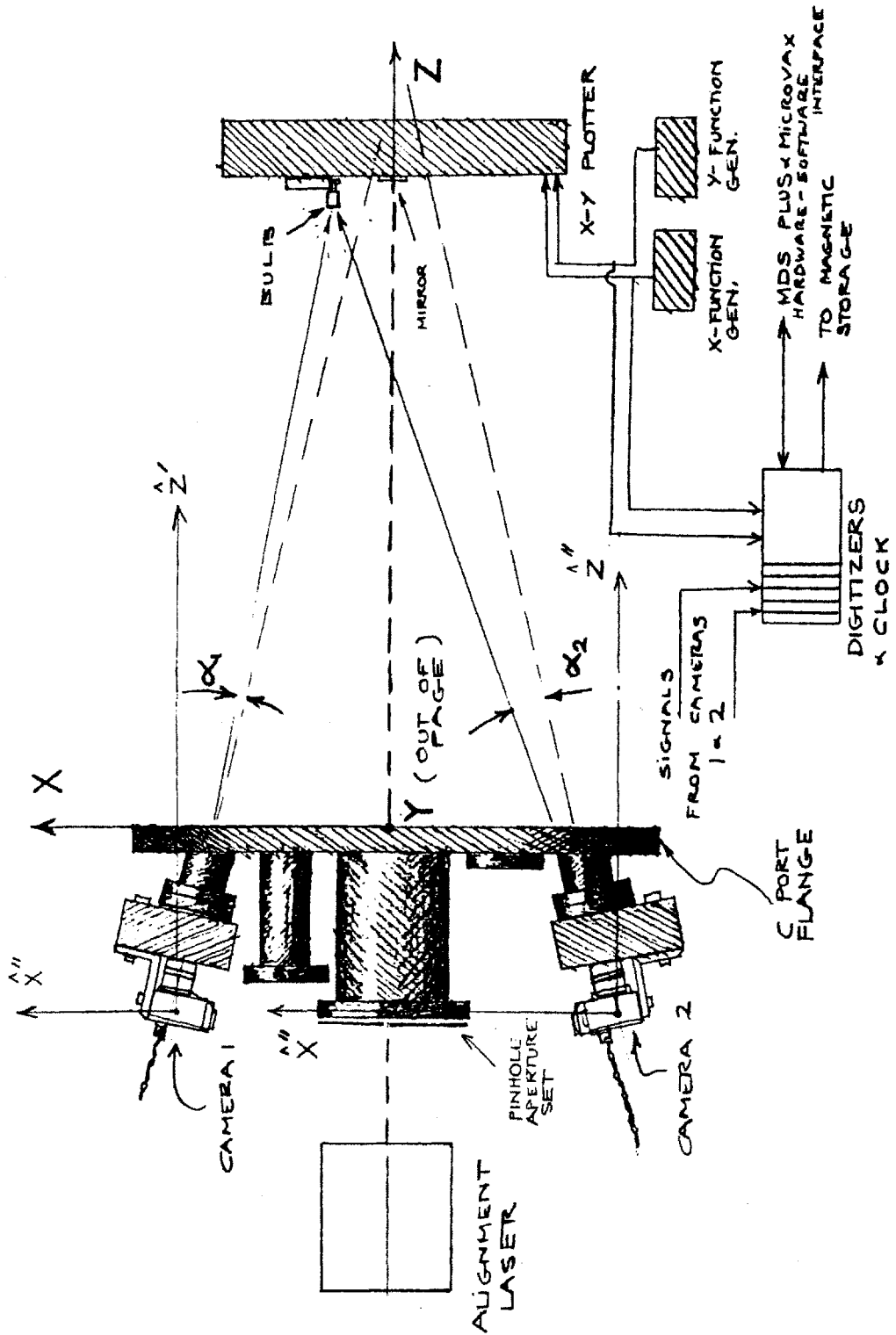
Fig 5.1.3: The tracker calibration apparatus, showing the C-port flange and
plotter.

The procedure for taking a calibration "shot" was to apply triangular wave sweep voltages to the X and Y voltage inputs of the plotter, thereby moving the illuminated bulb in the X and Y dimensions. Here X,Y and Z refer to the axis of a rectangular coordinate system centered on the C-port flange and not the subscripted values which are derived from the camera diode voltages. During a typical eighty second scan, the bulb completes approximately one cycle in the X dimension and ten cycles in the Y dimension. The data recorded for each shot consists of 8192 data points on each of ten channels, four to each camera and two for the sweep voltages to the plotter. Data is also taken with the camera shutter closed so that the background voltage level may be recorded and later subtracted from the recorded calibration voltages.

Nine calibration shots were taken, each with the plotter at a different fixed (Z) distance from the flange. The plotter X-Y plane and flange surfaces were held parallel through the use of an alignment laser. The alignment beam passes through two apertures centered in the injection line port and reflects off a mirror mounted on the plotter surface. This process of the beam reflecting back on itself ensures that the two surfaces are parallel. The beam is also used to set the position of the plotter so that the zero voltage position of the bulb coincides with zero in the flange X and Y coordinates. The sweep velocity of the bulb was kept below 4 centimeters per second to minimize inertial effects at the sweep turn points. Light bulbs used in the calibration procedure have a well localized light emitting region of approximately one mm square.

The calibration data was analyzed with the IDL routine PEL_TRAK3. The program first opens the calibration shot files and reduces the 800,000 calibration data points by skipping and averaging in steps of N and M where N and M are user defined constants. A linear regression routine determines the constants C_1 to C_{12} in equations 5.1.2 for the two cameras.

Table 5.1.1 : Tracker Calibration Constants

Camera #1 Constants:

C1= -.1103	C2= -.0006510	C3= -.2170
C4= -.0004796	C5= .09882	C6= .01026

Camera #2 Constants:

C7= -.1144	C8= -.001926	C9= .1907
C10= -.002520	C11= .09955	C12= -.01410

The constants listed above are related to the location and orientation of the two cameras with respect to the flange centered coordinate system. It is a worthwhile exercise to check the fitted constants to see that they conform to our expectations as based on the known geometry of the system. Note that for camera #1, C1 is larger in magnitude than C2 and on camera #2, C7 is also larger than C8. This makes sense since these constants are used in the equation for the lines of sight in the flange vertical plane . C1 and C7 are the fitting constants for the signals from the diode's vertical axis. The converse relationship holds for constants C4 and C5 of camera #1 and C10 and C11 of camera #2. In this case, C5 and C11 are larger than C4 and C10 because the equations here are for sight lines in the flange horizontal plane. Ideally, the value for the "out of plane" fitting constant should be zero. This is not so because the horizontal and vertical axes of the photodiode and flange may not be exactly coincident, perhaps due to a slight rotational misalignment of the chip within the camera. The constants C3 and C9 should be exactly equal to the tangent of the angles that the optical axes of cameras one and two make with respect to the C-port flange Y-Z plane (see fig. 5.1.3). Under ideal circumstances, these would correspond to the 11.9 degree angle the camera mounting flanges are tilted with respect to the C-port flange surface. The constants C6 and C9, in fact, correspond to angles of 12.2 and 10.8 degrees so the actual camera orientation is off by as much as one degree from what we might expect. The positive feature of the calibration procedure is that these errors which would be very difficult to measure directly are determined through the calibration and their effect is incorporated into the procedure for trajectory reconstruction. The constants C6 and C12 are similarly related to the tangent of the angle between the cameras optical axis and the flange X-Z plane. This angle should ideally be equal to zero but the constants for cameras one and two

indicate that the axes are angled .6 and .8 degrees respectively with respect to the X-Z plane.

Pellet trajectories into the plasma are determined from tracker signals using the IDL routine PEL_PATH1. This program uses the calibration constants previously determined by PEL_TRAK3 to reconstruct the pellet trajectory in time. The procedure determines the equations of the lines of sight to the pellets from both cameras with respect to a rectangular coordinate system centered on the flange. The calculated pellet position with respect to the C port flange coordinates, is at the center of the line segment joining the two points of the closest approach on the lines of sight from each camera. The transformation to a cylindrical coordinate system (R,Z, ϕ) is made taking into account the C-port flange geometry with respect to the vacuum vessel. The coordinates are centered such that R is the radius from the tokamak central axis, Z is height above the torus mid-plane, and Phi is the toroidal angle with respect to the C port centerline. When injection data from the trackers is processed by PEL_TRAK3, the background voltage level on each channel is determined from the average of the first twenty voltage samples which occur prior to injection.

Figures 5.1.4 (top and bottom) and 5.1.5 (top), show the bulb "trajectory" along the X,Y and Z axes during calibration. The paths were reconstructed from the raw data using PEL_TRAK3. The distance between the two lines of sight is shown in the lower graph of figure 5.1.5 and is typically about one millimeter. The inter-line spacing may be used as a convenient measure of the "health" of the tracker system. Any single channel failure in either the amplifier electronics or cabling will result in an inter-line spacing at least an order of magnitude greater than that observed under normal circumstances.

The correlation coefficients for the regression of the calibration shot data proved to be in all cases better than .999 . Figures 5.1.6 and 5.1.7 show graphs of the difference between the fitted and actual bulb path. These provide some measure of the tracking system accuracy to be expected. The data shows the positional error to averages two millimeters in X and Y and five millimeters in Z. Possible sources of error for the tracking system include:

1) Reflections : Stray reflections can cause the detectors to see a light centroid shifted in position away from the ablation source. During calibration, reflections were minimized by reducing the background lighting and by covering all imaged surfaces with

Camera 1 X Pellet Position, Shot no. 1167

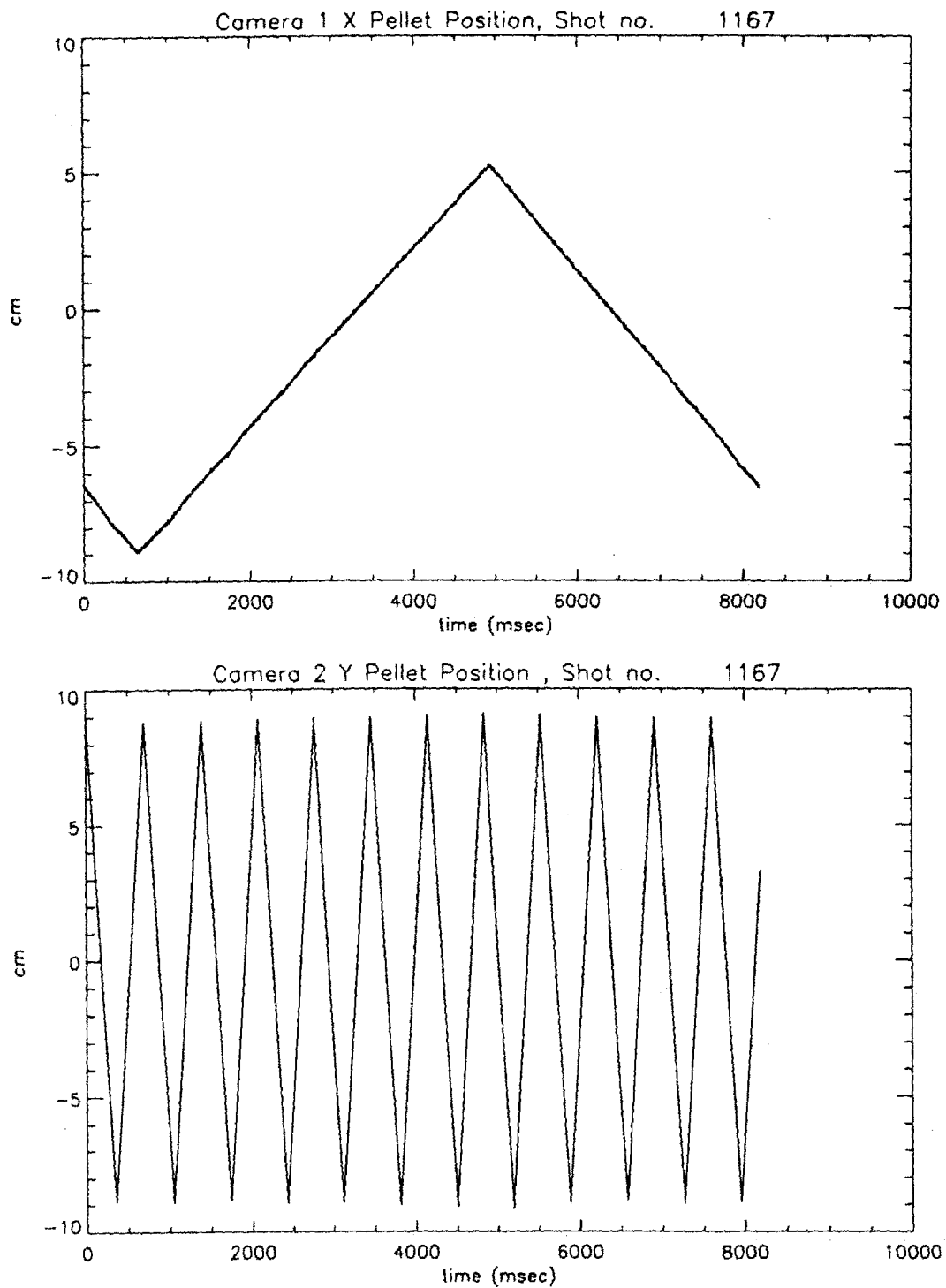Camera 2 Y Pellet Position , Shot no. 1167

Fig 5.1.4: Bulb trajectories in X (top) and Y(bottom) during the calibration "shot"
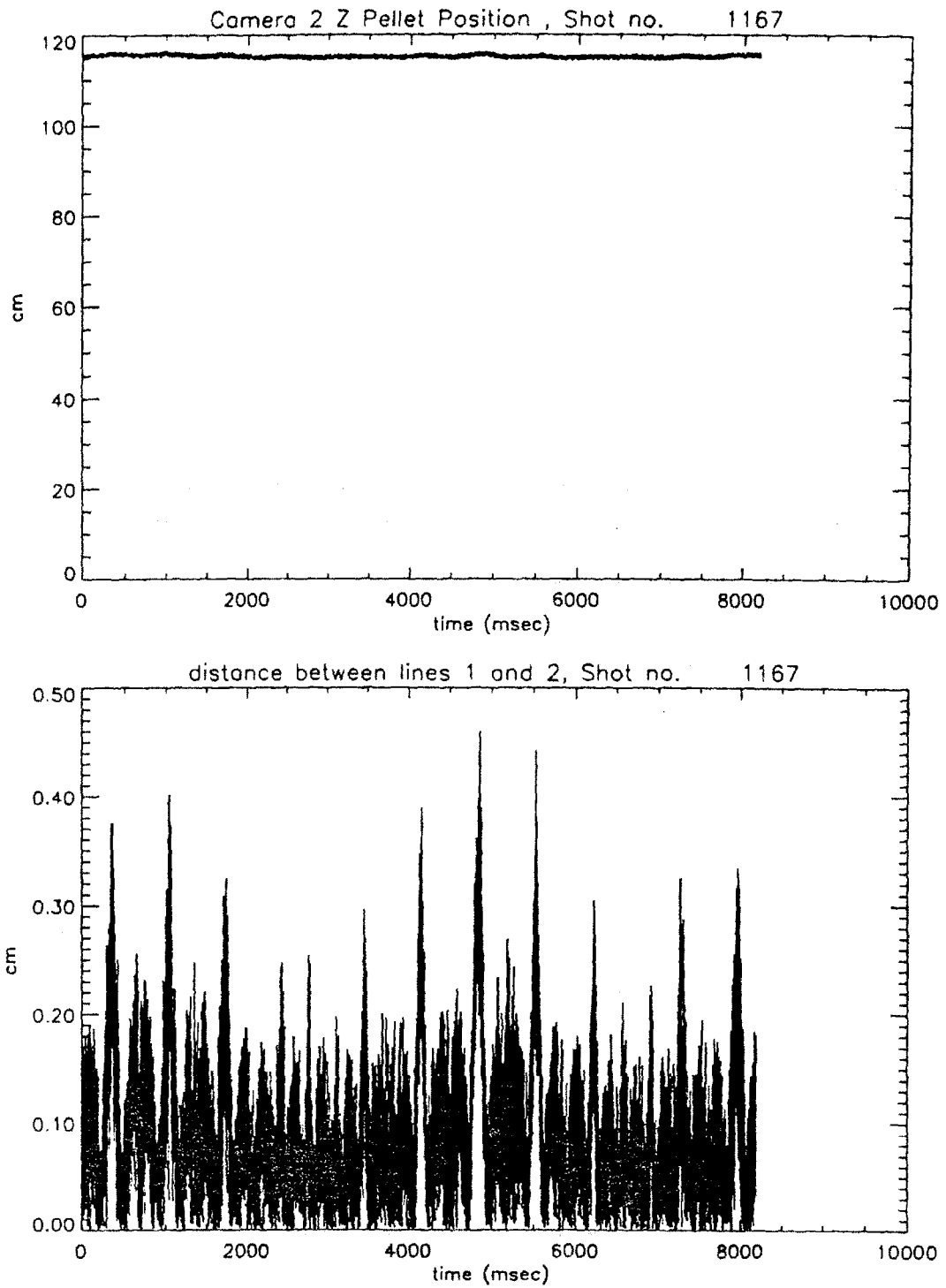as reconstructed from the camera signals and the fitted constants.

125

Fig 5.1.5: Bulb trajectories in Z (top) during calibration and the distance between between the two camera lines of sight (bottom).
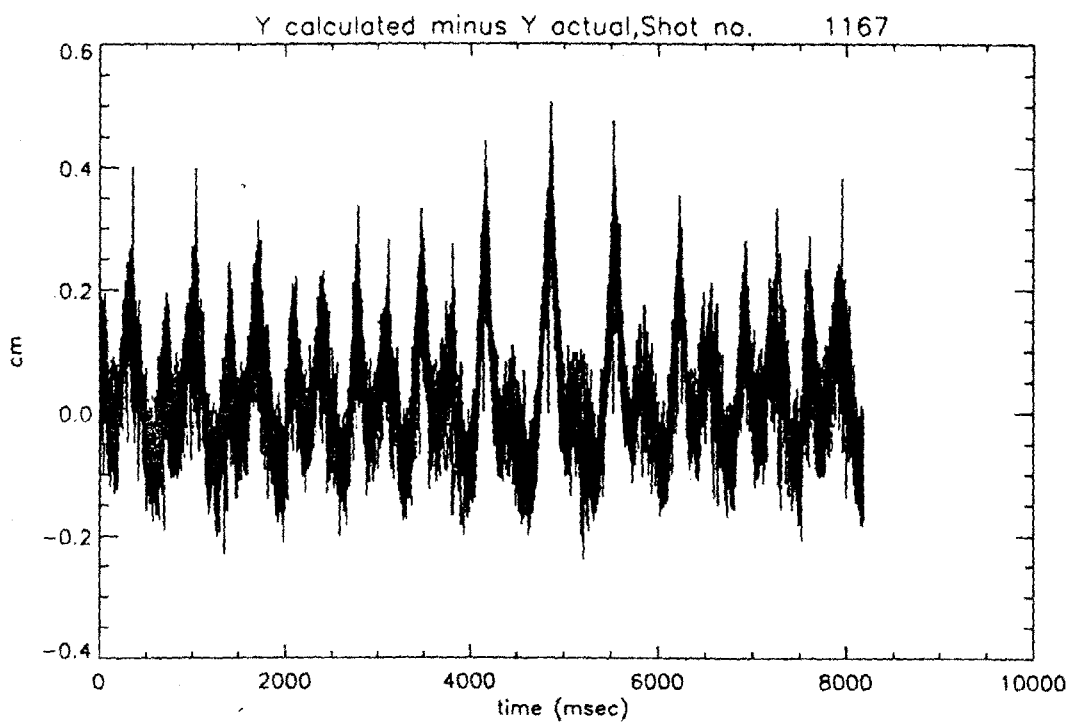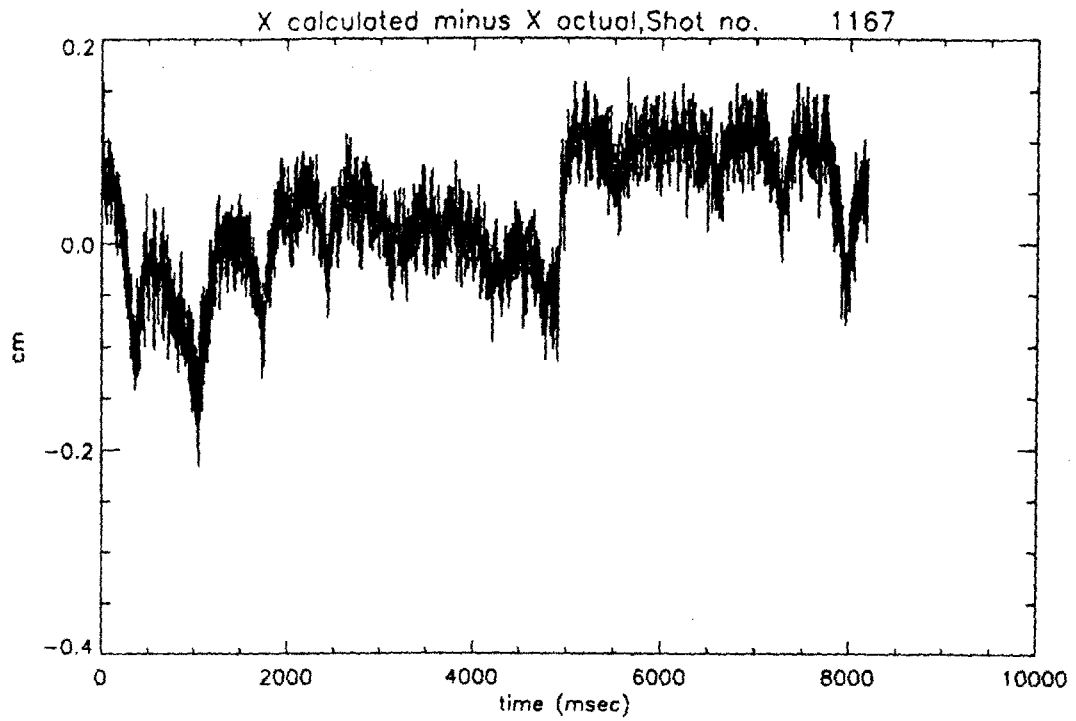
Fig. 5.1.6: (top) Residuals for the X coordinate.
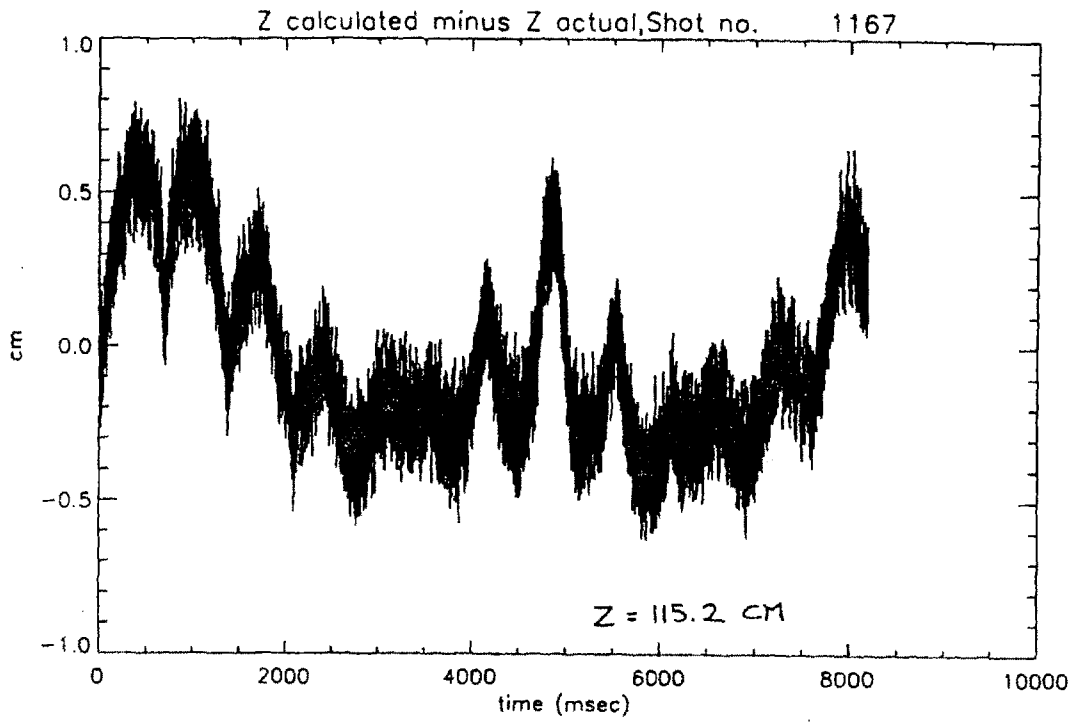(bottom) Residuals for the Y coordinate.

127

Fig. 5.1.7:   Residuals for the Z coordinate.
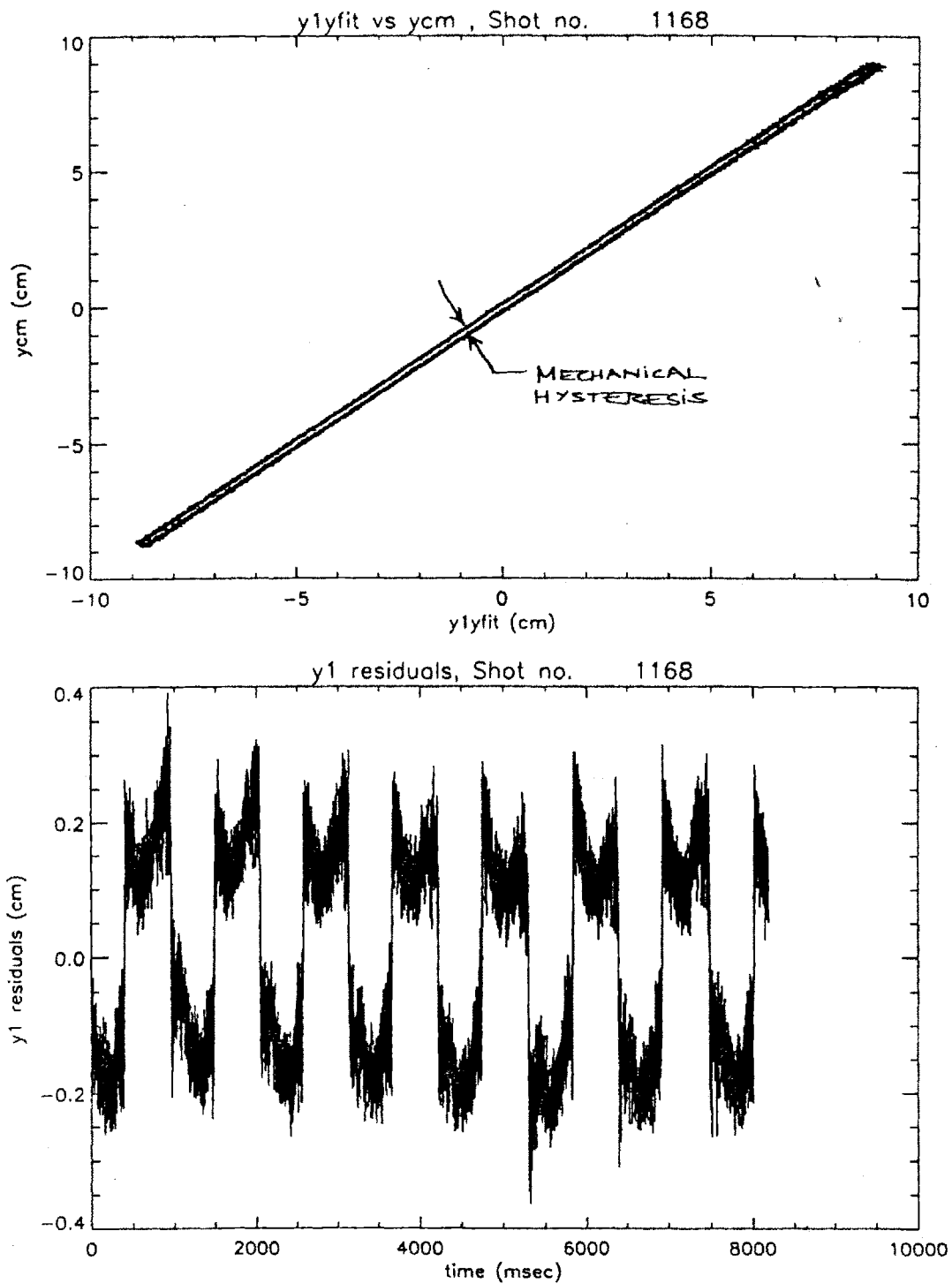
Fig. 5.1.8: (top) The reconstructed Y coordinate vs. the actual, shown prior to the correction for mechanical hysteresis.

(bottom) Residuals of the Y coordinate prior to correction.

129

flat black paper. No significant reflections were therefore present to cause errors during the calibration procedure. Successful operation of the trackers on C-Mod requires that there are be no significant reflections in the camera field of view. To eliminate possible reflections, the tracking cameral field of view is sized so that it does not include the highly reflective sides of C port. The cameras view includes only the low reflectivity, molybdenum tiles of the central core. The convex shape of the central core also acts to prevent ablation light reflections into the field of view.

2) <u>Diode Non-Linearity</u> : The photo diode electrode design and location limits non-linearity to less than 50 μ m over ninety percent of the detector surface area. The corresponding positional error at the torus major radius is less than half a millimeter. The effect is therefore relatively insignificant.

3) <u>Edge effects</u> : The camera lens imaging field at the film plane is slightly larger than the surface area of the detector. It is therefore possible to view a light source at the extreme periphery of the lens field without detecting it on the diode surface. This problem is eliminated in calibration by limiting the light source translation to a field of view well within that of the detector. The problem is academic on the tokamak because the maximum pellet translation in the imaging plane falls well within the detector's field of view.

4) <u>Mechanical Effects</u> : Some mechanical hysteresis was detected in the plotter Y sweep direction where the bulb holder was found to lag approximately two mm behind the position corresponding to the plotter input voltage. The effect is caused by the slight stretching of the thin steel drive cables used to move the plotter carriage. Careful measurement of the bulb position indicated that the effect occurs only when the carriage is moving. Figure 5.1.8 (top) shows a plot the fitted versus the actual path in Y. This source of error was removed from the calibration data by adding or subtracting the positional error based on the plotter direction of motion. Figure 5.1.8 (bottom) depicts the fitting error prior to the correction for cable stretch.

At the turn points of the plotter sweep motion, the bulb is subject to an inertial force caused by the rapid acceleration of the carriage. A slight shifting of the bulb results, causing a one to two mm positional error. This source of error was removed from the calibration data set by discarding data taken near the carriage turn points.

5) _Amplification Electronics_ : The amplifier circuits used consist of one current to voltage stage followed by a second voltage gain stage with a 50 ohm driver. All channels must have the same gain in order for the difference over the sum to vary linearly with position for each dimension. The resistors were balanced to within .1 %, thereby reducing the error to below one mm. This error cannot be compensated for during calibration since the amplifier gain resistors must be changed after calibration to a value appropriate for the higher light levels encountered during pellet ablation.

6) _Optical Distortion_: Optical distortions from the camera lens system have not been directly quantified, but their contribution to positional errors in the tracking system are insignificant. Wide field of view lenses have magnification factors which may be dependent on the off axis distance of the light ray. Possible magnification errors are minimized due to the narrow (10.4°) viewing angle of the lens and because of the small aperture employed to prevent signal saturation also limits the admission of off axis light. In any event, the calibration procedure outlined should correct for errors, at least for the case where the magnification error is linearly proportional to the off axis distance.

The tracking system functioned very successfully during the initial injection experiments on Alcator C-Mod. Data from the trackers, obtained during these experiments is presented in chapter six.

5.2 Velocity Measurement

Velocity measurements are made for all pellets both during laboratory testing and for operation on C-Mod. During the laboratory test period, velocity measurements proved invaluable not only as an important measure of injector performance but also because signals from the diodes were used to diagnose pellet condition and barrel reliability. For injection experiments on Alcator, the velocity data can provide an independent check on the trackers. The timing of the first signals from the tracker should closely correspond with the arrival of the pellet at the plasma outer edge as predicted by the velocity measurements. Similarly, the radial velocity measured by the trackers should correspond to that measured in the injection line, at least for the beginning of the ablation profile where the pellet trajectory is more purely ballistic.

Pellet velocity measurements are made by recording the pellet time of flight between two laser-photodiode sight flanges or "gates". Making velocity measurements this way is nothing new, however, the large number of barrels on the C-Mod injector and their close spacing necessitated that instead of employing separate timing gates for each barrel as is the usual practice, a single pair of gates be used for all twenty barrels. Besides reducing the parts count, the use of a single light source and with a longer path length also increases detection sensitivity. The transparency and low index of refraction of solid hydrogen makes the pellet act like a small cylindrical lens as it passes through the beam. The perturbing effect on the light is very slight however, and most of the affected light is refracted only a few degrees away from the original light path. These factors make detection with a closely spaced light source and diode pair very difficult, because most of the light still makes it to the detector. By employing a laser and a longer light path, the light transmitted through the pellet is refracted over a larger area. Detection sensitivity may then be greatly increased by using a spatial filter to remove the refracted light component from the original beam.

A schematic drawing of the detection gates and their location in the injection line are shown in figures 5.3.1 and 5.3.2. The light source employed is a .9 milliwatt helium neon laser mounted on an external optics table. The beam of this laser enters the sight flange through a small window and is reflected back and forth across the pellet trajectory paths of each of the 20 barrels by six rotatable mirrors mounted in the sight flange. A laser is used as a light source because it remains well collimated after multiple
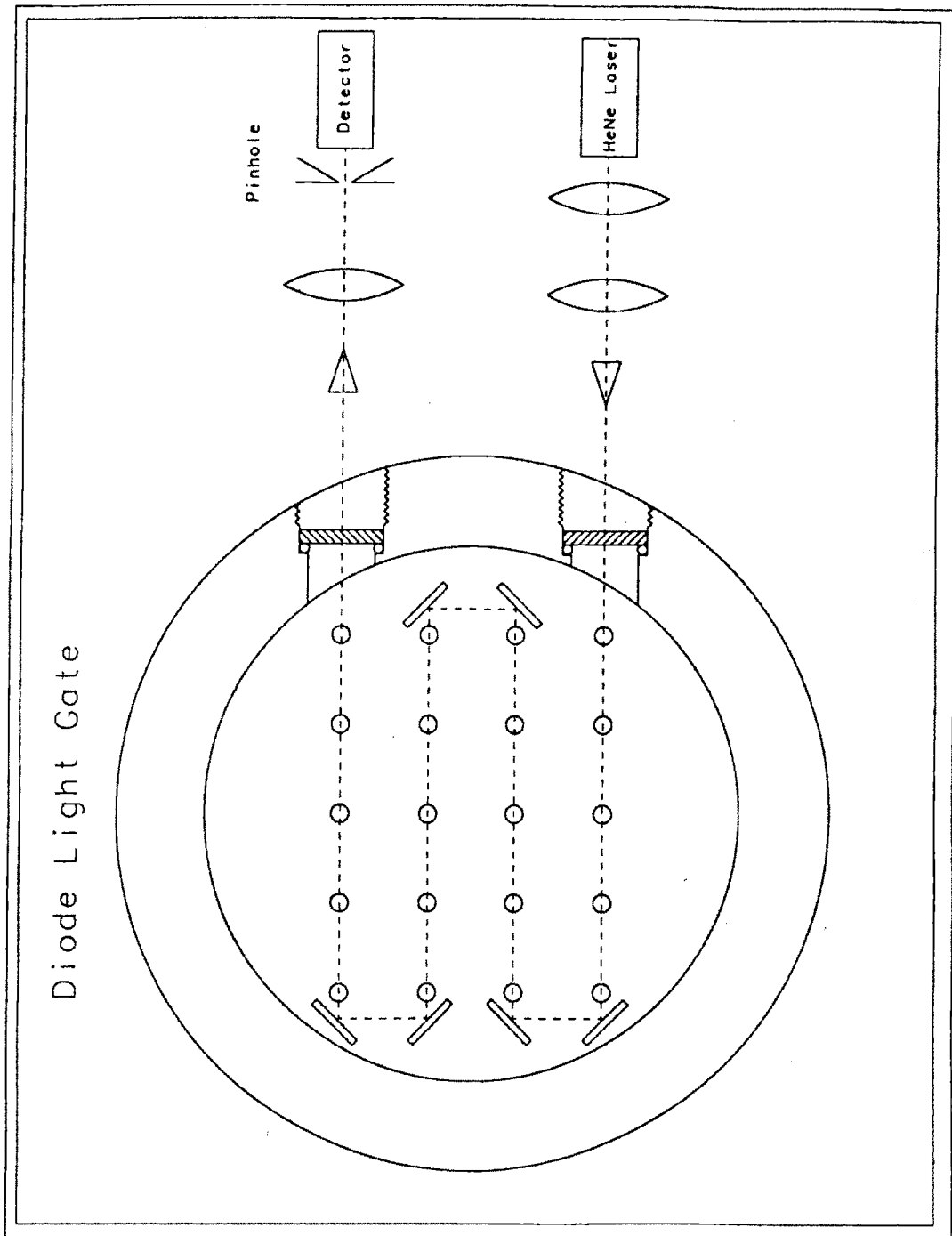
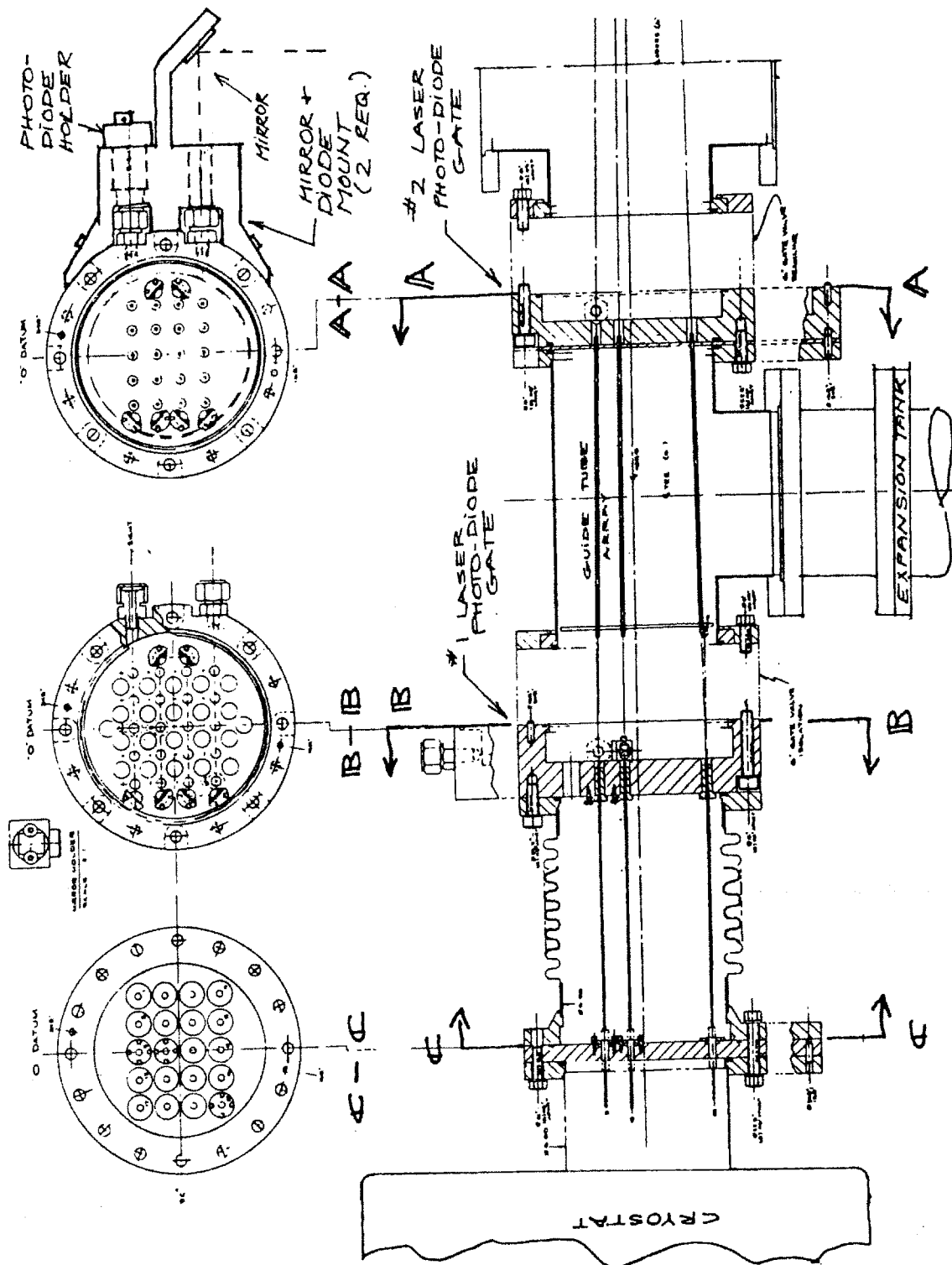Fig. 5.2.1: Schematic of the Laser-Diode gate.

Fig. 5.2.2: Sectional view of the injection line showing the two laser-diode gates and the guide tube array for diverting propellant gas into the expansion tank.

reflections, allowing a single source and detector pair to be used for all 20 barrels. The beam exits the injection line through a second window and is focused with a convex lens through a pinhole aperture onto the detector surface. The lens-aperture pair provides spatial filtering of the beam, resulting in increased sensitivity to beam perturbations at the detector. Photodiode output level drops for the length of time it takes for the pellet to travel the beam diameter plus the pellet length. Signals from the photo diodes are amplified with a current to voltage amplifier and digitized at 500 kilohertz.

The pellet velocity is determined from the raw data by dividing the distance between the two diode gates by the time difference between the photodiode signal minimums (see figure 5.2.5). Alternatively, velocities may be resolved with a counting

circuit which is started and stopped when the photodiode signal drops below a pre-set discriminator level. The latched count value is proportioned to the time of flight and may be either read electronically or viewed directly through a board mounted LED display. The perpendicular beam dimension must be wide enough however, so that there is no possibility of the pellet missing the beam.

An optical table located on the right side of the expansion tank serves as a mount for the two helium neon lasers and the beam shaping and alignment optics (see fig. 5.2.3). The beams from each laser are directed upwards through beam expanders which increase the diameters to the size required to ensure all possible pellet paths are intersected. The intensity and shape of the beam is controlled by a combination slit aperture and cross polarizing variable attenuator. A lexan enclosure surrounds the table and reduces the exposure of the optical components to dust.

Each beam is directed through the sight flange with two movable mirrors mounted on the optics table. These mirrors give each beam the two spatial and two angular degrees of freedom needed to align the beam with the mirrors of the sight flange. The angular orientations of the sight flange mirrors are set with the flange removed from the injector. The procedure is to direct an alignment beam through two fixed apertures positioned at the entrance and exit windows. The mirrors are then set so that the beam
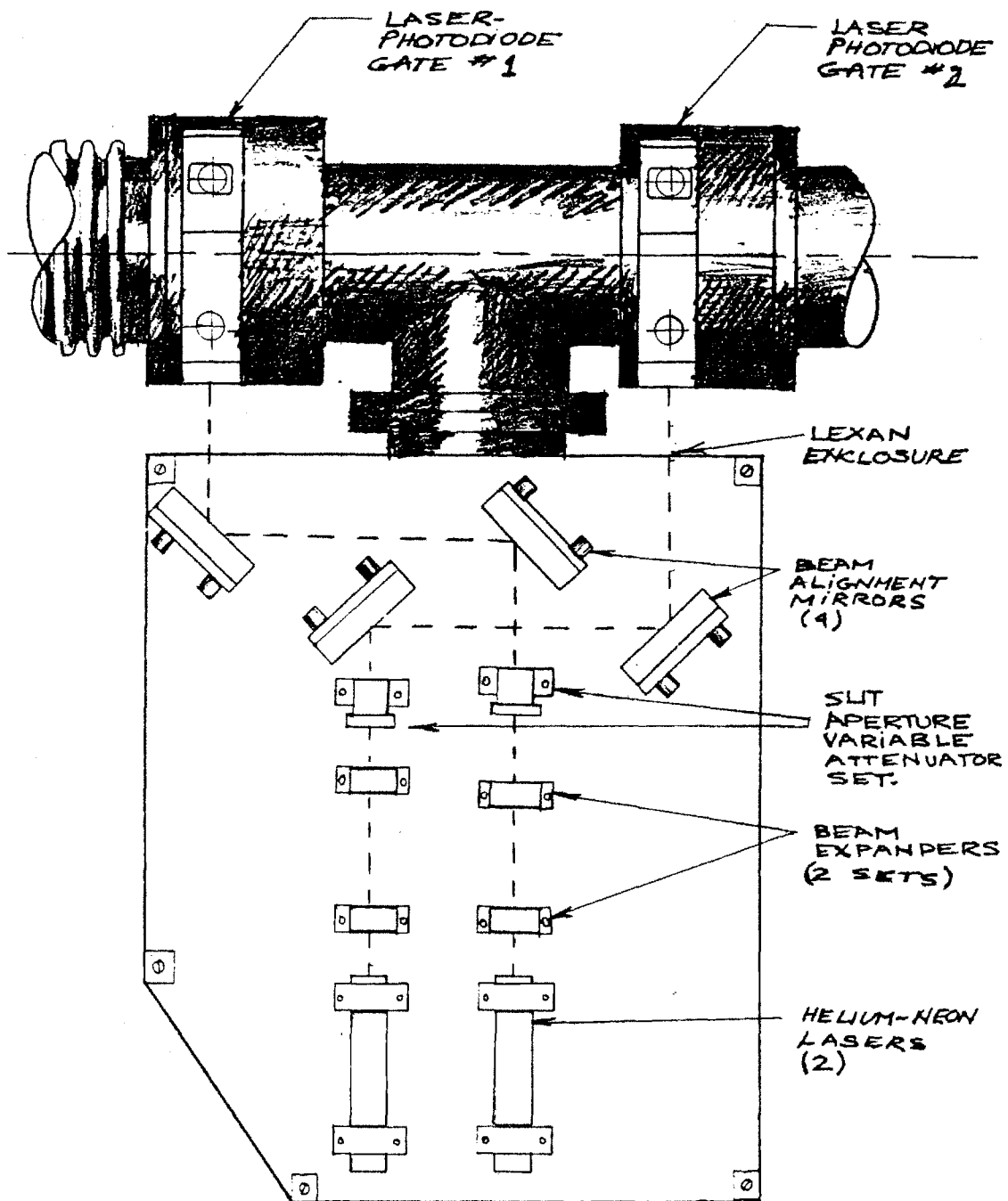
Fig. 5.2.3: Optic table showing the two helium neon lasers, the beam expanders and the alignment mirrors.

path intersects the pellet paths from all four rows of barrels. After mounting the sight flange to the injection line, the beam is directed through the same entrance and exit apertures using the optic table alignment mirrors. This ensures a replication of the original and correct beam position within the sight flange.

Raw data from the photodiode signal amplifier is shown in figure 5.2.4 (top). The vertical lines are the drops in signal level coincident with the passage of the pellet. Extinction ratios for the first and second photo diodes are typically between sixty and twenty percent and are easily discriminated from noise. Amplifier signals are digitized in a window around each barrel firing lasting typically for 1 millisecond. Figure 5.2.4 (bottom) shows the data for 14 barrels with an expanded time base of 5 microseconds per segment centered around the signal from each pellet. The data indicates that the diode signals are useful in detecting both non-functional barrels and fragmented pellets. Figure 5.2.5 shows the signals from the first and second diodes plotted with a common time base. The steep drop and the symmetric shape of the signal indicates the pellet is not

fragmented. The error in the velocity measurements is due to the uncertainty in the inter-beam distance of approximately ± 2 mm. This results in a velocity measurement error .6%. Figure 5.2.6 shows expanded views of the diode signals from a complete and fragmented pellets.

A second timing reference for velocity measurement is available from a piezo electric microphone epoxied to a retractable target plate located in the injection line test section. A linear motion pneumatic actuator is linked through a pivot arm to the target plate which pivots about its upper edge in and out of the injection line. The test section and target actuator are shown in Figure 5.2.7. Target microphone signals are digitized and the time at which the differentiated signal level rises above some minimum value is taken as the impact time. Typical microphone signals are shown in Figure 5.2.8. Velocities are then determined from the time differences between the microphone and first diode signal. Agreement between the photodiode and microphone measured velocities is typically within 1%. The rms value of the differentiated signal has been shown to be proportional to the pellet mass. Because the pellets are destroyed when impacting the target plate, it is not possible to make microphone derived velocity measurements during actual injection experiments.
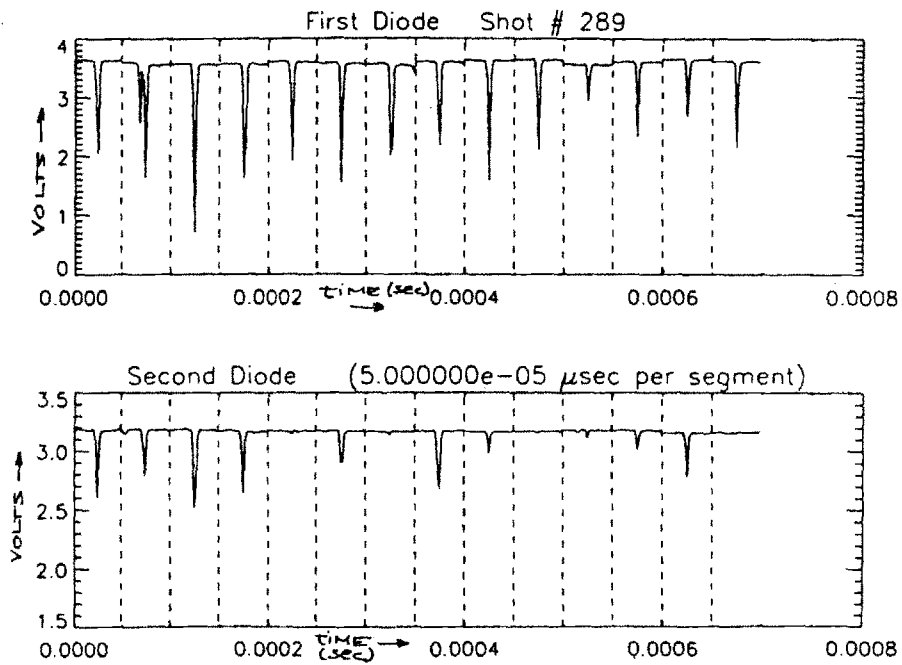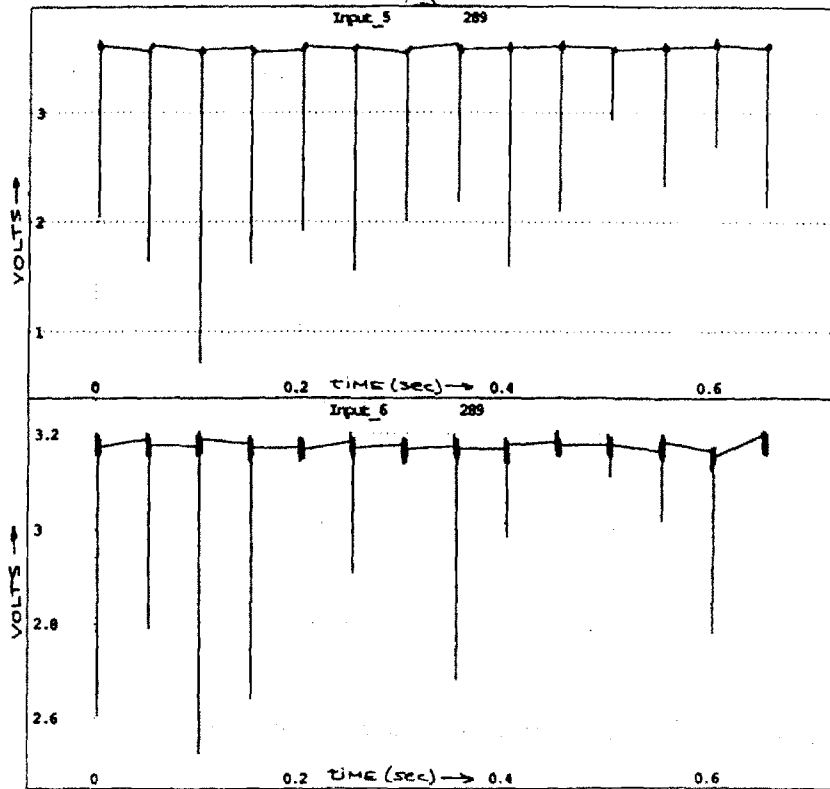
Fig. 5.2.4: (top) Diode signals from the two diode gates.
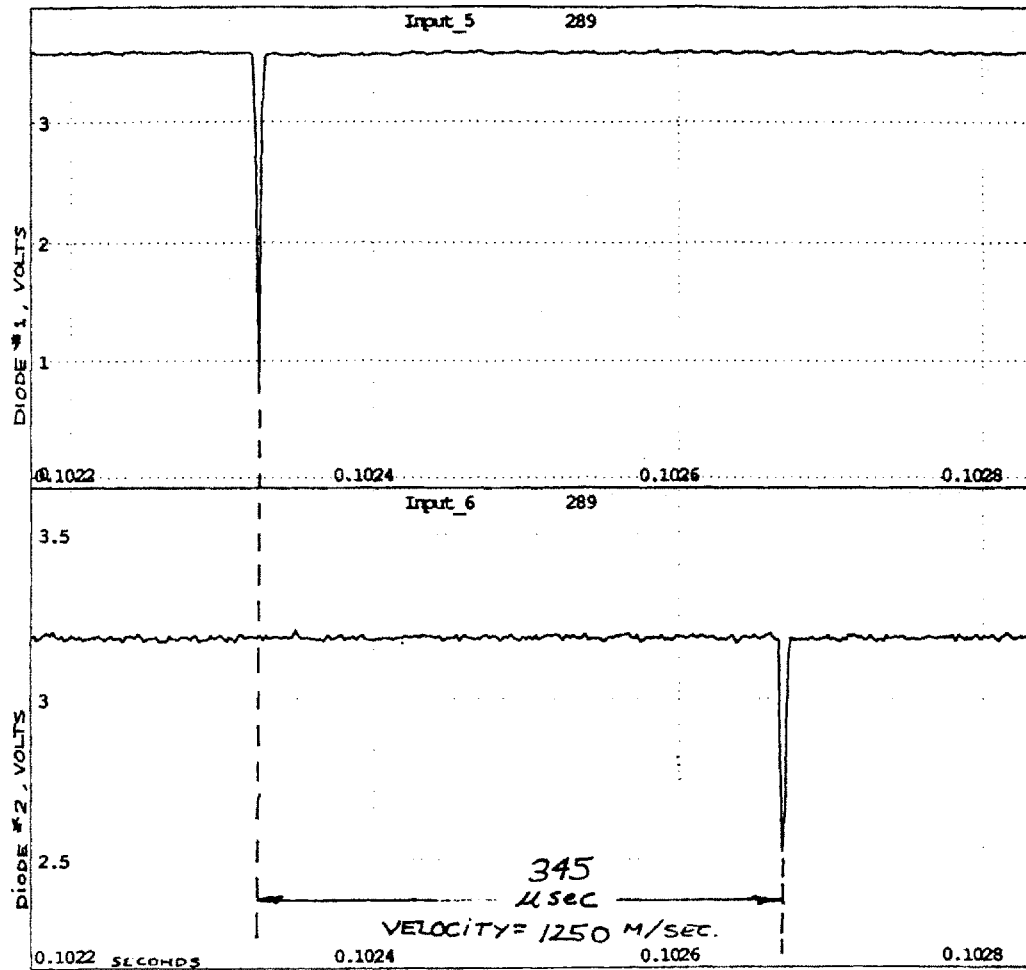(bottom) Diode signals with an expanded time base.

Fig. 5.2.5: Diode signals from the two diode gates for a single pellet
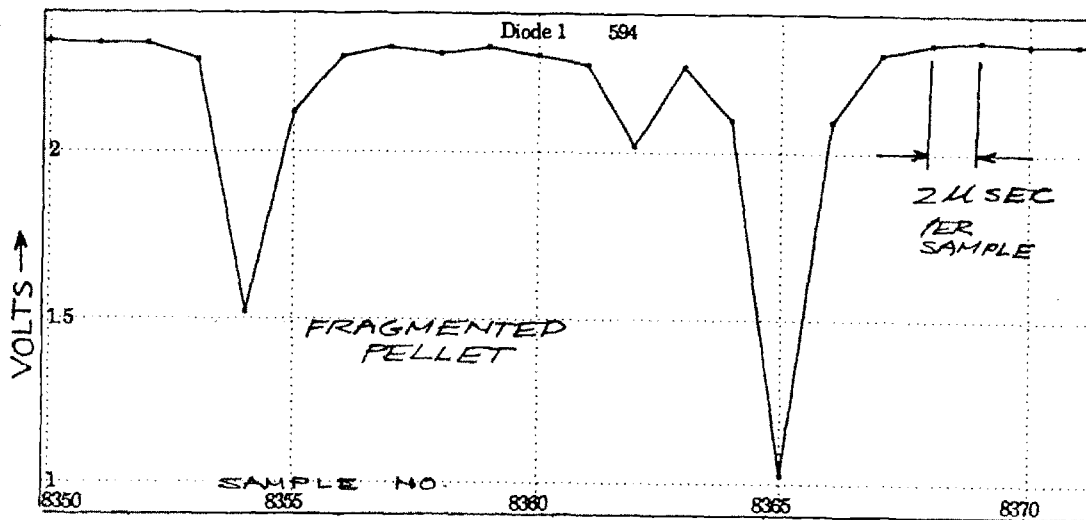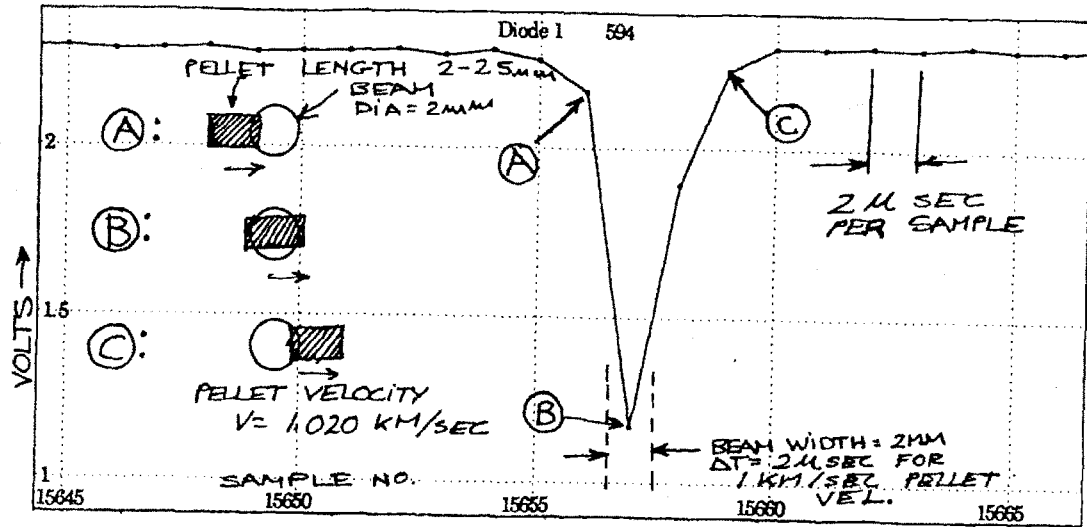and time of flight velocity measurement.

Fig 5.2.6: Expanded view of the diode signal from a complete (top) and
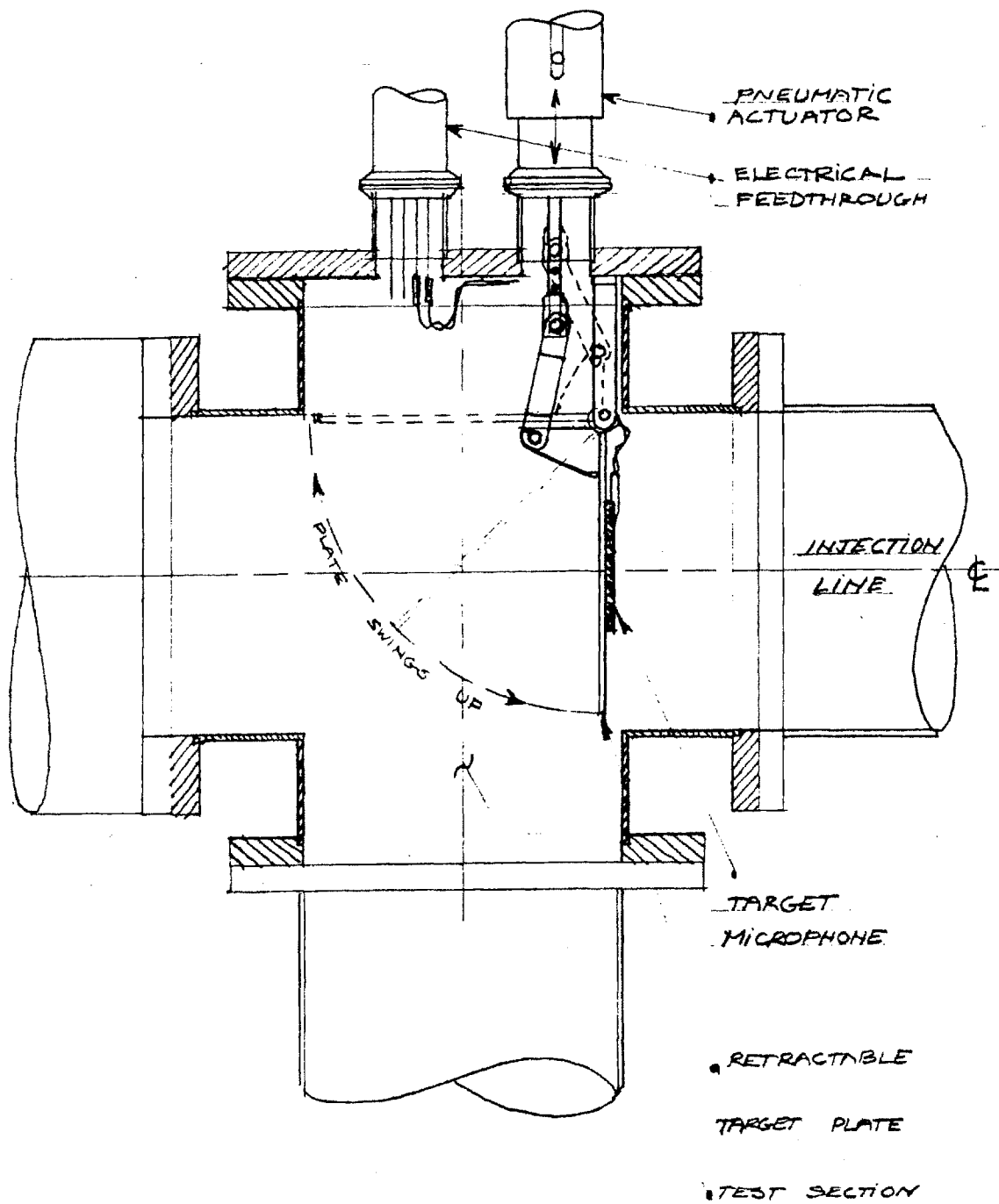fragmented (bottom) pellet.
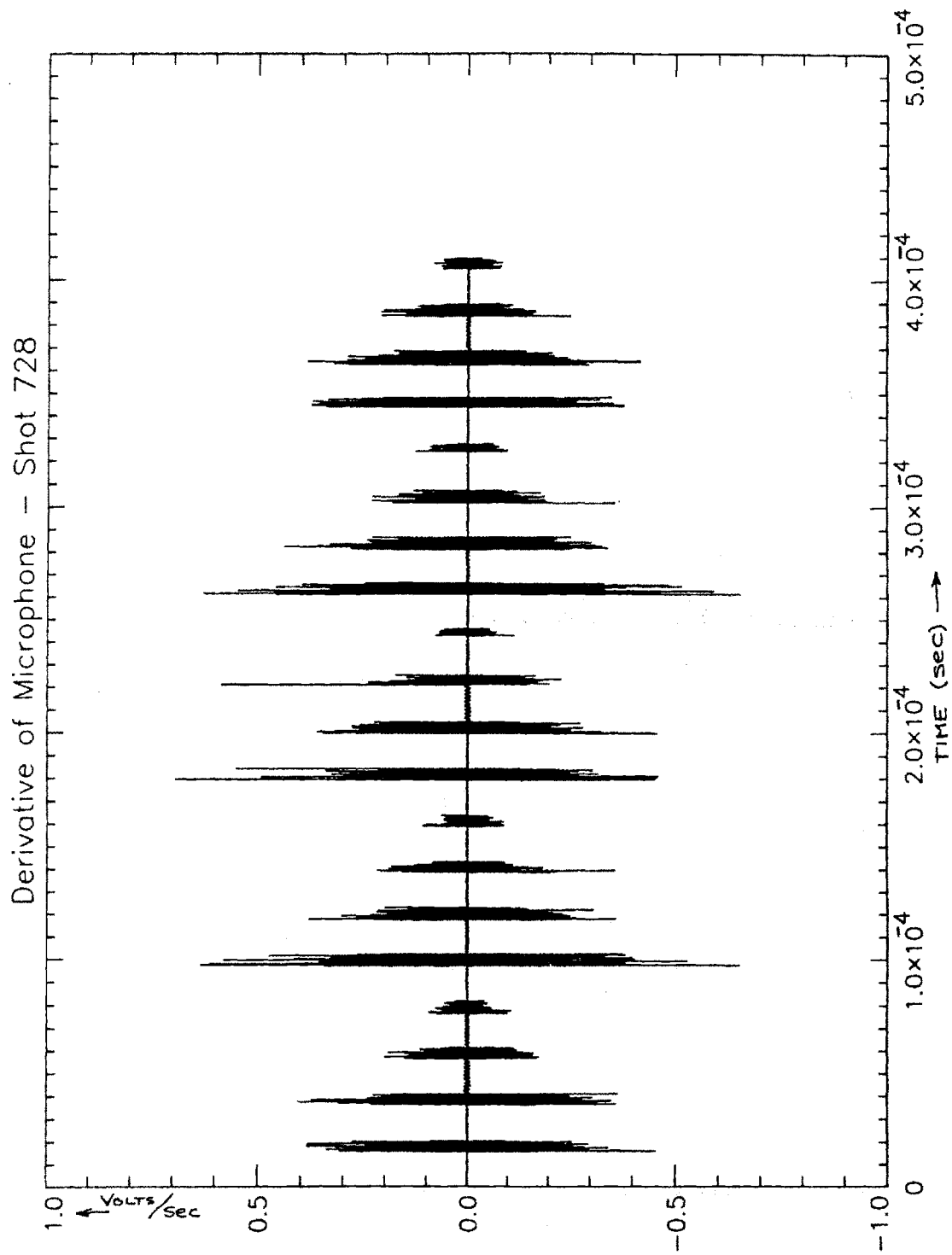
Fig 5.2.7: Test section with retractable target plate.

Fig 5.2.8: Target microphone signals.

5.3 Pellet Photography

The purpose of pellet photography on the injector is to determine pellet mass, size and condition. There are several different ways to record mass. One method is to shoot pellets into a fixed volume and to record the pressure rise. If velocity is known a ballistic pendulum may also be used. With these methods, propellant gas effects interfere with the measurement. Also, because the methods are destructive, one cannot measure the actual mass of a pellet used in fueling. This is desirable not just for transport and ablation studies but also to correlate anomalous or low energy confinement shots with small or fragmented fueling pellets. Mass may also be measured by recording the changes in the resonant frequency of a small microwave cavity through which the pellets pass. For the C-Mod injector geometry, this method has the disadvantage of requiring twenty separate resonance cavities, one for each barrel. Mass measurements with photography have the advantage in that a single camera may be mounted external to the injection line and moved to view pellets from all twenty barrels. The apparatus used, a flash lamp and CCD camera with a video recorder, are relatively inexpensive and available commercially. Photography is also advantageous in that it provides specific dimensional information about the pellet such as length and diameter. This in turn may be employed to estimate barrel temperature profiles and the degree of pellet erosion during firing.

In the Spring of 1990, experiments were performed to verify best methods and apparatus for photographing pellets from the injector. Initial experiments were done prior to the operation of the injector. The gun used for the experiments consisted of a stainless steel barrel, fifty millimeters in length, with an internal diameter of 1.2 mm. A solenoid valve at the end of the barrel was fed with a regulated supply of helium and operated with a solid state triggered capacitor bank. The short length of the barrel and low pressure of the propellant (150 psi) limited the available muzzle velocity to below 200 meters per second. Pellets used for the experiments were made by cutting short pieces of transparent plastic fishing line. The camera used was a XYBION Systems Inc. CCD camera with a 6.5 X zoom lens. This lens system has a variable magnification dependent on the

camera-focal plane distance. The screen magnification used for the tests was 20, and the field of view was approximately one square centimeter.

A high intensity, short duration light source is required to capture images with minimal blurring. The Xenon Corporation Model 437 nanopulser lamp employed uses a pulse forming network to generate a spark discharge in a Xenon gas tube. The resulting light pulse has a 5 nanosecond rise time with a 10 nanosecond half width. Peak power is 50,000 watts and is centered in the optical and UV frequency range. Image blurring will occur over approximately 24 micrometers, assuming a total pulse time of 20 nanoseconds and 1.2 km/sec pellet velocity. This corresponds to only 1/100 of the pellet's overall length so that blurring does not impede mass measurement.

On the injector, pellets are photographed more than half a meter from the barrel ends as they pass through the injection line test section. The nanolamp is triggered using signals from the two laser-Photodiode gates. The signal from the first gate starts a "count up timer". When the signal from the second gate is received, the count up timer is stopped and the value is latched and displayed. The timer meanwhile begins counting down at a preset rate different from the count up rate. When the timer reaches zero, a TTL pulse is sent to trigger the nanolamp. The count up-count down rates are set so that the nanolamp fires when the pellet is in the camera's field of view. This occurs when the up to down count rate ratio is equal to the ratio between photodiode gate spacing and the distance between the second gate and the camera.

Light from the nanolamp is projected onto a frosted glass plate behind the focal plane and external to the injection line. This provides a uniform and diffuse illumination of the pellet. Images are formed from refracted light rather than reflected light with the pellet acting like a cylindrical lens. The light regions in the center of the pellet corresponds to areas where light has been transmitted through the pellet to the camera. In the dark outer edges, the light has been refracted away.

The apparatus used for photographing pellets on the injector was modeled directly from that used to take test photographs and is shown in figure 5.3.1. A six-way union is set into the injection line, forward of the expansion tank and guide tube array. The two horizontal parts have Pyrex glass windows. On the left side of the injection line an
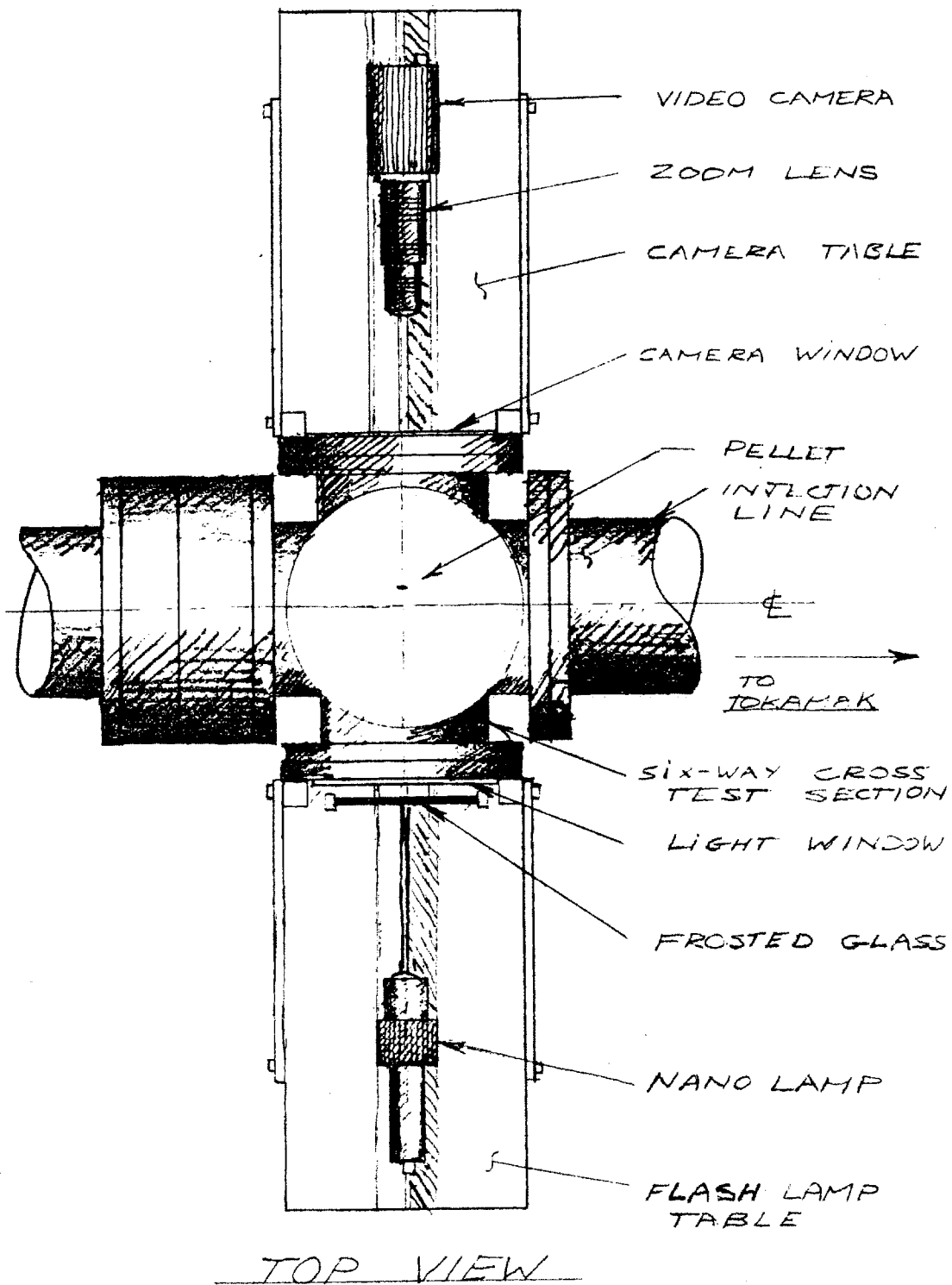
VIDEO CAMERA

ZOOM LENS

CAMERA TABLE

CAMERA WINDOW

PELLET
INJECTION
LINE

TO
TOKAMAK

SIX-WAY CROSS
TEST SECTION

LIGHT WINDOW

FROSTED GLASS

NANO LAMP

FLASH LAMP
TABLE

TOP VIEW

Fig. 5.3.1: Photography apparatus.

145

adjustable table-rail system holds the nanolamp aimed at a pane of frosted glass held in place outside of the window. On the right side of the beamline an adjustable table-rail system allows for both horizontal and vertical movement of the CCD camera. The camera lens magnification is generally held fixed and the camera is moved horizontally along the rails to marked positions for focusing on pellets from each of the 5 columns of barrels. Spacer blocks placed under the camera are used to position the camera vertically for correct alignment with the four rows of barrels. The nanolamp, opposite the camera, is also mounted on a two axis rail system and is positioned similarly. The narrow depth of field of the lens system necessitates that the camera be re-positioned for each barrel. It may be possible, however, to image an entire row of barrels by using a more powerful light source and smaller aperture camera lens.

Chapter 6 : Initial Injection Results and Observations

6.1   Introduction and Scope

The pellet injector was installed on the Alcator C-Mod tokamak in July 1993 with injection experiments beginning in August of the same year. This final chapter will review some of the results from the approximately fifty pellet fueled discharges taken during the period from August to November 1993. Observations from these discharges will be presented in two sections. The first section will cover events following injection which occur on the equilibrium timescale (tens of milliseconds). The focus here will be on density and temperature profile evolution. The second section will present observations which occur on the pellet transit timescale of about 200μ seconds. This section includes pellet tracker data. A comparison will be made of the ablation rates as inferred from H_α measurements versus those predicted from four different pellet ablation models. Localized density perturbations on the q=1 surface, termed "snakes", were also frequently observed during pellet discharges. Some general characteristics of the phenomena are discussed.

The injector orientation with respect to C-port may be seen in figure 6.1.1. Injection is parallel to the tokamak major radius along the C-port centerline and within one centimeter of the torus horizontal midplane. Placement and orientation of the injector was accomplished through the use of an alignment laser. The arrangement involved mounting the laser rigidly to the injector and reflecting its beam into the injection line directly coincident with the path of injection. A window in the C-Port gate valve allowed the beam to enter the vessel and to be viewed through the flange widows as a bright red spot reflected on the vacuum vessel central column. The injector was then positioned to locate the beam on a marked reference point on the midplane of the central column . The injector carriage was then clamped onto the support stand to prevent
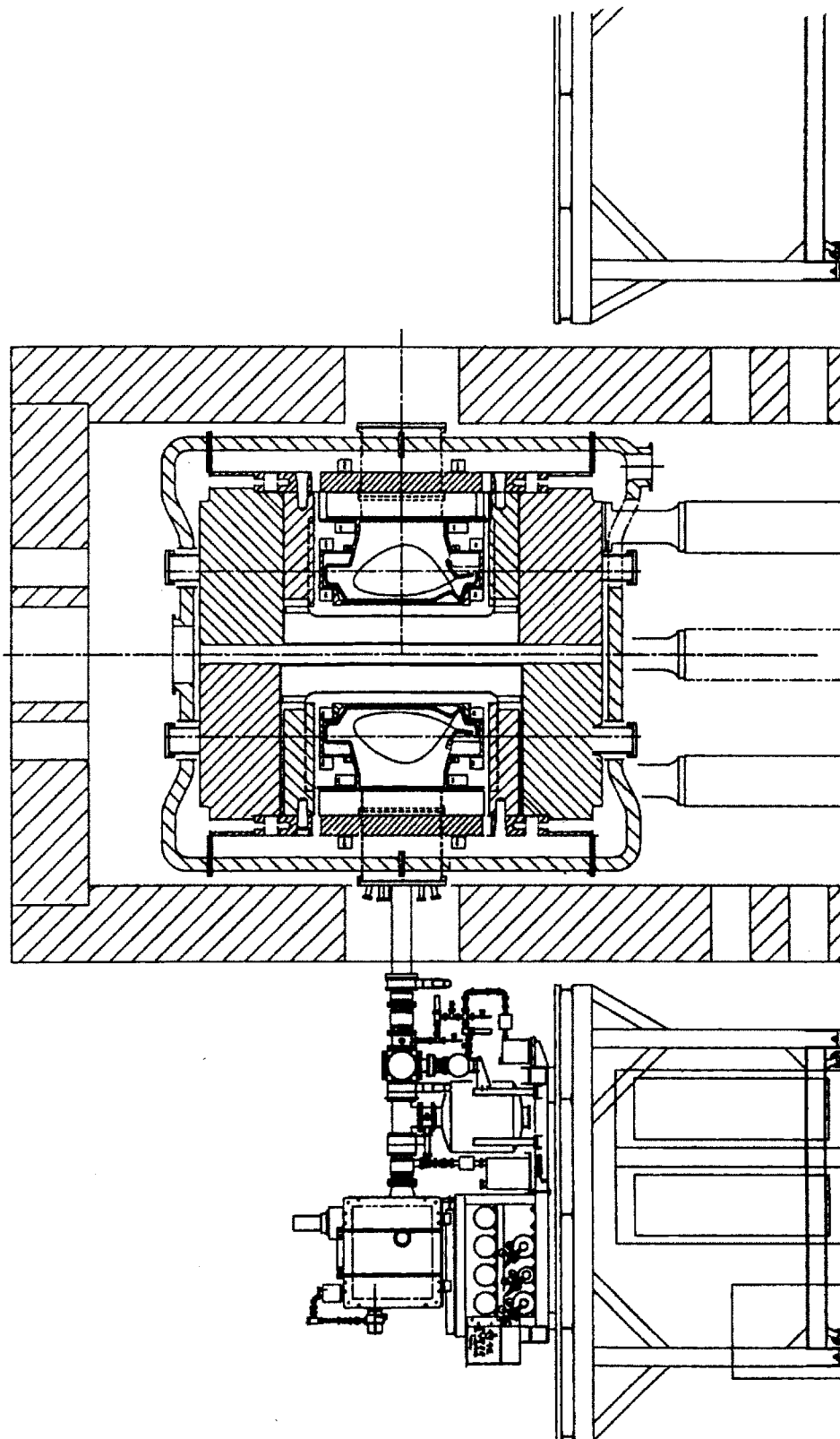
Fig. 6.1.1: Cross section of Alcator C-Mod with Injector on diagnostics stand.
Injection is along the mid-plane and radially inwards.

148

shifting. The injector electronics rack and refrigerator compressor unit are located beneath the support stand on the cell floor.

The purpose of this final chapter is to give an introduction to some of the phenomena observed during pellet fueling, and to provide closure to the work performed on the injector. The chapter does not cover all subjects significant to pellet injection such as transport and confinement time analysis.

6.2 Equilibrium Timescale Observations

6.2.1 Density Profiles

The target plasmas employed in the initial injection experiments were purely ohmic deuterium discharges with current levels ranging from 400 to 800 k amps. Pre-injection peak density for these discharges ranged from below $1 \times 10^{20} / m^3$ to just above $2 \times 10^{20} / m^3$. Peak electron temperatures ranged between .5 and 2 keV. The toroidal magnetic field for these discharges was between 5.1 and 5.3 Tesla.

Electron density measurements were made with a Two Color Interferometer system (TCI). The instrument employs ten vertical chords from a CO_2 laser and four chords from a Helium-Neon laser to measure the electron density profiles. The distinguishing feature of the TCI is that the use short wavelengths and a high modulation frequency allow the system to follow rapid density changes without the loss of fringes. This is a necessary feature for studying pellet fueling due to the rapid density rise following injection. The negative aspect of using the shorter wavelengths is susceptibility to mechanical vibrations. The use of a second, superimposed helium-neon beam provides the information necessary to correct for vibrational effects. Spatial resolution for the system is about 1.7 centimeters with a maximum time resolution of 2 μ sec.

For discharges with currents in the 400 k amp range, two different pellet sizes were used corresponding to $.5 \times 10^{20}$ and $.9 \times 10^{20}$ deuterium atoms. Scope data for shots #930817007 and #930817015 are shown in figures 6.2.1 and 6.2.3. The density profile evolutions of the two discharges are typical of those observed for other discharges with the same pellet size and plasma current. Figure 6.2.2 (top) depicts the time history of the central line integral density for shot #930817007, where a deuterium pellet of $.5 \times 10^{20}$ atoms was injected 240 msec. into the shot with a velocity of 1071 m/sec. . Tracker data indicates that for this shot, pellet penetration was 9 cm. Plasma minor radius was determined to be 23 cm at the time of injection. giving a 39 % penetration depth. The term " minor radius" here refers to the distance from the magnetic axis to the plasma outer edge as determined from magnetic reconstructions.
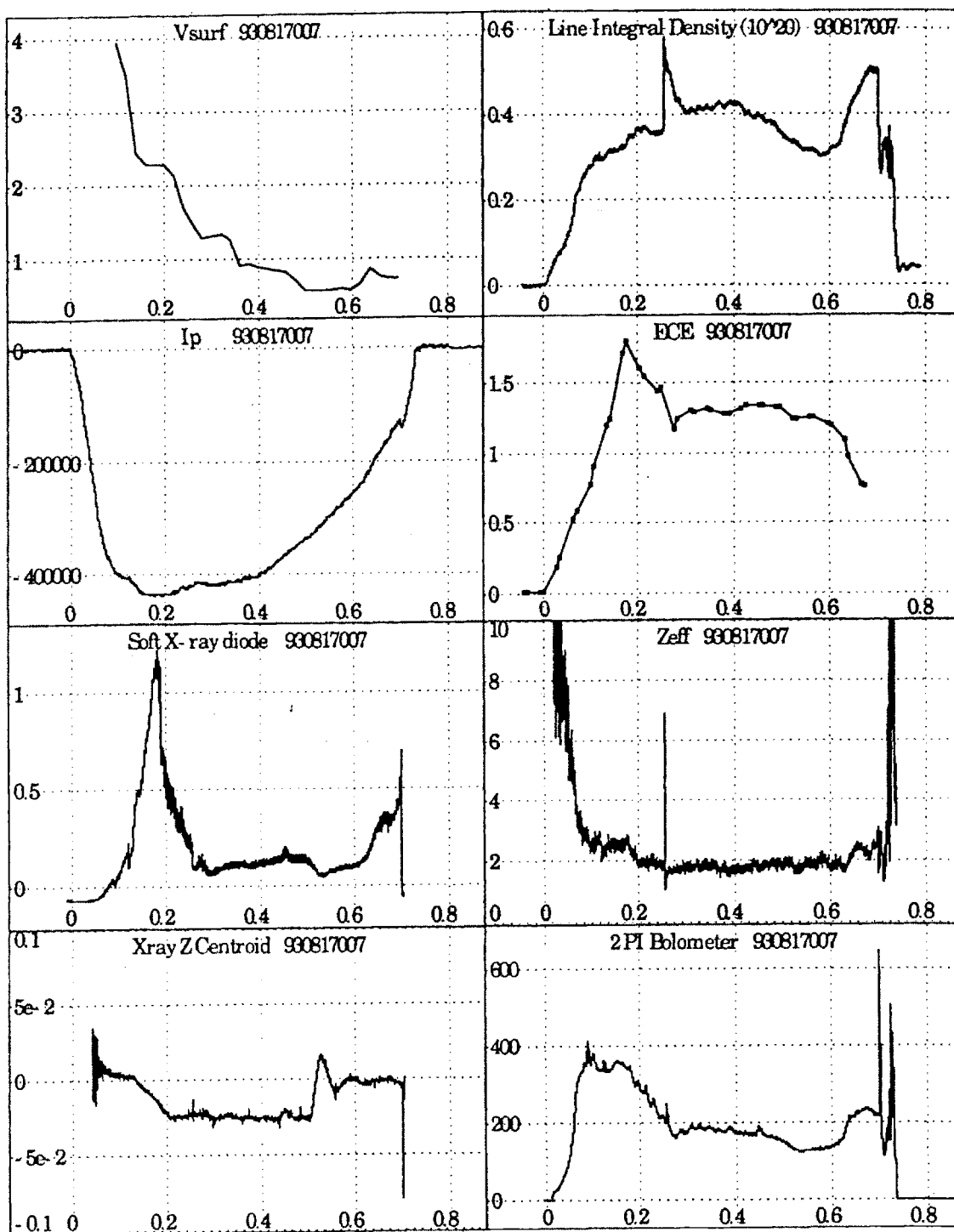
150

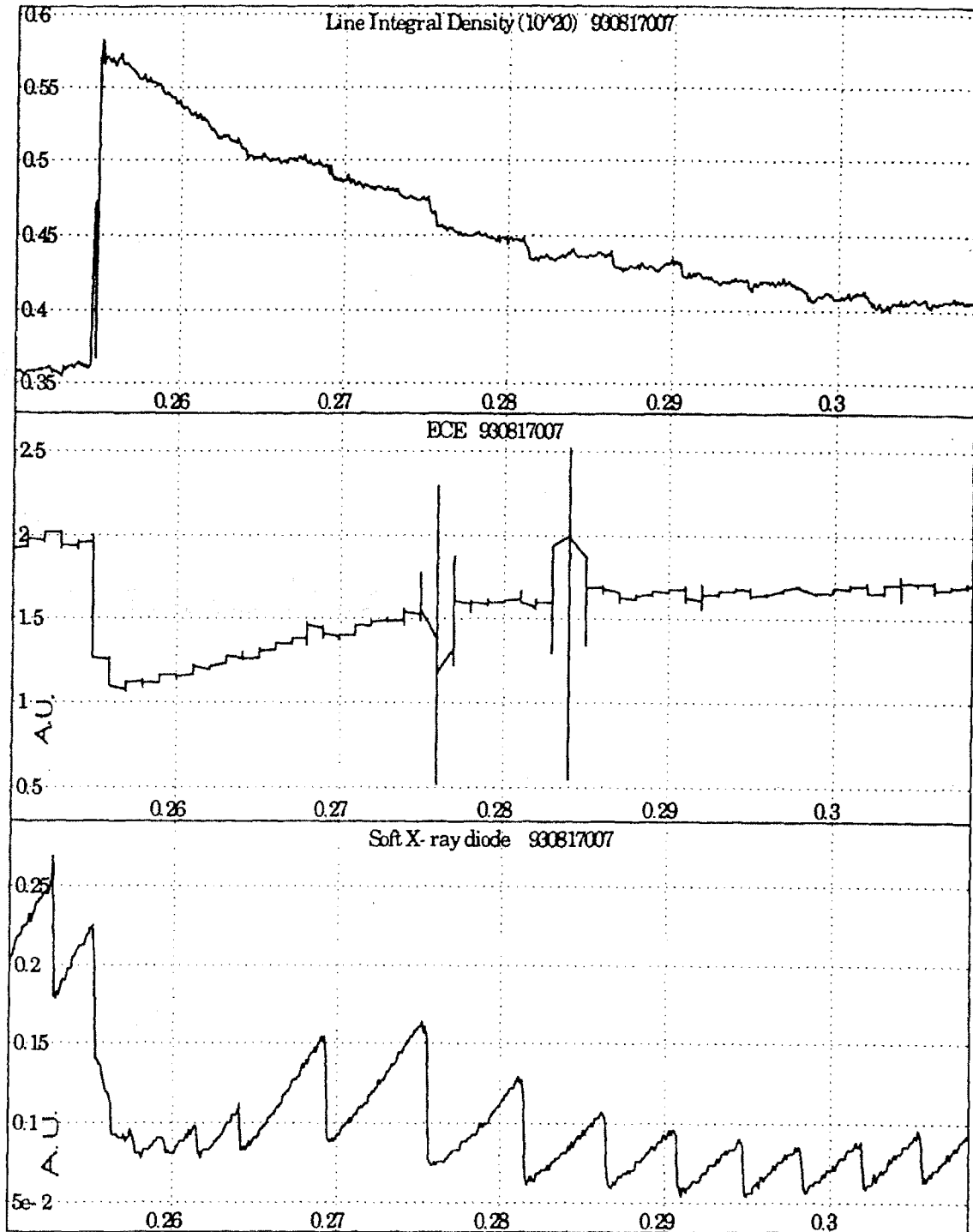Fig. 6.2.1: Scope of shot 930817007.

Fig. 6.2.2 : Expanded time history of shot 930817007 showing central line
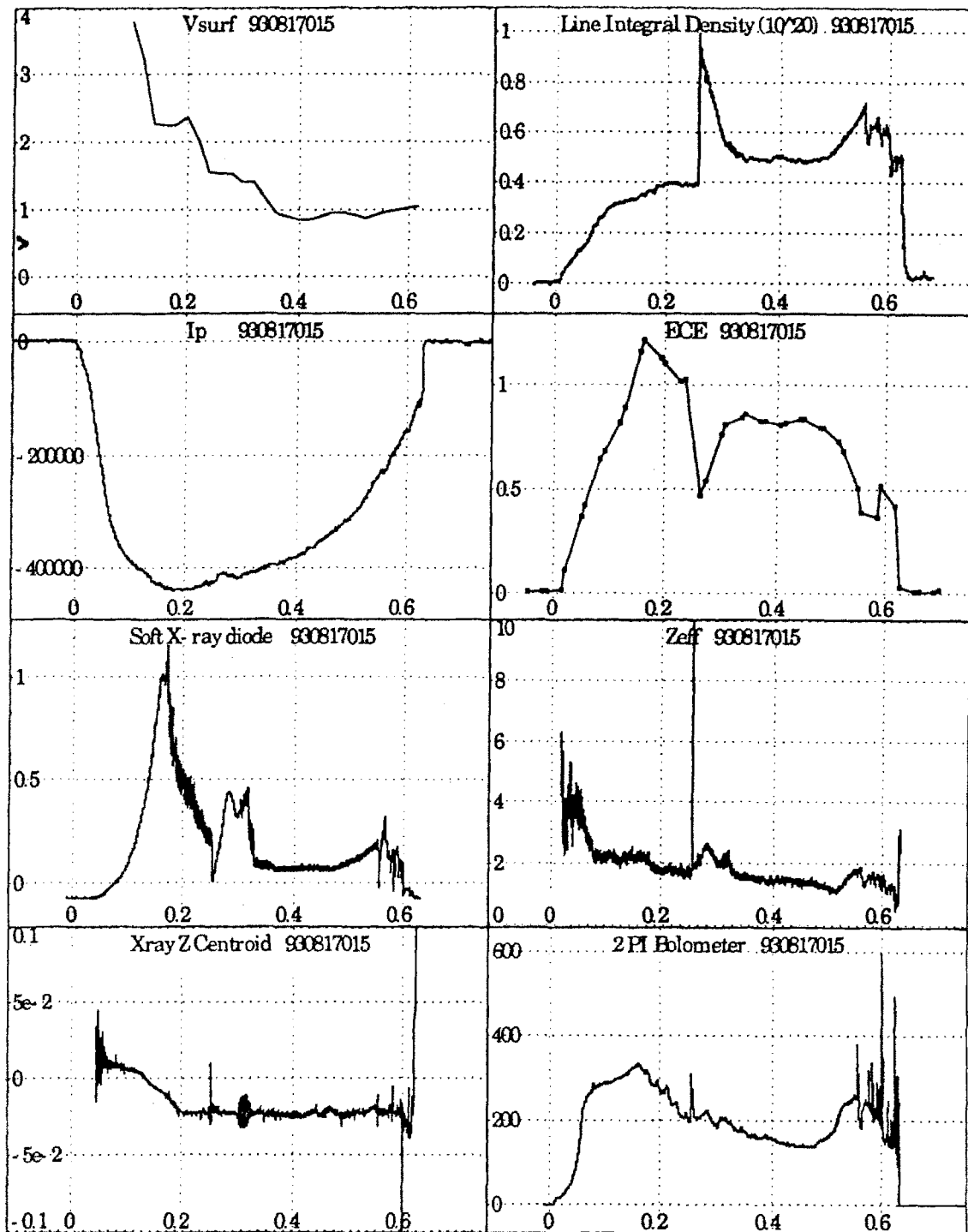integral density, ECE emission, and soft X-ray emission.
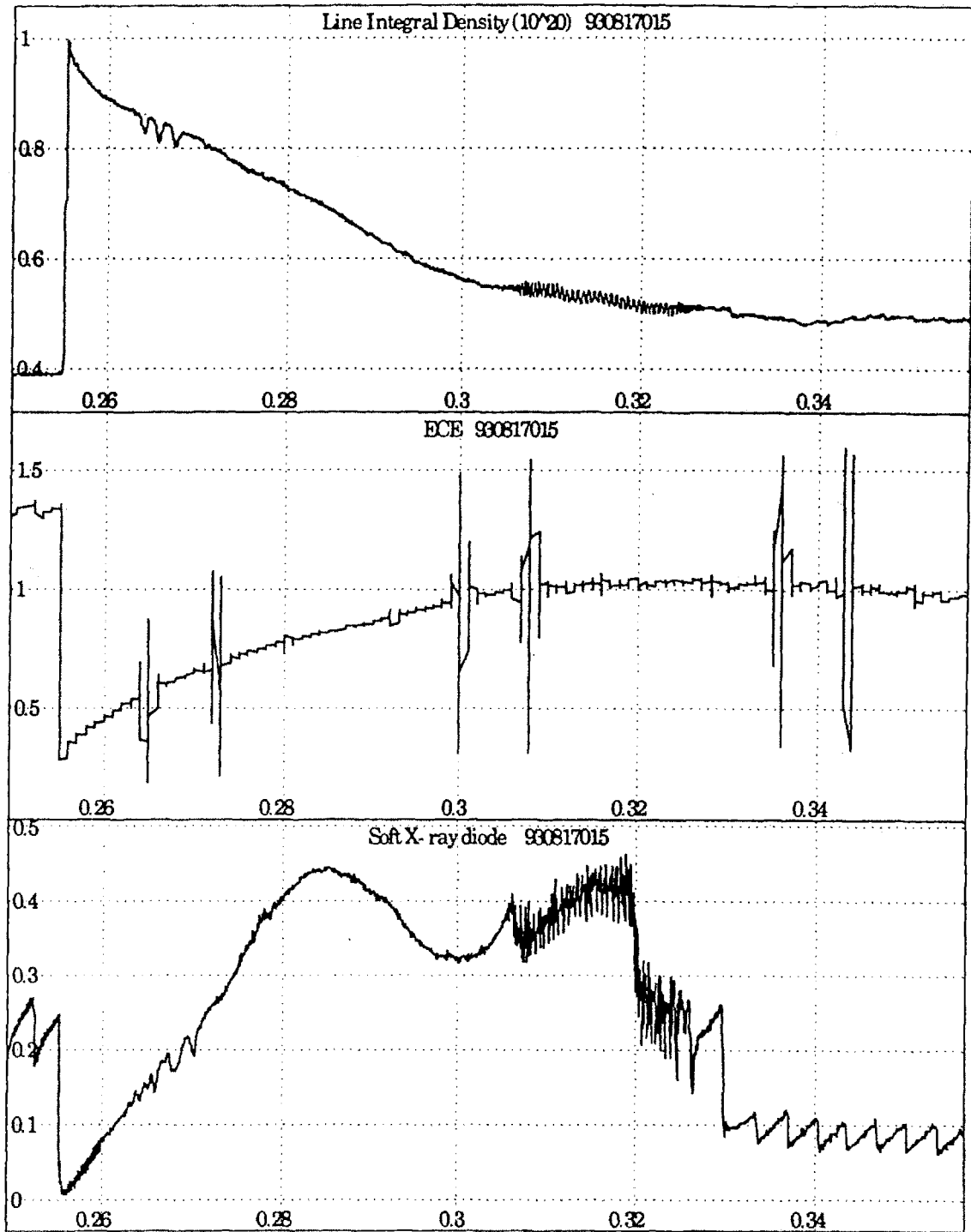
152

Fig. 6.2.3: Scope of shot 930817015.

153

Fig. 6.2.4 : Expanded time history of shot 930817015 showing central line
integral density, ECE emission, and soft X-ray emission.

154

Figure 6.2.7 shows the time evolution of the peak density, particle inventory, peaking factor and volume averaged density for shot # 930817007. The data shows an initial and rapid peak density rise of about 50% , from 1.0×10^{20} to $1.5 \times 10^{20} /m^3$. The volume averaged density exponentially decays to a value approximately 10% higher than the pre-injection valve with a characteristic decay time of 30 milliseconds. Figure 6.2.4 (top) and 6.2.8 show the central line integral density history and density parameters for shot # 930817015. This shot was similar to -007 in terms of background plasma conditions but in this case a larger pellet size was used, and some differences in the density evolution are apparent. Penetration was 11 cm for the larger pellet, or 48% of the 23 cm minor radius. The greater depth of penetration is a natural result of the larger pellets increased lifetime in the plasma. Peak density prior to injection is $1.0 \times 10^{20} /m^3$ and the final density is $2.6 \times 10^{20} / m^3$ for a peak density rise of over 160%. The characteristic decay time is again approximately 30 milliseconds but in this case the volume averaged density equilibrates to a value 25% greater than the pre-injection value. The data from comparisons such as these suggest that for identical background plasmas (with the same current), larger pellets deposit more fuel in the plasma. This is probably the result of the greater penetration depth for the larger pellets.

A number of pellets were injected into discharges with plasma currents of up to 800 kilo amps at 5.2 tesla. Figures 6.2.5 for shows the general parameters of shot # 931014024. In this shot, two deuterium pellets with sizes of $.9 \times 10^{20} /m^3$ and $1.6 \times 10^{20} /m^3$ were injected at .6 and .675 seconds into the discharge. Figures 6.2.6 (top) and 6.2.9 depict line integral density history and the average density, peak density, particle inventory and density profile as a function of time for the discharge. The first pellet raises the peak density 30% from 1.3×10^{20} to $1.7 \times 10^{20} /m^3$ and the second pellet raises it from 1.6×10^{20} to $2.7 \times 10^{20} /m^3$ for a 68% increase in peak density.

A comparison of the total particle inventory before and after injection indicates that the fraction of retained pellet mass appears to increase with pellet size. For shot #930817007 a pellet of $.5 \times 10^{20}$ was employed and for this case 60 % of the mass is retained. This is significantly less than the 83 % retained in shot # 930817015 where a larger pellet size of $.9 \times 10^{20}$ was used. This behavior was also observed in shot # 931014024 where 35 % of the smaller pellet's mass is retained compared to 70 % of the larger size. The increase in the mass retention is probably correlated to the increased penetration depth observed for the larger pellets.
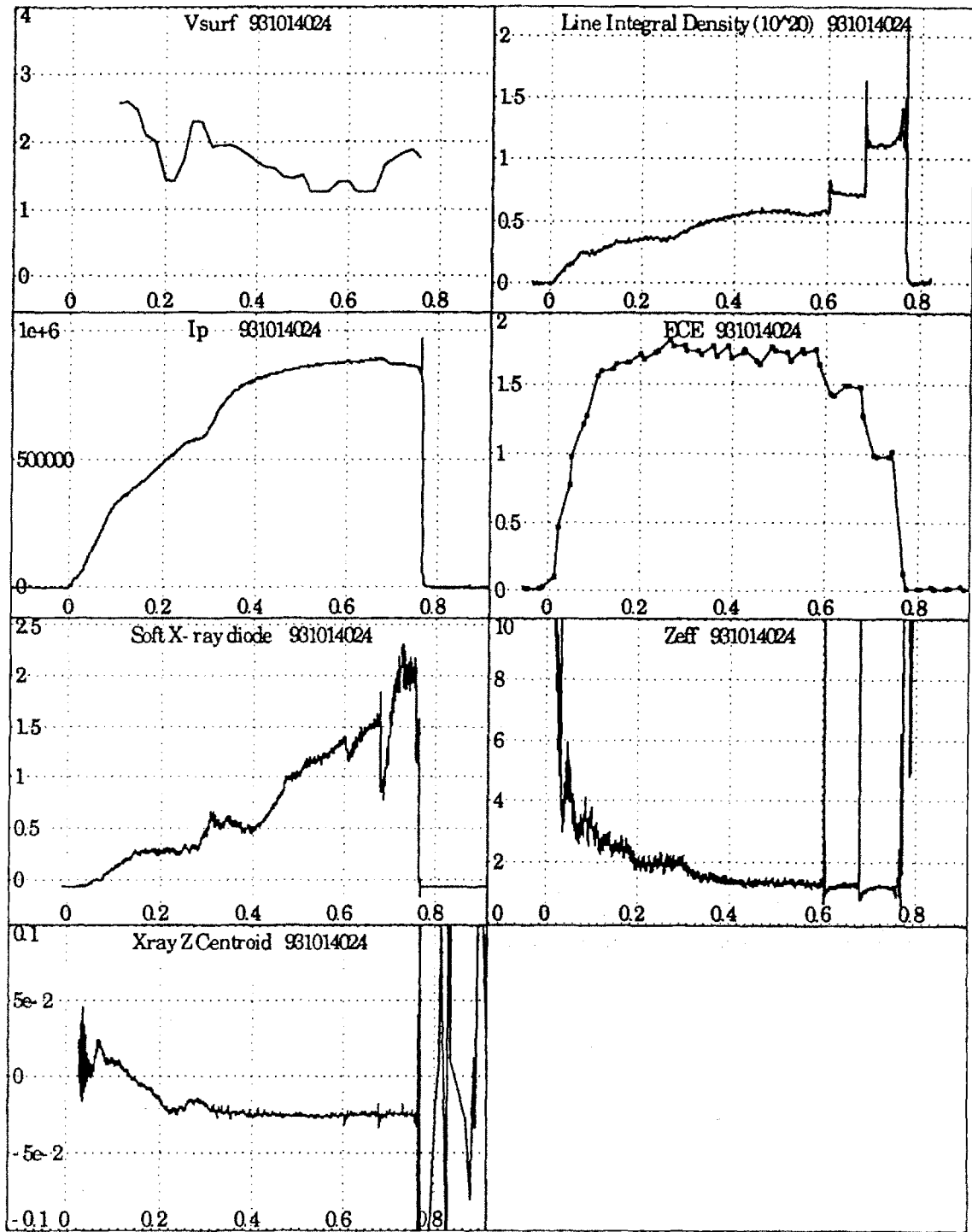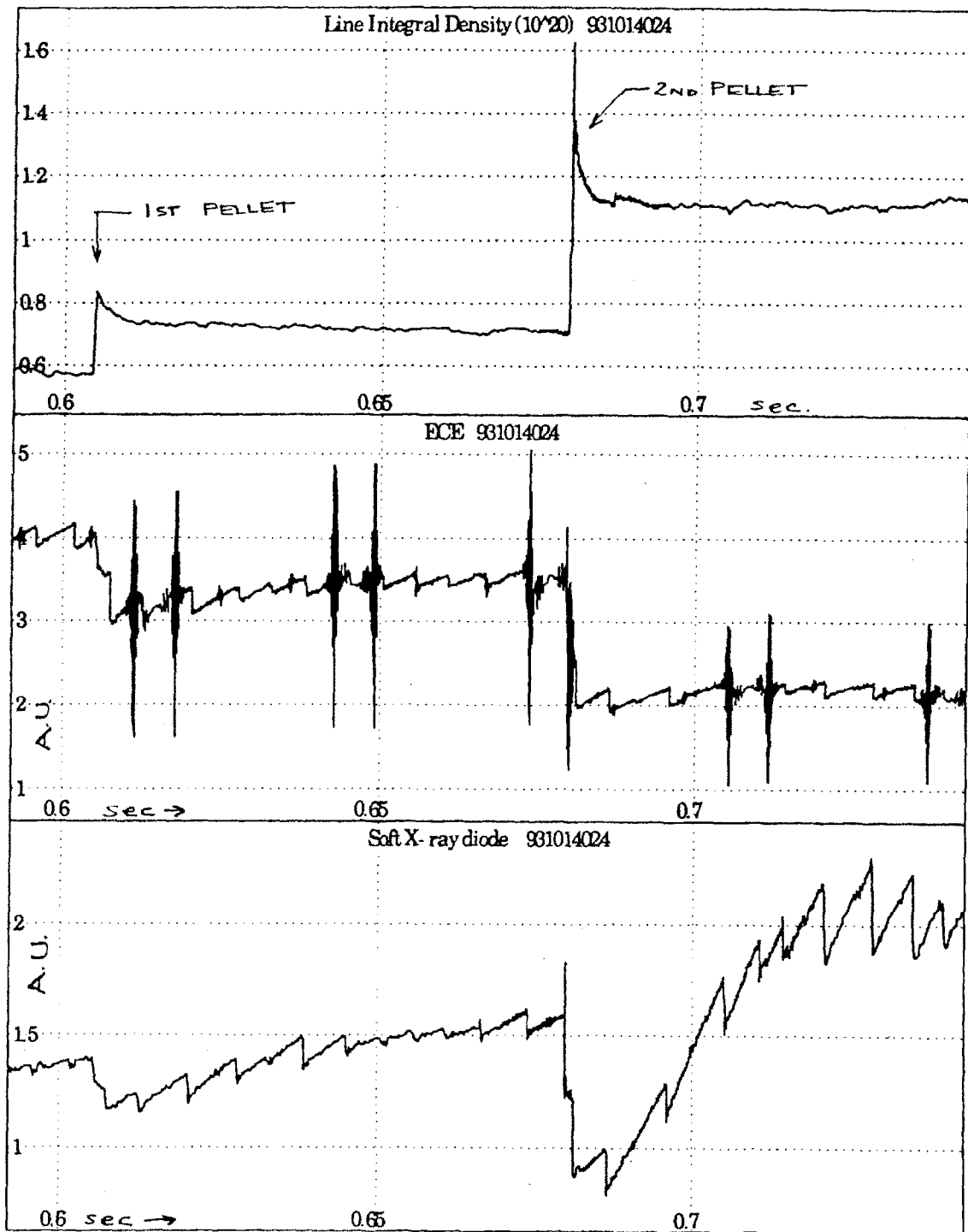
Fig. 6.2.5: Scope of shot 931014024.

Fig. 6.2.6 : Expanded time history of shot 931014024 showing central line integral density, ECE emission, and soft X-ray emission.
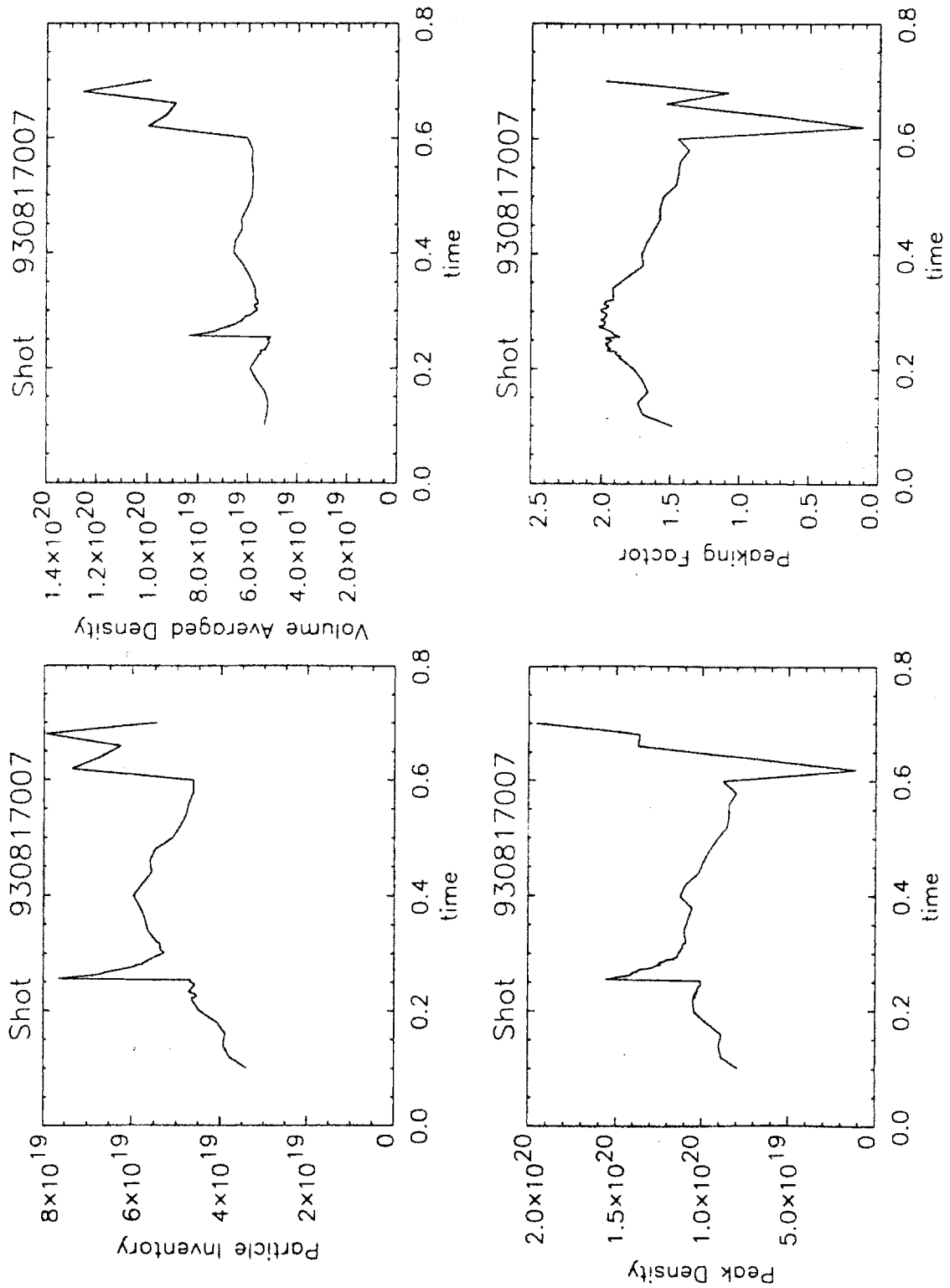
Fig. 6.2.7: Density parameters for shot 930817007 including particle inventory, volume averaged density, peak density, and peaking factor.
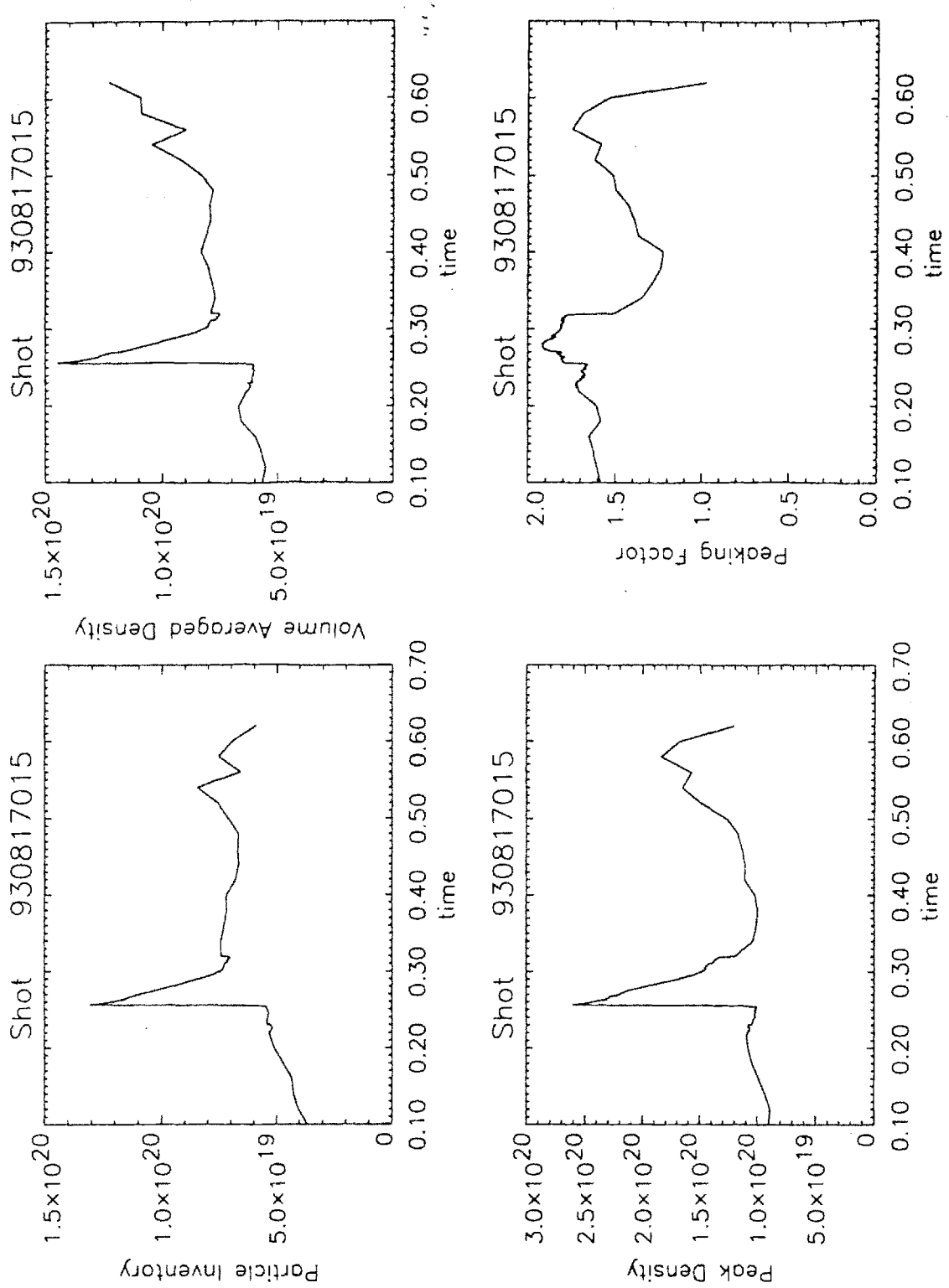
Fig. 6.2.8: Density parameters for shot 930817015 including particle inventory, volume averaged density, peak density, and peaking factor.
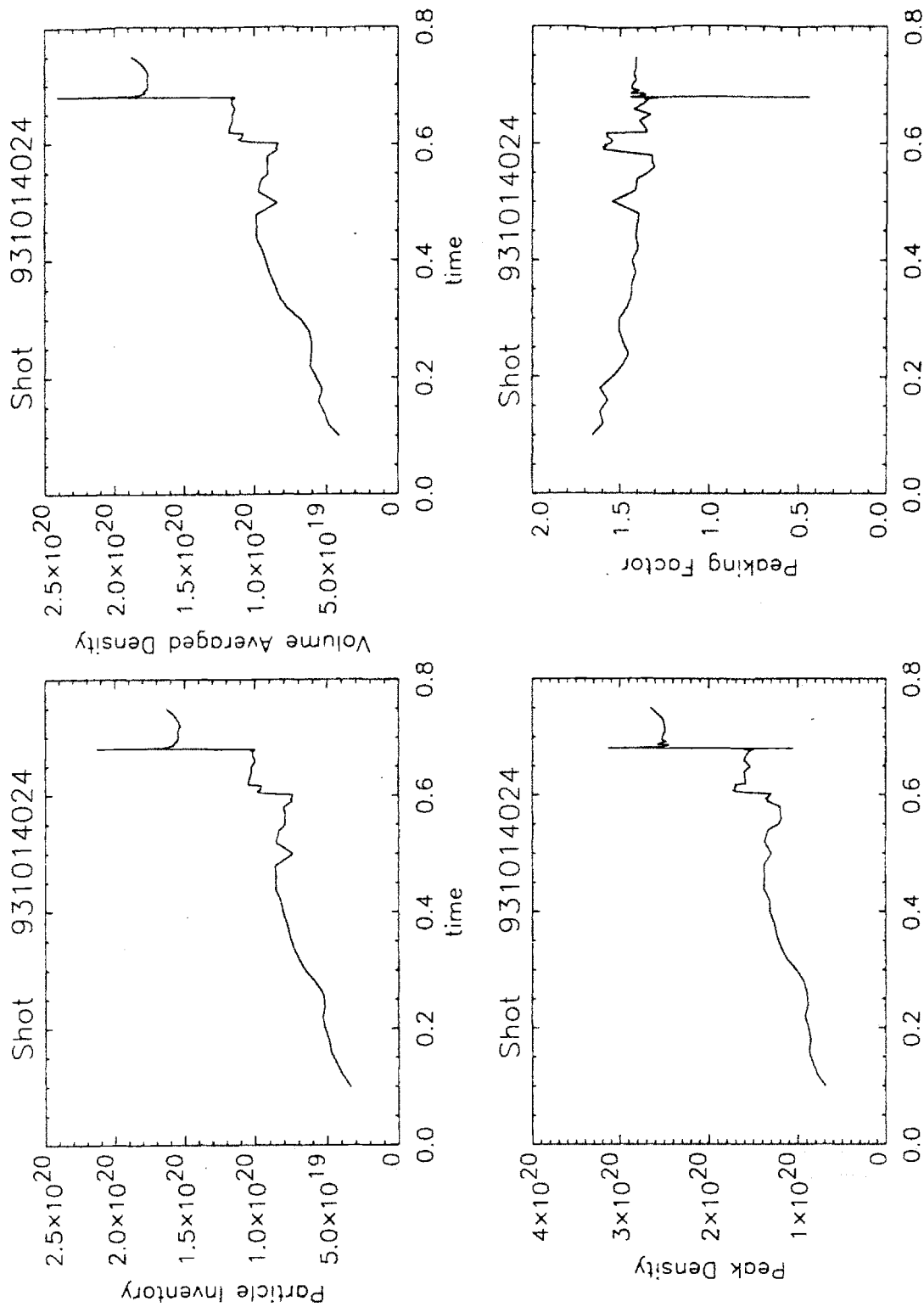
Fig. 6.2.9: Density parameters for shot 931014024 including particle inventory, volume averaged density, peak density, and peaking factor.

For the first pellet, injection velocity was measured to be 1024 m/sec with a penetration depth of 8 cm of the 21 cm minor radius. The 38 % penetration is significantly smaller than the 48% observed for the same size pellet into the 400 k amp plasma (shot # 930817015). The difference is primarily due to increased ablation at the higher electron temperature (1.5 Kev vs. keV) of the 800 K amp discharge. The velocity of the second pellet was measured to be 1120 m/sec with a 15.5 cm penetration depth to 74 % of the minor radius. The great depth of penetration for this case is the result of both the increased pellet size and the reduced electron temperatures following the first pellet. These observations were seen for all double pellet shots.

Multiple pellets have been used to nearly triple the background density. Two pellets injected into shot #931014012 resulted in a peak density of over 9×10^{20} /m^3, the highest achieved thus far on Alcator C-Mod. The density profile time evolution for this discharge may be seen figure 6.2.12.

6.2.2 Temperature Profiles

Electron temperature profile measurements are made by electron cyclotron emission (ECE) in the second harmonic by Michelson interferometer. Time resolution for this instrument is variable but averages about 15 msec. Spatial resolution is approximately 2.5 cm. Ion temperature measurements may be inferred from the Doppler broadening of argon impurity lines and for deuterium plasmas by neutron emission.

Following injection, electron and ion temperatures are seen to drop sharply. ECE temperature measurements are derived from ECE interferograms. Because each interferogram is generated over one cycle of Michelson mirror motion, the temperature sampling rate may be no higher than the mirror linear motion frequency. The instrument therefore cannot follow the rapid temperature drop immediately after injection. It can however record the total radiated power for wavelengths greater than about .1 mm at a sampling rate of up to 200 kHz.. The power output for wavelengths above .1 mm is dominated by the ECE emission integrated over all harmonics which does have a strong temperature dependence. The rapid drop in the ECE power emission following injection may be used to establish that the timescale of the temperature drop is at least as fast as
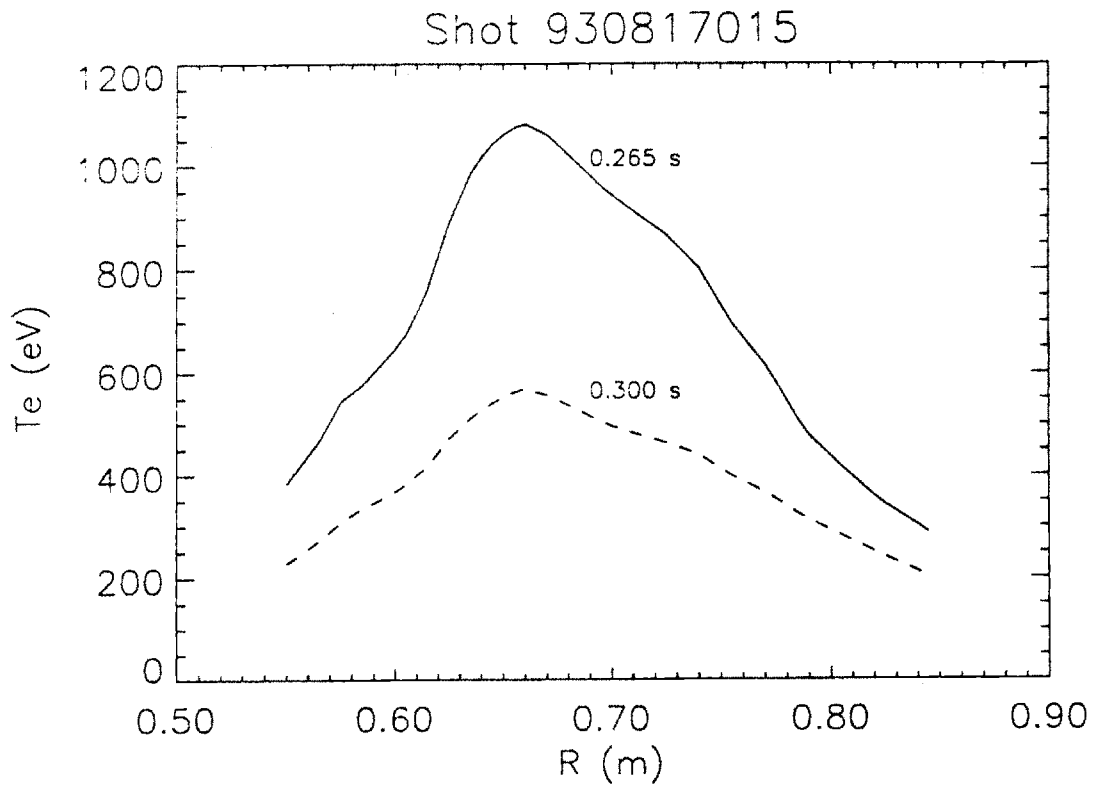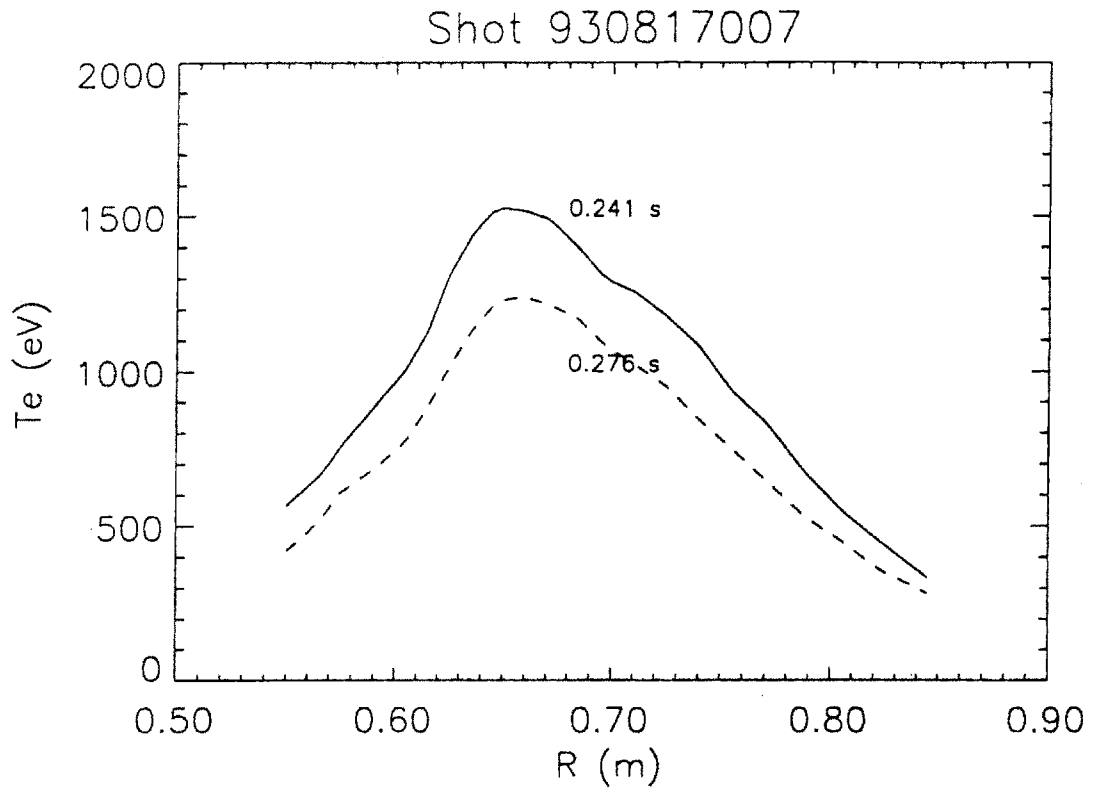
Fig. 6.2.10: ECE temperature profiles before and after injection for shots 930817007 and 930817015.
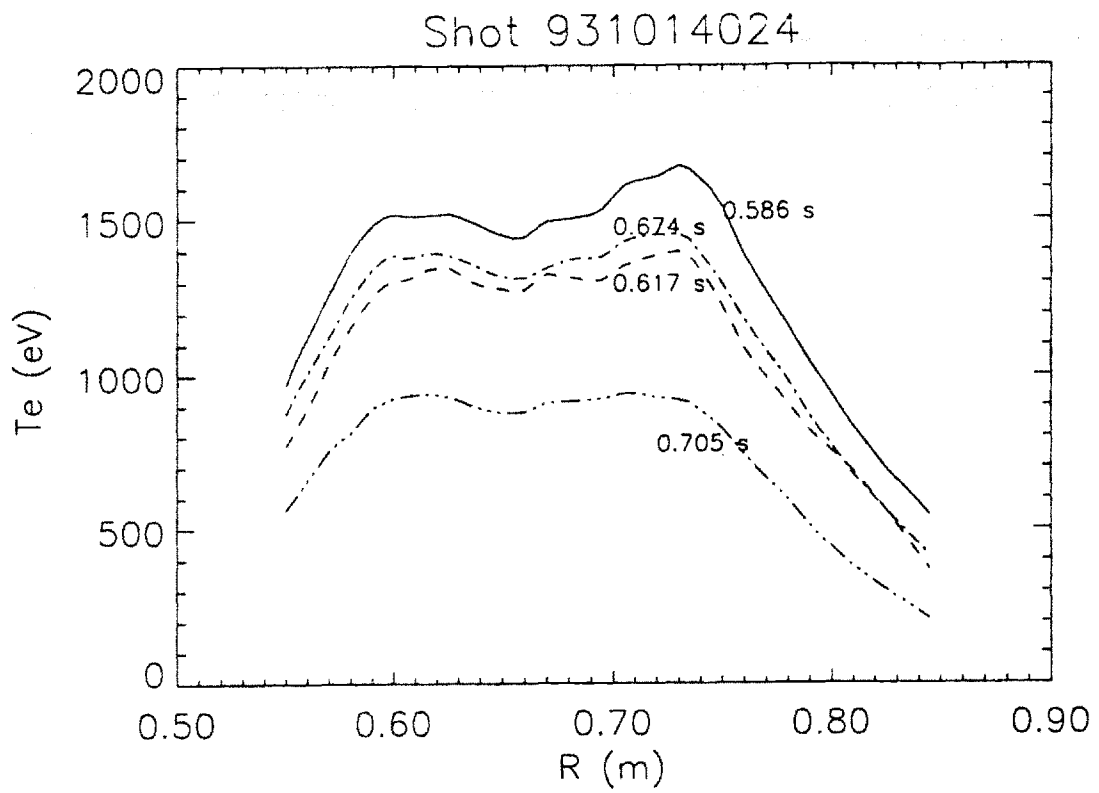
Shot 931014024

Fig. 6.2.11: ECE temperature profiles before and after injection for shot 931014024.

that of the density increase, i.e. on the pellet transit timescale. This statement would be true only if no region of the plasma viewed by the beamline optics exceeds the cutoff density.

Like the ECE emission, soft X-Ray emission is also electron temperature dependent and shows a precipitous drop immediately following injection. Figure 6.2.2 depicts the central line integral density, soft X-Ray emission and electron cyclotron emission (integrated over all harmonics) for shot # 930817007. The ECE and soft X-ray data indicate temperature recovery occurs over twenty to thirty msec, a timescale comparable to that for the density recovery.

Figures 6.2.10 , and 6.2.11 show the electron temperature profiles before and after injection for shots #930817007, #930817015 and #931014024 respectively. The data indicate that at least on the equilibrium timescale, injection does not radically change the "peakedness" or general shape of the temperature profile. The profiles for shot # 931014024 are centrally flatter than the other two. This is unrelated to injection and is instead the result of the higher current (800 kamps), flatter central q profile and the rapid energy transport interior to the q=1 surface resulting from "sawtooth" events. Peak densities after the second pellet are close to the cutoff frequency for second harmonic ECE emission so the accuracy of temperature data after .675 seconds are suspect.

Integration of the density and temperature profiles before and after injection indicates that the total kinetic energy of the plasma remains approximately unchanged during injection and that the fueling process is therefore adiabatic.
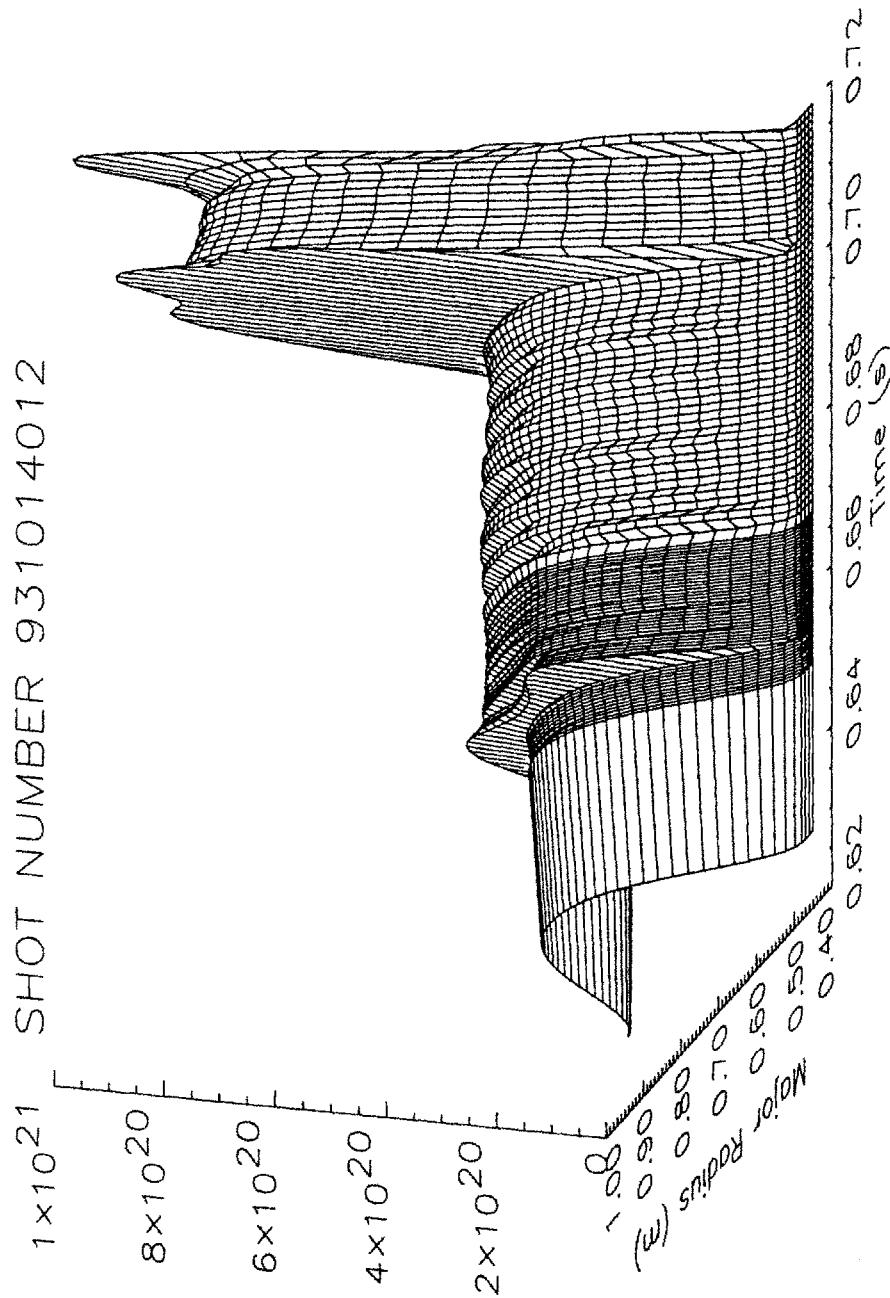
SHOT NUMBER 931014012

Fig. 6.3.12: Density profile evolution for shot 931014012 where two pellets were injected .65 and .70 seconds into the discharge.

6.3   Pellet Transit Timescale Observations

6.3.1   Tracker data : General Observations and Results

Pellet tracker data were recorded for over forty pellets. The data indicates that for single pellet shots penetration is between 8 and 19 centimeters or from 36 to 86 percent of the plasma minor radius. For cases where two successive pellets are used, pellet penetration through the magnetic axis has been observed.

Examples of tracker data are shown in figures 6.3.1-4. For the discharge shown,   the plasma current was just over 420 kiloamps with a pre-injection plasma central electron temperature of 1 keV and a density of $1X\ 10^{20}$ / m^3. Pellet size was $.9$ x 10^{20} atoms with an injection velocity of just over one kilometer per second.

Figure 6.3.1 (top and bottom) depicts the reconstructed trajectory in the R Z and R Φ planes.   Figure 6.3.2 (bottom) shows the radial location of the H_α emitting centroid as a function of time. For the discharge shown, the plasma outer boundary is at R=93 cm and the pellet travels five centimeters before H_α emission reaches two percent of the maximum.   The two percent discriminator level was selected as the minimum level necessary to exclude non-injection events from the trajectory reconstructions. The dotted line of figure 6.3.2 (lower) indicates the extrapolated radial position in time as based on time of flight measurements made on the pellet in the injection line. Typically, pellets display a nearly constant velocity in R, closely following a vacuum ballistic trajectory. Towards the last ten to twenty percent of the path there is usually some reduction in radial velocity as the pellet mass is decreased. Deviations from the straight line path are not necessarily indicative of the actual pellet movement, but may be the result of fluctuations in the ablation cloud causing shifting in the location of the location of the light emitting centroid.

Figure 6.3.2 (top) depicts the vertical centroidal trajectory in time. The figure shows the path to be one centimeter below the midplane and fairly straight with typical

deflections of less than half a centimeter. The drop in negative Z direction is a feature occasionally seen and may be coincident with the streaming of the H_α cloud in the electron drift direction, a feature seen by ablation researchers on machines such as TFTR [26] and ASDEX.

Figure 6.3.3 (bottom) displays the trajectory in the azimuthal or R*Φ direction, which generally shows a deflection in the direction of the toroidal electron current. Pellet deflections in the direction current flow have often been observed on other tokamaks such as ASDEX [3] JET and TFTR [26]. Deflection velocities of up to 500 m/sec have been measured for pellets in Alcator C-Mod. The direction of deflection was seen to be reversed for shots taken after a change in the direction of toroidal current flow. The deflection is most likely due to a rocket effect caused by enhanced pellet ablation on the pellet side facing the electron current. Figure 6.3.3. (top) shows the minimum distance between the lines of sight from the two tracking cameras. As stated in chapter five this distance is a convenient indicator of the tracking accuracy. where problems with cabling or signal saturations have occurred, the inter-line spacing may grow to several centimeters. For most of the trajectories reconstructed however, this value was generally below half a centimeter, a value comparable to that measured during calibration. The close spacing of the lines both during calibration and during injection experiments is indicative that significant reflections are not present to cause problems for either case.

The H_α emission intensity as a function of time and major radius are given in figures 6.3.4 top and bottom. The emission profile indicates that for this particular discharge a drop in intensity occurs at a major radius of 77.5 centimeters. The decrease in emission may correlate to the location of rational flux surfaces as has been suggested Mansfield and others [25] [42] . Because these features are seen only occasionally, no definitive statements may currently be made as to their correlation with rational flux surfaces.
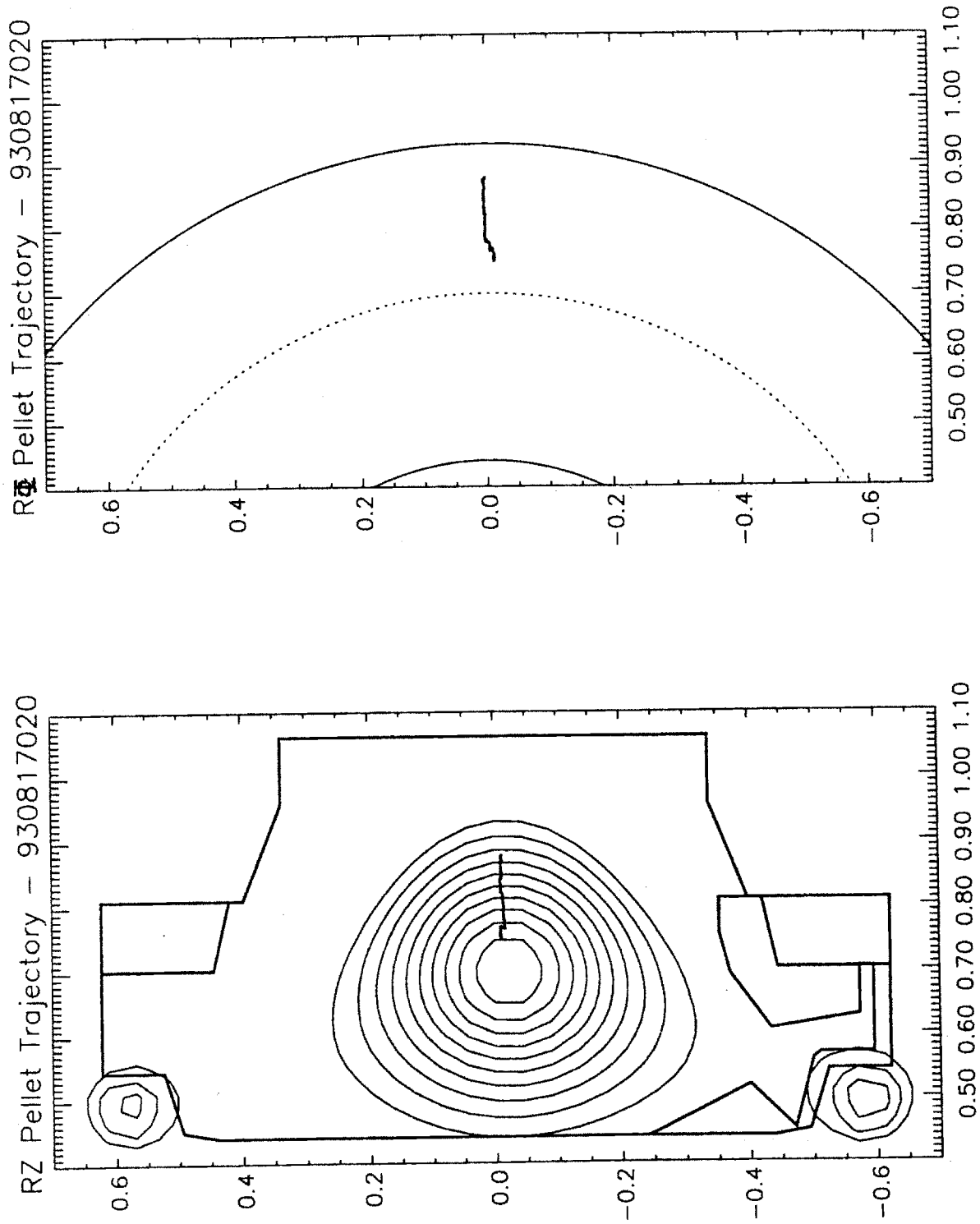
Fig. 6.3.1: The reconstructed pellet trajectory in the Rɸ (top) and RZ (bottom) planes.
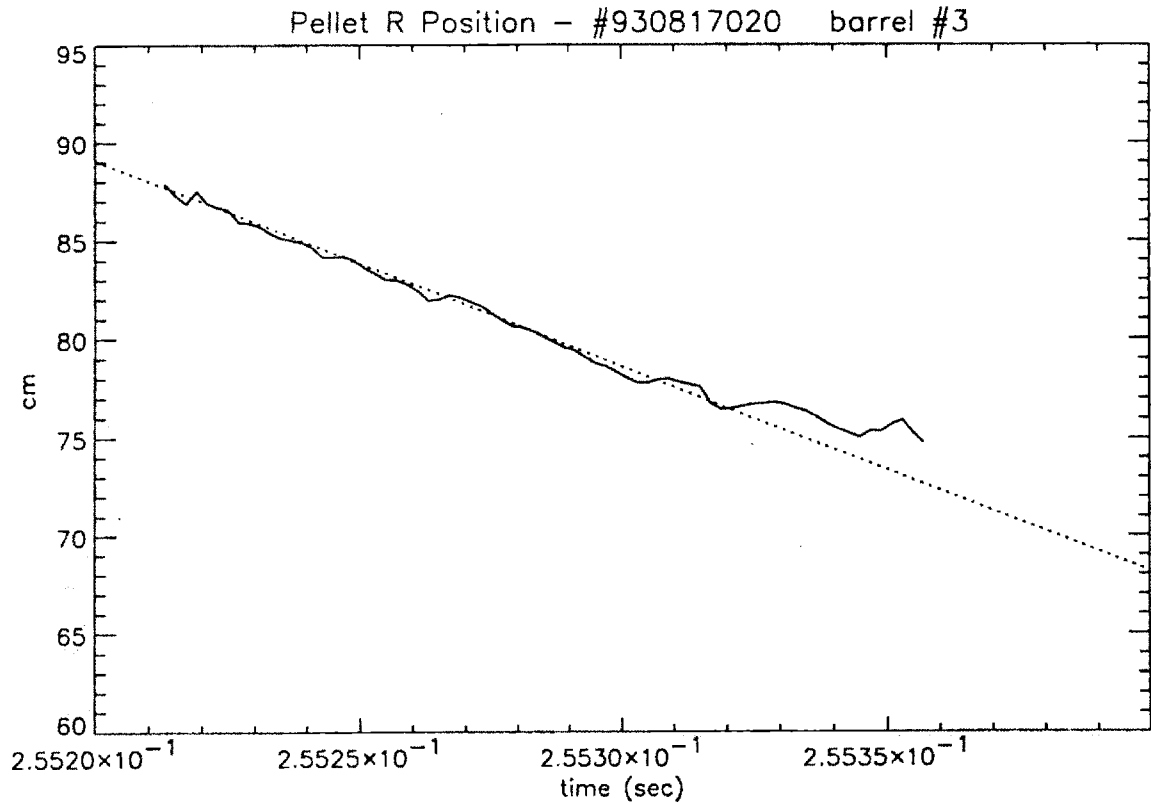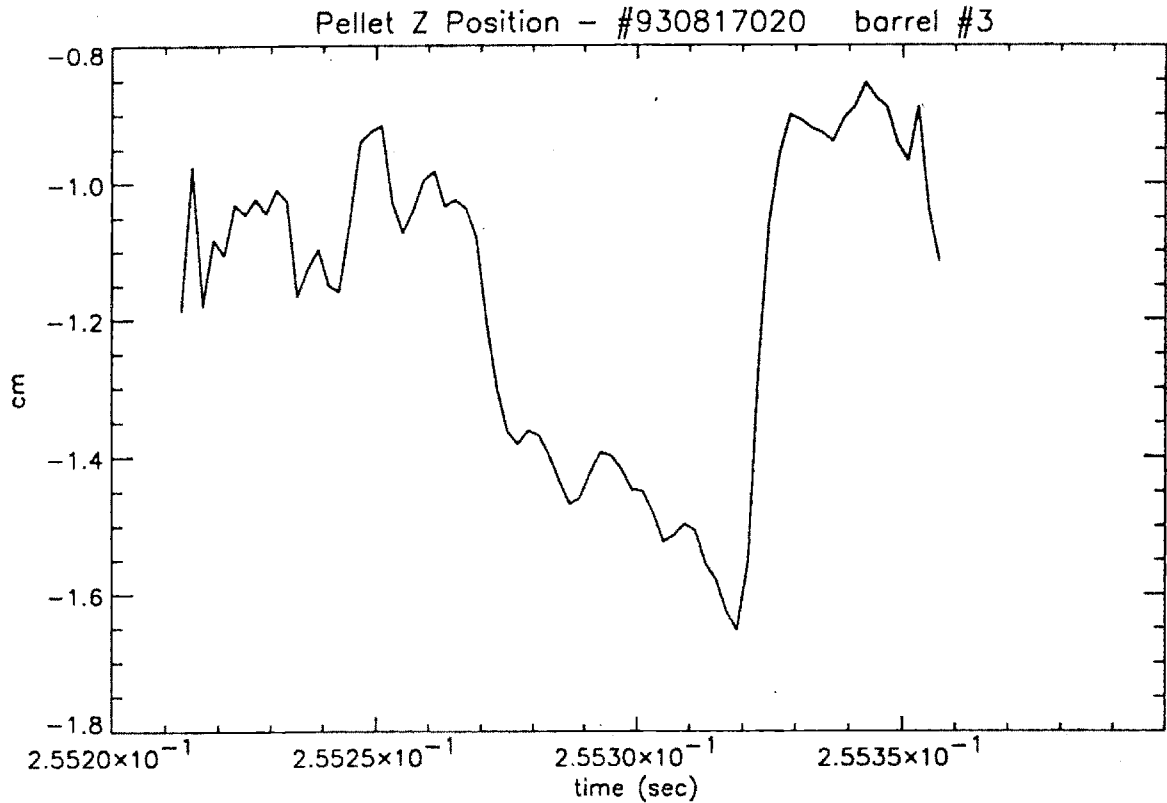
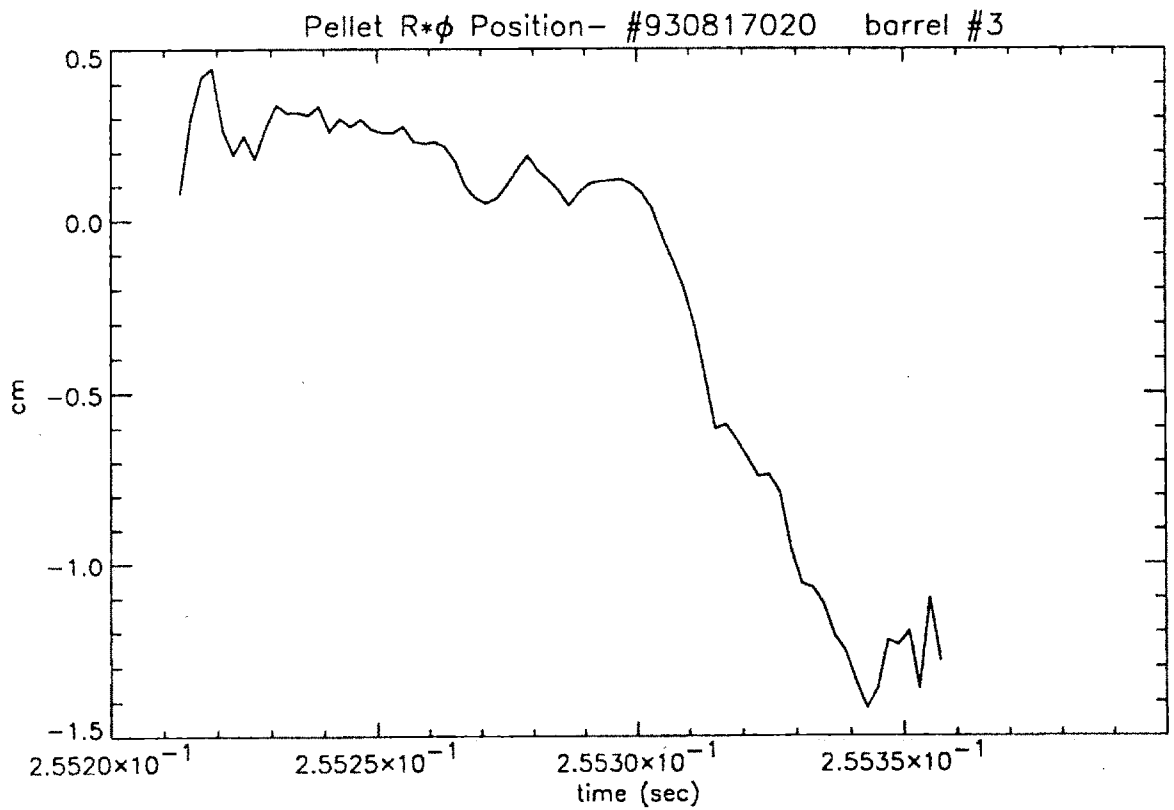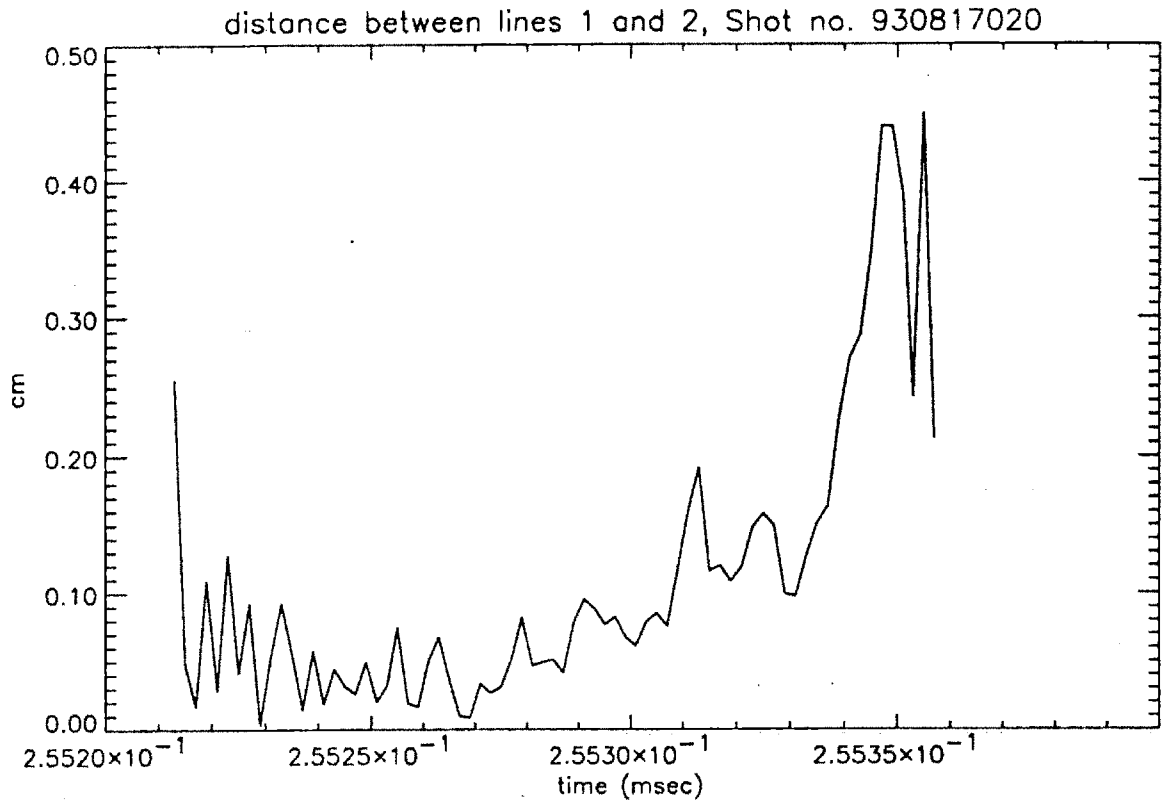Fig. 6.3.2: The trajectory in Z vs. time(top) and R vs. time (bottom).

169

Fig. 6.3.3: The distance between the camera lines of sight (top) and the trajectory in the R Φ or azimuthal direction (bottom).
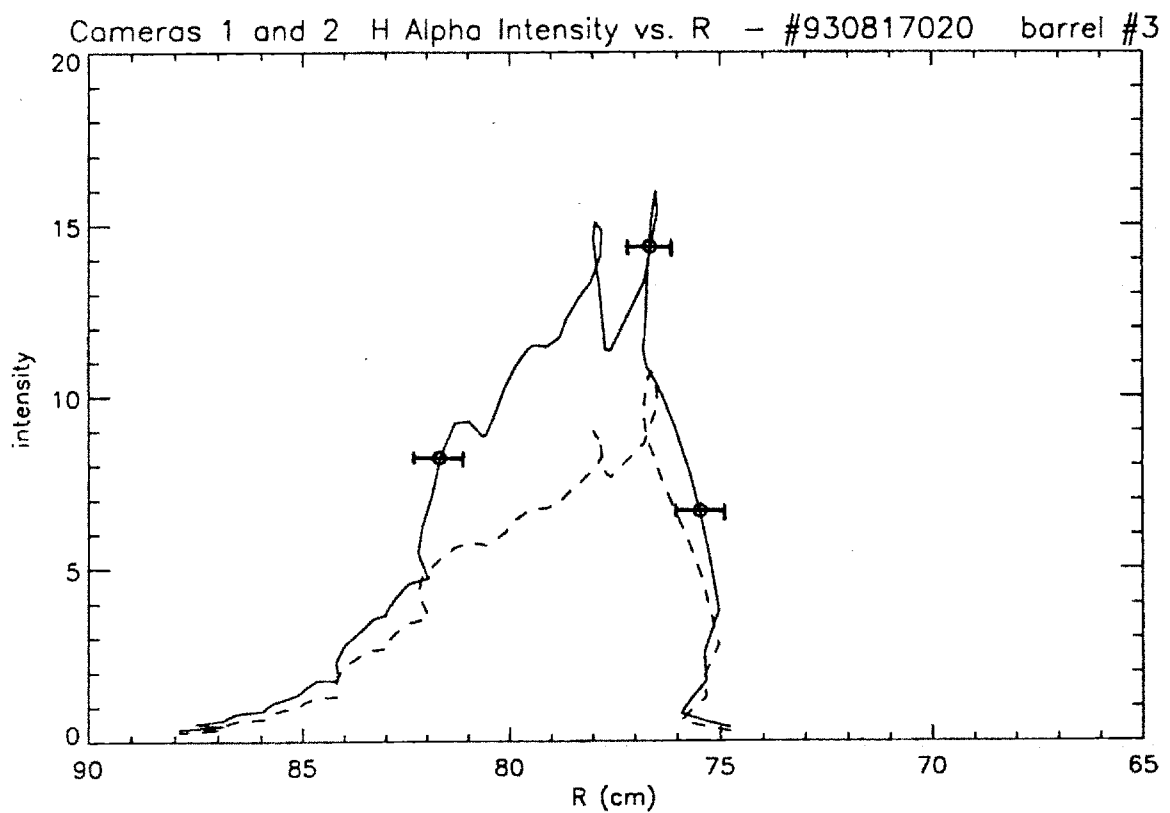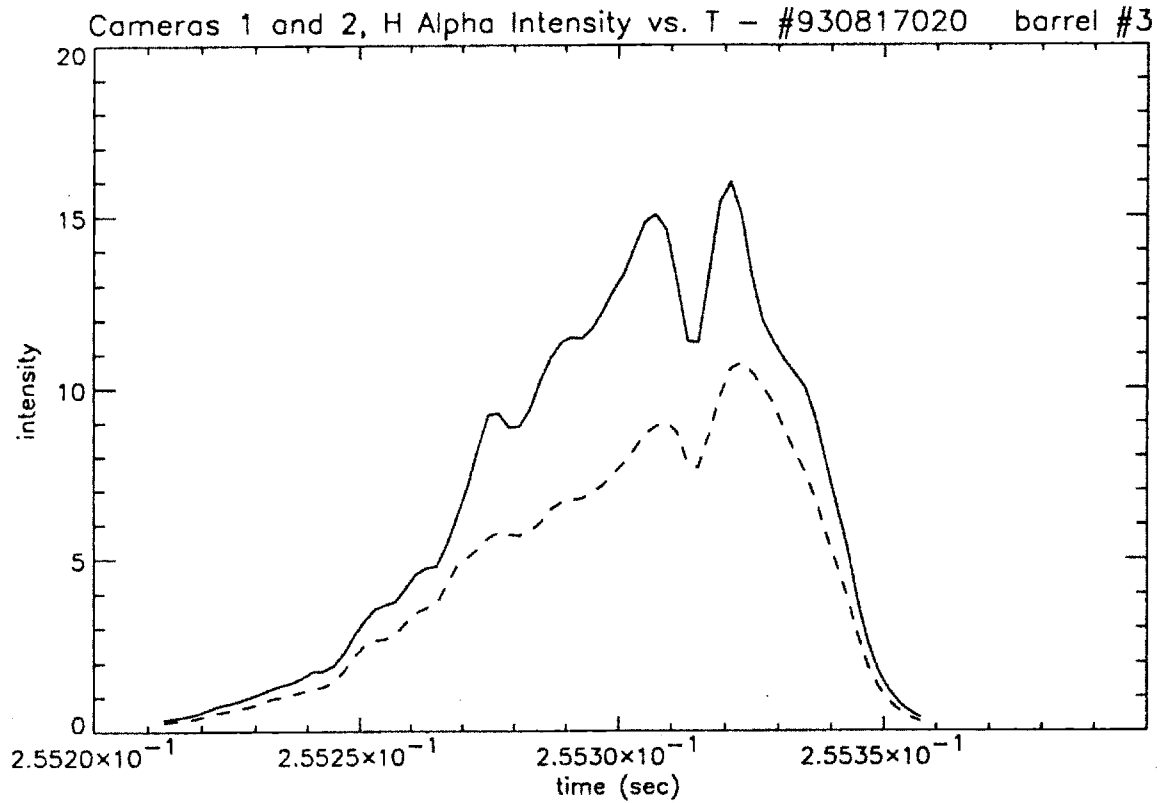
Fig. 6.3.4: H_α emission intensity as a function of time (top) and major radius (bottom).

6.3.2 Pellet Ablation Rate Measurements; A Comparison of Experimental Measurements with Theoretical Models.

The ablation source function is defined as the number of atoms ablated from the pellet per centimeter of path traversed radially. The function may be measured indirectly from H_α line emission if the assumption is made that a fixed number of H_α photons are emitted per ionization and therefore that the emission intensity is directly proportional to the ablation rate. This assumption has been frequently used by ablation researchers [42].

A comparison of experimentally observed ablation rates with those calculated using ablation models is necessary to establish both the predictive power and the validity of pellet ablation codes. These codes may then be applied with a greater degree of confidence and understanding in predicting ablation rates and pellet penetration depth in tokamak designs such as TPX and ITER. Research by Houlberg, Milora and others indicates that pellet penetration to 100% of the plasma major radius in Tokamaks the like ITER may require pellet velocity in the range of 10 Km/sec [6]. These velocities are not achievable through any extrapolation of existing injector technology. Fortunately, due to enhanced inwards particle diffusion, 100% penetration to the plasma core is not necessary to fuel the plasma and effective fueling has been observed in experiments where pellets do not penetrate to the plasma center [4]. The two necessary factors in determining the effectiveness for pellet fueling in future tokamak designs are a characterization of the fueling effectiveness with the fractional radius penetrated and a pellet ablation model capable of accurately predicting ablation profiles and penetration depth over a wide range of plasma parameters.

The FORTRAN code PELLET used to determine the neutral particle source function was developed in 1986 by Wayne Houlberg at ORNL [39]. The pellet ablation code determines the ablation rate based on the neutral shielding model developed by Parks, Turnbull and Foster [52], and later modified by Milora and Foster [53]. PELLET is particularly useful for exploring the physical assumptions of ablation in that four different variations of the model are available. The computed ablation rates for the four models (#0,#1,#2,#3) will be compared to results derived from the experimentally

172

measured H_α profiles to see if any observations can be made on the predictive power and validity of the different models.

Pellet Ablation Models

Before presenting results it is appropriate to outline the physical basis for the ablation models used in the code. All four models employ three separate resistive elements in determining the heat flow from the bulk plasma to the pellet surface. They are the neutral shield, the cold plasma shield, and self-limiting plasma response.

The Neutral Shield: The principle physical barrier to heat transfer to the pellet surface is the existence of an outwardly flowing, spherically symmetric, neutral gas cloud. The radius of the neutral gas cloud determines the energy attenuation of the incident electrons, hence the heat flux, to the pellet surface. With the heat flux known, an energy balance calculation is made at the pellet surface to determine the molecular sublimation rate. The sublimation rate, in turn, affects rate of neutral gas evolution and hence the radius the neutral shield. It is therefore clear that the solution for the sublimation rate must involve the simultaneous solution of the mass, momentum and energy equations as applied to the neutral cloud. The solution obtained for the uniform heating by electrons of a spherically symmetric neutral gas cloud is given by Milora [53]:

$$\dot{r}_p = \frac{-.625}{r_p n_s^m} \int_{r_p}^{r_o} n^o dl \left(q^o r_p \frac{(\gamma - 1)}{2} \right)^{1/3} \tag{6.3.1}$$

where r_p = the pellet radius, r_o is neutral gas cloud outer radius, n_s^m is the solid molecular density, n^o the neutral density, and γ the ratio of gas specific heats for hydrogen gas (7/5). q^o is the net energy flux to the cloud normalized to the line integrated density of the neutral cloud i.e.. [39]:

$$q^o \equiv \frac{(Q^o - Q^p)}{2 A_p m_p \int_{r_p}^{r_o} n_o dl} \tag{6.3.2}$$

173

where A_p and m_p are the pellet area and mass. Q^o is the neutral cloud average incident energy flux and Q^p is the average energy flux incident on the pellet surface. An energy balance applied to the pellet surface may be used to relate r_p with Q^p [39]:

$$\left(\frac{\lambda_s^m}{2}\right)\dot{N} = -\lambda_s^m n_s^m (4\pi r_p^2)\dot{r}_p = 4\pi r_p^2 Q^p \qquad (6.3.3)$$

equations 6.3.3 and 6.3.1 may be combined to eliminate $\dot{r}_p$, leaving a single equation involving Qp, Qo and $\int_{r_p}^{r_o} n^o dl$. Qo is determined from the external plasma properties. Qp, the averaged energy flux at the pellet surface, is determined from the energy flux incident at the cloud outer radius, Q_o, by integrating the stopping energy equation from r_o to r_p for the species in question :

$$\frac{dE_s}{dl} = -n\sigma_e^o \qquad (6.3.4)$$

for electrons above about 100 eV the stopping cross section in molecular hydrogen is :

$$\sigma_e^o = \frac{1}{a_{e1} + a_{e2}E_e} \qquad (6.3.5)$$

where $a_{e1} = 4.7 x 10^{21}$ and $a_{e2} = 8.0 x 10^{21}$ $atom/m^2 Kev^2$ integrating 6.3.4 with the boundary conditions $E_e(r_o) = E_e^o$ and $E_e(r_p) = E_e^p$ and solving for E_e^p gives [39] :

$$E_e^p = -\frac{a_{e1}}{a_{e2}} + \sqrt{\left(\frac{a_{e1}}{a_{e2}} + E_e^o\right)^2 - \frac{2}{a_{e2}}\int_{r_p}^{r_o} n^o dl} \qquad (6.3.6)$$

the averaged energy flux at the pellet surface is then:

174

$$Q_e^p = \frac{E_e^p}{E_e^o} Q_e^o \qquad (6.3.7)$$

The incident electron energy is assumed to be monoenergetic as in a beam and a maxwellian energy distribution would be modeled by summing the energy flux contributions from electrons separated into discrete energy groups. The energy contribution from fast ions and alphas are considered similarly such that :

$$Q^p = Q_e + Q_i + Q_\alpha \qquad (6.3.8)$$

for Ohmic Alcator plasmas the electron contribution clearly dominates due to the electrons' greater mobility and the lack of higher energy ions from either auxiliary heating or fast alphas from fusion reactions.

Equations 6.3.1 and 6.3.5 form a closed set of equations which may be directly solved. The ionization radius is not computed explicitly, but for a given pellet radius r_p, the value of the line integral density may be solved and therefore the ablation rate.

The Cold Plasma Shield: After the ablated hydrogen becomes ionized it flows along the magnetic field lines at the plasma streaming velocity v in both directions away from the pellet. This cold plasma may have a background density as much as 100 times higher than that of the ambient plasma [6]. On C-Mod the cold plasma flux tube is sometimes visible in video images of the plasma. The shielding effect of this cold, dense plasma is important for electrons where the gyro orbit is smaller than the cold plasma tube diameter. The electrons from the ambient plasma therefore pass through a cold, dense plasma shield. Energy attenuation through this shield significantly reduces the heat flow to the outer surface of the neutral cloud. The atomic ablation rate $\dot{N}$ may be related to the plasma density in the tube n^+ and the plasma streaming velocity v. The plasma streaming velocity is given by the ion sound speed for the cold ablatant plasma where Te' ≈ 10 eV [4] [39] . The speed is then approximated by :

$$v = \left(\frac{kT_e{}'}{m_i} \right)^{1/2}$$

Under steady state conditions the atomic ablation rate is then given by [39]:

175

$$\dot{N} = n^{+}v\left(2\pi r_{o}^{2}\right)$$

(6.3.9)

assuming a constant cross section for the tube, and integrating over time and distance, gives an equation for the integrated density of the tube [39].

$$\int_{r_{o}}^{\infty} n^{+}dl = \frac{\dot{N}}{\pi r_{o}v_{p}}$$

(6.3.10)

where v_{p} is the pellet velocity and the time of integration is taken as the time the pellet neutral cloud takes to cross a flux surface [39]:

$$\tau_{p} = \frac{2r_{o}}{v_{p}}$$

(6.3.11)

Energy attenuation in the cold plasma is determined from the coulomb scattering cross section [39]:

$$\sigma_{ab} = 1x10^{-6}\left(\frac{m_{a}}{m_{b}}\right)\frac{2\pi e^{2}Z_{a}^{2}Z_{b}^{2}\lambda_{ab}}{E_{a}(4\pi\varepsilon_{o})^{2}}$$

(6.3.12)

In equation 6.3.12 λ_{ab} is the coulomb logarithm. The subscripts A and B refer to either the electrons or ions in the cold plasma. The mass dependence shows that electron-electron collisions are primarily responsible for dissipating energy and a λ_{ee} of 10 is used. Integrating the energy stopping equation 6.3.4 through the cold plasma tube from the cloud outer radius (r_{o}) to infinity gives and expression for the electron energy at the ionization radius in terms of the bulk plasma electron energy Ee [39] i.e.:

$$E_{e}^{o^{2}} = E_{e}^{2} - 2E_{e}\sigma_{ee}\int_{r_{o}}^{\infty} n^{+}dl$$

(6.3.13)

176

The electron energy flux at the neutral cloud Q_e^o is then:

$$Q_e^o = \frac{Q_e}{2} \frac{E_e^o}{E_e}$$

(6.3.14)

where Qe is the background electron energy flux given by :

$$Q_e = \frac{n_e T_e}{2} \left(\frac{8kT_e}{\pi m_e} \right)^{1/2}$$

(6.3.15)

The energy flux at the neutral cloud outer radius may be computed from 6.3.8 and 6.3.11-13 based on the bulk plasma properties and r_o. Unfortunately, the cloud outer radius, r_o is unknown. The simple approach of determining the outer radius based on the energy flux needed to ionize the ablatant is given by :

$$\dot{N} E_{ion} = Q_e^o 4\pi r_o^2$$

(6.3.16)

This method was found to produce the non-physical result where r_o collapsed to zero. Three alternative methods are used in Houlberg's code to determine r_o. The first is to assume a fixed plasma shield fraction F, i.e.:

$$F = \frac{\int_{r_o}^{\infty} n^+ dl}{\int_{r_p}^{r_o} n^o dl}$$

(6.3.17)

177

The second is to assume a fixed neutral shield thickness, :

$$r_o = r_p + \Delta_o \qquad (6.3.18)$$

and the third is to assume a fixed ionization radius:

$$r_o = cr_p \qquad (6.3.19)$$

In equation 6.3.19, c has been empirically determined by Kaufmann and others to be approximately 2.5.

Self Limiting Plasma Response: The time required for the pellet to pass a flux surface τ_p is given by $2r_o / v_p$ (eq. 6.3.11) and is sufficiently long that the electron energy distribution may be significantly reduced from its initial state during the time the pellet takes to cross the surface. This effect is termed "self limiting". Two timescales may be compared to the flux surface transit time, τ_p . The first is the parallel electron-electron energy collision time τ_{ee}^E and the second is the parallel flow time τ_d. The parallel flow time may be thought of as the maximum time required for electrons on the ablation flux surface to interact with the neutral gas cloud.   These two quantities are given by:

$$\tau_{ee}^E \cong \frac{(4\pi\varepsilon_o)^2 m_e v_{te}^2}{8\pi e^4 \lambda_{ee} n_e}\left(\frac{v}{v_{te}}\right)^2 \qquad (6.3.20)$$

$$\tau_d \equiv \frac{8\pi^2 rr_o R}{2\pi r_o^2 v_{ll}} \qquad (6.3.21)$$

For monoenergetic electron groups, the parallel flow velocity is given by:

$$v_{ll} = \frac{v_e}{4}$$

In cases where the parallel flow time is shorter than the flux surface transit time, τ_p, the self limiting plasma response is appropriate. If the electron-electron energy collision time

is longer than the flux surface transit time, a collisionless plasma response is also valid. For the self-limiting plasma response and a collisionless plasma, the energy incident on the cold plasma shield is reduced by eq. 6.3.22:

$$Q_e^+ = Q_e \frac{\tau_d}{\tau_{po}} \left(1 - e^{-\tau_{po}/\tau_d} \right) \tag{6.3.22}$$

Q_e^+ is reduced plasma heat flux which is then used in equation 6.3.7 in place of Q_e.

The PELLET code has three different plasma response alternatives. The first is the unperturbed plasma response which treats the background plasma temperature as fixed. This approach is used in ablation model #0. The second is an adiabatic response where the incident electron energy is reduced to a level consistent with energy conservation between the non-ionized neutral gas and the unperturbed plasma. This is the approach of model #1. The third response is the collisionless, self-limiting plasma response using the energy reduction factor of equation 6.3.22. This response is employed for both models #2 and #3.

Computational Solution Method : The pellet code determines ablation rates and neutral particle deposition profiles by first dividing the plasma into a number of toroidally concentric shells within which the plasma properties are assumed constant. The cell volume, the path distance through the cell and the time the pellet spends in each cell is computed. The assumption is made of a constant pellet radial velocity. The solution method involves substitution of the hydrodynamic equation for the neutral cloud (6.3.1) into the energy conservation equation at the pellet surface (6.3.3.). For the first time step, the pellet radius is determined from initial conditions, and the neutral shield integral is taken as the parameter of iteration until the equation is satisfied and hence the ablation rate determined. For each iteration, the heat flux at the pellet surface Qp is determined by ascertaining energy attenuation through the neutral shield, the plasma shield and the attenuation due to plasma self limiting. The pellet is then stepped forward in time along its' trajectory with the new pellet radius r_p adjusted by the amount necessary to satisfy mass conservation at the pellet surface. Plasma properties and the pellet radius are considered invariant during each time step. Background plasma properties are

considered to change only when the pellet advances to a new cell. After the pellet has exited the cell, the perturbed density and temperature are computed by summing the ablation mass from each time step taken within the cell. This total is then added to the cell to arrive at a new cell density. The new temperature is computed by assuming an adiabatic mixing of the ablatant with the background plasma. Note that this assumption is made for all four models and does not affect ablation rates while the pellet is in the cell.

The PELLET code may be used to compute ablation profiles for four different variations of the neutral shield model. These are outlined below:

Model #0: This model uses a neutral shield with a fixed plasma shield fraction as per equation 6.3.17. Bulk plasma properties are considered unperturbed during the flux surface transit time. This model employs no plasma self limiting so that the background electron energy groups are considered fixed when determining ablation rates.

Model #1: This model uses a neutral shield with a fixed plasma shield fraction. In this case the plasma energy is reduced to a level consistent with the adiabatic mixing of the ablatant with the background plasma. The ablation rate for each time step is determined consistent with this adiabatic mixing.

Model #2: The neutral shield is again used, but in this case the ionization radius of the neutral cloud is assumed fixed as per the equation 6.3.19. A collisionless self-limiting plasma response is used with electron energies reduced by the factor given in equation 6.3.22.

Model #3: This model employs a neutral shield of a fixed thickness as per equation 6.3.18. The plasma response is again considered collisionless and self limiting as in Model #2.

Results:

The experimental value for the source function, S, (# atoms ablated per centimeter radial path traversed) is calculated by summing all four signals from tracking camera #1 and dividing by a constant, C. The constant is found by dividing the radial path integral of the summed signal by the number of atoms in the pellet. This is equivalent to setting the area under the source function vs. radial position curve equal to the mass of the pellet. Since the PELLET code is also given the pellet mass, the areas

under the experimental and predicted source functions will be set equal through the use of the constant. The use of the constant also implies the physical assumption that a fixed number of H_α photons are emitted for each ablated atom [4].

Experimental and theoretical source profiles were compared for 15 different shots with 3 different pellet sizes. The discharges were purely Ohmic with no RF power input. Pre-injection central electron temperatures were typically between 1 and 2 keV and with initial electron densities between $1-5\times10^{19}$ /m^3. Input parameters to the ablation code included density and temperature profiles as determined from the Two Color Interferometer (TCI) and ECE Michelson interferometer. Input to the code also included the plasma major and minor radiuses, elongations and the pellet size, velocity and molecular weight (D2 or H2). The plasma was divided into 55 radial cells and 10 electron energy groups were used to simulate a thermal electron energy distribution. Increasing the number of energy groups beyond ten was shown by Houlberg to have a negligible effect on results [39]. No fast ion or alpha energy groups were included in accordance with the ohmic plasmas of the pellet fueled discharges.

The results were consistent for all discharges analyzed and show the 0 th model to be the most successful in predicting ablation rates and penetration depth. Typical results for pellet sizes of .4 , .9 and 1.6×10^{20} atoms/pellet are shown in Figs. 6.3.5, 6.3.6 and 6.3.7 respectively. In these figures, the solid line represents the measured source function and the dotted lines represent the results from the four different ablation models.

The first and 0 th models are identical in their treatment of the neutral shield. The only difference between the two is that for model #1, the plasma on the ablation flux surface is assumed to be cooled by adiabatic mixing with the cold ablatant plasma whereas the plasma energy groups of the 0 th model are held fixed. Model #1 therefore assumes energy is conserved on the ablation flux surface, at least during the timescale of the pellets' passage.

In contrast to model #0, The assumptions of model #1 are seen to underestimate heat transfer to the pellet. The self limiting plasma response is physically valid. The failure of the model is most probably due to the omission of cross field energy transport. The implication is therefore that heat flow from the plasma interior takes place on a timescale comparable to the flux surface transit time. The rapid flow of heat from the interior flux surfaces would tend to maintain temperatures on the flux surfaces where

181

the pellet is located and increase ablation. Because the plasma energy is maintained by heat flow from the interior, the fixed plasma energy response of the 0th model is most effective in predicting ablation. It should again be stated that all the models presented neglect cross field energy transport, and that the success of model #0 is not due to the validity of the physical assumptions made but is instead due to the fact that fixing the plasma energy simulates the effect of cross field energy transport.

While the argument is admittedly crude, it is supported by experimental data. Figure 6.3.8 shows data from the soft X-ray arrays. On the X axis is plotted the channel number which is roughly proportional to radial location. The Y axis is proportional to emission intensity which is in turn dependent on density, temperature and impurity concentration. The figure presents radial emission profiles for ten different times each taken twelve microseconds apart. A correlation of the emission profile with the pellet radial location (as determined by the tracker), indicates that the plasma core temperature has fully collapsed while the pellet itself is still ten centimeters away from the magnetic axis. This then is evidence that a cooling wave precedes the pellet and therefore that cross field transport must be considered when attempting to accurately predict ablation rates. Temperature measurements made by grating polychrometer on the Alcator C Tokamak also suggested that a cooling wave preceded the pellet to the plasma interior. Unfortunately, quantitative temperature measurements on the microsecond timescale are currently un-available on C-Mod.

Figure 6.3.5-7 also present the results for the second and third models. While the two models have similarly shaped profiles to the source function observed, both overestimate penetration depth by at least 50%. The overestimation of penetration depth by models two and three was observed for all discharges studied and may be attributed to the assumptions made both about the plasma response and the neutral shield thickness. The background plasma response employed for both models was that of a collisionless, self-limiting plasma with no cross field energy transport. Under this assumption, electron energy fluxes from each energy group are depleted by the factor given in equation 6.3.22. The second assumption made was to fix in two different ways the size of the neutral shield. For model #2, a fixed ionization radius was employed as per equation 6.3.19 and in model #3 a fixed neutral shield thickness was used as in equation 6.3.18. Of the two models, the assumption of a fixed ionization radius results in the highest shielding and largest penetration depths. It is unclear for models #2 and #3

what the relative shielding contributions are from plasma self-limiting versus changes to the neutral shield thickness. It is clear however, that both effects contribute to shielding.

Results are qualitatively similar for the three pellet sizes observed. It must be stated that the ablation results presented were measured from purely Ohmic discharges with a fairly narrow temperature range (1-2 keV peak electron temperature). Consequently, results must not be generalized to include RF or neutral beam heated plasmas where the non-thermal energy fraction may be significant.
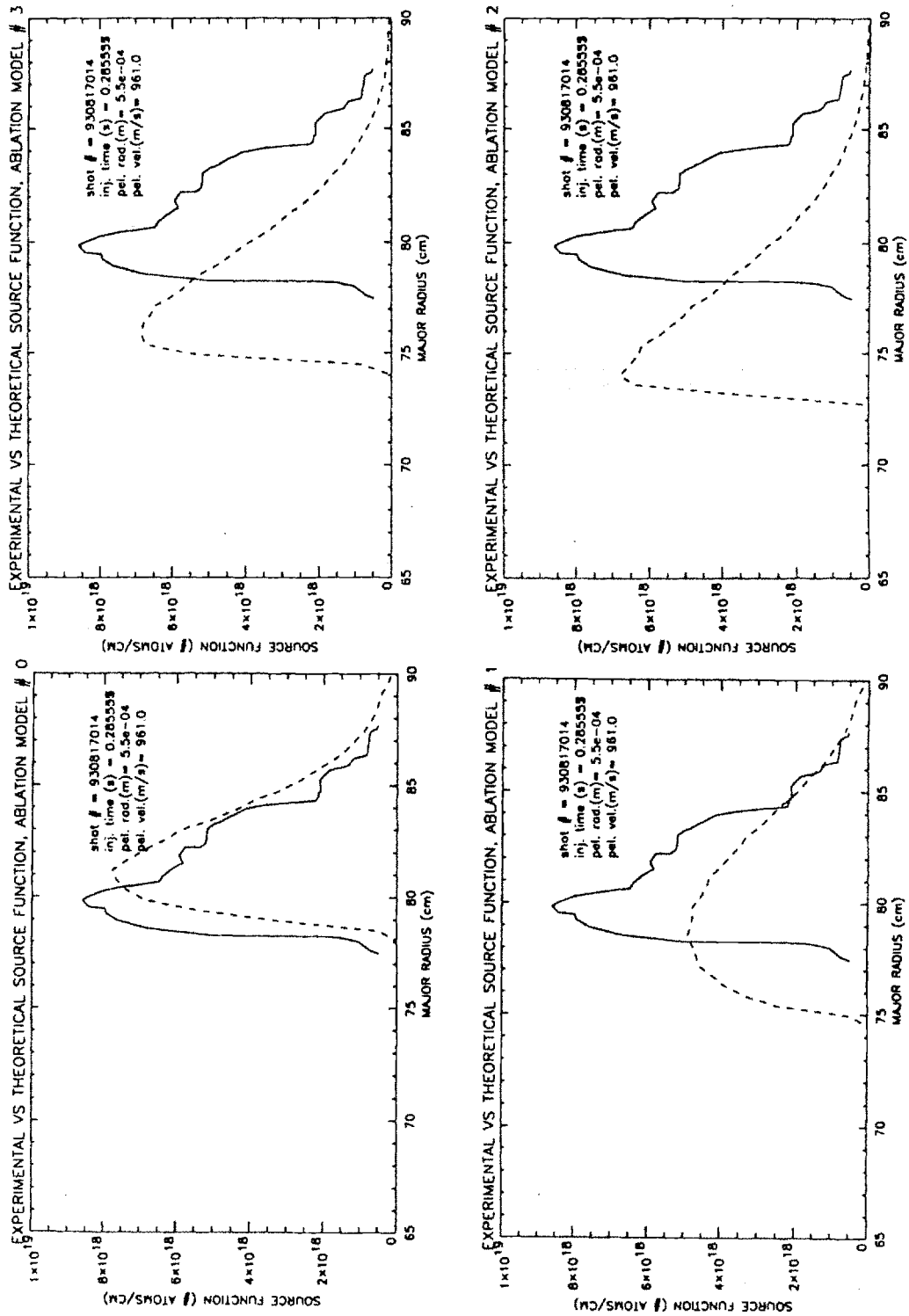
Fig. 6.3.5: Experimental vs. theoretical source function for models #0-#3.
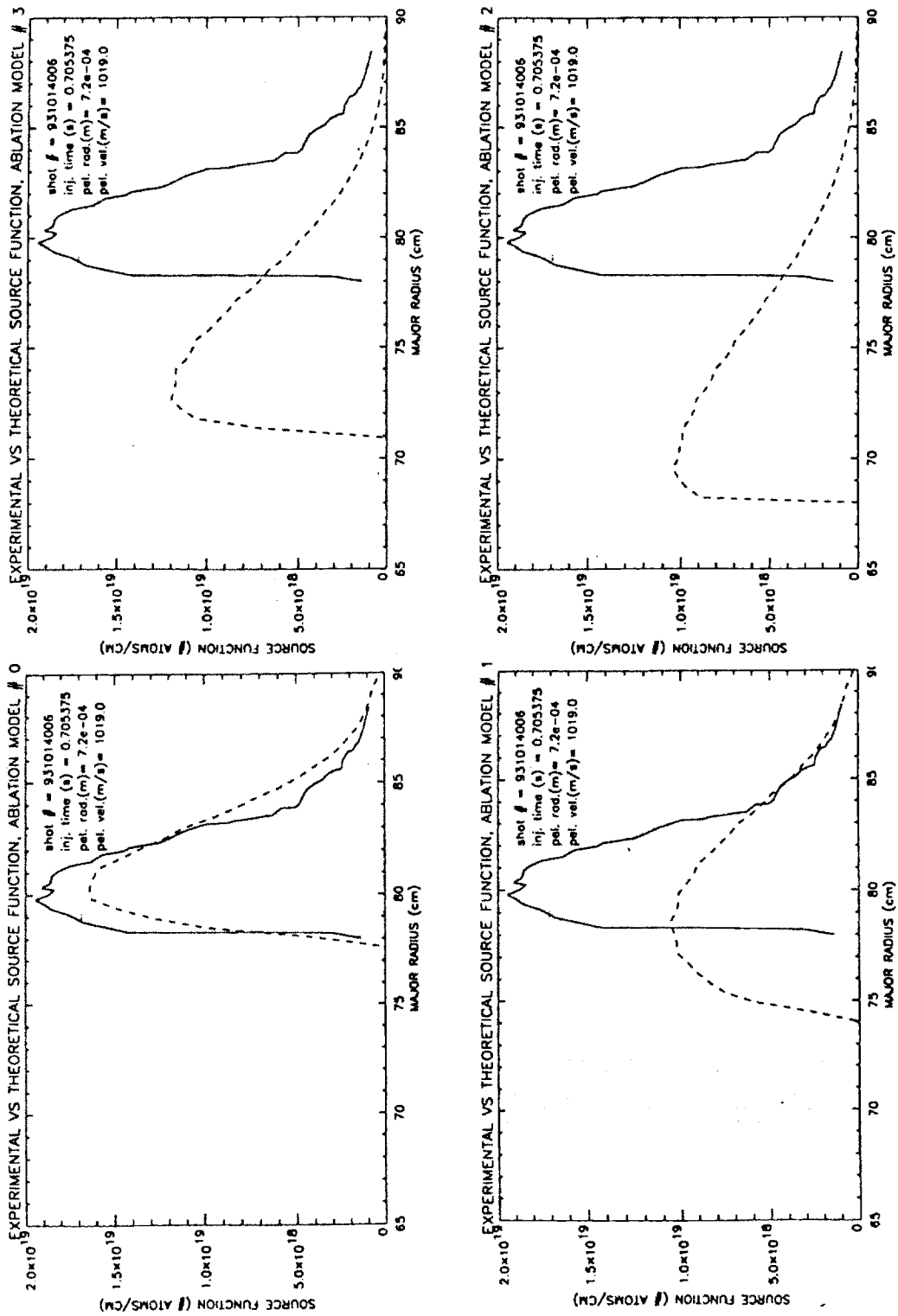(17 Ga. pellet). Dotted lines represent the theoretical prediction.

Fig. 6.3.6: Experimental vs. theoretical source function for models #0-#3.
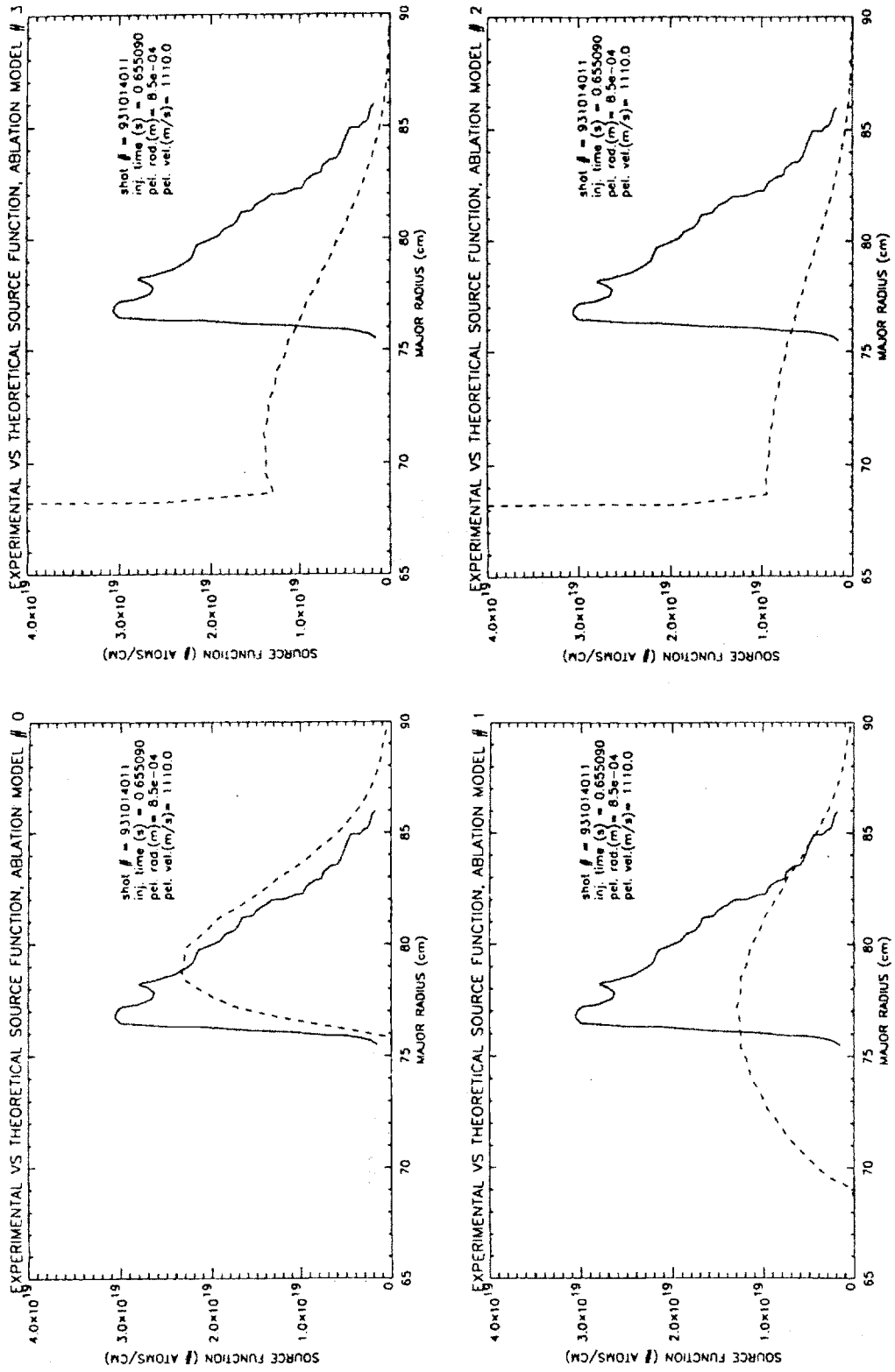(15 Ga. pellet). Dotted lines represent the theoretical prediction.

Fig. 6.3.7: Experimental vs. theoretical source function for models #0-#3. (13 Ga. pellet). Dotted lines represent the theoretical prediction.
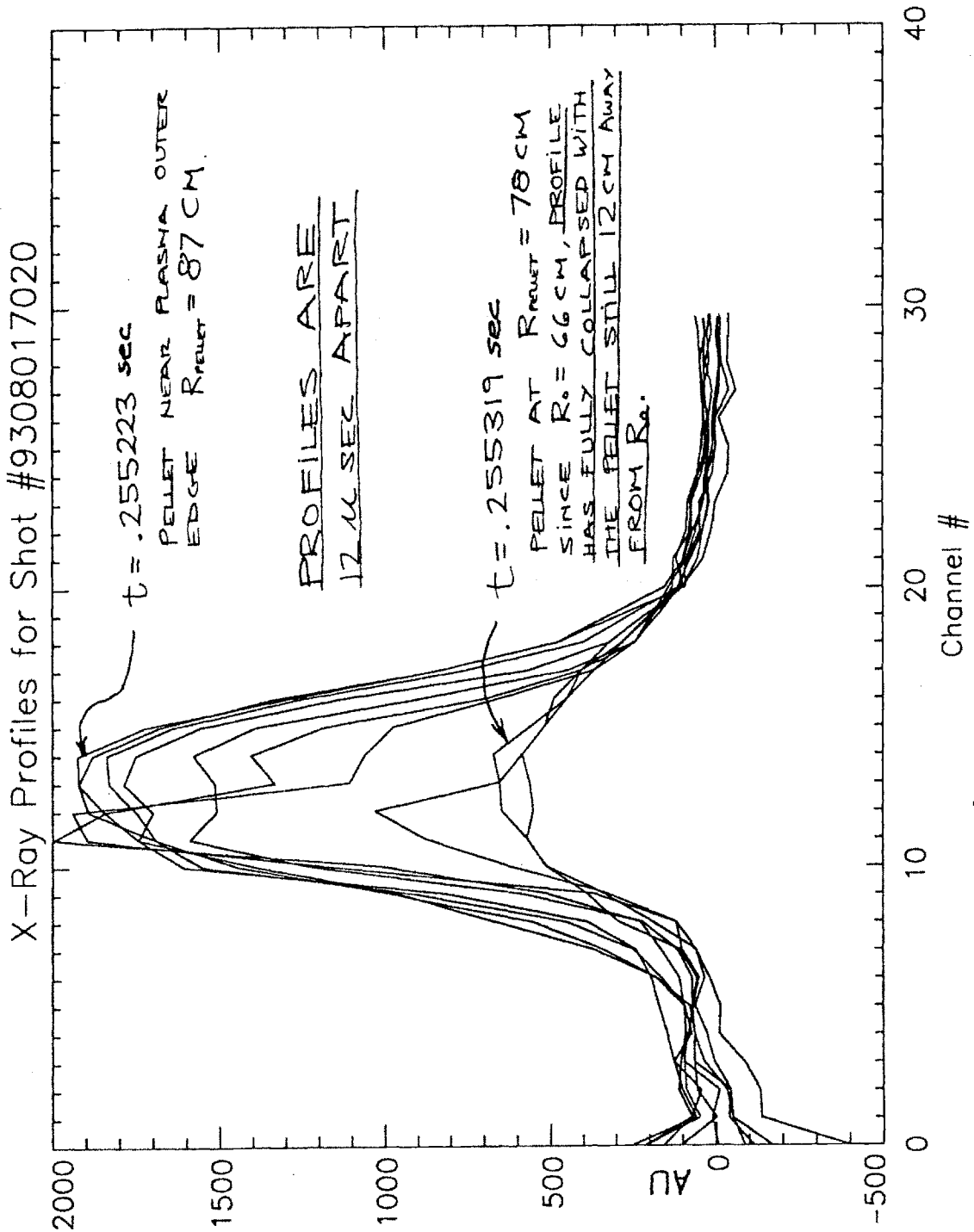
Fig. 6.3.8: Soft X-ray emission profiles taken 12 μ seconds apart show that a cooling wave precedes the pellet into the plasma.

187

6.3.3   Density Perturbations On the q=1 Rational Flux Surface

The C-Mod soft X-ray imaging system and two color interferometer (TCI) have been used to observe highly localized perturbations in both density and x-ray emission following deuterium pellet injection. The data appears to be consistent with the formation on the q=1 surface of a high density plasma helix or "snake" with an m=1, n=1 periodicity. These structures are seen immediately following pellet injection and have been observed to persist for up to 35 milliseconds after injection.

Historically, these perturbations were first observed following pellet injection on the JET Tokamak in the United Kingdom by A. Weller, R. Granetz and others using a soft x-ray imaging system [58]. These perturbations were found to have an m=1, n=1 structure and radial location consistent with their formation on the q=1 surface. Density measurements by multichannel far-infrared interferometer and microwave transmission interferometer indicated maximum density perturbations of up to twice the local plasma density. Electron temperature measurement by ECE polychromator indicated a temperature drop immediately following injection followed by a full recovery after 100 milliseconds [58]. The regions of enhanced x-ray emission and density were often found to persist for the remainder of the discharge ($\geq$ 1.9 seconds) [58].

Observations made on Alcator C-Mod using soft x-ray detector arrays and the TCI interferometer indicate that the phenomena observed have features consistent with the snakes observed on JET. Soft x-ray emission measurements are made using two 38 channel photodiode arrays. The two diode arrays are box mounted on the vacuum vessel wall at discrete poloidal locations. Each array employs a 1 x 3 mm slit aperture with each diode in the array viewing emission along a specific chord in the plasma. The array of viewing chords forms a fan shaped pattern which encompasses the plasma cross section. Signals from two arrays may be used to form two dimensional emission profiles using tomographic reconstruction techniques [59]. Beryllium filters fifty microns thick are

employed on two arrays to limit the diode's response to emissions with energies above 1 keV [59].

Figure 6.3.9 shows the central line integrated density and soft x-ray emission on a single detector channel following the injection of a deuterium pellet of $.9 \times 10^{20}$ atoms. The small perturbation in density and x-ray emission following injection is the result of the high density, helical plasma tube sweeping through the detector and interferometer viewing chords. The apparent poloidal rotation of the snake may be due to bulk plasma rotation either poloidally or toroidally. Figure 6.3.10 shows the emission profile from all thirty eight x ray channels as a function of time. Light regions correspond to areas of enhanced emission.

The cross sectional size of the snake may be deduced from the width of the emission perturbation and is between 2 and 3 centimeters in diameter. Spatial resolution for the x-ray array is approximately 2 cm.

The figure 6.3.11 depicts density measurements from the TCI interferometer. The data are presented in the same way as for soft X ray emission, that is with the channel number, hence radial position, on the horizontal axis and time on the vertical. Regions of increased density appear lighter. For a 2-cm diameter snake, the density perturbations measured indicate the average snake internal density is approximately 50 percent higher than that of the background plasma.

The m=1, n=1 helicity of the snake was experimentally confirmed by recording the phase angle difference between measurements made with x-ray arrays and the interferometer. For a snake with n=1 this phase angle will correspond to the angular separation between the toroidal locations of the two instruments. X-ray emission measurements made from different poloidal locations were used to establish the m=1 structure. Data from the soft X-ray detector arrays confirm that the snake radial location is closely coincident with the sawtooth inversion radius. Experimentally, this supports the view that the snake resides on the q=1 surface and therefore that the structure of the snake follows that of the magnetic field lines [65]. Measurements have confirmed that the snakes observed on C-Mod have a m/n =1 structure to within 1% [60]. The snake therefore serves as an accurate marker for the q=1 surface. Figure 6.3.10 indicates the snake survives sawtooth events. Changes in the radial location of the q=1 surface before and after sawtooth collapse may be used to yield information about the q profiles and
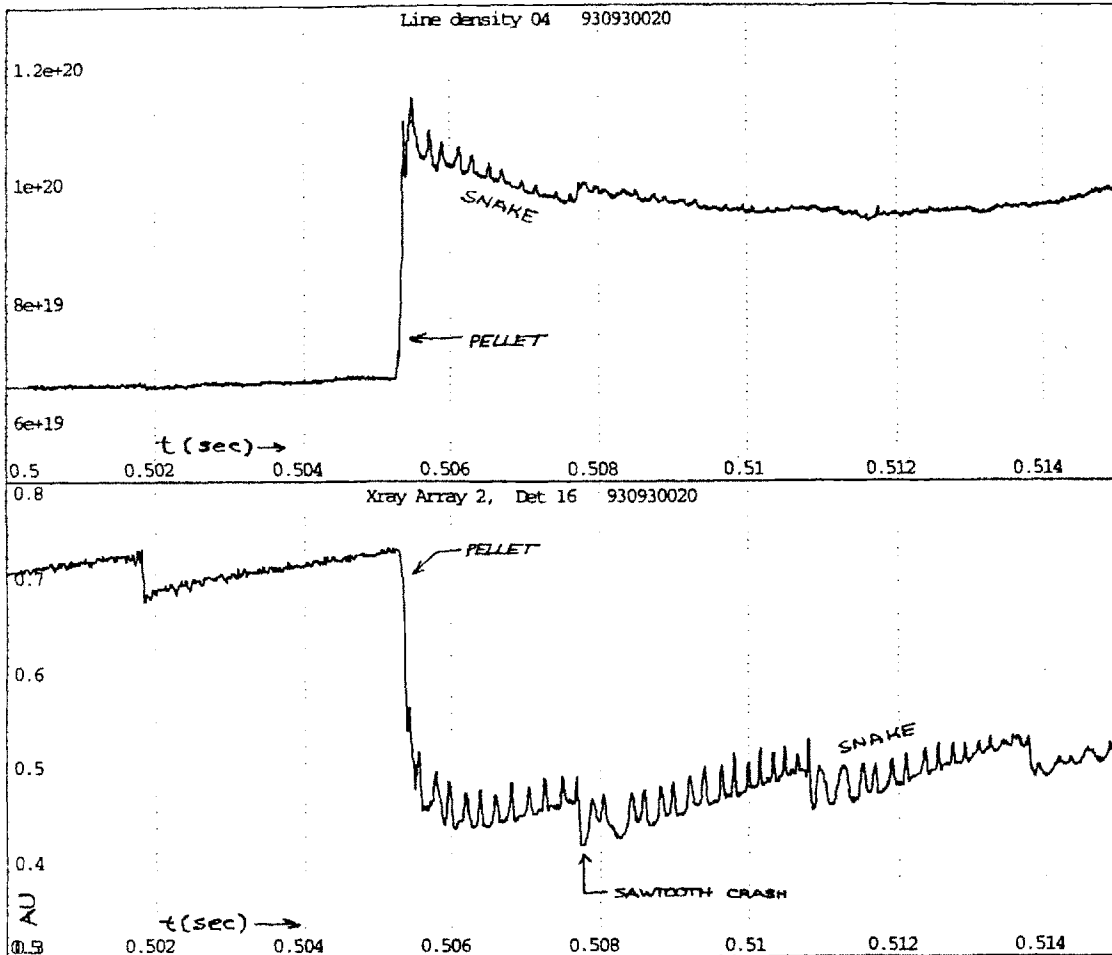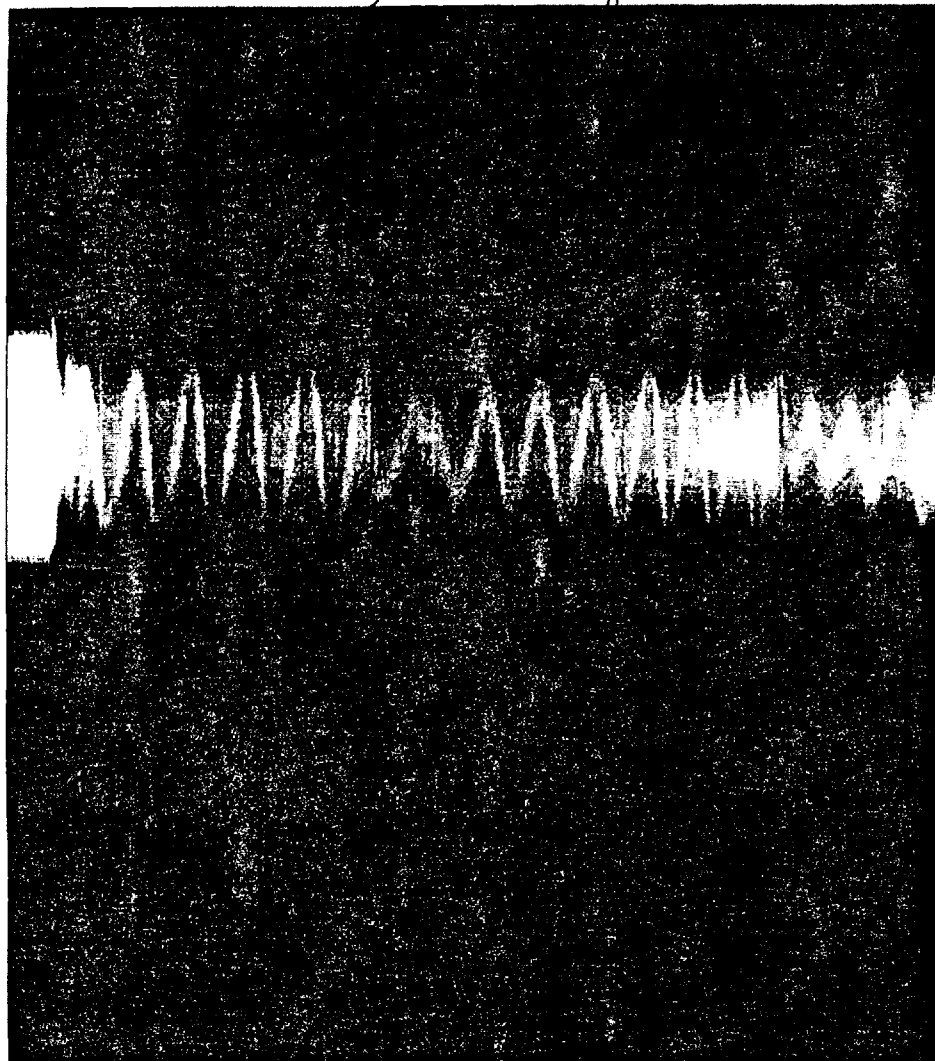
Fig. 6.3.9: Single channel soft X-Ray emission and TCI Interferometer signals showing the "snake" density perturbation following pellet injection.

190

Fig. 6.3.10: X-ray emission profile vs. time for all 38 detector channels.
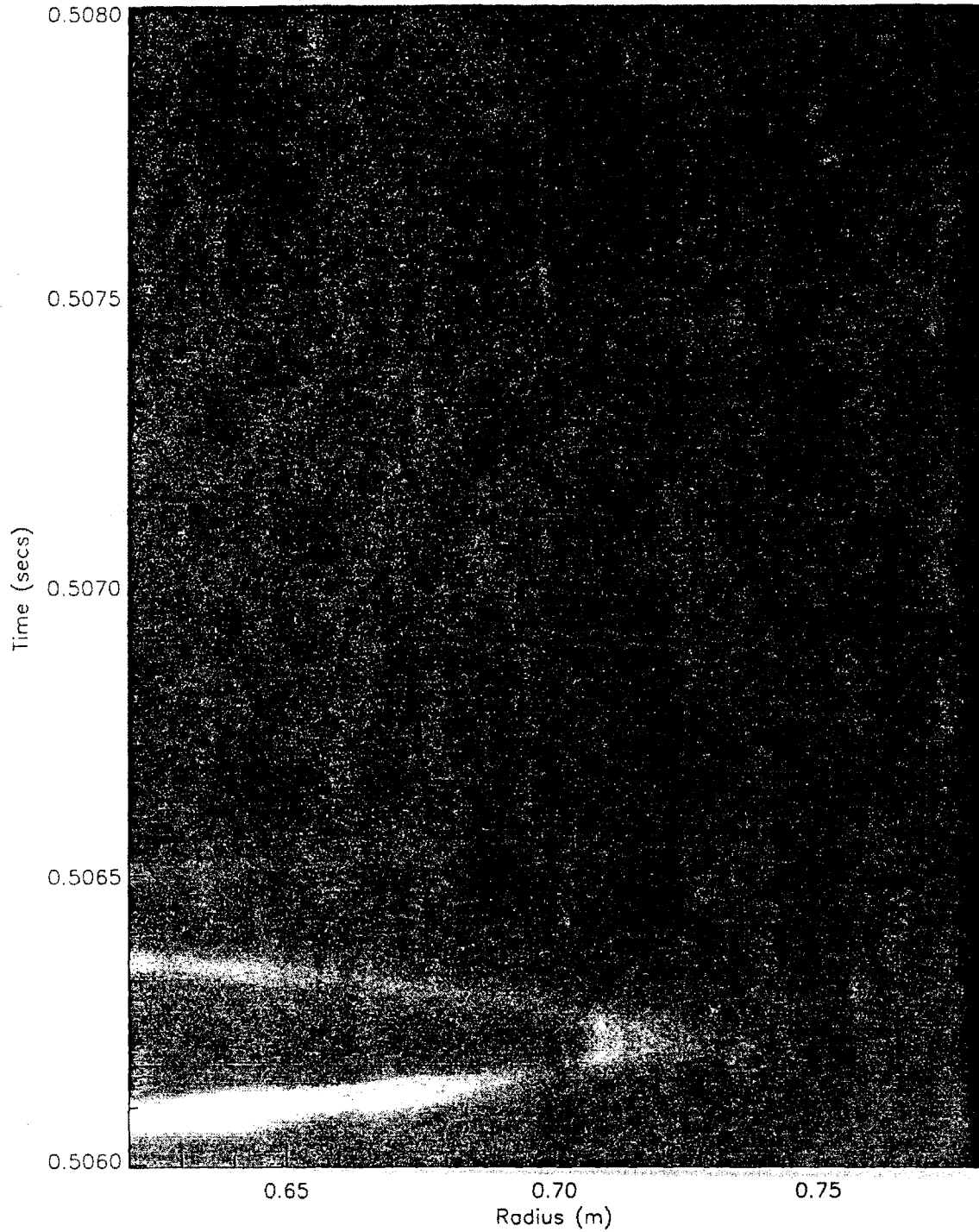Light areas represent enhanced emission.

Fig 6.3.11: TCI Interferometer density profile vs. time. Light areas represent regions of higher line integrated density.

poloidal current distribution [60]. The observed frequency of rotation of the snake is typically 2.5 kHz. If the assumption is made that the snake structure is fixed within the bulk plasma this then becomes an indictor of plasma bulk rotation at the q=1 surface, though the direction may be either toroidal or poloidal.

A particularly interesting feature of snakes is their particularly long effective particle confinement. On C-Mod Snakes have been observed to persist for periods of up to 35 m seconds following injection without decay. The decay itself does not appear to be strictly exponential and the snake often disappears suddenly, sometimes coincident with a sawtooth crash. It is unclear whether the persistence of the snake is due to reduced particle transport from the snake, or whether pellet injection has allowed access to a new non-axisymmetric equilibrium configuration with regions of high localized density as is speculated by Weller and others for snakes on JET[59]. If the persistence is due to enhanced particle confinement, one expects the snake itself to be composed of ions originating from the pellet. The upper bound on particle confinement would then be based on the collisional diffusion time. A rough estimate may be made of the diffusion coefficient for the snake by dividing the square of its radial dimension by its observed lifetime. The upper limit of the diffusion coefficient thus obtained is approximately 30 cm^2 / sec. Diffusion within the snake is therefore between one and three orders of magnitude less than the 1000 to 10,000 cm^2 / sec values typical of the background plasma. The classical electron-deuteron collisional diffusion coefficient for the bulk plasma is still two orders of magnitude less than the lower limit observed for the snake. It should be stressed however that because the snakes often do not appear to decay exponentially the diffusion coefficient may actually be much less than 30 cm^2 / sec observed.

Estimates of the snake energy confinement require quantitative temperature measurements within the snake. Because this information is currently not available on C-Mod, no definitive statements may be made about snake energy confinement time. Weller and Granetz suggest that enhanced particle confinement may be due to the magnetic island formation resulting from the altered plasma resistivity within the snake [58] [60]. Another explanation may be that density gradients in the snake give rise to radial electric fields in the snake which then support E x B plasma rotation about the snake centerline. This rotation is then conjectured to reduce particle transport by decreasing the scale length of turbulent eddies. These arguments have the same flavor as those used to explain the H-mode behavior.

A discussion about snakes has been included here both as an example of interesting plasma phenomena resulting from pellet injection and also as an area which clearly warrants further study. Quantifying the particle and energy confinement of snakes and attempting to understand the mechanism of enhanced confinement may provide valuable information on the physics of anomalous transport and enhanced tokamak confinement . My warmest thanks go to both Dr. Robert Granetz and Dr. James Irby for their assistance in studying the phenomena.

Chapter 7:   Conclusions

It is important at some point to review the original goals of this work and to asses to what degree these goals were met. Equally important is to summarize what was learned and what significant questions were raised by the research.

From an engineering and viewpoint, the work of the project could be divided into two phases. The first phase was to design and build an injector for use on Alcator C-mod. The design was directed to fulfill three primary requirements: 1) Operational flexibility 2) High reliability 3) Remote operation with minimal maintenance. To meet these goals, a number of novel features were incorporated into the design. These features include a configuration with twenty barrels and a closed cycle refrigerator for *in-situ* condensation of the fuel gas. The second phase of the project was to test the injector both in the lab and during injection experiments on C-Mod. This stage of the project attempted to characterize injector performance and to establish the degree to which the original design goals were met. The final testing phase of the projects shifts perspective slightly to include preliminary observations made during injection experiments. The final phase was in many ways the most rewarding, both as a vindication of the design and because of the potential to observe new and interesting plasma phenomena.

In hindsight, fabrication of the injector proved remarkably trouble free. This is was a testimony to the fact that the design was well thought out from the point of view of fabrication ease and assembly (The credit here goes primarily to Martin Greenwald and Art Gentile). The only exception was the barrel to conduction disk brazing which required more time and effort than originally anticipated.

Initial thermal tests of the injector sought to establish both the heat loads to the refrigerator and the temperature gradients across the thermal system components. These tests revealed the closed cycle refrigerator to be successful in cooling the barrels to temperatures below that required to freeze deuterium (14 K.). Hydrogen freezing proved impossible though due to higher than anticipated temperatures drops across the felt metal joints. This was traced to the failure of the "equivalent length" model used to

predict thermal resistance at temperatures below 20 K. To correct these problems, a new single piece thermal link was employed between the refrigerator cold head and the barrel cold plate. Feltmetal joints were replaced with highly polished surfaces and a thin coat of vacuum grease to improve surface contact. With the single piece thermal connection, temperatures were reduced to 12K. at the barrel freezing zone and hydrogen pellets were successfully formed and accelerated.

Laboratory testing of the injector sought to demonstrate successful pellet freezing and acceleration and to quantify the effects of varying parameters in the freezing process such as freeze time and fueling pressure. The tests required the use of the laser -photodiode light gates for velocity measurement and pellet photography for mass measurement. Initially not all barrels froze pellets. This was found to be due to poor thermal connections between the barrel conduction disk and the barrel cooling plate. After improving the thermal connection and changing to the single piece thermal link, pellets could be reliably be made in all barrels. Deuterium pellets were found to freeze under a range of pressures from 8 to 85 torr, for freeze times as short as ninety seconds. Hydrogen pellets were found to require between 35 and 75 torr and freeze times of at least 100 seconds. Mass measurements were made for both deuterium and hydrogen pellets to establish the variation of pellet mass with freeze time and pressure. While deuterium pellets could be held in vacuum for up to half an hour before firing without any detectable mass reduction, hydrogen pellets were found to sublimate rapidly and could not be detected after more than five minutes exposure to vacuum. Velocity measurements established the maximum attainable pellet velocity to be around 1300 m/second with hydrogen propellant pressures of 1500 P.S.I.. Optimized deuterium and hydrogen pellet freezing "recipes" were incorporated into PLC controlled freezing cycles. The automated freezing cycles were found to improve shot to shot "batch" uniformity and facilitated reliable pellet formation. Repetitive mass measurements were then made to establish barrel reliability, and to find the average and standard deviation in the pellet mass from all barrel sizes.

Only a few relatively minor engineering changes are recommended. These include the use of quarter inch tubing for all process gas system lines to facilitate line purging and leak checking. It might also have been beneficial to locate the solenoid actuated fueling valves outside of the cryostat, since the effective cooling of the valves in a vacuum proved difficult. Also recommended are the addition of a set of conduction limiting valves to reduce the propellant gas load into the tokamak. These valves are

196

currently under development and should be installed in the injector early in 1994. It would also be desirable to reduce the freezing zone temperature a few degrees or from twelve to perhaps nine or ten degrees Kelvin. While this is not necessary for deuterium operation, it would have the beneficial effect of reducing hydrogen pellet fragmentation and sublimation upon exposure to vacuum. Unfortunately, a review of currently available closed cycle refrigerators indicates the CRYOMECH GB37 refrigerator employed has the minimum available cold head temperature (9K). Some refrigerators using a third stage Joule-Thompson cycle can reach lower temperatures but not with the required heat capacity. Operation on Alcator thus far has required freezing only deuterium pellets, and the closed cycle system has accomplished this task reliably without the problems and expense of liquid helium heat exchangers.

Over fifty pellet fueled discharges were made in the period from August to November of 1993. Three different pellet sizes were used corresponding to .5, .9 and 1.6 x 10^{20} atoms/pellet. Background plasma electron temperature for these discharges was between .5 and 2 keV with average densities ranging from .5 to 1 x 10^{20} / m^3. Plasma currents ranged between 400 and 800 Kilo amps with toroidal magnetic fields of five tesla. Following injection, a rapid density increase is seen on the pellet transit timescale ($\equiv 200 \ \mu$ sec) followed by an exponential decay to a new level typically between 10 and 50 percent higher than the pre-injection value. Comparisons of the plasma total particle inventory immediately before and after injection indicate that the fraction of retained pellet mass increases with pellet size. This is probably a result of the greater penetration depth observed for the larger pellets. Electron temperature measurements indicate that the density rise is accompanied by a drop in temperature also on the transit timescale to a level consistent with an adiabatic injection process.

The Pellet tracker was successfully used in injection experiments to record the three dimensional trajectory of pellets into the tokamak plasma and to experimentally determine the ablation source function by correlating H_α emission to the pellet radial location. The trackers were designed to have an improved tracking resolution and the system was the first to use two, two dimensional position sensing photo detectors in a stereoscopic camera system. Data obtained during calibration experiments indicates the system has a time resolution of 2 μ seconds and a spatial resolution of three millimeters transverse to the line of sight and six millimeters parallel. Data from the trackers was used to establish that pellet radial penetration depth for single pellet discharges ranged from thirty to eighty six percent of the plasma minor radius. Penetration depth was

observed to decrease with pellet size and plasma temperature. The radial paths of the pellets were seen to closely follow a straight ballistic trajectory, except towards the end of the path where some slowing was observed which was generally accompanied by a deflection of the pellet path in the direction of electron current with velocities of up to 500 m/sec.

A comparison was made of the experimentally derived source function with four different variations of the neutral shield model. The best agreement with experimental data was obtained for the model that assumes the background plasma energy on the pellet flux surface is fixed, at least during the timescale of the pellets passage. This result suggests that a cooling wave precedes the pellet and that the plasma energy is therefore maintained approximately fixed on the pellet flux surface by the rapid flow of heat from the plasma interior. This hypothesis is further confirmed by data from soft x-ray diode arrays which indicate that the plasma core temperature has fully collapsed while the pellet is still ten centimeters away from the magnetic axis. The assumptions of the first model are the most successful because they reproduce the effects of cross field energy transport from the plasma interior. The conclusion to be reached is that the effects of cross field energy transport should be considered when attempting to accurately predict pellet ablation rates and penetration depth.

Localized density perturbations on the q=1 flux surface were observed following pellet injection. Measurements made with soft X-ray arrays and the TCI interferometer were consistent with the formation of a ring of high density plasma with a specific m=1 n=1 periodicity and location on the q=1 flux surface. The ring was measured to have a cross section of approximately two centimeters in diameter and an average density fifty percent higher than that of the background plasma. The phenomena were observed to persist for up to 35 m seconds following injection, and therefore possesses particularly good effective particle confinement.

With the conclusion of the initial injection experiments on Alcator C-Mod, it becomes possible to judge how well the initial design goals of the injector were met. Operational flexibility was certainly achieved in that pellets of three different sizes were used and these were fired both individually and sequentially with any desired timing. The goal of high reliability was also clearly attained in that pellets were successfully fired into all discharges requested. Remote operation with minimal maintenance was also demonstrated in that the injector could remain cooled down and operational under

198

remote control for periods in excess of five days. This was done without the need for any direct maintenance and was the standard operating procedure. The pellet trackers also operated with remarkably good spatial resolution, both in following the pellet trajectories and in providing the ablation source function. Some shots were lost due to cabling faults and signal level saturation but these problems were easily correctable.

The injection experiments performed thus far on Alcator should only be thought of only as a beginning. The largest pellet size has yet to be fired as these will require the megamp plasma current levels made possible by the installation of the flywheel to the alternator. Future injection experiments will certainly see the attainment of densities well into the $1 \times 10^{21} / m^3$ range. The pellet tracker should also prove to be a useful diagnostic in studying transport issues on the pellet transit timescale.

References

1. C. T. Chang et al., "The Feasibility of Pellet Re-Fuelling Of A Fusion Reactor," *Nuclear Fusion* , Vol. 20 (1980), 859-93.

2. Thomas James Dolan, *Fusion Research , Vol 3* (New York, N. Y.: Pergamon Press, 1982), 738.

3. M. Greenwald et al., "Studies of the Regime of Improved Particle and Energy Confinement Following Pellet Injection into Alcator C," *PFC report CP-86-20* ,(1986), 1-16.

4. M. Kaufman, "Review On Pellet Fueling," *Controlled Fusion*, Vol. 28, (1986), 1342.

5. H. P. Furth, "Magnetic Confinement Fusion,"*Science*, Vol.249 (1990), 1522-27.

6. S. L. Milora, "Review of Pellet Fuelling," *Journal of Fusion Energy*, Vol.1, No.1 (1981), 15-48.

7. I. H. Hutchinson et al., "The Physics and Engineering of Alcator C-MOD," *PFC report RR-88-11* , (1988), 1-27.

8. S. M. Wolfe et al., "Effect of Pellet Fueling On Energy Transport In Ohmically Heated Alcator C Plasmas," *PFC Report 8662-10-1*, (1986), 1-12.

9. S. K. Combs, " A Three-Barrel Repeating Pneumatic Pellet Injector For Plasma Fueling Of The Joint European Torus, " *ORNL Conf-871125-1* (1992), 1-8.

10. D. D. Schuresko et al., "Pellet Injector Research at Ornl," ORNL *DE87-010402* , (1992).

11. S.L. Milora et al., "Results of Hydrogen Pellet Injection Into ISX-B," *Nuclear Fusion* , Vol. 20, No. 12 (1980), 1491-99.

12. Robert A. Gross, *Fusion Energy* (New York, N.Y., John Wiley & Sons, 1984), 188-227.

13. Nicholas A.Krall and Alvin Trivelpiece, *Principles of Plasma Physics*, (New York, N.Y., McGraw-Hill Book Co., 1973)

14. Francis F. Chen, *Introduction to Plasma Physics and Controlled Fusion, Volume 1: Plasma Physics*, 2nd ed. (New York, N. Y., Plenum Press, 1985).

15. M. J. Dunning et al., "Time Dependent Simulation of Pellet Evaporation in Tokamak Plasmas," *Nuclear Fusion,* Vol. 30, No. 5 (1990), 919-24.

16. S. K. Combs et al., "Pellet Fueling Development at Ornl," ORNL *DE87-000360* (1992) .

17. M. Kaufmann et al., "Refuelling and Helium Pumping in a Tokamak Reactor," *Nuclear Fusion,* Vol.25, No.1 (1985), 89-93.

18. J. Lafferranderie et al., "Experimental Test of 6mm Diameter D2 Pellets Produced by In-Situ Condensation," *Fusion Technology 1986: Proceedings of the 14th Symposium* (1986), 1367-73.

19. D. F. Duchs, "Recent Steps Towards a Controlled Thermonuclear Fusion Reactor from the JET Tokamak Device," *JET-P (92)91* (1992).

20. M. J. Gouge et al., "The CIT Pellet Injection System: Description and Supporting Research and Development," *Review of Scientific Instruments 61* (1989), 1241-43.

21. M. J. Gouge et al., "The Ornl Plasma Fueling Program," ORNL *CH280-9/89/0000-1299, IEEE* (1989).

22. M. Greenwald et al., "Pellet Fuelling Experiments in Alcator C," *Proceedings of the Tenth International Conference on Plasma Physics and Controlled Fusion Research, IAEA , London* 1984,

23. M. Greenwald et al,. "A New Look at Density Limits in Tokamaks," *PFC/JA-86-22* (1988), 1-12.

24. R. R. Parker et al,. "Progress in Tokamak Research at MIT," *Nuclear Fusion,* Vol.25, No. 9 (1985), 1127-31.

25. A. L. Qualls et al., "Pellet Ablation and Particle Deposition Studies on TFTR," *DE-AC05-84OR21400* (1990).

26. G. A. Wurden et al., "High Resolution Pellet Diagnostics on TFTR," *LANL-92-2209* (1992).

27. M. J. Gouge et al., "A Combined Microwave Cavity and Photographic Diagnostic For High Speed Projectiles," *Review of Scientific Instruments, 61* (1990), 2102-5.

28. B. B. Kadomtsev et al., "Tokamaks," *Nuclear Fusion,* Vol. 30, No. 9 (1990), 1675-90.

29. S. K. Combs et al., "Operation and Reliability of a Pneumatic Hydrogen Pellet Injection System on the Joint European Torus," *CH2820-9/89/0000-1305 IEEE* (1989) , 1305-9.

30. M. Onozuka et al., "Development Of Upgraded Pellet Injector For JT-60," *CH2820-9/89/0000-125 IEEE* (1989), 1260-64.

31. A. L. Qualls et al., "Eight-Shot Pneumatic Pellet Injector For The Advanced Toroidal Facility," *CH2820-9/89/0000-1244 IEEE* (1989), 1245-47.

32. A. C. Anderson and R. B. Rauch, "Another Comparison of Thermal Bonding Agents," *Review of Scientific Instruments , Nov.* (1969), 470.

33. A. C. Anderson and R. E. Peterson, "Selection of a Thermal Bonding Agent for Termperatures Below 1 K," *Cryogenics, Oct.* (1970), 43033.

34. J. Kopp and G. A. Slack, "Thermal Contact Problems In Low Temperature Thermocouple Thermometry," *Cyrogenics, Feb.* (1971), 22-24.

35. M. M. Kreitman, "Low Temperature Thermal Conductivity of Several Gases," *Review of Scientific Instruments,* Vol 40, No. 12 (1990), 1563-5.

36. M. A. Brown, "A Reliable Low Thermal Resistance Bond Between Dielectrics And Metals For Use At Low Temperatures," *Cyrogenics, Oct. 1970* (1970), 439.

37. A. C. Anderson and R. B. Rauch, "Low-Temperature Thermal Conductivity of a Suspension of Copper Particles," Journal of Applied Physics, Vol. 41, No. 9, (1970), 3649-51.

38. J. G. Hust, "Thermal Anchoring of Wires in Cryogenic Apparatus," *Review of Scientific Apparatus,* Vol. 41, No. 5 (1970), 622-4.

39. W. A. Houlberg et al., "Neutral And Plasma Shielding Model For Pellet Ablation," *Nuclear Fusion,* Vol. 28, No. 4 (1988), 595-610

40. M. Kaufmann et al., "Plasma Shielding Of Hydrogen Pellets," *Nuclear Fusion,* Vol. 26, No. 2 (1986), 171-7.

41. P. B. Parks and R. J. Turnbull, "Effect of Transonic Flow in the Ablation Cloud on the Lifetime of a Solid Hydrogen Pellet in a Plasma," *Physics Fluids 21 (10), Oct.* (1978), 1735-41.

42. B. Pegourie and M. A. Dubois, "Diagnostic Of The Current Density Profile In the Vicinity Of Q=1: The H_α Emission Of Ablated Pellets," *Nuclear Fusion,* Vol. 30, No. 8 (1990), 1575-83.

43. R. D. Durst et al., "Experimental Observations Of The Dynamics Of Pellet Ablation On The Texas Experimental Tokamak," *Nuclear Fusion,* Vol. 30, No. 1 (1990), 3-8.

44. S. L. Milora et al., "Pellet Injection Into PDX Diverted Plasmas," *Nuclear Fusion,* Vol. 22, No. 10 (1982), 1263-70.

45. S. K. Combs, "Pellet Injection Technology," *Review Of Scientific Instruments,* Vol. 64, No. 7 (1993), 1679-94.

46. F. S. Felber et al., "Effects Of Atomic Processes On Fuel Pellet Ablation In A Thermonuclear Plasma," *Nuclear Fusion,* Vol. 19, No. 8 (1979), 1061-71.

47. M. Grapperhaus et al., "Low Pellet Velocity Fueling Options for ITER,"

ORNL-work under contract DE-AC05-84OR21400 (1992).

48. C. T. Chang, "The Magnetic Shielding Effect Of A Re-Fuelling Pellet," *Nuclear Fusion,* Vol. 15, (1975), 595-603.

49. P. B. Parks, "Magnetic-Field Distortion Near An Ablating Hydrogen Pellet," *Nuclear Fusion,* Vol. 20, No. 3 (1980), 311-20.

50. L. R. Baylor et al., "Local Transport In Pellet-Fueled, ICRF Heated Discharges In TFTR," *ORNL DE-AC05-84OR21400* (1992).

51. W. L. Rowan et al., "Transport With Pellet Fuelling In The Texas Experimental Tokamak," *Nuclear Fusion,* Vol 30, No. 5 (1990), 903-18.

52. P. B. Parks et al., *Nuclear Fusion,* Vol. 17 (1977), 539.

53. S. L. Milora, *IEEE Transactions Plasma Science,* Vol. 6, (1978) , 578.

54. ISML, "Math Library Version 2.0 User's Manual," IMSL, (1991).

55. B. A. Hands, *Cryogenic Engineering,* Academic Press (1986).

56. Cryomech, "Model GB37 Cryogenic Refrigerator Operation and Service Manual", Cryomech, Syracuse, N.Y.

57. A. F. Mills, *Heat Transfer* (Homewood, IL.: Irwin, 1992).

58. A. Weller et al., "Persistent Density Perturbations At Rational -q Surfaces Following Pellet Injection In The Joint European Torus," *Physical Review Letters,* Vol. 59, No. 20 (1987), 2303-6.

59. R. S. Granetz and L. Wang, "Design of the X-ray Tomography System on Alcator C-MOD," *PFC Report* (1992), 1-13.

60. Granetz, Robert, private communication, MIT Plasma Fusion Center, 1993.

61. L. D. Landau and E. M. Lifshitz, *Fluid Mechanics* (Reading, MA.: Addison-Wesley, 1959).

62. P.C. Souers, *Cryogenic Hydrogen Data Pertinent to Magnetic Fusion*

Energy, Lawrence Livermore National Library, Livermore CA, 1979.

63. United Detector Technologies Inc., "Position Sensing Photo Detectors," 12525 Chadron Ave., Hawthorne, CA. 90250.

64. Lakeshore Cryotronics Inc., " Temperature Sensing Diode Data Sheet", 64 E. Walnut St., Westerville, Oh. 43081.

65. R. Granetz, A. Edwards, R. Gill, A. Weller. "Study of MHD Phenomena in JET with Small Signal X-Ray Imaging" , 14 th European Conference on Plasmas and Controlled Fusion., (pg. 1258) June 1987, Madrid.

Acknowledgments